Title
Polypyridyl–Metal Complexes for the Electrocatalysis and Activation of Small Molecules

Author
Zee, David Zhi Hong

Publication Date
2017

Polypyridyl–Metal Complexes for the Electrocatalysis and Activation of Small Molecules

By

David Zhi Hong Zee

A dissertation submitted in partial satisfaction of the

requirements for the degree of

Doctor of Philosophy

in

Chemistry

in the

Graduate Division

of the

University of California, Berkeley

Committee in charge:

Professor Jeffrey R. Long, Chair
Professor Richard A. Andersen
Professor Bryan D. McCloskey

Fall 2017

Abstract

Polypyridyl–Metal Complexes for the Electrocatalysis and Activation of Small Molecules

By

David Zhi Hong Zee

Doctor of Philosophy in Chemistry

University of California, Berkeley

Professor Jeffrey R. Long, Chair

One of the key challenges of modern chemistry is to couple renewable energy sources, such as sunlight, to energy storage, by efficiently converting energy-poor molecules into energy-rich ones. Nature accomplishes these intricate multi-electron, multi-proton transformations using enzymes deriving from earth-abundant elements. As chemists, we must take inspiration from Nature and create viable and robust catalysts. The work herein describes progress towards electrocatalytic hydrogen evolution, electrocatalytic carbon dioxide reduction, and small molecule activation using earth abundant transition metal complexes. These investigations focus on first-row transition metal complexes with bio-inspired, weak ligand field polypyridine ligands.

To introduce this work, *Chapter 1* surveys recent work undertaken by the Long and Chang laboratories towards electrochemical and photochemical hydrogen evolution using cobalt- and molybdenum- polypyridine complexes. In particular, the Chapter highlights a key advantage of synthetic molecular catalysts—through judicious design, molecular catalysts can retain the small, functional units of their biological or materials counterparts. This is accomplished with the use of semi-rigid polypyridine ligands that stabilize the transition metal ion. In conjunction with the appropriate anions, these catalyst systems are soluble in water, which is the most abundant proton source and solvent on this planet. Furthermore, the activities of these catalysts are sensitive to electronic tuning of the peripheral ligand, thus providing another synthetic opportunity to optimize catalytic performance.

Taking into account the tunability of molecular catalysts, *Chapter 2* focuses on electronic modifications in a family of isostructural pentapyridine cobalt complexes for hydrogen evolution. Using a combination of synthetic methods, crystallography, and electrochemical methods, it is identified that the redox-active ligand scaffold $PY4IqMe_2$ ($PY4IqMe_2$ = 1,3-bis(1,1-di(pyridin-2-yl)ethyl)isoquinoline) affords a low-valent cobalt(I) ion that is protonated to form a cobalt(III) hydride fastest. This kinetic advantage is due to the levelling of two one-electron redox couples, which enables a single metal center to better perform two-electron reactions. Moreover, electrochemical kinetic analyses identify an ECEC′ mechanism as the dominant pathway for hydrogen evolution catalysis by pentapyridine cobalt complexes.

Chapter 3 applies the concepts established in proton reduction chemistry in *Chapters 1* and *2* towards noble metal-free electrocatalytic carbon dioxide reduction. A series of iron(II) complexes

of the functionalized tetrapyridine ligands bpy^{R}PY2Me (bpyPY2Me = 6-(1,1-di(pyridin-2-yl)ethyl)-2,2′-bipyridine) is systematically studied in pursuit of water-stable molecular Fe complexes that are selective for the electrocatalytic formation of carbon monoxide from carbon dioxide. Taking advantage of the inherently high degree of tunability of this ligand manifold, protic functional groups of varying acidities (–H, –OH, –OMe, –NHEt, and –NEt$_2$) were installed into the ligand framework to systematically modify the second coordination sphere of the Fe center. Comparative catalytic evaluation of this set of compounds via voltammetry and electrolysis experiments identified [(bpy^{NHEt}PY2Me)Fe]$^{2+}$ in particular as an efficient, iron-based, non-heme CO$_2$ electro-reduction catalyst that displays significant selectivity for the conversion of CO$_2$ to CO in acetonitrile solutions with 11 M water. We propose that the NH group either acts as a local proton source or is involved in CO$_2$ capture. Interestingly, the complex with the most acidic functional group in the second coordination sphere, [(bpy^{OH}PY2Me)Fe]$^{2+}$, favors formation of H$_2$ over CO. These results highlight the sensitivity of catalytic metrics to adjustment of the acidity of the second coordination sphere functional group and emphasize the continued untapped potential that synthetic molecular chemistry offers in the pursuit of next-generation CO$_2$ reduction electrocatalysts.

Leveraging the electrophilicity of divalent metal–polypyridine complexes, *Chapter 4* presents the synthesis of coordinatively-unsaturated, cationic metal complexes towards the binding and activation of weak σ donors such as N$_2$, CO, H$_2$, and ethylene. Using a weakly coordinating borate anion, pentapyridine–metal chloride complexes of the form [(PY5Me$_2$)MCl]$^+$ (PY5Me$_2$ = 2,6-bis[1,1-bis(2-pyridyl)ethyl]pyridine) are synthesized for the first-row transition metals, with the exception of Mn(II). Notably, the complex [(PY5Me$_2$)TiCl]$^+$ represents a rare, well-defined titanium(II) cation without π-acidic ligands. Using Grignard reagents, the chloride ligand in Cr(II), Fe(II), Co(II), and Ni(II) complexes can be exchanged for alkyl and aryl ligands to form cationic [(PY5Me$_2$)MCH$_3$]$^+$ and [(PY5Me$_2$)MC$_6$H$_5$]$^+$ complexes. Protonolysis of these complexes in solvents with low donor strength result in highly electrophilic, coordinatively-unsaturated coordination fragments that rapidly scavenge trace water or bind ethereal donors.

Table of Contents

List of Figures ... v

List of Tables ... x

Acknowledgments ... xi

Chapter 1. Metal-Polypyridyl Catalysts for Electro- and Photochemical Reduction of Water to Hydrogen ... 1

1.1. Introduction ... 1

1.2. Polypyridyl Ligands for Catalysis in Water ... 2

1.3. A Water-Compatible Tetrapyridyl-Cobalt Catalyst ... 3

1.4. Electrocatalytic Proton Reduction in Neutral Water using $[(PY5Me_2)MoO]^{2+}$ ... 5

1.5. $[(PY5Me_2)MoS_2]^{2+}$ as an Functional Molecular Mimic of Molybdenum Disulfide ... 8

1.6. $[(PY5Me_2)Co(H_2O)]^{2+}$ as a Tunable Platform for Water Reduction in Neutral Water ... 10

1.7. Redox-Active Ligands for Redox-Leveling and Facilitating Multi-Electron Electrocatalysis ... 12

1.8. Optimizing Photocatalytic Hydrogen Generation ... 13

1.9. Concluding Remarks ... 16

1.10. Acknowledgments ... 16

1.11. References ... 16

Chapter 2. Syntheses and Kinetic Analyses of Polypyridyl–Cobalt Complexes for Electrocatalytic Hydrogen Evolution ... 22

2.1. Introduction ... 22

2.2. Experimental ... 23

  2.2.1. Materials and Methods ... 23

  2.2.2. Synthesis ... 24

  2.2.3. Crystal Structure Determinations ... 29

2.3. Results and Discussion ... 29

  2.3.1. Design Elements and Syntheses of Pentapyridine Ligands ... 29

2.3.2. Synthesis and Characterization of Pentapyridine M(II) Complexes 32

2.3.3. Redox Trends in Polypyridyl M(II) Complexes 36

2.3.4. Kinetics of Electrocatalytic Reduction of Dimethylanilinium to Hydrogen 39

2.3.5. Chemical Reduction of Pentapyridine Co(II) Complexes—Isolation of Co(I) Intermediates and Decomposition Products 42

2.4. Conclusions and Outlook 46

2.5. Acknowledgments 47

2.6. Supplementary Information 47

2.7. References 64

Chapter 3. Tuning Second Coordination Sphere Interactions in Polypyridyl–Iron Complexes to Achieve Selective Electrocatalytic Reduction of Carbon Dioxide to Carbon Monoxide . 69

3.1. Introduction 69

3.2. Experimental 70

3.2.1. Materials and Methods 70

3.2.2. Synthesis 70

3.2.3. Crystal Structure Determinations 74

3.2.4. Electrochemical Methods 74

3.2.5. ^{1}H NMR Analysis of Electrolysis Solutions 75

3.2.6. Electrochemical Characterization of Electrode Post-Electrolysis 75

3.2.7. SEM and EDX Analysis of Electrode Post-Electrolysis 75

3.3. Results and Discussion 76

3.3.1. Design Elements and Synthesis of Functionalized Ligand Set 76

3.3.2. Synthesis and Characterization of Tetrapyridyl Complexes 76

3.3.3. Cyclic Voltammetry 78

3.3.4. Controlled-Potential Electrolyses in CO_2-Saturated Wet Acetonitrile 81

3.3.5. Catalytic Role of the Second Coordination Sphere Aniline 85

3.3.6. Controlled-Potential Electrolyses in CO_2-Saturated Water 86

3.4. Conclusions 87

3.5. Acknowledgments 88
3.6. Supplementary Information 88
3.7. References 104
Chapter 4. Towards Coordinatively-Unsaturated First-Row Transition Metal Pentapyridine Complexes with Tetrakis(3,5-(Trifluoromethyl)phenyl)borate Anions 112
4.1. Introduction 112
4.2. Experimental 112
  4.2.1. Materials and Methods 112
  4.2.2. Silanization of Glassware 113
  4.2.3. Synthesis 114
  4.2.4. Crystal Structure Determinations 118
4.3. Results and Discussion 119
  4.3.1. Cationic First-Row Transition Metal Chloride Complexes 119
  4.3.2. Cationic Metal Alkyl and Aryl Complexes 122
  4.3.3. Coordinatively-Unsaturated Pentapyridine Metal Dications 125
  4.3.4. Chloride Abstraction Reactions 127
  4.3.5. Coordinated Trifluoromethanesulfonate Complexes of Vanadium and Titanium . 128
4.4. Conclusions and Outlook 129
4.5. Acknowledgments 130
4.6. Supplementary Information 131
4.7. References 141
Appendix A. Improved Syntheses of Molybdenum Complexes of PY5Me$_2$ 144
A.1. Overview 144
A.2. Experimental 147
  A.2.1. Materials and Methods 147
  A.2.2. Syntheses 147
  A.2.3. Crystal Structure Determinations 149
A.3. Acknowledgments 149

A.4. References 149

Appendix B. Proton-Responsive Pentapyridine Ligands and their Cobalt Complexes 151

B.1. Overview 151

B.2. Experimental 154

B.2.1. Materials and Methods 154

B.2.2. Syntheses 155

B.2.3. Crystal Structure Determinations 157

B.3. Acknowledgments 157

B.4. Supporting Information 158

B.5. References 159

Appendix C. Automated Extraction of Gas Chromatograph Data 160

C.1. Motivation 160

C.2. Instructions 160

C.3. Acknowledgements 162

C.4. References 162

List of Figures

Chapter 1. Metal-Polypyridyl Catalysts for Electro- and Photochemical Reduction of Water to Hydrogen

Figure 1.1. Hydrogenase enzymes (far left) and MoS_2 (molybdenite, second from left) are proton reduction catalysts from biology and materials, respectively. Black circles delineate the small and sparse active sites among the large, overall structures: the [NiFe] cofactor of [NiFe]-hydrogenase enzymes (molecular weight ~60,000 kDa), and the disulfide-terminated (1 0 -1 0) edge of MoS_2. Molecular catalysts (right) can capture the functional essence of these biological and materials systems in a compact and tunable active site. 2

Figure 1.2. Molecular metal-polypyridyl H_2 evolution catalysts from our laboratories. 3

Figure 1.3. Cyclic voltammogram of **1.1** in a 1:1 water/CH_3CN (v/v) mixture (black), with a glassy carbon working electrode. The Co(II/I) couple occurs *ca.* −1.4 V versus the ferrocenium/ferrocene couple ($Fc^{+/0}$). Increasing concentrations of TFA give corresponding rises of catalytic current (red, green blue, cyan, and purple). The inset shows the crystal structure of **1.1**, R_1 (wR_2) = 5.20% (13.3%). 4

Figure 1.4. (a) CV of **1.2** in CH_3CN at a glassy carbon electrode (black). Addition of acetic acid causes current enhancement at the third reduction, with plateaus occurring at *ca.* −2.25 V vs $Fc^{+/0}$. The inset shows the crystal structure of **2**, R_1 (wR_2) = 3.64% (9.82%). (b) Rotating disk electrode voltammograms (100 to 3600 rpm) of **1.2** in CH_3CN (glassy carbon). Traces show three distinct plateaus, indicating three reduction processes. (c) CV in a 0.6 M aqueous phosphate buffered to pH 7 at a Hg pool electrode in the absence (red), and presence of **1.2** (black). (d) CPE at −1.40 V vs SHE in the absence (red) and presence of **1.2** (2 μM, black) in 3.0 M phosphate buffered to pH 7. Complex **1.2** remains catalytically active after 72 h of electrolysis. 7

Figure 1.5. Reaction coordinate for the liberation of H_2 from H, which is formed by the reduction of **1.2**. 8

Figure 1.6. (a) CVs of **1.3** in 0.05 M phosphate buffered to pH ranging from 3 to 7. The first reductive wave shifts by *ca.* 60 mV per unit change in pH, suggesting that the reduction is proton-coupled. Inset shows the crystal structure of **1.3**, R_1 (wR_2) = 2.85% (6.08%). (b) CVs of 1 M acetate buffer at pH 3 at a mercury pool electrode (red) with **1.2** (130 μM, black) and **1.3** (130 μM, blue). (c) CPE of **3** (66 μM) in 3 M aqueous acetate buffer (blue) versus the buffer alone (red) at −0.96 V vs SHE (η = 0.78 V). 9

Figure 1.7. (a) Crystal structures of **1.4**, **1.5**, and **1.6**, R_1 (wR_2) = 3.04% (8.19%), 2.62% (6.67%), and 6.11% (18.9%). (b) Normalized CVs of **1.4** (red), **1.5** (black) and **1.6** (blue) in 1 M phosphate buffer at pH 7 at a Hg pool electrode. (c) CPE at −1.30 V vs SHE of **4** (black), $[(PY5Me_2)Zn(H_2O)]^{2+}$ (green), $PY5Me_2$ ligand (red) and without additives (blue). Control experiments show that the ligand or metal alone or an isostructural $PY5Me_2$ complex with Zn(II) are inactive for catalysis. Only the $CoPY5Me_2$ unit shows competent reactivity. All electrolyses were performed in 2 M phosphate buffer at pH 7. 11

Figure 1.8. Photochemical generation of H_2 by **1.5** photosensitized with either $[Ru(bpy)_3]^{2+}$ (left) or GaP nanowires (right), with ascorbate as a sacrificial reductant. 12

Figure 1.9. (a) To reduce a weak acid such as water, catalysis may involve a Co(II/0) process, with a driving force of E1 (red). Introduction of a ligand-based redox state gives a new driving force E2 that can afford catalysis at less extreme potentials (blue). (b) Crystal structures of **1.7** and **1.8**, R_1 (wR_2) = 3.61% (9.25%) and 3.32% (7.83%). Blue areas highlight one of the redox-active bpy moieties. (c) Photocatalytic H_2 evolution in water by **1.7** and **1.8**. Once catalysis levels off, addition of $[Ru(bpy)_3]^{2+}$ regenerates activity. 13

Figure 1.10. Crystal structures of **1.9**, **1.11**, **1.14**, and **1.15**, R_1 (wR_2) = 2.53% (6.58%), 2.75% (11.3%), 2.77% (6.60%), and 2.96% (7.01%). Compounds **1.9**, **1.11** and **1.14** contain two *cis* open sites while 16 has two *trans* open sites. 14

Figure 1.11. (a) Photocatalytic hydrogen production versus time of different Co catalysts. (b) Catalysis is limited by photosensitizer stability. (c) Transient absorption difference spectra shows formation of a Co(I) species of **1.9** coinciding with disappearance of $[Ru(bpy)_3]^{+}$. (d) TONs of different Co catalysts at their respective optimal pH. 15

Chapter 2. Syntheses and Kinetic Analyses of Polypyridyl–Cobalt Complexes for Electrocatalytic Hydrogen Evolution

Figure 2.1. Overview of pentapyridine ligands previously studied for cobalt water reduction electrocatalysts, and the ligands prepared and studied in this Chapter. 30

Figure 2.2. Single crystal X-ray structure of $PY4IqMe_2{\cdot}0.5\ CH_2Cl_2$. Gray and blue spheres represent C and N atoms, respectively. H atoms and the CH_2Cl_2 solvent molecule are omitted for clarity. 31

Figure 2.3. Molecular structures of the $[(PY4IqMe_2)Co(CF_3SO_3)]^{+}$ and $[(PY4IqMe_2)Co(CH_3CN)]^{2+}$ ions in compounds **2.1** and **2.1′**. Purple, blue, gray, red, yellow, and green spheres represent Co, N, C, O, S, and F atoms, respectively. H atoms are omitted for clarity. Unbound solvent and anions are also not shown. 33

Figure 2.4. Molecular structure of the $[((CF_3)_5PY5Me_2)Co(CH_3OH)]^{2+}$ ion in compound **2.2**, grown from methanol/diethyl ether. Purple, blue, gray, red, green, and light blue spheres indicate Co, N, C, O, F, and H atoms, respectively. Carbon-bound H atoms, uncoordinated anions and solvent molecules are omitted for clarity. 35

Figure 2.5. Molecular structure of a $[(NMe_3PY5Me_2)Co(CH_3CN)]^{3+}$ ion in compound **2.4**, crystallized from acetonitrile and diethyl ether. Purple, blue, and gray spheres represent Co, N, and C atoms, respectively. H atoms, anions, and solvent molecules are omitted for clarity. 36

Figure 2.6. CVs showing the Co(III/II) and Co(II/I) redox couples for compounds **2.1**, **2.2**, **2.4**, $[(CF_3PY5Me_2)Co(CH_3CN)]^{2+}$, $[(PY5Me_2)Co(CH_3CN)]^{2+}$, and $[(NMe_2PY5Me_2)Co(CH_3CN)]^{2+}$. CVs were collected with 1 mM solutions of compound in acetonitrile with 0.1 M NBu_4PF_6, under argon. Scan rate = 100 mV/s. 37

Figure 2.7. Plot of k_1 versus E[Co(III/II)] 41

Figure 2.8. CVs of 1 mM $[(NMe_2PY5Me_2)Co(CH_3CN)]^{2+}$, without (red) and with 1 mM *N*,*N*-dimethylanilinium (light green). The addition of acid introduces a reversible redox couple at −2.18 V, which is assigned to the Co(III)H/Co(II)H redox couple 42

Figure 2.9. Single crystal X-ray structures of the cobalt(I) ions $[(PY5Me_2)Co(CH_3CN)]^+$ (left) and $[((CF_3)_5PY5Me_2)Co(CH_3CN)]^+$ (right) in compounds **2.5** and **2.6** 44

Figure 2.10. Molecular structure of a tricationic decomposition product of compound **2.7**, showing activation and coupling of two acetonitrile molecules. Purple, blue, and gray spheres indicate Co, N, and C atoms, respectively. H atoms and unbound anions are omitted for clarity. 45

Figure 2.11. Molecular structure of the dicobalt dication deriving from the decomposition of compound **2.8**. Note that a carbon-carbon bond of the $PY4IqMe_2$ ligand has been cleaved. Purple, blue, and gray spheres indicate Co, N, and C atoms, respectively. H atoms and unbound anions are omitted for clarity. Highlighted interatomic distances: *d*(Co–Co) = 2.5910(15) Å. 46

Chapter 3. Tuning Second Coordination Sphere Interactions in Polypyridyl–Iron Complexes to Achieve Selective Electrocatalytic Reduction of Carbon Dioxide to Carbon Monoxide

Figure 3.1. Single crystal X-ray structures of Fe-containing complexes in **3.1**–**5**. Orange, blue, gray, red, yellow, green, and white spheres represent Fe, N, C, O, S, F, and H atoms, respectively. H atoms, except those in the hydroxyl and aniline moieties, are omitted for clarity. Unbound solvent and $CF_3SO_3^-$ molecules are also not shown. The dashed orange line in **3.4** depicts an intramolecular hydrogen bond. 78

Figure 3.2. Cyclic voltammograms of complexes **3.1**–**6** in argon-saturated acetonitrile solutions with 0.1 M NBu_4PF_6 as supporting electrolyte. All scans were performed at 0.1 V/s. 79

Figure 3.3. CVs of a 1 mM solution of **3.4** in CH_3CN with 11 M H_2O, saturated with 1 atm of N_2 (black) or CO_2 (red). Scans were performed at 0.1 V/s. For i/i_p, the currents are normalized to the peak current i_p of the Fe(III/II) couple. 81

Figure 3.4. Top: Charge buildup during controlled-potential electrolyses of various complexes in CO_2-saturated CH_3CN/H_2O at −1.91 V versus $Fe(C_5H_5)_2^{+/0}$, with 240 μM of catalyst. Bottom: The solid black line and its surrounding gray area indicate the charge passed during electrolysis for **3.4** and the standard deviation. The red, blue, and purple squares correspond to the charge equivalents of GC-detected H_2, CO, and their combined total. Standard deviations for gas detection were calculated at each measurement, but plotted at hourly intervals here for clarity. The activity of the bare glassy carbon electrode has been subtracted from the plotted data. 82

Figure 3.5. Faradaic efficiencies for CO_2 to CO (blue) and water to H_2 (red) conversion obtained during 12-h electrolyses at $E = -1.91$ V for compounds **3.1**–**4**. 83

Figure 3.6. Controlled-potential electrolysis of a 240 µM solution of **3.4** in 0.1 M aqueous KPF_6 at −1.71 V (versus SHE). The solid black line and its surrounding gray area indicate the charge passed and its standard deviation. The red, blue, and purple squares correspond to the charge equivalents of H_2, CO, and their combined total detected charge. The activity of the bare glassy carbon electrode has been subtracted from the data. 87

Chapter 4. Towards Coordinatively-Unsaturated First-Row Transition Metal Pentapyridine Complexes with Tetrakis(3,5-(Trifluoromethyl)phenyl)borate Anions

Figure 4.1. Crystal structures of the monocationic complexes in compounds **4.1Cl**, **4.2Cl**, **4.3Cl**, **4.4Cl**, **4.5Cl**, and **4.6Cl**. Dark green, orange, purple, green, aqua, white, blue-green, blue, and gray spheres represent Cr, Fe, Co, Ni, Cu, Zn, Cl, N, and C atoms, respectively. H atoms, $B(C_6H_3(CF_3)_2)_4^-$ anions, and solvent are not shown for clarity. 121

Figure 4.2. Crystal structures of the dicationic complexes in compounds **4.7Cl** and **4.8Cl**, and the monocations in **4.9Cl** and **4.10Cl**. Dark blue, dark purple, blue-green, blue, and gray spheres represent Ti, V, Cl, N, and C atoms, respectively. H atoms, $B(C_6H_3(CF_3)_2)_4^-$ anions, and solvent are not shown for clarity. 122

Figure 4.3. Crystal structures of the monocationic metal alkyl complexes **$4.1CH_3$**, **$4.2CH_3$**, **$4.3CH_3$**, and **$4.4CH_3$**. Dark green, orange, purple, green, blue, gray, and light blue spheres represent Cr, Fe, Co, Ni, N, C, and H atoms, respectively. H atoms (except for those of the M–CH_3 group), $B(C_6H_3(CF_3)_2)_4^-$ anions, and solvent are omitted for clarity. 124

Figure 4.4. Crystal structure of the cation in **4.2Ph**. Orange, blue, and gray spheres represent Fe, N, and C atoms, respectively. H atoms, $B(C_6H_3(CF_3)_2)_4^-$ anions, and solvent molecules are omitted for clarity. 126

Figure 4.5. Crystal structures of **$4.1(OH_2)_{0.64}$**, **$4.2OH_2$**, **$4.3(OH_2)_{0.21}$**, and **$4.4(OH_2)_{0.63}$**. Dark green, orange, purple, green, blue, gray, and light blue spheres represent Cr, Fe, Co, Ni, N, C, and H atoms, respectively. H atoms (except those of the aquo ligand), $B(C_6H_3(CF_3)_2)_4^-$ anions, and solvent are omitted for clarity. Due to the low occupancy of the aquo ligand in **$4.3(OH_2)_{0.21}$**, the H atoms of the aquo ligand could not be located. 127

Figure 4.6. Molecular structure of the $[(PY5Me_2)V(\mu\text{-}Cl)V(PY5Me_2)]^{3+}$ ion in **4.10(*μ*-Cl)**. Dark purple, blue-green, blue, and gray spheres represent V, Cl, N, and C atoms, respectively. H atoms, $[B(C_6H_3(CF_3)_2)_4]^-$ anions, and solvent are omitted for clarity. 128

Figure 4.7. Molecular structure of the cation in **$4.10CF_3SO_3$**. Dark purple, yellow, red, green, blue, and gray spheres represent V, S, O, F, N, and C atoms, respectively. H atoms, $[B(C_6H_3(CF_3)_2)_4]^-$ anions, and solvent are omitted for clarity. 129

Appendix A. Improved Syntheses of Molybdenum Complexes of $PY5Me_2$

Figure A.1. Single crystal X-ray structure of the complex $[(PY5Me_2)MoO][B(C_6H_3(CF_3)_2)_4]_2$. Green, blue, red, and gray spheres represent Mo, N, O, and C atoms, respectively. H atoms, $[B(C_6H_3(CF_3)_2)_4]^-$ anions, and solvent molecules are omitted for clarity. 145

Appendix B. Proton-Responsive Pentapyridine Ligands and their Cobalt Complexes

Figure B.1. Postulated ligand-assisted proton-coupled electron transfer in $[(HOPY5Me_2)Co]^{n+}$ complexes. 151

Figure B.2. Molecular structures of the dications in compounds $[(EtOPY5Me_2)Co(CH_3CN)(CF_3SO_3)_2$ and $[(HOPY5Me_2)Co(CH_3CN)](CF_3SO_3)_2$. Purple, blue, gray, red, and light blue spheres represent Co, N, C, O, and H atoms, respectively. Carbon-bound H atoms, $CF_3SO_3^-$ anions, and solvent molecules are omitted for clarity.. 153

Figure B.3. Cyclic voltammograms of 1 mM solutions of $[(EtOPY5Me_2)Co(CH_3CN)(CF_3SO_3)_2$ and $[(HOPY5Me_2)Co(CH_3CN)](CF_3SO_3)_2$ in acetonitrile........ 154

Appendix C. Automated Extraction of Gas Chromatograph Data

Figure C.1. An example of the output file provided by the data extraction script........ 161

List of Tables

Chapter 1. Metal-Polypyridyl Catalysts for Electro- and Photochemical Reduction of Water to Hydrogen

Table 1.1. Controlled-potential electrolysis data of hydrogen-producing catalysts. 5

Table 1.2. Photolytic hydrogen production by molecular cobalt catalysts.[a] 15

Chapter 2. Syntheses and Kinetic Analyses of Polypyridyl–Cobalt Complexes for Electrocatalytic Hydrogen Evolution

Table 2.1. Redox potentials of pentapyridine cobalt complexes.[a] 38

Table 2.2. Kinetic parameters of pentapyridine cobalt complexes. 41

Table 2.3. Highlighted metal-ligand bond distances in pentapyridine Co(II) and Co(I) complexes. 44

Chapter 3. Tuning Second Coordination Sphere Interactions in Polypyridyl–Iron Complexes to Achieve Selective Electrocatalytic Reduction of Carbon Dioxide to Carbon Monoxide

Table 3.1. Faradaic efficiencies of Fe-containing electrocatalysts for CO_2 reduction. 84

Chapter 4. Towards Coordinatively-Unsaturated First-Row Transition Metal Pentapyridine Complexes with Tetrakis(3,5-(Trifluoromethyl)phenyl)borate Anions

Table 4.1. Selected bond distances of $[(PY5Me_2)MCl][B(C_6H_3(CF_3)_2)_4]$ complexes......... 122

Table 4.2. Selected bond distances of $[(PY5Me_2)MCH_3][B(C_6H_3(CF_3)_2)_4]$ complexes...... 124

Appendix A. Improved Syntheses of Molybdenum Complexes of $PY5Me_2$

Table A.1. Crystallographic details for complex $[(PY5Me_2)MoO][B(C_6H_3(CF_3)_2)_4]_2$.[a] 146

Appendix B. Proton-Responsive Pentapyridine Ligands and their Cobalt Complexes

Table B.1. Highlighted bond distances in complexes $[(EtOPY5Me_2)Co(CH_3CN)(CF_3SO_3)_2$ and $[(HOPY5Me_2)Co(CH_3CN)](CF_3SO_3)_2$. 153

Acknowledgments

This PhD was quite the journey. I would not have succeeded without the help of many people. I have many people to thank.

First and foremost, I thank my advisor, Jeff Long, for his magnetic (no pun intended) passion for research. His broad interests and insightful thinking are infectious. Also, I sincerely thank him for letting me into his lab. Having spent several years away from chemistry, I was a risky venture. Despite that, Jeff afforded me free rein, undue patience, and unending support. I hope to repay that faith by becoming a professor and guiding a younger generation of students towards being independent and inquisitive scientists.

This work would not have been possible without our close collaborator, Chris Chang. I want to thank Chris for essentially being a second advisor to me. He also deserves immense credit for spurring my interest in bio-inorganic chemistry. Chapter 1 of this Thesis was written with the invaluable help of his student, Annie Chantarojsiri, who is a fantastic colleague.

I thank Professors Angie Stacy, Dick Andersen, Don Tilley, and Jeff Reimer for giving me an eye-opening Qualifying Exam. Since then, I have learnt to be a voracious consumer of the chemical literature. Additionally, a big thank you to Dick Andersen and Bryan McCloskey for reading my dissertation, for providing much appreciated feedback, and for giving priceless career advice. I will definitely take up on your offers to stop by your offices to catch up. I thank Don for taking care of the Mol Cat project at JCAP.

I am thankful for the opportunities to teach under Michelle Chang, Dick Andersen, and Chris Chang. Not only were they great mentors, but, through Chem 103, Michelle also introduced me to my eventual wife.

I am also indebted to the many great facilities managers at UC Berkeley. Hasan Celik taught me many NMR techniques. Elena Kreimer ran hundreds of EAs for me. Jim Breen fixed a lot of carelessly broken glassware.

Shela Deguzman, our group's administrator, ensured that I was paid.

During grad school, I acquired a reasonable repertoire of synthetic skills. I owe all of this to Drs. Michael Nippe and Chris Letko. Michael patiently watched over my shoulder as I tried not to mess things up. Letko taught me how to work up a reaction properly. And we all know the workup is the most crucial step of synthesis.

During grad school, I learned to appreciate just how important a healthy, vibrant lab is to productive science. So, I heartily thank all of the grad students and post docs of the Long group, past and present. Specifically, Jordan, Jarad, Joe, Miguel, Dianne, Ziebel, and Colin made day-to-day operations in lab so much more fun. Thank you, Jordan, for braving Catalysis together with me. Jarad, hugs. Joe, I hope you feel better from the flight from NOLA. Miguel, I'm sorry I no longer work the late shift. I miss the days we were both arms-deep in the double box at 3 am. Dianne, thanks for all the gossip. Ziebel, thanks for all the SSBM breaks and for entertaining my random ideas. Colin, thank you for appreciating the advice I give. You gave me confidence that I can be okay at advising others.

Although they were not physically at Berkeley, I owe a lot to my friends and family. Ian, Phil, and Steve, thank you for editing my chapters for grammar. I understand that a chemistry thesis was not the easiest read, but you guys came through. Matt, thank you again for helping with the Python code. That code saved so many hours of work. Aside from coming to my aid when I needed it, my college friends also provided a reprieve from science. My parents, Winston and Peggy, have given me everything. I would not be the person I am today without their love and support.

Lastly, and most importantly, I am eternally thankful for my wife, Dr. Stephanie Rhianon Jones. You are the best co-GSI and best co-cat parent ever. You made me smile every single day, no matter how difficult grad school was. You also brought Florence's fluffiness into our lives. I would not have survived without her therapeutic purring. To the both of you, I love you more than words can describe.

Chapter 1. Metal-Polypyridyl Catalysts for Electro- and Photochemical Reduction of Water to Hydrogen

1.1. Introduction

Increasing global demand for energy and concerns over anthropogenic climate change drive the search for sustainable, alternative energy sources. Solar energy is a preeminent candidate as it achieves the scale needed to meet the demand, but suffers from critical problems in energy storage and transport.[1] One attractive solution to this problem is solar-to-fuel conversion, where energy is stored by converting energy-poor molecules into energy-rich ones. In particular, hydrogen is an appealing carbon-neutral fuel as both its feedstock and combustion product are water.[2] Platinum can catalyze the reduction of water to hydrogen at fast rates near thermodynamic equilibrium, but its low abundance and high cost prohibit its widespread use.[3] As such, it is attractive to develop inexpensive, earth-abundant hydrogen-evolution catalysts that can, when interfaced with electrodes or photoelectrodes, convert solar energy into chemical energy in a sustainable manner.[4]

In this context, biology and materials provide unifying concepts to drive the development of new solar-fuel chemistry. Within the framework of hydrogen production, hydrogenase enzymes can convert protons and electrons to hydrogen utilizing only iron and/or nickel in their active sites with high speed and efficiency on a per molecule basis.[5,6] However, the activity of enzymes on a per volume basis is limited by size constraints, as most of the protein structure is devoted to its biological regulation for cellular function while critical catalytic reactions occur at relatively small active sites within these larger scaffolds (Figure 1.1). A similar situation is observed in heterogeneous materials, where catalytically active sites are often restricted to minor edges or faces and the bulk of the material is inert and provides but a scaffold for stability purposes. With these principles in mind, molecular catalysts can retain the small, functional units of their biological or materials counterparts, but achieve higher volumetric activities by discarding the superfluous regulatory or stabilizing scaffolds. Indeed, molecular proton reduction catalysis is a vibrant area of research and has been the subject of numerous excellent and comprehensive reviews.[7-15] A key challenge is achieving efficient and sustainable catalysis in water, and we focus this Chapter on strategic efforts from our laboratories to meet this goal by employing metal-polypyridyl complexes.

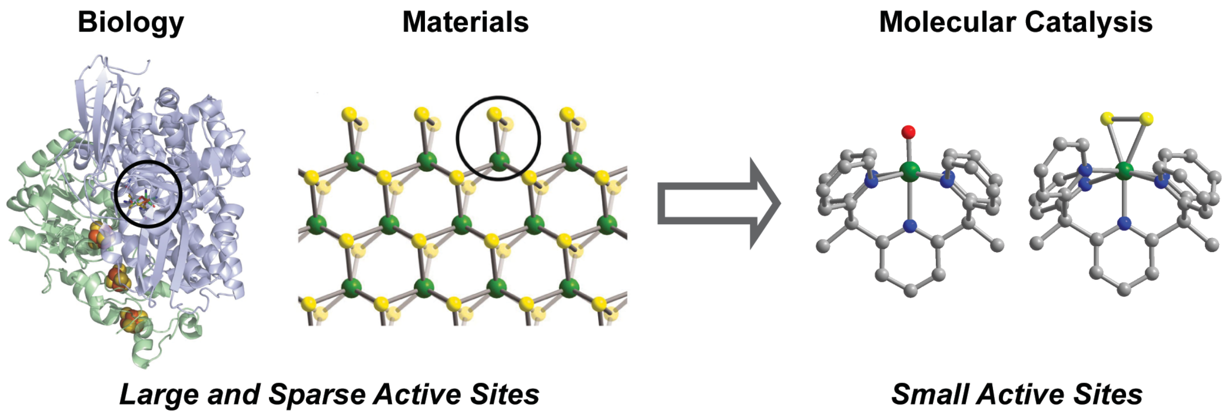

Figure 1.1. Hydrogenase enzymes (far left) and MoS_2 (molybdenite, second from left) are proton reduction catalysts from biology and materials, respectively. Black circles delineate the small and sparse active sites among the large, overall structures: the [NiFe] cofactor of [NiFe]-hydrogenase enzymes (molecular weight ~60,000 kDa), and the disulfide-terminated (1 0 -1 0) edge of MoS_2. Molecular catalysts (right) can capture the functional essence of these biological and materials systems in a compact and tunable active site.

1.2. Polypyridyl Ligands for Catalysis in Water

An important goal of proton reduction catalysis is to use water as both substrate and solvent, as water is the most abundant source of protons and offers the benefit of maintaining high substrate concentrations without organic waste produced during fuel generation or combustion. In this regard, many elegant examples of molecular proton reduction catalysts have been reported, but aqueous compatibility remains a challenge, as many molecular catalysts lack solubility in water while others are irreversibly decomposed by water and cannot be funneled back into the catalytic pathway. Our research program has centered on multidentate polypyridine ligands to address these issues. First, the use of a neutral polypyridyl scaffold coordinated to a metal ion gives a charged complex, which, combined with an appropriate charge-balancing anion, provides aqueous solubility. Moreover, being aromatic and possessing strong bonds, pyridine ligands are resistant to hydrolysis. Finally, we reasoned that the strong σ-donor capabilities of pyridines coupled with their ability to participate in metal-to-ligand π back-bonding should stabilize reduced metal species. Figure 1.2 summarizes water-compatible polypyridyl scaffolds we have successfully applied in the catalytic reduction of protons to hydrogen.

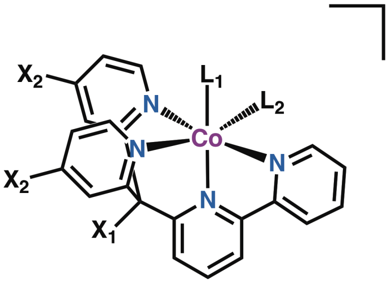

1.1 X_1 = OMe, X_2 = H, $L_1 = L_2 = CH_3CN$, n = 2
1.9 X_1 = Me, X_2 = H, $L_1 = CH_3CN$, $L_2 = CF_3SO_3^-$, n = 1
1.10 X_1 = Me, $X_2 = CF_3$, $L_1 = CH_3CN$, $L_2 = CF_3SO_3^-$, n = 1
1.11 X_1 = OH, X_2 = H, $L_1 = CH_3CN$, $L_2 = CF_3SO_3^-$, n = 1

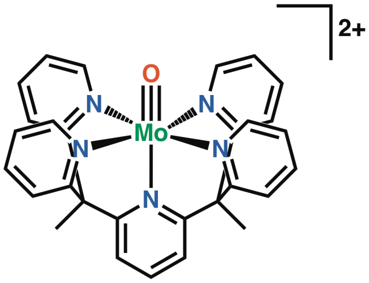

1.2

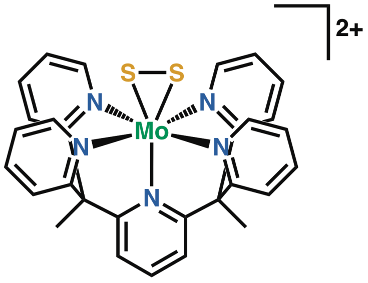

1.3

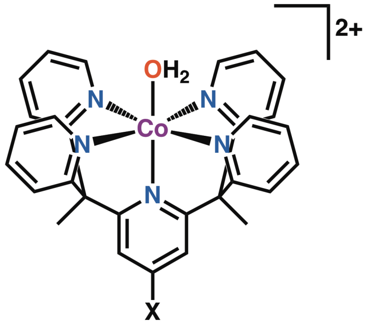

1.4 X = H
1.5 X = CF_3
1.6 X = NMe_2

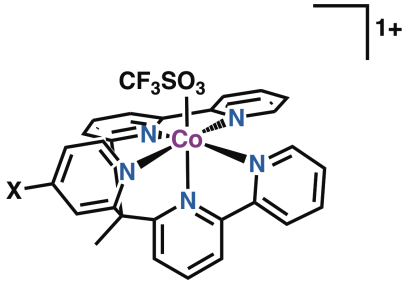

1.7 X = H
1.8 X = CF_3

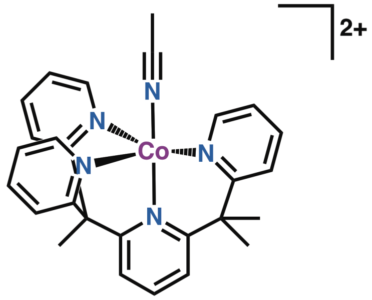

1.12

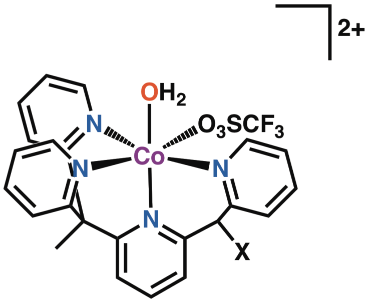

1.13 X = Me
1.14 X = H

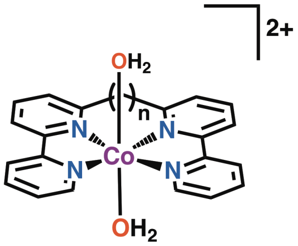

1.15 n = 0
1.16 n = 3

Figure 1.2. Molecular metal-polypyridyl H_2 evolution catalysts from our laboratories.

1.3. A Water-Compatible Tetrapyridyl-Cobalt Catalyst

Our initial foray into electrocatalytic proton reduction centered on the cobalt(II) complex $[(PY4)Co(CH_3CN)_2]^{2+}$ (**1.1**, Figure 1.2).[16] The cyclic voltammogram (CV) of **1.1** in acetonitrile displays a reversible Co(II)/(I) redox couple at modest reduction potentials. Addition of trifluoroacetic acid (TFA) triggered proton reduction catalysis, with ~99% Faradaic yield (Table 1.1). Importantly, we found that electrocatalytic reduction of TFA by **1.1** was observed even when the water content in the electrolyte solution was increased to 50%, although the complex was insoluble at higher water levels (Figure 1.3). Nevertheless, the results established the viability of our strategy.

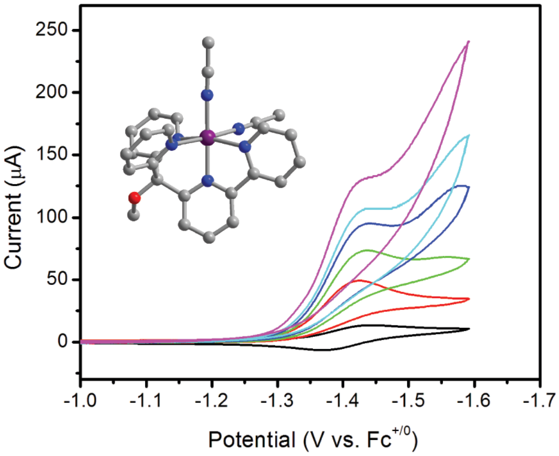

Figure 1.3. Cyclic voltammogram of **1.1** in a 1:1 water/CH_3CN (v/v) mixture (black), with a glassy carbon working electrode. The Co(II/I) couple occurs *ca.* −1.4 V versus the ferrocenium/ferrocene couple (Fc$^{+/0}$). Increasing concentrations of TFA give corresponding rises of catalytic current (red, green blue, cyan, and purple). The inset shows the crystal structure of **1.1**, R_1 (wR_2) = 5.20% (13.3%).

Table 1.1. Controlled-potential electrolysis data of hydrogen-producing catalysts.

	applied potential (η^{a})	faradaic efficiency (%)	TON (reaction time) (mol H_2 (mol cat)$^{-1}$)	TOF (mol H_2 (mol cat h)$^{-1}$)	electrode^{b}	electrolyte	ref
1.1	−1.40 V vs Fc$^{+/0}$ (0.62 V)	99	–^{c}	40^{d}	GC	65 mM TFA^{e} in CH_3CN^{f}	16
1.2	−1.40 V vs SHE (0.99 V)	100	610,000 (72 h)	8,500^{g}	Hg	3.0 M pH 7 phosphate in H_2O	26
1.2	−2.24 V vs Fc$^{+/0}$ (0.90 V)	99	3.7 (1 h)	3.7^{g}	GC	170 eq AcOH^{h} in CH_3CN^{f}	27
1.3	−0.96V vs SHE (0.78 V)	100	19,000,000 (23 h)^{i}	830,000^{i,j}	Hg	3.0 M pH 3 acetate in H_2O	35
1.3	−1.73 V vs Fc$^{+/0}$ (0.39 V)	100	5.7 (2.75 h)	2.1^{g}	GC	160 eq AcOH^{h} in CH_3CN^{f}	35
1.4	−1.30 V vs SHE (0.89 V)	100	55,000 (60 h)	920^{g}	Hg	2.0 M pH 7 phosphate in H_2O	36
1.5	−0.96 V vs SHE (0.55 V)	95	–^{c}	–^{c}	GC	0.1 M pH 7 phosphate in H_2O	41
1.7	−1.80 V vs Fc$^{+/0}$ (0.46 V)	90	–^{c}	–^{c}	GC	AcOH^{h} in CH_3CN^{f}	64

[a] η = overpotential = applied potential − (0.059 V × pH) in water. η = applied potential − [($E°_{H+/H2}$) − (0.059 V × pK_a)] for nonaqueous systems.[71] [b] GC, glassy carbon. [c] –, no published data available. [d] Estimated from CV data. [e] $E°$ = −0.78 V vs Fc$^{+/0}$. [f] With 0.1 M NBu_4PF_6 as supporting electrolyte. [g] These numbers are estimated from the CPE data assuming all catalyst molecules in solution participate in the reaction at any given time. Thus they represent a *lower bound* of the true TOF. [h] $E°$ = −1.34 V vs Fc$^{+/0}$. [i] Calculated based on the estimated surface coverage of the catalyst on the Hg pool. [j] In an optimized medium, the TOF reaches 480 moles H_2 per mole catalyst per second.[35]

1.4. Electrocatalytic Proton Reduction in Neutral Water using $[(PY5Me_2)MoO]^{2+}$

Concurrently, longstanding efforts in molecular magnetism led us to explore polypyridyl capping ligands to prepare coordination clusters. In particular, we became interested in the PY5 ligand investigated by Stack and coworkers for bioinorganic model chemistry,[17-19] but found its preparation synthetically challenging. As such, we developed a convenient, multigram-scale preparation for the related ligand $PY5Me_2$,[20] which enabled us to pursue parallel investigations in both molecular magnetism and reactivity.

Inspired by elegant water activation studies in the organometallic literature,[21-25] particularly the work of Yoon and Tyler[23] on MCp_2 fragments, we focused on low-valent molybdenum chemistry supported by PY5Me$_2$. We reasoned that substituting the neutral PY5Me$_2$ for the anionic cyclopentadienyls would leave at least one open coordination site available for chemistry and shift reductions to more positive potentials, enabling reactivity nearer the thermodynamic potential for water reduction. Indeed, the Mo(II) complex $[(PY5Me_2)Mo(CF_3SO_3)]^{1+}$ reacts with water to form the molybdenum(IV)-oxo ion $[(PY5Me_2)MoO]^{2+}$ (**1.2**, Figure 1.2), with concomitant release of H_2.[26] This quantitative stoichiometric reactivity encouraged us to test **1.2** as an electrocatalyst and we were delighted to observe that it is capable of reducing acetic acid to hydrogen in acetonitrile at 100% Faradaic efficiency (Figure 1.4a, Table 1.1).[27] Cyclic and rotating disk voltammetry experiments unambiguously establish the active catalyst to be molecular in nature. Complex **1.2** proved to be sufficiently soluble and active in water, displaying two reduction events preceding a sharp rise in current corresponding to catalysis. Controlled-potential electrolyses (CPE) of **1.2** at −1.40 V versus the standard hydrogen electrode (SHE) showcase its activity and durability in water, with turnover frequencies (TOF) of at least 8,500 moles of H_2 per mole of catalyst per hour, turnover numbers (TON) over 600,000 moles of H_2 per mole of catalyst after 72 h without loss of activity, and 100% Faradaic efficiency (Figure 1.4d, Table 1.1). Computational investigations suggest that in aqueous solution the first two reductions are proton-coupled and those electrons are placed into orbitals antibonding in character with respect to the Mo–O bond to make the oxo moiety more nucleophilic and basic.[28] A third electron yields a Mo(I) center that cleaves the H–OH bond of the ligated water to form a seven-coordinate Mo(III) complex $[(PY5Me_2)Mo(H)(OH)]^{+}$ (Figure 1.5). Finally, the catalyst was found to be highly active in unpurified seawater, suggesting that the PY5Me$_2$ ligand not only provides a catalytically active molybdenum site, but also prevents catalyst poisoning by adventitious impurities.

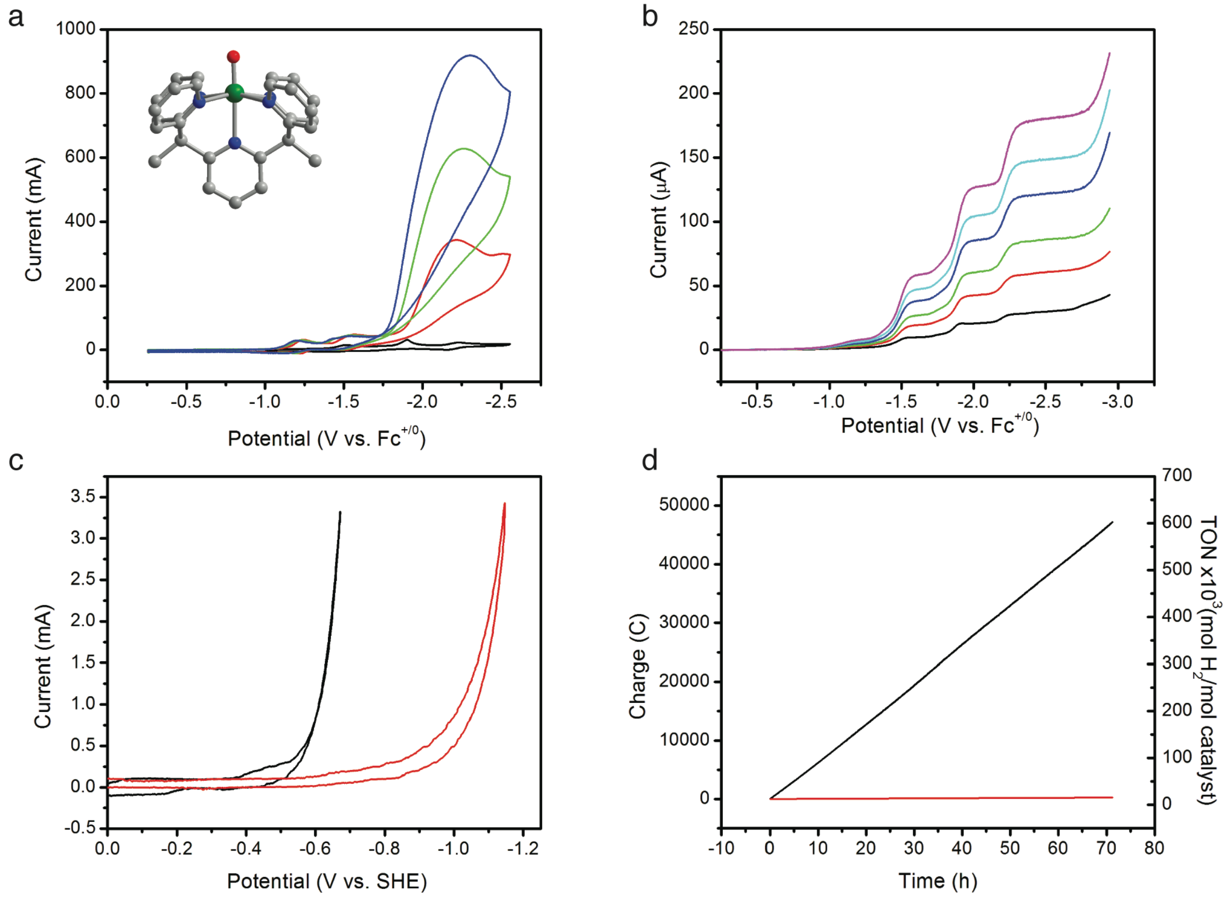

Figure 1.4. (a) CV of **1.2** in CH_3CN at a glassy carbon electrode (black). Addition of acetic acid causes current enhancement at the third reduction, with plateaus occurring at *ca.* −2.25 V vs Fc$^{+/0}$. The inset shows the crystal structure of **2**, R_1 (wR_2) = 3.64% (9.82%). (b) Rotating disk electrode voltammograms (100 to 3600 rpm) of **1.2** in CH_3CN (glassy carbon). Traces show three distinct plateaus, indicating three reduction processes. (c) CV in a 0.6 M aqueous phosphate buffered to pH 7 at a Hg pool electrode in the absence (red), and presence of **1.2** (black). (d) CPE at −1.40 V vs SHE in the absence (red) and presence of **1.2** (2 μM, black) in 3.0 M phosphate buffered to pH 7. Complex **1.2** remains catalytically active after 72 h of electrolysis.

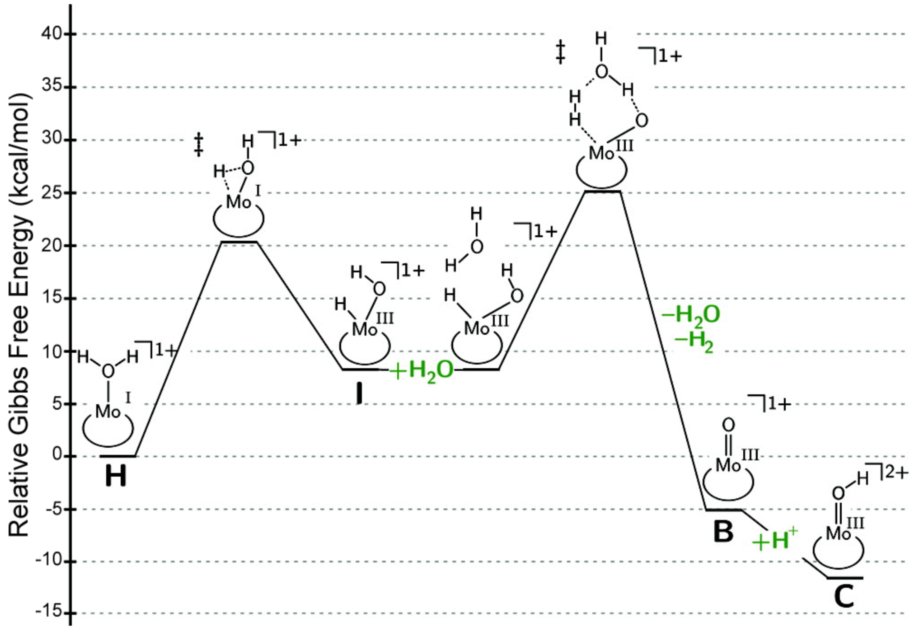

Figure 1.5. Reaction coordinate for the liberation of H_2 from H, which is formed by the reduction of **1.2**.

1.5. $[(PY5Me_2)MoS_2]^{2+}$ as an Functional Molecular Mimic of Molybdenum Disulfide

While investigating **1.2** for water reduction, we recognized growing efforts in using nanoparticular and amorphous MoS_2 for this same purpose,[29-34] where catalysis is postulated to occur at MoS_2 triangular edges.[29,30] These observations prompted us to prepare the Mo(IV)-disulfide $[(PY5Me_2)MoS_2]^{2+}$ (**1.3**, Figure 1.2) with a molecular MoS_2 triangle that not only structurally resembles the active edge sites of MoS_2, but also functionally supports catalytic activity for reduction of protons to hydrogen in water.[35] The CV of **1.3** in acetonitrile displays a set of well-defined and reversible reduction events at potentials more positive than those of **1.2**, presaging that stabilization of the reduced states by the S_2^{2-} moiety could result in a catalyst with lower overpotentials. Indeed, catalysis by **1.3** in acetonitrile or acidic water initiates at 400 mV of overpotential, whilst **1.2** requires an additional 300 mV of driving force to operate at similar current densities (Figure 1.6, Table 1.1). This redox tuning emphasizes the molecular nature of **1.3**, which is additionally confirmed by complementary electrochemical and spectroscopic experiments that show no evidence of Mo deposits. The catalyst also retains activity for at least one day with 100 % Faradaic efficiency, and its sustained activity in untreated seawater again highlights the ability of the $PY5Me_2$ ligand to furnish robust transition metal catalysts in aqueous media. In a broader sense, this work establishes a path towards functional molecular mimics of heterogeneous catalysts, in analogy to the use of coordination complexes as models for enzyme active sites.

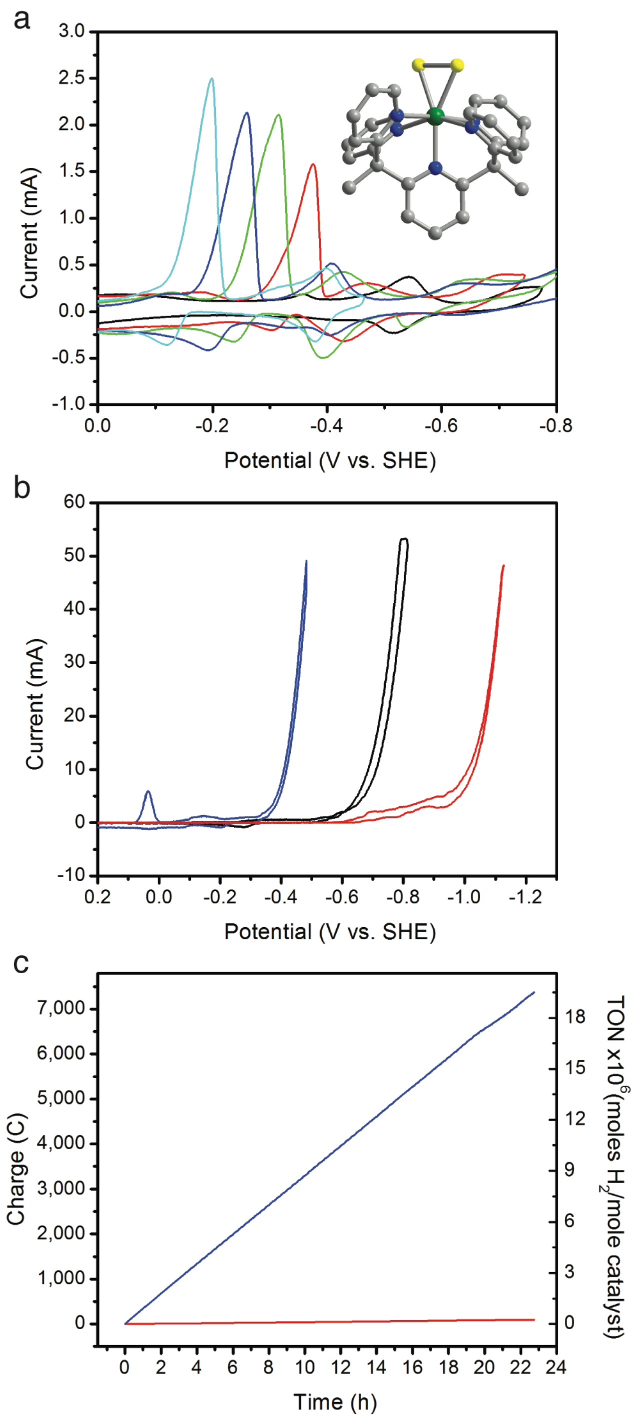

Figure 1.6. (a) CVs of **1.3** in 0.05 M phosphate buffered to pH ranging from 3 to 7. The first reductive wave shifts by *ca.* 60 mV per unit change in pH, suggesting that the reduction is proton-coupled. Inset shows the crystal structure of **1.3**, R_1 (wR_2) = 2.85% (6.08%). (b) CVs of 1 M acetate buffer at pH 3 at a mercury pool electrode (red) with **1.2** (130 μM, black) and **1.3** (130 μM, blue). (c) CPE of **3** (66 μM) in 3 M aqueous acetate buffer (blue) versus the buffer alone (red) at −0.96 V vs SHE (η = 0.78 V).

1.6. $[(PY5Me_2)Co(H_2O)]^{2+}$ as a Tunable Platform for Water Reduction in Neutral Water

Given the structural similarities between PY5 and $PY5Me_2$, as well as the established use of the former as a ligand for first-row transition metals, we reasoned that the $PY5Me_2$ ligand could support first-row transition metal water reduction catalysts with the reactivity, durability, and solubility necessary to function in aqueous media. Indeed, CVs collected in water with $[(PY5Me_2)Co(H_2O)]^{2+}$ (**1.4**, Figure 1.2)[36] show an irreversible reduction followed by hydrogen evolution catalysis (Figure 1.7b). Like its molybdenum predecessors, electrolysis with **1.4** generates H_2 with 100% Faradaic efficiency for at least 60 h (Figure 1.7c, Table 1.1), suggesting that the $PY5Me_2$ ligand helps prevent decomposition via non-productive pathways.

Although **1.4** operates at a fairly high overpotential, the most salient feature of this system is the ability to tune potentials in a rational molecular manner. Introduction of an electron-withdrawing trifluoromethyl substituent at the 4-position of the central pyridine affords the electronically deficient complex **1.5** (Figure 1.2) and anodically shifts the initial one-electron reduction and subsequent catalysis without loss in Faradaic efficiency (Figure 1.7b, Table 1.1). By voltammetry, catalysis by **1.5** reaches 2.25 mA at −0.80 V vs SHE (η = 390 mV), whereas the unsubstituted parent complex **1.4** requires −0.97 V vs SHE (η = 560 mV). Introduction of an electron-donating dimethylamino substituent (**1.6**, Figure 1.2) increases the requisite driving force by another 100 mV. Independent preparation of the Co(I) complex $[(PY5Me_2)Co]^+$ reveals that it shares its square pyramidal coordination geometry and its intense blue coloration with the cobaloxime anions,[37-40] but instead possesses a high-spin d^8 electron configuration. In addition, we established that **1.5** can generate hydrogen from neutral water under photocatalytic conditions with visible light irradiation, $[Ru(bpy)_3]^{2+}$ as a molecular photosensitizer, and ascorbic acid as a sacrificial reductant (Figure 1.8).[41] Likewise, **1.5** enhanced the hydrogen photolysis yield of GaP nanowires in water, demonstrating that this molecular catalyst platform can be interfaced with heterogeneous photosensitizers.[41] Taken together, these results suggest that judicious modifications of the ancillary ligand can furnish catalysts active in water, utilizing either sustainable solar or electrical input.

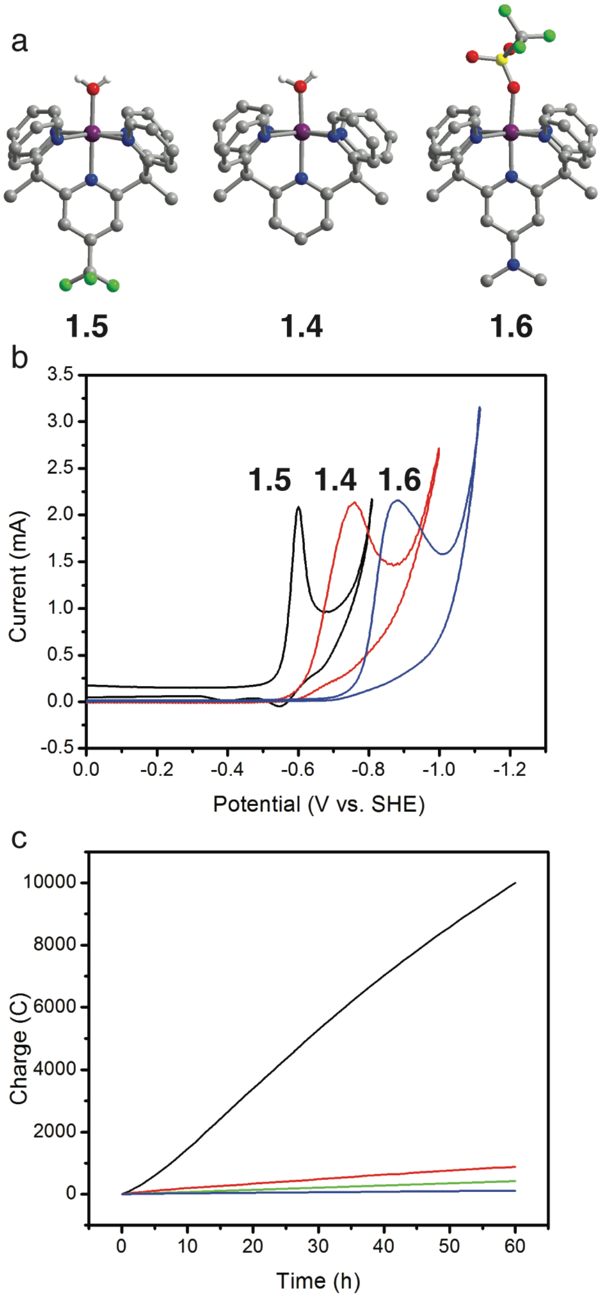

Figure 1.7. (a) Crystal structures of **1.4**, **1.5**, and **1.6**, R_1 (wR_2) = 3.04% (8.19%), 2.62% (6.67%), and 6.11% (18.9%). (b) Normalized CVs of **1.4** (red), **1.5** (black) and **1.6** (blue) in 1 M phosphate buffer at pH 7 at a Hg pool electrode. (c) CPE at −1.30 V vs SHE of **4** (black), $[(PY5Me_2)Zn(H_2O)]^{2+}$ (green), $PY5Me_2$ ligand (red) and without additives (blue). Control experiments show that the ligand or metal alone or an isostructural $PY5Me_2$ complex with Zn(II) are inactive for catalysis. Only the $CoPY5Me_2$ unit shows competent reactivity. All electrolyses were performed in 2 M phosphate buffer at pH 7.

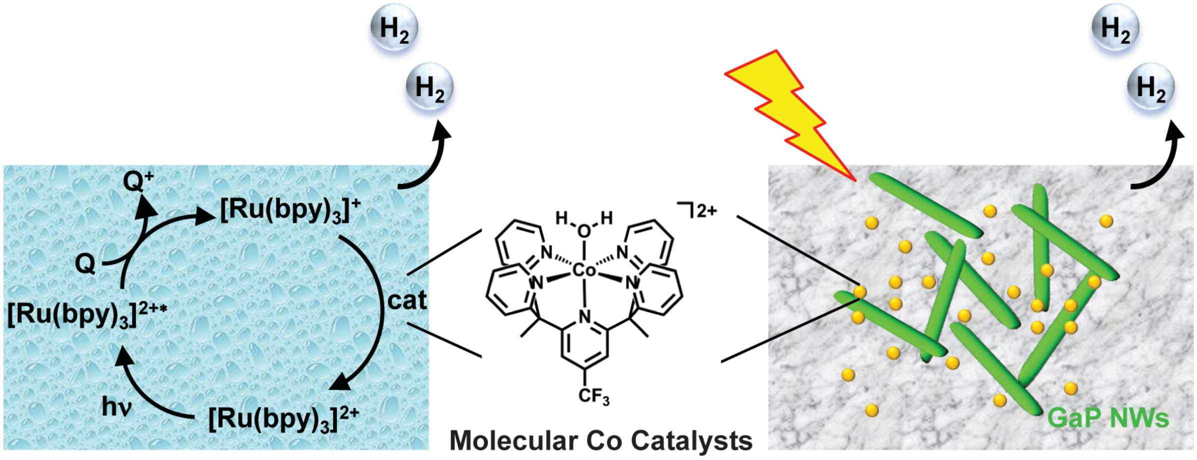

Figure 1.8. Photochemical generation of H_2 by **1.5** photosensitized with either $[Ru(bpy)_3]^{2+}$ (left) or GaP nanowires (right), with ascorbate as a sacrificial reductant.

1.7. Redox-Active Ligands for Redox-Leveling and Facilitating Multi-Electron Electrocatalysis

The prevalence of molecular cobalt-based proton reduction catalysts,[9,39,40,42-63] including contributions from our laboratories,[11,16,36,37,41,64,65] has attracted many experimental and computational mechanistic investigations. Though the operative mechanism for these catalysts can vary widely, formation of a cobalt-hydride is commonly invoked.[37,48] With interest in minimizing catalyst overpotentials, Co(I) centers capable of deprotonating water (or $H^+_{(aq)}$) are more desirable than resorting to the undoubtedly more basic Co(0) species, which require an additional reducing equivalent, and thus more negative potentials (Figure 1.9a). In cases where protonation of Co(I) is inefficient, however, we reasoned that introduction of another ligand-based redox event between the Co(II/I) and Co(I/0) couples may lower catalyst overpotentials. This concept is challenging to put into practice, however, as incorporation of a redox-active ligand can have detrimental effects. For example, the delocalization of spin onto the ligand framework in Co-bisglyoxime[39,40,42] and trisglyoxime[66] catalysts have been shown to promote ligand hydrogenation[67-70] during catalysis, significantly reducing catalyst longevity.

We therefore designed the complex $[(bpy_2PYMe)Co(CF_3SO_3)]^{1+}$ (**1.7**, Figure 1.2),[64] which contains two 2,2′-bipyridine (bpy) moieties that are not only redox-active, but also expected to be robust against hydrogenation, vis-à-vis oximes, owing to their aromatic nature (Figure 1.9b). Indeed, the CV of **1.7** in acetonitrile displays a metal-centered Co(II/I) couple followed by two bpy$^{0/\bullet-}$ reductions. Addition of acetic acid, which possesses a H^+/H_2 reduction potential midway of the Co(II/I) and bpy$^{0/\bullet-}$ couples, engenders electrocatalysis. Complex **1.7** can also reduce water photocatalytically in fully aqueous conditions with $[Ru(bpy)_3]^{2+}$ and ascorbic acid. Though the catalyst is not indefinitely stable under irradiation, this photocatalytic system is apparently limited by the durability of the photosensitizer. Addition of $[Ru(bpy)_3]^{2+}$ after catalysis levels off restores activity (Figure 1.9c), while addition of fresh catalyst in parallel experiments did not. Photocatalysis by **1.4** and **1.5**, which are devoid of redox-active ligands, result in *ca.* six-fold decrease in activity relative to **1.7** (Table 1.2), showcasing synergy between ligand and metal redox activity.

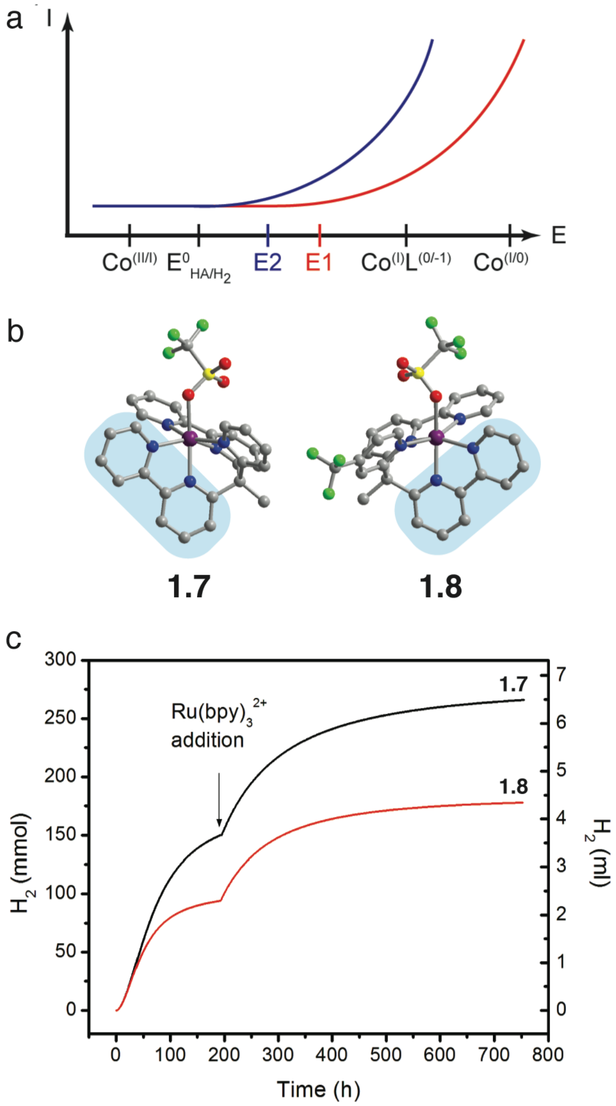

Figure 1.9. (a) To reduce a weak acid such as water, catalysis may involve a Co(II/0) process, with a driving force of E1 (red). Introduction of a ligand-based redox state gives a new driving force E2 that can afford catalysis at less extreme potentials (blue). (b) Crystal structures of **1.7** and **1.8**, R_1 (wR_2) = 3.61% (9.25%) and 3.32% (7.83%). Blue areas highlight one of the redox-active bpy moieties. (c) Photocatalytic H_2 evolution in water by **1.7** and **1.8**. Once catalysis levels off, addition of $[Ru(bpy)_3]^{2+}$ regenerates activity.

1.8. Optimizing Photocatalytic Hydrogen Generation

The foregoing results prompted us to evaluate the photocatalytic performance of other cobalt(II)-based molecular catalysts. Importantly, these experiments required catalyst concentrations only at the micromolar level, enabling us to interrogate complexes that were not soluble enough for conventional aqueous electrochemistry. Again, using $[Ru(bpy)_3]^{2+}$ and an aqueous ascorbate buffer, we evaluated the photocatalytic properties of ten cobalt-polypyridyl catalysts, including **1.9**, **1.11**, **1.14**, and **1.16** (Figure 1.10), using a high-throughput photochemical reactor developed by Castellano.[65] These findings highlighted several trends. First, Co(II) complexes bearing tetradentate ligands that enforce *cis* divacant coordination sites, such as **1.1**, **1.9**, **1.10**, and **1.11**, show higher activity for photocatalytic hydrogen generation compared those with ligands that enforce *trans* sites, **1.15** and **1.16** (Figure 1.11a). Second, sustained photochemical hydrogen production is limited by the stability of $[Ru(bpy)_3]^{2+}$, not the catalyst (Figure 1.11b). Third, transient absorption measurements suggest that a putative Co(I) intermediate forms during photocatalysis (Figure 1.11c). Finally, changes in pH had different effects on the activity for each catalyst. With each catalyst evaluated at its optimal pH, comparison of TONs reveal that catalysts with tetradentate ligands exhibit higher activity than those bearing pentadentate ligands, without losses in stability (Figure 1.11d, Table 1.2). The performance of **1.14**, which does not contain redox-active ligands, exemplifies the importance of denticity and implies that the operative photocatalytic mechanism in water substantially differs from the electrochemical mechanism utilizing weak organic acids.

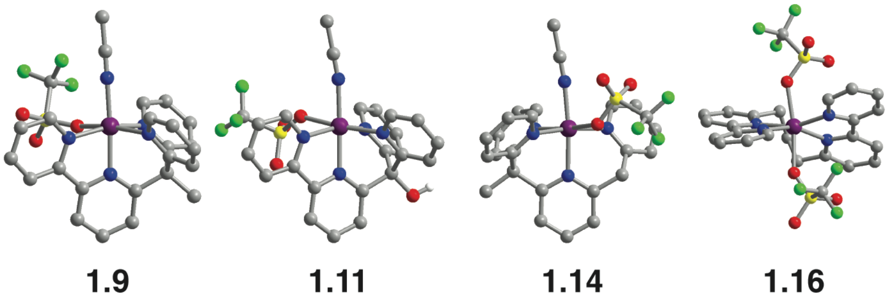

Figure 1.10. Crystal structures of **1.9**, **1.11**, **1.14**, and **1.15**, R_1 (wR_2) = 2.53% (6.58%), 2.75% (11.3%), 2.77% (6.60%), and 2.96% (7.01%). Compounds **1.9**, **1.11** and **1.14** contain two *cis* open sites while 16 has two *trans* open sites.

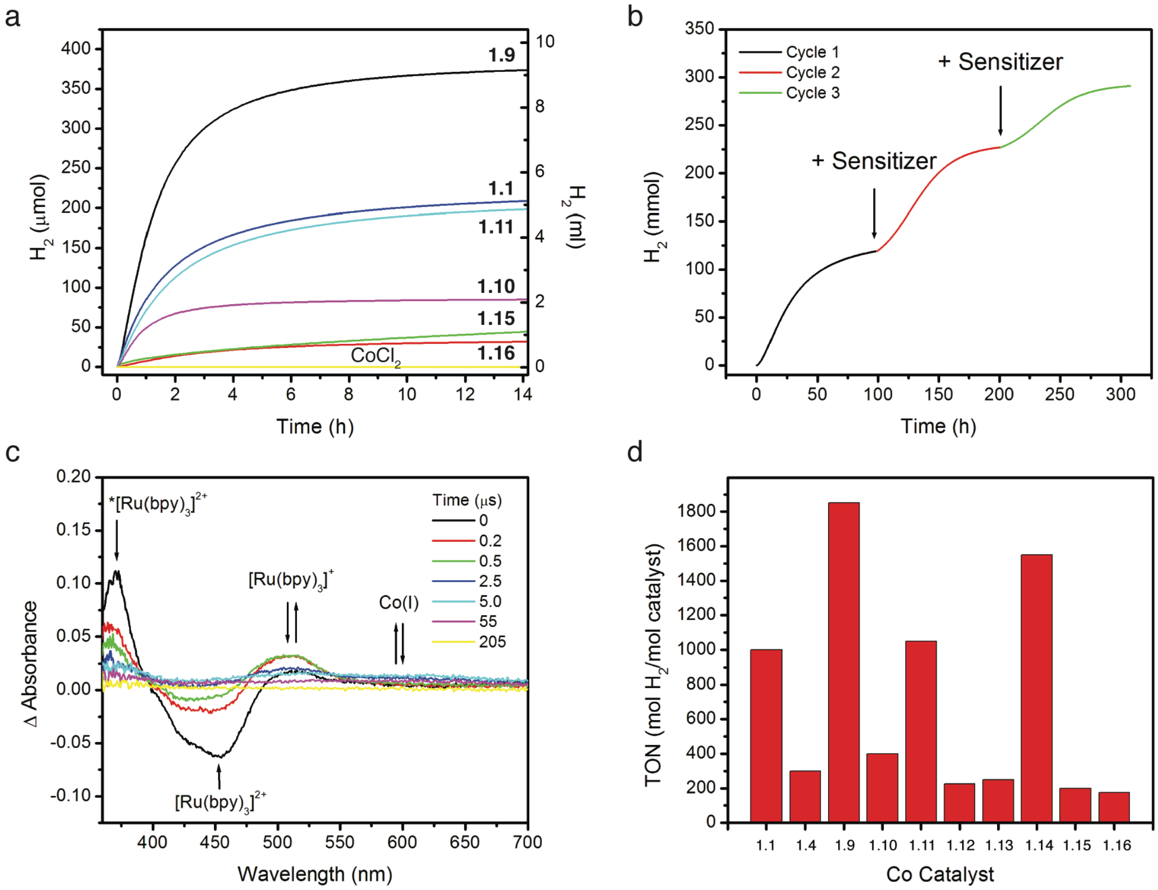

Figure 1.11. (a) Photocatalytic hydrogen production versus time of different Co catalysts. (b) Catalysis is limited by photosensitizer stability. (c) Transient absorption difference spectra shows formation of a Co(I) species of **1.9** coinciding with disappearance of $[Ru(bpy)_3]^+$. (d) TONs of different Co catalysts at their respective optimal pH.

Table 1.2. Photolytic hydrogen production by molecular cobalt catalysts.[a]

	TON (mol H_2 (mol cat)$^{-1}$)	TOF (mol H_2 (mol cat h)$^{-1}$)	pH with highest activity	reaction time (h)	ref
1.1	1015	73	4.5	14	65
1.4	290	22	6.0	13	64
1.5	300	23	6.0	13	64
1.7	1625	125	4.0	13	64
1.8	1375	106	4.5	13	64
1.9	1875	134	4.0	14	65
1.10	425	30	4.5	14	65
1.11	1065	76	4.0	14	65
1.12	235	13	5.0	18	65
1.13	260	14	5.5	18	65
1.14	1565	87	5.0	18	65
1.15	225	16	5.5	14	65
1.16	150	11	5.0	14	65

[a] Photolysis conditions: 330 μM $[Ru(bpy)_3]^{2+}$, 0.3 M ascorbate buffer, and 20 μM catalyst in water, irradiated at 452 nm with 540 mW output

1.9. Concluding Remarks

In this Chapter, we have summarized recent progress in our laboratories in the creation of molecular catalysts for electrochemical and photochemical water reduction. Specifically, we have developed a family of molybdenum- and cobalt-polypyridyl proton reduction catalysts that operate in pure water with high, selective, and robust activity. The foregoing examples highlight how molecular systems can conceptually and practically shed large portions of enzymatic and heterogeneous catalysts while retaining the minimal chemical unit needed for catalytic function. As such, molecular systems provide a useful, complementary approach to biological and materials catalysts for sustainable solar-to-fuel conversion. This work sets the stage for the broader application of polypyridyl systems to catalysis under environmentally benign aqueous conditions.

1.10. Acknowledgments

This Chapter includes work published in: Zee, D. Z.; Chantarojsiri, T.; Long, J. R.; Chang, C. J. Metal–Polypyridyl Catalysts for Electro- and Photochemical Reduction of Water to Hydrogen. *Acc. Chem. Res.* **2015**, *48* (7), 2027–2036. This work is funded by DOE/LBNL Grant 101528-002 (T.C. and C.J.C.) and the Joint Center for Artificial Photosynthesis, a DOE Energy Innovation Hub, supported through the Office of Science of the U.S. Department of Energy award DE-SC0004993 (D.Z.Z. and J.R.L.). T.C. is supported by a DPST scholarship from the Thai government. D.Z.Z. thanks the National Science Foundation for a Graduate Research Fellowship. C.J.C. is an Investigator with the Howard Hughes Medical Institute.

1.11. References

(1) Bard, A. J.; Fox, M. A. Artificial Photosynthesis: Solar Splitting of Water to Hydrogen and Oxygen. *Acc. Chem. Res.* **1995**, *28*, 141–145.
(2) Turner, J. A. Sustainable Hydrogen Production. *Science* **2004**, *305*, 972–974.
(3) Gordon, R. B.; Bertram, M.; Graedel, T. E. Metal Stocks and Sustainability. *Proc. Natl. Acad. Sci. U.S.A.* **2006**, *103*, 1209–1214.
(4) Lewis, N. S.; Nocera, D. G. Powering the Planet: Chemical Challenges in Solar Energy Utilization. *Proc. Natl. Acad. Sci. U.S.A.* **2006**, *103*, 15729–15735.
(5) Armstrong, F. Hydrogenases: Active Site Puzzles and Progress. *Curr. Opin. Chem. Biol.* **2004**, *8*, 133–140.
(6) Fontecilla-Camps, J. C.; Volbeda, A.; Cavazza, C.; Nicolet, Y. Structure/Function Relationships of [NiFe]- and [FeFe]-Hydrogenases. *Chem. Rev.* **2007**, *107*, 4273–4303.
(7) Barton, B. E.; Olsen, M. T.; Rauchfuss, T. B. Artificial Hydrogenases. *Curr. Opin. Biotechnol.* **2010**, *21*, 292–297.
(8) Cook, T. R.; Dogutan, D. K.; Reece, S. Y.; Surendranath, Y.; Teets, T. S.; Nocera, D. G. Solar Energy Supply and Storage for the Legacy and Nonlegacy Worlds. *Chem. Rev.* **2010**, *110*, 6474–6502.
(9) Artero, V.; Chavarot-Kerlidou, M.; Fontecave, M. Splitting Water with Cobalt. *Angew. Chem. Int. Ed.* **2011**, *50*, 7238–7266.
(10) Wang, M.; Chen, L.; Sun, L. Recent Progress in Electrochemical Hydrogen Production with Earth-Abundant Metal Complexes as Catalysts. *Energy Environ. Sci.* **2012**, *5*, 6763–6778.
(11) Thoi, V. S.; Sun, Y.; Long, J. R.; Chang, C. J. Complexes of Earth-Abundant Metals

for Catalytic Electrochemical Hydrogen Generation Under Aqueous Conditions. *Chem. Soc. Rev.* **2013**, *42*, 2388–2400.

(12) McKone, J. R.; Marinescu, S. C.; Brunschwig, B. S.; Winkler, J. R.; Gray, H. B. Earth-Abundant Hydrogen Evolution Electrocatalysts. *Chem. Sci.* **2014**, *5*, 865–878.

(13) Bullock, R. M.; Appel, A. M.; Helm, M. L. Production of Hydrogen by Electrocatalysis: Making the H–H Bond by Combining Protons and Hydrides. *Chem. Commun.* **2014**, *50*, 3125–3143.

(14) Han, Z.; Eisenberg, R. Fuel From Water: the Photochemical Generation of Hydrogen From Water. *Acc. Chem. Res.* **2014**, *47*, 2537–2544.

(15) DuBois, D. L. Development of Molecular Electrocatalysts for Energy Storage. *Inorg. Chem.* **2014**, *53*, 3935–3960.

(16) Bigi, J. P.; Hanna, T. E.; Harman, W. H.; Chang, A.; Chang, C. J. Electrocatalytic Reduction of Protons to Hydrogen by a Water-Compatible Cobalt Polypyridyl Platform. *Chem. Commun.* **2010**, *46*, 958–960.

(17) Goldsmith, C. R.; Jonas, R. T.; Stack, T. D. P. C-H Bond Activation by a Ferric Methoxide Complex: Modeling the Rate-Determining Step in the Mechanism of Lipoxygenase. *J. Am. Chem. Soc.* **2002**, *124*, 83–96.

(18) Klein Gebbink, R. J. M.; Jonas, R. T.; Goldsmith, C. R.; Stack, T. D. P. A Periodic Walk: a Series of First-Row Transition Metal Complexes with the Pentadentate Ligand PY5. *Inorg. Chem.* **2002**, *41*, 4633–4641.

(19) Goldsmith, C. R.; Jonas, R. T.; Cole, A. P.; Stack, T. D. P. A Spectrochemical Walk: Single-Site Perturbation Within a Series of Six-Coordinate Ferrous Complexes. *Inorg. Chem.* **2002**, *41*, 4642–4652.

(20) Bechlars, B.; D'Alessandro, D. M.; Jenkins, D. M.; Iavarone, A. T.; Glover, S. D.; Kubiak, C. P.; Long, J. R. High-Spin Ground States via Electron Delocalization in Mixed-Valence Imidazolate-Bridged Divanadium Complexes. *Nature Chem.* **2010**, *2*, 362–368.

(21) Parkin, G.; Bercaw, J. E. (η^5-$C_5Me_5)_2W=O$: an Exceptionally Reactive Organometallic Oxo Derivative. Reduction with Dihydrogen and Reaction with Dioxygen Resulting in Insertion of Oxygen Into a Tungsten-Carbon Bond. *J. Am. Chem. Soc.* **1989**, *111*, 391–393.

(22) Silavwe, N. D.; Bruce, M. R. M.; Philbin, C. E.; Tyler, D. R. Descriptive Photochemistry and Electronic Structure of the Cp_2MoO and $(MeCp)_2MoO$ Complexes ($Cp = \eta^5$-C_5H_5; $MeCp = \eta^5$-$CH_3C_5H_4$). *Inorg. Chem.* **1988**, *27*, 4669–4676.

(23) Yoon, M.; Tyler, D. R. Activation of Water by Permethyltungstenocene; Evidence for the Oxidative Addition of Water. *Chem. Commun.* **1997**, 639–670.

(24) Baxley, G. T.; Avey, A. A.; Aukett, T. M.; Tyler, D. R. Photoactivation of Water by Cp'_2Mo and Photochemical Studies of Cp_2MoO. Investigation of a Proposed Water-Splitting Cycle and Preparation of a Water-Soluble Molybdocene Dihydride. *Inorg. Chim. Acta* **2000**, *300*, 102–112.

(25) Blum, O.; Milstein, D. Oxidative Addition of Water and Aliphatic Alcohols by $IrCl(Trialkylphosphine)_3$. *J. Am. Chem. Soc.* **2002**, *124*, 11456–11467.

(26) Karunadasa, H. I.; Chang, C. J.; Long, J. R. A Molecular Molybdenum-Oxo Catalyst for Generating Hydrogen From Water. *Nature* **2010**, *464*, 1329–1333.

(27) Thoi, V. S.; Karunadasa, H. I.; Surendranath, Y.; Long, J. R.; Chang, C. J. Electrochemical Generation of Hydrogen From Acetic Acid Using a Molecular

Molybdenum–Oxo Catalyst. *Energy Environ. Sci.* **2012**, *5*, 7762–7770.

(28) Sundstrom, E. J.; Yang, X.; Thoi, V. S.; Karunadasa, H. I.; Chang, C. J.; Long, J. R.; Head-Gordon, M. Computational and Experimental Study of the Mechanism of Hydrogen Generation From Water by a Molecular Molybdenum-Oxo Electrocatalyst. *J. Am. Chem. Soc.* **2012**, *134*, 5233–5242.

(29) Hinnemann, B.; Moses, P. G.; Bonde, J.; Jørgensen, K. P.; Nielsen, J. H.; Horch, S.; Chorkendorff, I.; Nørskov, J. K. Biomimetic Hydrogen Evolution: MoS_2 Nanoparticles as Catalyst for Hydrogen Evolution. *J. Am. Chem. Soc.* **2005**, *127*, 5308–5309.

(30) Jaramillo, T. F.; Jørgensen, K. P.; Bonde, J.; Nielsen, J. H.; Horch, S.; Chorkendorff, I. Identification of Active Edge Sites for Electrochemical H_2 Evolution From MoS_2 Nanocatalysts. *Science* **2007**, *317*, 100–102.

(31) Zong, X.; Yan, H.; Wu, G.; Ma, G.; Wen, F.; Wang, L.; Li, C. Enhancement of Photocatalytic H_2 Evolution on CdS by Loading MoS_2 As Cocatalyst Under Visible Light Irradiation. *J. Am. Chem. Soc.* **2008**, *130*, 7176–7177.

(32) Li, Y.; Wang, H.; Xie, L.; Liang, Y.; Hong, G.; Dai, H. MoS_2 Nanoparticles Grown on Graphene: an Advanced Catalyst for the Hydrogen Evolution Reaction. *J. Am. Chem. Soc.* **2011**, *133*, 7296–7299.

(33) Merki, D.; Fierro, S.; Vrubel, H.; Hu, X. Amorphous Molybdenum Sulfide Films as Catalysts for Electrochemical Hydrogen Production in Water. *Chem. Sci.* **2011**, *2*, 1262–1267.

(34) Lukowski, M. A.; Daniel, A. S.; Meng, F.; Forticaux, A.; Li, L.; Jin, S. Enhanced Hydrogen Evolution Catalysis From Chemically Exfoliated Metallic MoS_2 Nanosheets. *J. Am. Chem. Soc.* **2013**, *135*, 10274–10277.

(35) Karunadasa, H. I.; Montalvo, E.; Sun, Y.; Majda, M.; Long, J. R.; Chang, C. J. A Molecular MoS_2 Edge Site Mimic for Catalytic Hydrogen Generation. *Science* **2012**, *335*, 698–702.

(36) Sun, Y.; Bigi, J. P.; Piro, N. A.; Tang, M. L.; Long, J. R.; Chang, C. J. Molecular Cobalt Pentapyridine Catalysts for Generating Hydrogen From Water. *J. Am. Chem. Soc.* **2011**, *133*, 9212–9215.

(37) King, A. E.; Surendranath, Y.; Piro, N. A.; Bigi, J. P.; Long, J. R.; Chang, C. J. A Mechanistic Study of Proton Reduction Catalyzed by a Pentapyridine Cobalt Complex: Evidence for Involvement of an Anation-Based Pathway. *Chem. Sci.* **2013**, *4*, 1578–1587.

(38) Shi, S.; Daniels, L. M.; Espenson, J. H. Molecular Structure of a Cobalt(I) Complex Lacking a Carbonyl Ligand. A Unique Example of Cobalt-Nitrogen Bond Shortening. *Inorg. Chem.* **1991**, *30*, 3407–3410.

(39) Hu, X.; Cossairt, B. M.; Brunschwig, B. S.; Lewis, N. S.; Peters, J. C. Electrocatalytic Hydrogen Evolution by Cobalt Difluoroboryl-Diglyoximate Complexes. *Chem. Commun.* **2005**, 4723–4725.

(40) Hu, X.; Brunschwig, B. S.; Peters, J. C. Electrocatalytic Hydrogen Evolution at Low Overpotentials by Cobalt Macrocyclic Glyoxime and Tetraimine Complexes. *J. Am. Chem. Soc.* **2007**, *129*, 8988–8998.

(41) Sun, Y.; Sun, J.; Long, J. R.; Yang, P.; Chang, C. J. Photocatalytic Generation of Hydrogen From Water Using a Cobalt Pentapyridine Complex in Combination with Molecular and Semiconductor Nanowire Photosensitizers. *Chem. Sci.* **2013**, *4*, 118–124.

(42) Razavet, M.; Artero, V.; Fontecave, M. Proton Electroreduction Catalyzed by Cobaloximes: Functional Models for Hydrogenases. *Inorg. Chem.* **2005**, *44*, 4786–4795.
(43) Baffert, C.; Artero, V.; Fontecave, M. Cobaloximes as Functional Models for Hydrogenases. 2. Proton Electroreduction Catalyzed by Difluoroborylbis(Dimethylglyoximato)Cobalt(II) Complexes in Organic Media. *Inorg. Chem.* **2007**, *46*, 1817–1824.
(44) Fourmond, V.; Jacques, P.-A.; Fontecave, M.; Artero, V. H_2 Evolution and Molecular Electrocatalysts: Determination of Overpotentials and Effect of Homoconjugation. *Inorg. Chem.* **2010**, *49*, 10338–10347.
(45) McCrory, C. C. L.; Uyeda, C.; Peters, J. C. Electrocatalytic Hydrogen Evolution in Acidic Water with Molecular Cobalt Tetraazamacrocycles. *J. Am. Chem. Soc.* **2012**, *134*, 3164–3170.
(46) Jacobsen, G. M.; Yang, J. Y.; Twamley, B.; Wilson, A. D.; Bullock, R. M.; Rakowski DuBois, M.; DuBois, D. L. Hydrogen Production Using Cobalt-Based Molecular Catalysts Containing a Proton Relay in the Second Coordination Sphere. *Energy Environ. Sci.* **2008**, *1*, 167–174.
(47) Fang, M.; Wiedner, E. S.; Dougherty, W. G.; Kassel, W. S.; Liu, T.; DuBois, D. L.; Bullock, R. M. Cobalt Complexes Containing Pendant Amines in the Second Coordination Sphere as Electrocatalysts for H_2 Production. *Organometallics* **2014**, *33*, 5820–5833.
(48) Dempsey, J. L.; Brunschwig, B. S.; Winkler, J. R.; Gray, H. B. Hydrogen Evolution Catalyzed by Cobaloximes. *Acc. Chem. Res.* **2009**, *42*, 1995–2004.
(49) Dempsey, J. L.; Winkler, J. R.; Gray, H. B. Kinetics of Electron Transfer Reactions of H_2-Evolving Cobalt Diglyoxime Catalysts. *J. Am. Chem. Soc.* **2010**, *132*, 1060–1065.
(50) Stubbert, B. D.; Peters, J. C.; Gray, H. B. Rapid Water Reduction to H_2 Catalyzed by a Cobalt Bis(Iminopyridine) Complex. *J. Am. Chem. Soc.* **2011**, *133*, 18070–18073.
(51) Marinescu, S. C.; Winkler, J. R.; Gray, H. B. Molecular Mechanisms of Cobalt-Catalyzed Hydrogen Evolution. *Proc. Natl. Acad. Sci. U.S.A.* **2012**, *109*, 15127–15131.
(52) McNamara, W. R.; Han, Z.; Alperin, P. J.; Brennessel, W. W.; Holland, P. L.; Eisenberg, R. A Cobalt–Dithiolene Complex for the Photocatalytic and Electrocatalytic Reduction of Protons. *J. Am. Chem. Soc.* **2011**, *133*, 15368–15371.
(53) McNamara, W. R.; Han, Z.; Yin, C.-J. M.; Brennessel, W. W.; Holland, P. L.; Eisenberg, R. Cobalt-Dithiolene Complexes for the Photocatalytic and Electrocatalytic Reduction of Protons in Aqueous Solutions. *Proc. Natl. Acad. Sci. U.S.A.* **2012**, *109*, 15594–15599.
(54) Probst, B.; Guttentag, M.; Rodenberg, A.; Hamm, P.; Alberto, R. Photocatalytic H_2 Production From Water with Rhenium and Cobalt Complexes. *Inorg. Chem.* **2011**, *50*, 3404–3412.
(55) Rodenberg, A.; Orazietti, M.; Probst, B.; Bachmann, C.; Alberto, R.; Baldridge, K. K.; Hamm, P. Mechanism of Photocatalytic Hydrogen Generation by a Polypyridyl-Based Cobalt Catalyst in Aqueous Solution. *Inorg. Chem.* **2015**, *54*, 646–657.
(56) Chen, L.; Wang, M.; Han, K.; Zhang, P.; Gloaguen, F.; Sun, L. A Super-Efficient Cobalt Catalyst for Electrochemical Hydrogen Production From Neutral Water with 80 mV Overpotential. *Energy Environ. Sci.* **2013**, *7*, 329–334.
(57) Zhang, P.; Wang, M.; Gloaguen, F.; Chen, L.; Quentel, F.; Sun, L. Electrocatalytic

Hydrogen Evolution From Neutral Water by Molecular Cobalt Tripyridine-Diamine Complexes. *Chem. Commun.* **2013**, *49*, 9455–9457.

(58) Singh, W. M.; Baine, T.; Kudo, S.; Tian, S.; Ma, X. A. N.; Zhou, H.; DeYonker, N. J.; Pham, T. C.; Bollinger, J. C.; Baker, D. L.; Yan, B.; Webster, C. E.; Zhao, X. Electrocatalytic and Photocatalytic Hydrogen Production in Aqueous Solution by a Molecular Cobalt Complex. *Angew. Chem. Int. Ed. Engl.* **2012**, *51*, 5941–5944.

(59) Lee, C. H.; Dogutan, D. K.; Nocera, D. G. Hydrogen Generation by Hangman Metalloporphyrins. *J. Am. Chem. Soc.* **2011**, *133*, 8775–8777.

(60) Singh, W. M.; Mirmohades, M.; Jane, R. T.; White, T. A.; Hammarström, L.; Thapper, A.; Lomoth, R.; Ott, S. Voltammetric and Spectroscopic Characterization of Early Intermediates in the Co(II)–Polypyridyl-Catalyzed Reduction of Water. *Chem. Commun.* **2013**, *49*, 8638–8640.

(61) Mandal, S.; Shikano, S.; Yamada, Y.; Lee, Y.-M.; Nam, W.; Llobet, A.; Fukuzumi, S. Protonation Equilibrium and Hydrogen Production by a Dinuclear Cobalt–Hydride Complex Reduced by Cobaltocene with Trifluoroacetic Acid. *J. Am. Chem. Soc.* **2013**, *135*, 15294–15297.

(62) Tong, L.; Zong, R.; Thummel, R. P. Visible Light-Driven Hydrogen Evolution From Water Catalyzed by a Molecular Cobalt Complex. *J. Am. Chem. Soc.* **2014**, *136*, 4881–4884.

(63) Letko, C. S.; Panetier, J. A.; Head-Gordon, M.; Tilley, T. D. Mechanism of the Electrocatalytic Reduction of Protons with Diaryldithiolene Cobalt Complexes. *J. Am. Chem. Soc.* **2014**, *136*, 9364–9376.

(64) Nippe, M.; Khnayzer, R. S.; Panetier, J. A.; Zee, D. Z.; Olaiya, B. S.; Head-Gordon, M.; Chang, C. J.; Castellano, F. N.; Long, J. R. Catalytic Proton Reduction with Transition Metal Complexes of the Redox-Active Ligand bpy2PYMe. *Chem. Sci.* **2013**, *4*, 3934–3945.

(65) Khnayzer, R. S.; Thoi, V. S.; Nippe, M.; King, A. E.; Jurss, J. W.; Roz, El, K. A.; Long, J. R.; Chang, C. J.; Castellano, F. N. Towards a Comprehensive Understanding of Visible-Light Photogeneration of Hydrogen From Water Using Cobalt(II) Polypyridyl Catalysts. *Energy Environ. Sci.* **2014**, *7*, 1477–1488.

(66) Voloshin, Y. Z.; Dolganov, A. V.; Varzatskii, O. A.; Bubnov, Y. N. Efficient Electrocatalytic Hydrogen Production From H+ Ions Using Specially Designed Boron-Capped Cobalt Clathrochelates. *Chem. Commun.* **2011**, *47*, 7737–7739.

(67) Anxolabéhère-Mallart, E.; Costentin, C.; Fournier, M.; Nowak, S.; Robert, M.; Savéant, J.-M. Boron-Capped Tris(Glyoximato) Cobalt Clathrochelate as a Precursor for the Electrodeposition of Nanoparticles Catalyzing H_2 Evolution in Water. *J. Am. Chem. Soc.* **2012**, *134*, 6104–6107.

(68) Ghachtouli, El, S.; Fournier, M.; Cherdo, S.; Guillot, R.; Charlot, M.-F.; Anxolabéhère-Mallart, E.; Robert, M.; Aukauloo, A. Monometallic Cobalt–Trisglyoximato Complexes as Precatalysts for Catalytic H_2 Evolution in Water. *J. Phys. Chem. C* **2013**, *117*, 17073–17077.

(69) Ghachtouli, El, S.; Guillot, R.; Brisset, F.; Aukauloo, A. Cobalt-Based Particles Formed Upon Electrocatalytic Hydrogen Production by a Cobalt Pyridine Oxime Complex. *ChemSusChem* **2013**, *6*, 2226–2230.

(70) Anxolabéhère-Mallart, E.; Costentin, C.; Fournier, M.; Robert, M. Cobalt-Bisglyoximato Diphenyl Complex as a Precatalyst for Electrocatalytic H_2 Evolution. *J.*

Phys. Chem. C **2014**, *118*, 13377–13381.
(71) Artero, V.; Savéant, J.-M. Toward the Rational Benchmarking of Homogeneous H_2-Evolving Catalysts. *Energy Environ. Sci.* **2014**, *7*, 3808–3814.

Chapter 2. Syntheses and Kinetic Analyses of Polypyridyl–Cobalt Complexes for Electrocatalytic Hydrogen Evolution

2.1. Introduction

The increasing demand for energy, uncertainty in fossil fuel supplies, and concerns over anthropogenic climate change are driving the development of sustainable, alternative energy sources.[1] Hydrogen is a particularly attractive fuel source as its combustion product is water,[1-3] but a renewable and cost-efficient production method of H_2 must first be discovered. The predominant source of hydrogen today is via steam reforming, a process dependent upon fossil fuel input.[3] In order to convert solar energy into fuel in a carbon-neutral fashion, efficient electrocatalysts for hydrogen evolution need to be coupled to solar capture. Although platinum effectively catalyzes the production of H_2 through the electrolysis of water, its low abundance and high cost discourage its widespread implementation in devices.[4-7] The development of catalysts deriving from cheap, earth-abundant elements provides a promising outlook to fabricating low-cost devices that sustainably produce H_2.

Nature utilizes molecular catalytic systems containing iron and/or nickel, transition metal elements with high natural abundances, in hydrogenase enzymes to catalyze hydrogen evolution from water with virtually zero overpotential and high turnover frequencies.[8-10] Yet the enzymes' large sizes, structural complexity, and tendency to decompose *in vitro* hinder their use in devices.[11,12] Synthetic [2Fe-2S] and [Fe-Ni-2S] clusters mimicking hydrogenase enzyme active sites have been found to evolve H_2, but generally require the use of organic acids and high overpotentials, which meant that as catalysts the clusters were energetically inefficient.[13,14] Many other electrocatalysts utilizing cobalt,[15-18] nickel,[19-22] and molybdenum[23,24] operate at moderate overpotentials, but require organic solvents and additives at their optimal working conditions. Making molecular catalysts for hydrogen generation from water that are derived from earth-abundant elements and that require no organic additives while maintaining high efficiency and activity in aqueous media is a significant challenge.

Transition metal complexes employing semi-rigid polypyridyine platforms are particularly promising systems for electrocatalytic hydrogen evolution because they can operate under aqueous conditions. The tetrapyridyl complex $[(PY4)Co(CH_3CN)_2]^{2+}$ (PY4 = 2-bis(2-pyridyl)(methoxy)methyl-6-pyridylpyridine evolved H_2 from trifluoroacetic acid in a 50:50 mixture of acetonitrile and water.[18] Moreover, the pentapyridyine scaffold 2,6-bis(1,1-bis(2-pyridyl)ethyl)pyridine ($PY5Me_2$) furnished robust electrocatalysts of molybdenum[25,26] and cobalt[27,28] that can generate H_2 from neutral water or even seawater for several days, without the need for organic cosolvents or acids.

Of particular interest is that synthetic chemistry can tune the catalytic performance of the pentapyridine cobalt system. Electron-withdrawing CF_3 and electron-donating NMe_2 groups can be installed at the 4-position of the axial pyridine of $PY5Me_2$, giving the ligands 4-trifluoromethyl-2,6-bis(1,1-di(pyridin-2-yl)ethyl)pyridine (CF_3PY5Me_2) and 4-dimethylamino-2,6-bis(1,1-di(pyridin-2-yl)ethyl)pyridine (NMe_2PY5Me_2).[27] The overpotential for water reduction by cobalt complexes $[(XPY5Me_2)Co(H_2O)]^{2+}$ was lowered by ~200 mV with X = CF_3, and increases by ~150 mV with X = NMe_2.[27] Previous mechanistic studies of $[(PY5Me_2)Co(CH_3CN)]^{2+}$ in acetonitrile with organic acids showed support protonation of a Co(I) species as a rate-determining step,[28] but additional work is needed for a full mechanistic understanding of the relationship between electronic tuning of the ligand scaffold and proton reduction catalysis.

In this vein, this Chapter further probes the structure–activity relationship of pentapyridine cobalt complexes. In particular, two different strategies for electronic tuning are pursued: 1. the monotonic shifting of both the Co(III/II) and Co(II/I) redox couples, and 2. tuning only the Co(II/I) redox couple by the selectively stabilizing the low-valent Co(I) oxidation state. The cobalt complexes are prepared, and the kinetic impact of the electronic tuning are examined electrochemically. In addition, several pentapyridine Co(I) complexes are prepared and discussed.

2.2. Experimental

2.2.1. Materials and Methods

Air- and/or moisture-sensitive compounds were synthesized and manipulated under air-free conditions, using either a Vacuum Atmospheres glovebox or standard Schlenk techniques under a dry nitrogen or argon atmosphere. Anhydrous tetrahydrofuran (THF), diethyl ether (Et_2O), acetonitrile, 1,4-dioxane, hexanes, toluene, and dichloromethane were dried and deoxygenated with a commercial solvent purification system from JC Meyer Solvent Systems, then stored under an inert atmosphere over beads of activated 3 Å molecular sieves. The compounds 1,3-dichloroisoquinoline, ethylmagnesium bromide, iron tris(acetylacetonate), diisopropylamine, *n*-butyllithium (^{n}BuLi), and anhydrous *N*-methyl-2-pyrrolidone were purchased from Sigma-Aldrich and used as received. The compounds 2-chloro-4-trifluoromethylpyridine and 2,6-dichloro-4-trifluoromethylpyridine were purchased from Oakwood Chemicals and used as received.

The compounds 1,1-bis(pyridyl)ethane,[29] $[(PY5Me_2)Co(CH_3CN)](CF_3SO_3)_2$,[27] $[(CF_3PY5Me_2)Co(CH_3CN)](CF_3SO_3)_2$,[27] $[(NMe_2PY5Me_2)Co(CH_3CN)](CF_3SO_3)_2$,[27] *N*,*N*-dimethylanilinium tetrafluoroborate,[30] and potassium cyclopentadienyldicarbonyl ferrate[31] were prepared according to literature procedures. The compound $Co(CF_3SO_3)_2(CH_3CN)_2$ was prepared by the reaction of finely divided cobalt metal with trifluoromethanesulfonic acid in dry acetonitrile, akin to the preparation of iron trifluoromethanesulfonate by Hagen.[32]

NMR spectra were obtained using a Bruker AVANCE III instrument and referenced relative to tetramethylsilane using residual solvent signals. Deuterated solvents were purchased from Cambridge Isotopes. $CDCl_3$ (99.8% D) was treated with anhydrous K_2CO_3. CD_3CN (99.8% D) was dried over powdered 3 Å molecular sieves for 48 h, separated from the sieves by vacuum transfer, deoxygenated by freeze-pump-thaw cycles, and stored over beads of 3 Å molecular sieves under an inert atmosphere.

Electrospray ionization mass spectrometry (ESI-MS) measurements were performed with an Agilent 6230 time-of-flight mass spectrometer equipped with an Agilent Jet Stream source or a Shimadzu 2020 liquid chromatography/mass spectrometer. C, H, and N analyses were performed at the Microanalytical Laboratory at the University of California, Berkeley. Electronic absorption spectra were taken with a Cary 5000 UV-vis-NIR spectrophotometer. Infrared spectra were collected on a Perkin Elmer Spectrum 400 FTIR spectrometer at 4 cm^{-1} resolution with an attenuated total reflectance accessory (diamond crystal).

Electrochemical measurements were performed with acetonitrile (EMD Millipore, OmniSolv Gradient grade). NBu_4PF_6 (Oakwood Chemical) was recrystallized from ethanol/water and dried under vacuum at 100 °C for 24 h before use. Cyclic voltammetry measurements were obtained with 1 mM of complex in CH_3CN using a glassy carbon disk (3.0 mm dia.) working electrode, a nonaqueous $Ag/AgNO_3$ (0.1 mM) reference electrode, and a graphite counter electrode with 0.1 M NBu_4PF_6 as supporting electrolyte. Between experiments, the working electrode was polished with agglomerate-free 0.05 μm alumina and subsequently sonicated in acetonitrile containing activated carbon.[33] Ferrocene was added after each CV experiment as an internal reference. The $Fe(C_5H_5)_2^{+/0}$

couple was found to be +0.19(1) V versus Ag/$AgNO_3$.

2.2.2. Synthesis

1,3-bis(1,1-di(pyridin-2-yl)ethyl)isoquinoline (PY4IqMe$_2$). 1,1-Bis(pyridyl)ethane (4.48 g, 24.3 mmol) was added to a 200 mL Schlenk flask equipped with a magnetic stir bar and dissolved into 1,4-dioxane (~30 mL). The solution was cooled with an ice bath. While stirring, ^{n}BuLi (2.5 M in hexanes, 9.72 mL, 24.3 mmol) was slowly added, resulting in a color change from light yellow to dark red. Stirring was continued for 15 min, then a solution of 1,3-dichloroisoquinoline (1.20 g, 6.08 mmol) in 1,4-dioxane (~30 mL) was added with a cannula. The cooling bath was removed, and the reaction was heated to reflux for 72 h. The reaction mixture was quenched with ~100 mL of water and the aqueous and organic layers were separated. At this point the workup was conducted under air. The aqueous layer was extracted with 3 × ~100 mL of ethyl acetate, and the organic layers were combined, extracted with ~100 mL of water, then ~100 mL of brine, then dried over $MgSO_4$. After filtration the solvent was removed under reduced pressure to afford an orange oil. The residue was dissolved in ~20 mL of hot CH_2Cl_2 and allowed to cool to room temperature. Colorless crystals were obtained by diffusing Et_2O into the CH_2Cl_2 solution over three days. The crystalline product was collected by filtration and washed with ~40 mL of ice-cold Et_2O and dried under high vacuum at 50 °C for 12 h to afford 2.67 g (82%) of product as a dichloromethane solvate (PY4IqMe$_2$·0.5CH_2Cl_2). ^{1}H NMR (500 MHz, $CDCl_3$) δ 8.54 (ddd, J = 4.9, 1.9, 0.8 Hz, 2H), 8.50 – 8.44 (m, 2H), 7.71 – 7.65 (m, 1H), 7.51 – 7.28 (m, 9H), 7.19 – 6.98 (m, 8H), 6.88 (dt, J = 8.1, 1.0 Hz, 2H), 5.30 (s, 1H, CH_2Cl_2), 2.31 (s, 3H), 2.24 (s, 3H). ^{13}C NMR (126 MHz, $CDCl_3$) δ 166.5, 165.4, 163.9, 156.1, 148.4, 148.2, 138.2, 135.6, 135.4, 128.8, 128.4, 127.7, 125.7, 125.0, 124.6, 121.0, 121.0, 118.1, 61.5, 59.7, 28.0, 26.7. IR (neat): 3058 (w), 2996 (w), 2929 (w) 1618 (w), 1585 (s), 1562 (s), 1492 (w), 1465 (s), 1422 (s), 1365 (w), 1318 (m), 1289 (w), 1261 (w), 1149 (w), 1072 (w), 1046 (w), 994 (s), 921 (w), 822 (w), 786 (w), 760 (s), 681 (m), 641 (w), 616 (w) cm^{-1}. ESI-MS m/z for $[C_{33}H_{27}N_5 + H]^+$ requires 494.2339, found 494.2344. Anal. Calcd. for $C_{33.5}H_{28}N_5Cl$ (PY4IqMe$_2$·0.5CH_2Cl_2): C, 75.06; H, 5.26; N, 13.06. Found: C, 75.76; H, 5.45; N, 13.11.

2-Ethyl-4-trifluoromethylpyridine. Ethylmagnesium bromide (3.0 M in Et_2O, 23.9 mL, 71.6 mmol) was slowly added to a 500 mL Schlenk flask containing a stirred solution of iron(III) acetylacetonate (973 mg, 2.76 mmol) and 2-chloro-4-trifluoromethylpyridine (7.09 mL, 55.1 mmol) in a mixture of tetrahydrofuran (275 mL) and *N*-methyl-2-pyrrolidone (25 mL) at 0 °C. The resulting dark violet solution was warmed to room temperature and stirred for an additional 20 min before quenching with 200 mL of saturated aqueous NH_4Cl. Subsequent workup was conducted in air. The aqueous and organic layers were separated and the aqueous layer was extracted with Et_2O (3 × 200 mL). The organic layers were combined, dried over $MgSO_4$ and filtered. Solvent removal under reduced pressure at 0 °C afforded a dark red liquid which was subsequently purified via flash chromatography (silica, 20:1 pentanes:Et_2O, R_f = 0.13). After concentration by rotary evaporation at 0 °C, followed by a brief (~30 s) application of high vacuum, the desired product was isolated as a volatile yellow liquid. Yield: 6.29 g (65%). ^{1}H NMR ($CDCl_3$, 500 MHz) δ 8.71 (1H, d), 7.38 (1H, s), 7.33 (1H), 2.92 (q, J = 7.6 Hz, 2H), 1.35 (t, J = 7.7 Hz, 3H). ^{13}C NMR ($CDCl_3$, 126 MHz) δ 165.2, 150.3, 138.7 (q, J_{CF} = 33.2 Hz), 123.1 (q, J_{CF} = 273.2 Hz), 117.8 (q, J_{CF} = 3.8 Hz), 116.7 (q, J_{CF} = 3.5 Hz), 31.6, 13.8. ^{19}F NMR ($CDCl_3$, 470 MHz) δ −64.8. ESI-MS m/z for $[C_8H_8F_3N + H]^+$ requires 176.0682, found 176.0683. Owing to this compound's high volatility, combustion analyses did not yield satisfactory results. This compound is best used immediately or stored at reduced temperature (0 °C or lower) in a sealed vessel (e.g. Schlenk or storage flask) to avoid losses due to evaporation.

2,2′-(ethane-1,1-diyl)bis(4-(trifluoromethyl)pyridine). Lithium diisopropylamide was prepared by cooling a solution of diisopropylamine (3.63 g, 5.07 mL, 35.9 mmol) in tetrahydrofuran (60 mL) to −78 °C, then adding ^{n}BuLi (2.5 M in hexanes, 14.4 mL, 35.9 mmol) in tetrahydrofuran (60 mL) dropwise via syringe. The resulting light yellow solution was stirred at −78°C for 1 h. The lithium diisopropylamide solution was then transferred using a cannula into a 500 mL Schlenk flask containing a magnetic stir bar and a solution of 2-ethyl-4-trifluoromethylpyridine (6.29 g, 35.9 mmol) in tetrahydrofuran (300 mL) that was cooled at −78°C. After the cannula transfer was complete, the resulting dark purple solution was stirred at −78°C for 1 h. 2-Chloro-4-trifluoromethylpyridine (4.36 g, 3.10 mL, 24.0 mmol) was added to the dark purple solution with a syringe. The cooling bath was removed and the reaction was warmed to room temperature, during which the reaction solution changed color from purple to blood red. The reaction was stirred at room temperature for 9 h. It is inadvisable to conduct the reaction at higher temperatures, as it encourages the formation of undesirable side reactions and lowers the yield of desired product. The reaction was quenched with ~300 mL of a saturated aqueous solution of NH_4Cl. Subsequent workup was conducted in air. The aqueous solution was extracted with 3 × ~300 mL of ethyl acetate. The organic washes were combined, extracted with ~100 mL of water, followed by 100 mL of brine, then dried over $MgSO_4$, and filtered to afford an orange solution. The filtrate was concentrated via rotary evaporation, then further concentrated under high vacuum to afford a brown liquid. The crude mixture was purified via vacuum distillation through a short-path condenser, into a receiving flask cooled at −78°C. The initial fraction (55 mTorr, vapor temperature 49 °C) comprised unreacted 2-chloro-4-trifluoromethylpyridine. The desired product was collected in the second fraction (55 mTorr, 59 °C). The product is a bright yellow liquid and is stable for at least one year when stored under an atmosphere of N_2 at room temperature. Samples exposed to air slowly darken, and can be re-purified by distillation. Yield: 5.31 g (69%). ^{1}H NMR (500 MHz, $CDCl_3$) δ 8.72 (d, J = 5.1 Hz, 2H), 7.55 (s, 2H), 7.35 (d, J = 5.1 Hz, 2H), 4.61 (q, J = 7.2 Hz, 1H), 1.79 (d, J = 7.3 Hz, 3H). ^{13}C NMR (126 MHz, $CDCl_3$) δ 164.6, 150.5, 139.0 (q, J_{CF} = 33.9 Hz), 122.9 (q, J_{CF} = 273.2 Hz), 118.2 (q, J_{CF} = 3.6 Hz), 117.6 (q, J_{CF} = 3.5 Hz), 50.0, 19.9. ^{19}F NMR (470 MHz, $CDCl_3$) δ −64.8. ESI-MS m/z for $[C_{14}H_{10}F_6N_2 + H]^+$ requires 321.0821, found 321.0821. Anal. Calcd. for $C_{14}H_{10}F_6N_2$: C, 52.51; H, 3.15; N, 8.75. Found: C, 52.24; H, 2.89; N, 8.93.

2,2′,2′′,2′′′-(4-(trifluoromethyl)pyridine-2,6-diyl)bis(ethane-1,1,1-triyl))tetrakis(4-(trifluoromethyl)pyridine) ($(CF_3)_5PY5Me_2$). The compound 2,2′-(ethane-1,1-diyl)bis(4-(trifluoromethyl)pyridine) (1.7 g, 5.3 mmol) was added to a 100 mL Schlenk flask equipped with a magnetic stir bar, dissolved into 1,4-dioxane (50 mL), then cooled with an ice bath. *n*-Butyllithium (2.5 M in hexanes, 2.1 mL, 5.3 mmol) was added dropwise via syringe, resulting in a deep red solution. The solution was allowed to stir for 10 minutes, then 2,6-dichloro-4-(trifluoromethyl)pyridine (0.29 g, 190 μL, 1.3 mmol) was added via syringe. The reaction was refluxed for 72 h. The reaction solution was cooled to room temperature and quenched with 50 mL of saturated aqueous $NaHCO_3$, after which the workup was conducted in air. The aqueous solution was extracted with 3 × ~50 mL of ethyl acetate. The organic washes were combined, extracted with ~100 mL of water, followed by ~100 mL of brine, then dried over $MgSO_4$ and filtered to afford an orange solution. The solvent was removed via rotary evaporation to afford a brown oil. Purification via column chromatography (silica, 10:1 hexanes:ethyl acetate) separated $(CF_3)_5PY5Me_2$ (R_f = 0.20) and excess 2,2′-(ethane-1,1-diyl)bis(4-(trifluoromethyl)pyridine) (R_f =

0.20) from other impurities. The more volatile 2,2′-(ethane-1,1-diyl)bis(4-(trifluoromethyl)pyridine) was removed by Kugelrohr distillation (300 mTorr, 170 °C, 50 rpm) to afford (CF$_3$)$_5$PY5Me$_2$ as an orange glass that can be pulverized to a free-flowing yellow powder. Yield: 0.65 g (62 %). ^{1}H NMR (500 MHz, CDCl$_3$) δ 8.65 (d, J = 5.0 Hz, 4H), 7.42 (s, 2H), 7.36 – 7.31 (m, 4H), 7.16 (s, 4H), 2.19 (s, 6H). ^{13}C NMR (126 MHz, CDCl$_3$) δ 166.1, 164.8, 149.7, 139.6 (q, J_{CF} = 33.6 Hz), 138.4 (q, J_{CF} = 34.0 Hz), 123.0 (q, J_{CF} = 273.7 Hz), 122.8 (q, J_{CF} = 273.3 Hz), 119.1 (q, J_{CF} = 3.4 Hz), 117.5 (q, J_{CF} = 3.3 Hz), 116.9 (q, J_{CF} = 3.5 Hz), 60.6, 26.8. ^{19}F NMR (470 MHz, CDCl$_3$) δ −64.3 (3F), −64.8 (12F). ESI-MS *m/z* for [C$_{34}$H$_{20}$F$_{15}$N$_5$ + H]$^+$ requires 784.1552, found 784.1566. Anal. Calcd. for C$_{34}$H$_{20}$F$_{15}$N$_5$: C, 52.12; H, 2.57; N, 8.94. Found: C, 52.20; H, 2.43; N, 8.85.

[(PY4IqMe$_2$)Co(CF$_3$SO$_3$)](CF$_3$SO$_3$) (2.1). In a N$_2$-filled glovebox, Co(CF$_3$SO$_3$)$_2$(CH$_3$CN)$_2$ (163 mg, 371 μmol) and PY4IqMe$_2$·0.5CH$_2$Cl$_2$ (199 mg, 371 μmol) were weighed into a 20 mL scintillation vial and dissolved into CH$_3$CN (~4 mL). The resulting pink slurry was stirred at room temperature for 8 h to afford a clear, orange solution. Diffusion of Et$_2$O into this solution over a period of two days afforded the product as red-orange block-shaped crystals suitable for X-ray crystallography. The mother liquor was removed, and the crystals were washed with Et$_2$O (3 × ~3 mL) and dried under vacuum for 2 h at room temperature to afford the title compound as an orange crystalline solid. Yield: 290 mg (87%). ^{1}H NMR (400 MHz, CD$_3$CN) δ 87.12 (br, $\Delta\nu_{1/2}$ = 100 Hz, 2H), 86.39 (br, $\Delta\nu_{1/2}$ = 100 Hz, 2H,), 41.00 (br, $\Delta\nu_{1/2}$ = 60 Hz, 4H), 38.13 (br, $\Delta\nu_{1/2}$ = 50 Hz, 2H), 37.08 (br, $\Delta\nu_{1/2}$ = 50 Hz, 2H), 29.65 (br, $\Delta\nu_{1/2}$ = 50 Hz, 1H), 28.20 (br, $\Delta\nu_{1/2}$ = 300 Hz, 2H), 25.55 (br, $\Delta\nu_{1/2}$ = 40 Hz, 3H), 20.34 (br, $\Delta\nu_{1/2}$ = 40 Hz, 3H), 18.25 (br, $\Delta\nu_{1/2}$ = 300 Hz, 1H), 10.23 (br, $\Delta\nu_{1/2}$ = 30 Hz, 1H), 7.98 (br, $\Delta\nu_{1/2}$ = 40 Hz. 2H), −2.87 (br, $\Delta\nu_{1/2}$ = 40 Hz, 1H), −3.35 (br, $\Delta\nu_{1/2}$ = 20 Hz, 1H). IR (paratone oil): 1615 (w), 1595 (m), 1578 (w), 1469 (m), 1441 (m), 1391 (w) 1372 (w), 1312 (m), 1273 (s), 1260 (s), 1236 (s), 1217 (s), 1161 (s), 1137 (s), 1058 (w), 1028 (s), 998 (m), 968 (w), 920 (w), 895 (w), 819 (w), 789 (w), 776 (w), 755 (s), 714 (w), 669 (w), 630 (s), 572 (m), 516 (s) cm^{-1}. ESI-MS *m/z* for [(PY4IqMe$_2$)Co(CF$_3$SO$_3$)]$^+$ requires 701.1119, found 701.1175. Anal Calcd. for C$_{35}$H$_{27}$CoF$_6$N$_5$O$_6$S$_2$: C, 49.42; H, 3.20; N, 8.23. Found: C, 49.28; H, 3.42; N, 8.61. Effective magnetic moment (CD$_3$CN, 295 K): $\mu_{\text{eff}} = 5.3\ \mu_{\text{B}}$.

[(PY4IqMe$_2$)Co(CH$_3$CN)](PF$_6$)$_2$ (2.1′). In a N$_2$-filled glovebox, PY4IqMe$_2$·0.5CH$_2$Cl$_2$ (340 mg, 640 μmol) and CoCl$_2$ (84 mg, 640 μmol) were weighed into a 20 mL scintillation vial. The solids were stirred in ~10 mL CH$_3$CN for 2 h, resulting a blue-green suspension. To this mixture was added TlPF$_6$ (450 mg, 1.30 mmol), which led to immediate formation of a white precipitate of TlCl and the solution to turn red-orange. The solution was filtered through a pad of Celite® to remove TlCl. Diffusion of Et$_2$O into the filtrate afforded the product as brown-orange block-shaped crystals suitable for X-ray crystallography. The mother liquor was removed, and the crystals were washed with Et$_2$O (3 × ~3 mL) and dried under vacuum to afford the title compound as a brown crystalline solid that was an acetonitrile solvate. Yield = 380 mg (62%). Anal Calcd. for C$_{39}$H$_{36}$CoF$_{12}$N$_8$P$_2$ (**2.1′**·2CH$_3$CN) C, 48.51; H, 3.76; N, 11.60. Found: C, 48.85; H, 3.80; N, 10.84.

[((CF$_3$)$_5$PY5Me$_2$)Co(CH$_3$CN)](CF$_3$SO$_3$)$_2$ (2.2). In a N$_2$-filled glovebox, (CF$_3$)$_5$PY5Me$_2$ (754 mg, 962 μmol) and Co(CF$_3$SO$_3$)$_2$(CH$_3$CN)$_2$ (422 mg, 962 μmol) were weighed into a 20 mL scintillation vial, dissolved into CH$_3$CN (~10 mL), then stirred at room temperature for 12 h to afford a clear, dark orange solution with trace pink solids. The solution was filtered through a pipette packed with Celite® and concentrated under reduced pressure to a volume of ~4 mL. Diffusion of Et$_2$O into this solution over 48 h at room temperature afforded orange crystals. The crystals were isolated from the mother liquor, washed with Et$_2$O (3 × ~3 mL), and dried under high vacuum at room temperature for 2 h. Yield: 0.963 g (85 %). IR (paratone oil): 2311 (w), 2281 (w), 1634 (w), 1589 (w), 1578 (w), 1494 (w), 1406 (m), 1331 (s), 1297 (m), 1266 (s), 1223 (m), 1202 (w), 1170 (m), 1131 (s), 1109 (s), 1079 (m), 1028 (s), 916 (e), 903 (m), 858 (w), 841 (w), 828 (w), 791 (w), 774 (w), 750 (w), 735 (w), 712 (w), 692 (w), 677 (m), 634 (s), 617 (m), 606 (m), 571 (w), 516 (m), 481 (w), 469 (w) cm^{-1}. ESI-MS *m/z* for $[((CF_3)_5PY5Me_2)Co(CF_3SO_3)]^+$ requires 991.0326, found 991.0312. Anal Calcd. for $C_{38}H_{28}CoF_{21}N_6O_6S_2$: C, 38.62; H, 1.96; N, 7.11. Found: C, 38.81; H, 2.09; N, 7.11.

$[(PY4IqMe_2)Zn(CF_3SO_3)](CF_3SO_3)$ (2.3). In a N_2-filled glovebox, $ZnCl_2$ (51 mg, 0.37 mmol) and $PY4IqMe_2 \cdot 0.5CH_2Cl_2$ (200 mg, 0.37 mmol) were weighed into a 20 mL scintillation vial and dissolved into acetonitrile (~4 mL). The white, turbid mixture was stirred at room temperature for 3 h. A solution of $AgCF_3SO_3$ (190 mg, 0.74 mmol) in 1 mL of acetonitrile was added to the reaction mixture, giving immediate precipitation of AgCl and a clear solution. The reaction was stirred in the dark for another 15 min, then filtered through Celite® to remove the AgCl precipitate. Diffusion of Et_2O into this solution over a period of two days afforded the product as colorless block-shaped crystals suitable for X-ray crystallography. The mother liquor was removed, and the crystals were washed with Et_2O (3 × ~3 mL) and dried under vacuum for 2 h at room temperature to afford the title compound as a white crystalline solid. Yield: 290 mg (87%). ^{1}H NMR (400 MHz, CD_3CN) δ 9.06 (ddd, J = 5.3, 1.9, 0.8 Hz, 2H), 8.87 (ddd, J = 5.3, 1.8, 0.8 Hz, 2H), 8.51 (d, J = 8.7 Hz, 1H), 8.33 (s, 1H), 8.07 – 7.93 (m, 7H), 7.89 (dt, J = 8.3, 1.0 Hz, 2H), 7.83 (ddd, J = 8.1, 6.8, 1.0 Hz, 1H), 7.69 (ddd, J = 8.4, 6.9, 1.4 Hz, 1H), 7.59 (ddd, J = 7.6, 5.2, 1.1 Hz, 2H), 7.53 (ddd, J = 7.0, 5.3, 1.5 Hz, 2H), 2.80 (s, 3H), 2.73 (s, 3H). Anal Calcd. for $C_{35}H_{27}F_6N_5O_6S_2Zn$: C, 49.05; H, 3.18; N, 8.17. Found: C, 49.07; H, 2.99; N, 8.28.

$[(PY5Me_2)Co(CH_3CN)](CF_3SO_3)_2$. This compound was prepared according to a literature procedure.[27] Its ^{1}H NMR spectrum was not reported and is reported here. ^{1}H NMR (500 MHz, CD_3CN) δ 91.96 (br, $\Delta\nu_{1/2}$ = 310 Hz, 3H), 45.94 (br, $\Delta\nu_{1/2}$ = 310 Hz, 2H), 40.45 (br, $\Delta\nu_{1/2}$ = 140 Hz, 4H), 29.81 (v br, $\Delta\nu_{1/2}$ = 1600 Hz, 1H), 27.41 (br, $\Delta\nu_{1/2}$ = 69 Hz, 4H), 24.91 (br, $\Delta\nu_{1/2}$ = 620 Hz, 3H), −10.38 (br, $\Delta\nu_{1/2}$ = 140 Hz, 1H).

$[(NMe_3PY5Me_2)Co(CF_3SO_3)](CF_3SO_3)_2$ (2.4). In a N_2-filled glovebox, **$[(NMe_2PY5Me_2)Co(CH_3CN)](CF_3SO_3)_2$** (50 mg, 59 µmol) was dissolved into ~1 mL of CH_2Cl_2 to give a yellow-orange solution. The solvent was removed with high vacuum to remove trace CH_3CN, then redissolved into ~1 mL of CH_2Cl_2. Methyltrifluoromethanesulfonate (500 mg, 3.0 mmol) ******Warning: Extremely hazardous. Avoid inhalation of vapors****** was added in one portion, and the yellow-orange solution stood at room temperature for 4 days, during which yellow orange crystals of **2.4** separate. The crystals were isolated from the mother liquor, washed with three 2 mL portions of hexanes, and dried under high vacuum at room temperature for 1 h. Yield: 36 mg (51%). Anal. Calcd. for $C_{37}H_{37}CoF_9N_6O_9S_3Cl_4$ (**2.4**$\cdot 2CH_2Cl_2$): C, 37.74; H, 3.17; N, 7.14. Found: C, 36.85; H, 3.22; N 7.51.

$(PY5Me_2)Co(CF_3SO_3)$ (2.5). In a N_2-filled glovebox, $[(PY5Me_2)Co(CH_3CN)](CF_3SO_3)_2$ (100 mg, 120 µmol) was weighed into a 20 mL scintillation vial and dissolved into ~3 mL of CH_3CN to give a yellow-orange solution. To this solution, while stirring, an orange solution of $[(C_5H_5)Fe(CO)_2]K$ (26 mg, 120 µmol) in ~1 mL of CH_3CN was added, giving an immediate color change to dark blue. The reaction was stirred at room temperature for an additional 5 min, then the solvent was removed under vacuum to give a dark blue solid. The solid was triturated three times with 10 mL of Et_2O, each time for 10 min, to remove the soluble $[(C_5H_5)Fe(CO)_2]_2$ byproduct. The first wash Et_2O was red-purple, while the second and third washes were colorless. The solid was recovered and dried under vacuum to afford a dark blue, free-flowing powder that was an equimolar mixture of **2.5** and KCF_3SO_3. Yield: 90 mg (90%). ^1H NMR (500 MHz, CD_3CN) δ 58.11 (br, $\Delta\nu_{1/2}$ = 140 Hz), 43.90 (br, $\Delta\nu_{1/2}$ = 180 Hz), 35.38 (br, $\Delta\nu_{1/2}$ = 38 Hz), 29.54 (br, $\Delta\nu_{1/2}$ = 660 Hz), 28.78 (br, $\Delta\nu_{1/2}$ = 410 Hz), 27.83 (br, $\Delta\nu_{1/2}$ = 140 Hz), 24.78 (br, $\Delta\nu_{1/2}$ = 230 Hz), $\Delta\nu_{1/2}$ = 23.38 (br, 140 Hz), 18.74 (br, $\Delta\nu_{1/2}$ = 16 Hz), 13.37 (br, $\Delta\nu_{1/2}$ = 290 Hz), 11.61 (br, $\Delta\nu_{1/2}$ = 130 Hz), 8.44 (s, $\Delta\nu_{1/2}$ = 10 Hz), 7.51 (s, $\Delta\nu_{1/2}$ = 17 Hz), 7.13 (s, $\Delta\nu_{1/2}$ = 12 Hz), 6.90 (s, $\Delta\nu_{1/2}$ = 8 Hz), 4.89 (s, $\Delta\nu_{1/2}$ = 8 Hz). ESI-MS *m/z* for $[(PY5Me_2)Co]^+$ requires 502.1442, found 502.1425. Anal. Calcd. for $C_{31}H_{25}CoF_6N_5KO_6S_2$ (**2.5**·KCF_3SO_3): C, 44.34; H, 3.00; N, 8.34. Found: C, 44.60; H, 2.87; N, 8.16. UV-vis (CH_3CN): λ_{max} (ε_M, M^{-1} cm^{-1}) 252 (1.7×10^3), 305 sh (3100), 384 (2500), 503 sh (2500), 646 (4700), 828 (4500), 1008 (3300) nm.

$((CF_3)_5PY5Me_2)Co(CF_3SO_3)$ (2.6). In a N_2-filled glovebox, compound **2.2** (100 mg, 85 μmol) was weighed into a 20 mL scintillation vial and dissolved into CH_3CN (~2 mL) to give an orange solution. An orange solution of $[(C_5H_5)Fe(CO)_2]K$ (18 mg, 85 μmol) in ~1 mL of CH_3CN was added, giving an immediate color change to dark blue. The reaction was stirred at room temperature for 5 min, then the solvent was removed under vacuum to afford a dark blue solid. The solid was triturated four times, each with ~20 mL portions of hexanes, each time for 10 min, to remove the soluble $[(C_5H_5)Fe(CO)_2]_2$ byproduct. The initial hexanes wash was red, and became progressively fainter in color until it was colorless in the final two washes. The solid was recovered and dried under vacuum to give the desired product as a dark blue, free-flowing solid that was a 1:1 mixture of **2.6** and KCF_3SO_3. Yield: 79 mg (79%). Anal. Calcd. for $C_{36}H_{20}CoF_{21}N_5KO_6S_2$ (**2.6**·KCF_3SO_3): C, 36.65; H, 1.71; N, 5.94. Found: C, 36.26; H, 1.80; N, 6.20.

$(CF_3PY5Me_2)Co(CF_3SO_3)$ (2.7). In a N_2-filled glovebox, $[(CF_3PY5Me_2)Co(CH_3CN)](CF_3SO_3)_2$ (100 mg, 110 μmol) was weighed into a 20 mL scintillation vial and dissolved into CH_3CN (~3 mL) to give an orange solution. An orange solution of $[(C_5H_5)Fe(CO)_2]K$ (25 mg, 110 μmol) in ~2 mL of CH_3CN was added, giving an immediate color change to dark blue. The reaction was stirred at room temperature for 5 min, then the solvent was removed under vacuum to afford a dark blue solid. The solid was triturated four times, each with ~20 mL portions of hexanes, each time for 10 min, to remove the soluble $[(C_5H_5)Fe(CO)_2]_2$ byproduct. The initial hexanes wash was red, and became progressively fainter in color until it was colorless in the final two washes. The solid was recovered and dried under vacuum to give the desired product as a dark blue, free-flowing solid that was a 1:1 mixture of **2.7** and KCF_3SO_3. Yield: 86 mg (83%). Anal. Calcd. for $C_{32}H_{24}CoF_9N_5KO_6S_2$ (**2.7**·KCF_3SO_3): C, 36.65; H, 1.71; N, 5.94. Found: C, 36.36; H, 1.80; N, 6.20.

$(PY4IqMe_2)Co(CF_3SO_3)$ (2.8). In a N_2-filled glovebox, compound **2.1** (100 mg, 120 μmol) was weighed into a 20 mL scintillation vial and dissolved into CH_3CN (~3 mL) to give an orange solution. An orange solution of $[(C_5H_5)Fe(CO)_2]K$ (25 mg, 120 μmol) in ~1 mL of CH_3CN was added, giving an immediate color change to dark navy. The reaction was stirred at room temperature for 5 min, then the solvent was removed under vacuum to afford a dark solid. The solid was triturated four times, each with ~20 mL portions of hexanes, each time for 10 min, to remove the soluble $[(C_5H_5)Fe(CO)_2]_2$ byproduct. The initial hexanes wash was red, and became progressively fainter in color until it was colorless in the final two washes. The solid was recovered and dried under vacuum to give the desired product as a black solid that was a 1:1 mixture of **2.8** and KCF_3SO_3. Yield: 97 mg (97%). Anal. Calcd. for $C_{35}H_{27}CoF_6N_5KO_6S_2$ (**2.8**·KCF_3SO_3): C, 47.25; H, 3.06; N, 7.87. Found: C, 46.91; H, 2.86; N, 7.54.

$(NMe_2PY5Me_2)Co(CF_3SO_3)$ (2.9). In a N_2-filled glovebox, $[(NMe_2PY5Me_2)Co(CH_3CN)](CF_3SO_3)_2$ (100 mg, 110 μmol) was weighed into a 20 mL scintillation vial and dissolved into CH_3CN (~3 mL) to give an orange solution. An orange solution of $[(C_5H_5)Fe(CO)_2]K$ (24 mg, 110 μmol) in ~2 mL of CH_3CN was added, giving an immediate color change to dark blue-black. The reaction was stirred at room temperature for 5 min, then the solvent was removed under vacuum to afford a dark solid. The solid was triturated four times, each with ~20 mL of hexanes, each time for 10 min, to remove the soluble $[(C_5H_5)Fe(CO)_2]_2$ byproduct. The initial hexanes wash was red, and became progressively fainter in color until it was colorless in the final two washes. The solid was recovered and dried under vacuum to give the desired product as a dark navy, free-flowing solid that was a 1:1 mixture of **2.9** and KCF_3SO_3. Yield: 93 mg (93%). Anal. Calcd. for $C_{33}H_{30}CoF_9N_6KO_6S_2$ (**2.9**·KCF_3SO_3): C, 44.90; H, 3.43; N, 9.52. Found: C, 45.17; H, 3.11; N, 9.52.

2.2.3. Crystal Structure Determinations

Slow diffusion of diethyl ether into acetonitrile solutions of compounds **2.1**, **2.1′**, **2.3** and **2.4** afforded single crystals suitable for X-ray diffraction analysis. Crystals of **2.2** were grown by diffusion of diethyl ether into a methanol solution. Crystals of **2.5** and **2.6** were grown by slow evaporation of acetonitrile solutions into toluene at room temperature. Acetonitrile solutions of **2.7** and **2.8** were unstable, but some decomposition products afforded crystalline material. Data collection was performed on single crystals coated with Paratone-N oil and mounted on Kapton loops. The crystals were cooled under a stream of N_2 (100 K; Oxford Cryostream 700) during measurements. Data were collected using a Bruker APEX II QUAZAR diffractometer equipped with a Microfocus Sealed Source (Incoatec IμS; Mo-K_α $\lambda = 0.71073$ Å) and APEX-II detector. Raw data were integrated and corrected for Lorentz and polarization effects using Bruker APEX2.[34] Absorption corrections were applied using SADABS.[35] Space group assignments were determined by examination of systematic absences, E-statistics, and successive refinement of the structures. Structures were solved using SHELXT[36] and all non-hydrogen atoms were refined anisotropically by full-matrix least-squares (SHELXL).[37,38] Carbon-bound hydrogen atoms were inserted at idealized positions and refined isotropically using a riding model with the appropriate HFIX command in SHELXL. The methanolic proton in **2.2** was located in the Fourier difference map and refined freely.

2.3. Results and Discussion

2.3.1. Design Elements and Syntheses of Pentapyridine Ligands

The pentapyridine ligands $PY5Me_2$,[29] CF_3PY5Me_2,[27] and NMe_2PY5Me_2[27] represent a trio of structurally congruous ligands, differing only at the 4-position of the axial pyridine (Figure 2.1). Upon metalation, the five pyridine ligands can occupy five out of six coordination sites of an octahedral metal ion. The electron-richness/poorness of the axial pyridine is related to the Hammett parameter (σ_p) of the functional group present, where a more positive σ_p value indicates a more electron-withdrawing functional group.[39] The σ_p values of –H, $-CF_3$, and $-NMe_2$ are 0, 0.43, and −0.16, respectively. To make the ligand more electron-deficient, and thus the corresponding Co(II) complex easier to reduce, we targeted the ligand $^{+}$**NMe₃PY5Me₂** (Figure 2.1). Due to its cationic nature, the triethylammonium group has a σ_p value of 0.88. Additionally, the ligand $(CF_3)_5PY5Me_2$, which has five electron-withdrawing trifluoromethyl groups, was prepared to evaluate the effect of electron-poor equatorial ligands.

As a distinct strategy, we also pursued the ligand **PY4IqMe₂**, which replaces the axial pyridine of $PY5Me_2$ with an isoquinoline ligand. It is thought that the isoquinoline ligand would uniquely stabilize the Co(I) oxidation state. The extended aromatic system (versus pyridine) should provide a better π overlap to accept electron density from the low-valent, soft Co(I) ion. Yet, comparing the pK_a values of pyridinium (5.3 in water[40]) and isoquinolinium (5.1 in water[41]) suggest that they should stabilize a small, hard ion such as Co(III) by similar degrees. Thus PY4IqMe2 should selectively stabilize only the Co(II/I) redox couple.

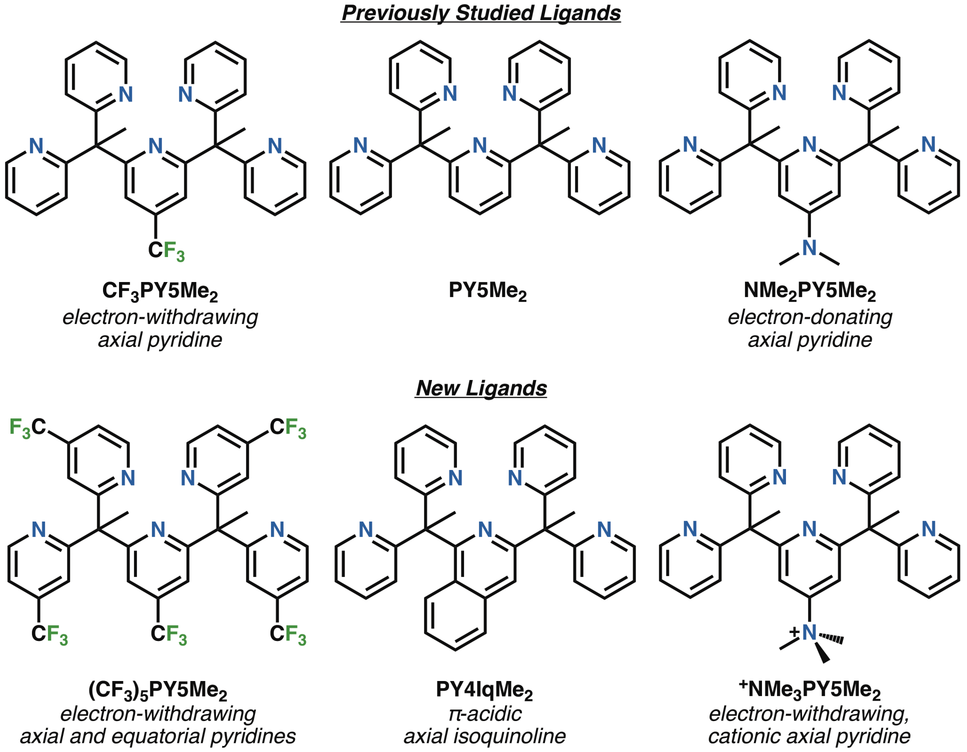

Figure 2.1. Overview of pentapyridine ligands previously studied for cobalt water reduction electrocatalysts, and the ligands prepared and studied in this Chapter.

The preparation of the ligand $PY4IqMe_2$ (Scheme 2.1) was developed based on the protocol for preparing $PY5Me_2$.[29] The molecule 1,1-bis(pyridyl)ethane[29] is deprotonated with one equivalent of *n*-butyllithium, then added to a solution of 1,4-dioxane containing 1,3-dichloroisoquinoline. The product is formed by the nucleophilic aromatic substitution reaction for chloride after 3 days of reflux. After quenching the reaction and workup, large crystals of the ligand $PY4IqMe_2 \cdot 0.5CH_2Cl_2$ are readily obtained by diffusing diethyl ether into a concentrated solution of crude product in dichloromethane, giving product in good (usually ~80%) yield. The CH_2Cl_2 solvate is not removed by heating under vacuum at 50 °C; its presence is confirmed by ^{1}H NMR spectroscopy, elemental analysis, and single crystal X-ray crystallography.

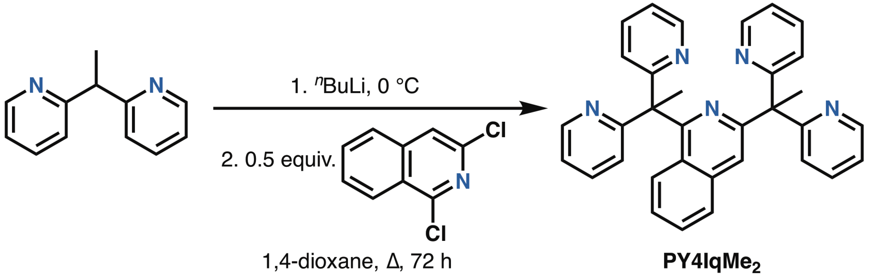

Scheme 2.1. Synthesis of the ligand PY4IqMe_2.

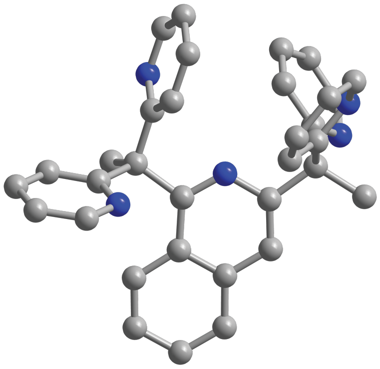

Figure 2.2. Single crystal X-ray structure of PY4Iq$Me_2 \cdot 0.5\ CH_2Cl_2$. Gray and blue spheres represent C and N atoms, respectively. H atoms and the CH_2Cl_2 solvent molecule are omitted for clarity.

The preparation of the electron-deficient ligand $(CF_3)_5$PY5Me_2 is summarized in Scheme 2.2. First, the precursor 2-ethyl-4-trifluoromethylpyridine is prepared by the iron-catalyzed cross-coupling[42] of 2-chloro-4-trifluoromethylpyridine with ethylmagnesium bromide. Because 2-ethyl-4-trifluoromethylpyridine is volatile, substantial losses of product can occur during workup. It is recommended to separate the product from the iron salts and tetrahydrofuran and *N*-methylpyrrolidone solvent mixture by flash chromatography in pentanes/diethyl ether. The 2-ethyl-4-trifluoromethylpyridine is then recovered by rotary evaporation at 0 °C. On a 10-g scale, typical yields are 40% to 60%. Subsequently, the 2-ethyl-4-trifluoromethylpyridine is deprotonated with lithium diisopropylamide and then treated with 2-chloro-4-trifluoromethylpyridine to give 2,2′-(ethane-1,1-diyl)bis(4-(trifluoromethyl)pyridine). Due to the electron-withdrawing trifluoromethyl group, it is important to use the milder, non-nucleophilic lithium diisopropylamide base. On the evidence of mass spectrometry, using *n*-butyllithium instead results in direct substitution at the pyridine ring to give presumably 2-butyl-6-ethyl-4-(trifluoromethyl)pyridine (m/z ($[M + H]^+$) = 232.13 Da). To minimize a side reaction that produces a tris-pyridine product, it is crucial to use a slight excess (1.5 equivalents) of lithiated 2-ethyl-4-trifluoromethylpyridine and to not heat the reaction. Finally, the compound 2,2′-(ethane-1,1-diyl)bis(4-(trifluoromethyl)pyridine) is deprotonated with *n*-butyllithium and allowed to react with 2,6-dichloro-4-(trifluoromethyl)pyridine, to give the desired product $(CF_3)_5$PY5Me_2. Owing to its high fluorine content, the $(CF_3)_5$PY5Me_2 ligand is not easily purified from other fluorine-containing impurities by crystallization. Instead, a two-step workup of column chromatography followed by Kugelrohr distillation is necessary.

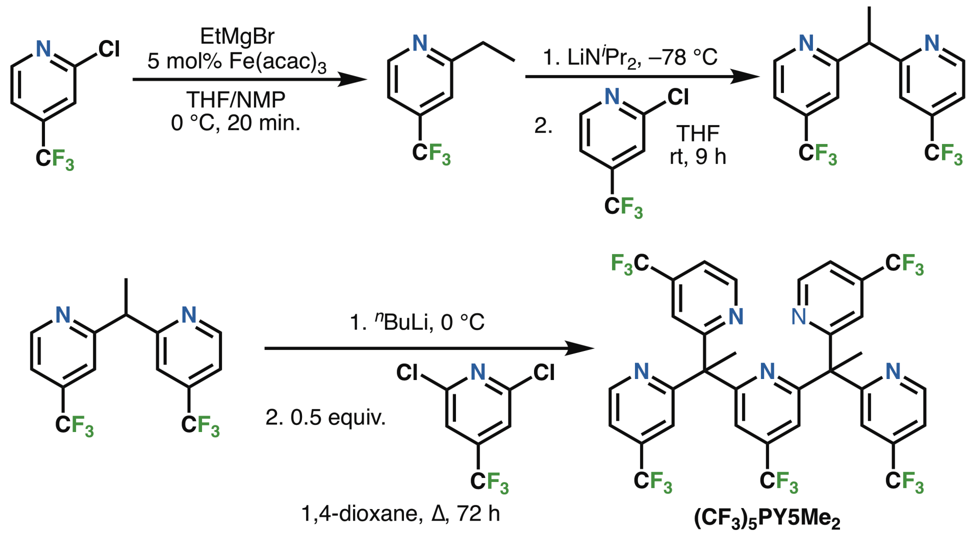

Scheme 2.2. Synthesis of the ligand $(CF_3)_5PY5Me_2$.

The cationic $^+NMe_3PY5Me_2$ ligand can, in principle, be prepared by the selective methylation of the dimethylamino functional group of the previously reported NMe_2PY5Me_2 ligand. However, since the pyridine nitrogen atoms are more nucleophilic than the dimethylamino nitrogen atom, such a synthetic route requires protecting groups to be installed at all five pyridines. This is conveniently done by using the Co(II) ion, which is further discussed in Section 2.3.3.

In an attempt to make mixed pentapyridine ligands with electron-withdrawing equatorial pyridines and electron-donating axial pyridines, the compound 2,2′-(ethane-1,1-diyl)bis(4-(trifluoromethyl)pyridine) was deprotonated and refluxed with 2,6-difluoropyridine and 2,6-difluoro-4-(dimethylamino)pyridine (Scheme 2.S1). However, ^1H NMR spectroscopy and mass spectrometry of the crude reaction mixtures did not show formation of any desired product, or even single substitution. This is likely due to mismatch of nucleophilicity and electrophilicity of the starting materials. The two electron-withdrawing trifluoromethyl groups stabilize the conjugate base of 2,2′-(ethane-1,1-diyl)bis(4-(trifluoromethyl)pyridine), rendering it insufficiently nucleophilic to react with the electron-rich 2,6-difluoropyridine and 2,6-difluoro-4-(dimethylamino)pyridine electrophiles.

2.3.2. Synthesis and Characterization of Pentapyridine M(II) Complexes

With the ligands in hand, Co(II) complexes of the $PY4IqMe_2$ and $(CF_3)_5PY5Me_2$ ligands were prepared by metalation with $Co(CF_3SO_3)_2$ in acetonitrile solution (Scheme 2.3). Diffusion of diethyl ether into their acetonitrile solutions furnish analytically pure, crystalline material of $[(PY4IqMe_2)Co(CF_3SO_3)](CF_3SO_3)$ (**2.1**) and $[((CF_3)_5PY5Me_2)Co(CH_3CN)](CF_3SO_3)_2$ (**2.2**). The solid-state structure of compound **2.1** was established using single crystal X-ray crystallography, which reveals the cobalt ion supported by the all five N donor atoms of the $PY4IqMe_2$ ligand in a pseudo-octahedral coordination environment (Figure 2.3). The Co–N_{ax} distance in **2.1** is 2.134(1) Å, while the Co–N_{eq} distances average 2.122(2) Å. These metal-ligand bond distances are consistent with those for a high-spin Co(II) ion. Here, the sixth coordination site is occupied by a trifluoromethanesulfonate anion.

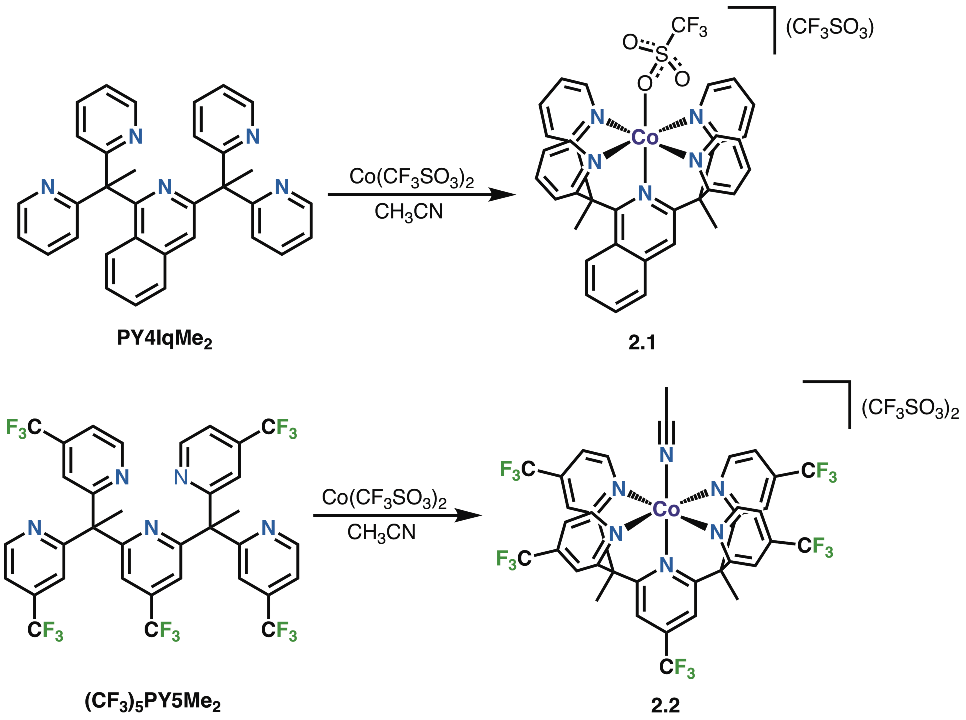

Scheme 2.3. Preparation of cobalt complexes **2.1** and **2.2**.

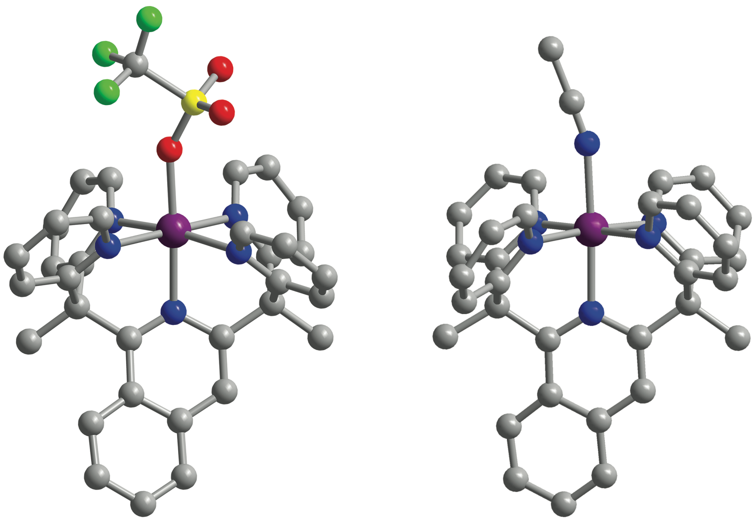

2.1 **2.1′**

Figure 2.3. Molecular structures of the $[(PY4IqMe_2)Co(CF_3SO_3)]^+$ and $[(PY4IqMe_2)Co(CH_3CN)]^{2+}$ ions in compounds **2.1** and **2.1′**. Purple, blue, gray, red, yellow, and green spheres represent Co, N, C, O, S, and F atoms, respectively. H atoms are omitted for clarity. Unbound solvent and anions are also not shown.

Although its metal-ligand bond distances are typical of complexes supported by pentapyridine ligands, the molecular structure of **2.1** also shows an unusually large distortion. The axial isoquinoline moiety bends away from the central plane of the complex (Figure 2.S2). The angle formed by the Co atom, the N atom, and the C-7 atom of the isoquinoline is 158.75(7)°. While the axial pyridine fragments of other first-row monometallic $PY5Me_2$ complexes exhibit some bending, their angles are less acute. The corresponding bond angles for $PY5Me_2$ complexes of V(II)[29,43], Cr(II)[44], Mn(II)[45,46], Fe(II)[46,47], Ni(II)[46,48], Cu(II)[46,48], and Zn(II)[27] range from 168.7(1)° to 174.6(2)°. The bending in **2.1** maximizes a face-to-face π-stacking interaction between two $[(PY4IqMe_2)Co(CF_3SO_3)]^+$ ions, with a centroid-centroid distance of 3.5708(4) Å (Figure 2.S3).

The compound **2.1** was additionally characterized by several other methods. Mass spectrometry shows the expected $[(PY4IqMe_2)Co(CF_3SO_3)]^+$ ion at m/z = 701.12 Da. The solution magnetic moment of **2.1** at 295 K, determined using Evans' method[49] in CD_3CN, is 5.3 μ_B. This value is consistent with a $S = 3/2$, d^7 Co(II) ion with a g value of 2.75 due to spin-orbit coupling. Related Co(II) complexes $[(PY5Me_2)Co(H_2O)]^{2+}$ and $[(PY5Me_2)Co(CH_3CN)]^{2+}$ have reported g values of 2.20 and 2.60, respectively.[27,48] Due to the paramagnetism of the Co(II) ion, the ^1H NMR spectrum of **2.1** exhibits proton resonances between +90 and −10 ppm, in a similar range of those observed in $[(PY5Me_2)Co(CH_3CN)]^{2+}$. The larger number of ^1H resonances observed in **2.1** than in $[(PY5Me_2)Co(CH_3CN)]^{2+}$ highlight the C_s symmetry imposed by the $PY4IqMe_2$ ligand, in contrast to the C_{2v} symmetry in complexes of $PY5Me_2$.

To evaluate whether trifluoromethanesulfonate anion in compound **2.1** is coordinated to the cobalt ion in the solution, the analogous cobalt(II) hexafluorophosphate complex $[(PY4IqMe_2)Co(CH_3CN)](PF_6)_2$ (**2.1′**) was also prepared (Scheme 2.S2). Diffusion of diethyl ether into acetonitrile solutions of compound **2.1′** similarly afforded orange-red crystals suitable for single crystal X-ray diffraction analysis (Figure 2.3). Owing to the higher charge state of the $[(PY4IqMe_2)Co(CH_3CN)]^{2+}$ ion and the compact acetonitrile ligand (versus $CF_3SO_3^-$), the Co–N_{eq} distances in **2.1′** (average of 2.0053(15) Å) are slightly shorter than those in **2.1′** (by ~0.12 Å). Of note, the $[(PY4IqMe_2)Co(CH_3CN)]^{2+}$ ions do not exhibit face-to-face π-stacking via the isoquinoline moieties, and there is almost no bending of the isoquinoline, either (∠Co–N–C = 176.04(8)°, Figure 2.S1). In addition, to probe the extent of redox non-innocence in the isoquinoline moiety, the ligand $PY4IqMe_2$ was metalated with zinc chloride and treated with two equivalents of silver trifluoromethanesulfonate to afford the zinc complex $[(PY4IqMe_2)Zn(CF_3SO_3)](CF_3SO_3)$, **2.3** (Scheme 2.S3). The molecular structure of **2.3** is shown in Figure 2.S3.

Although large, analytically pure crystals of compound **2.2** were grown from acetonitrile/diethyl ether mixtures, they suffered from extensive twinning. Instead, yellow crystals suitable for X-ray crystallography were grown by diffusion of diethyl ether into a methanol solution of compound **2.2** (Figure 2.4). The crystal structure reveals the that the cobalt ion is chelated by the $(CF_3)_5PY5Me_2$ ligand in the expected κ^5 coordination. The sixth coordination site is occupied by a methanol solvent molecule, highlighting the ease at which ligand substitution can occur at the vacant coordination site of these polypyridyl cobalt(II) complexes. The cobalt-pyridine bond lengths (d(Co–N_{ax}) = 2.122(3) Å, average d(Co–N_{eq}) = 2.157(3) Å) are also typical of octahedral, high-spin cobalt(II) complexes. Of note, the proton of the coordinated methanol molecule was located in the Fourier difference map, and it is involved in a hydrogen bonding interaction with a nearby trifluoromethanesulfonate anion. Thus, the charge of the coordination complex can be unambiguously assigned as 2+, supporting the oxidation state of the cobalt ion as Co(II).

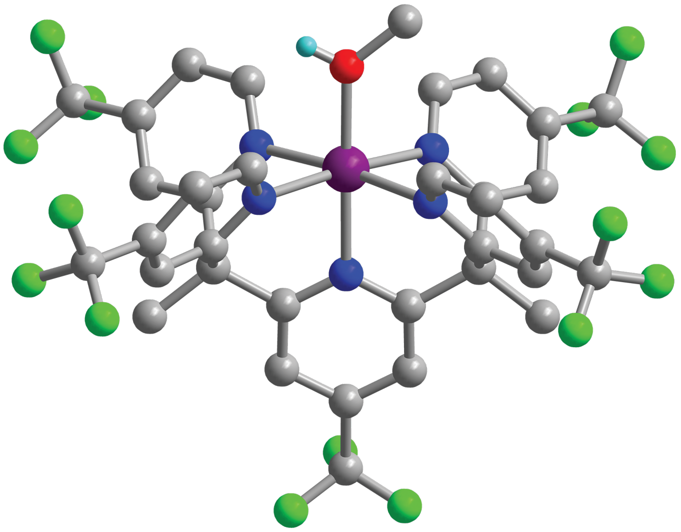

Figure 2.4. Molecular structure of the $[((CF_3)_5PY5Me_2)Co(CH_3OH)]^{2+}$ ion in compound **2.2**, grown from methanol/diethyl ether. Purple, blue, gray, red, green, and light blue spheres indicate Co, N, C, O, F, and H atoms, respectively. Carbon-bound H atoms, uncoordinated anions and solvent molecules are omitted for clarity.

As previously discussed, owing to the greater nucleophilicity of pyridine nitrogen atoms compared to dimethylaniline nitrogen atoms, the preparation of the $^{+}NMe_3PY5Me_2$ ligand would require protecting groups for each of the five pyridines. The cobalt(II) ion was identified as a convenient protecting group that simultaneously protects all five pyridines. (Scheme 2.4). Dissolving the cobalt complex $[(NMe_2PY5Me_2)Co(CH_3CN)](CF_3SO_3)_2$[27] into dichloromethane induces one of the trifluoromethanesulfonate anions to bind at cobalt, displacing the acetonitrile ligand. Excess methyltrifluoromethanesulfonate was added to this solution, which, after 4 days, separated orange crystalline material of $[(NMe_3PY5Me_2)Co(CF_3SO_3)](CF_3SO_3)_2$ (**2.4**). Recrystallization of **2.4** acetonitrile/diethyl ether afforded crystals suitable for single crystal X-ray diffraction analysis (Figure 2.5). Two crystallographically distinct molecules of $[(NMe_3PY5Me_2)Co(CH_3CN)]^{3+}$ are present in each asymmetric unit. Their metal-ligand bond distances are similar, differing by less than 0.03 Å. Of note, the cationic trimethylammonium group is tightly surrounded by trifluoromethanesulfonate ions in the crystal lattice. This is the likely reason for the axial trimethylammonium pyridine ligand bending away from the central plane of the molecule, giving a Co–N–C bond angle of 163.36(16)°.

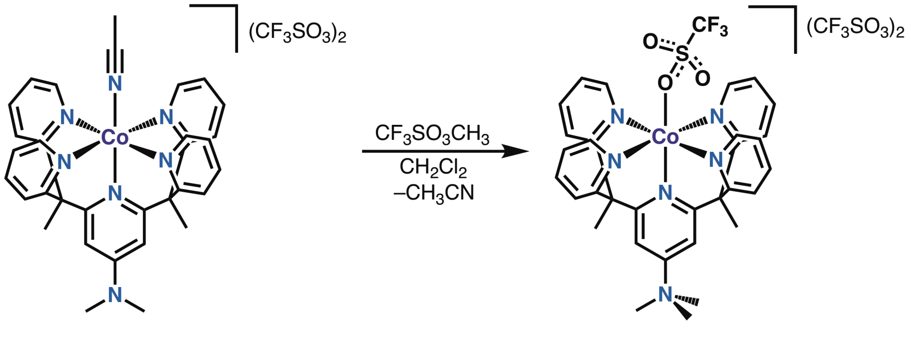

$[(NMe_2PY5Me_2)Co(CH_3CN)](CF_3SO_3)_2$

2.4

Scheme 2.4. Preparation of compound **2.4**.

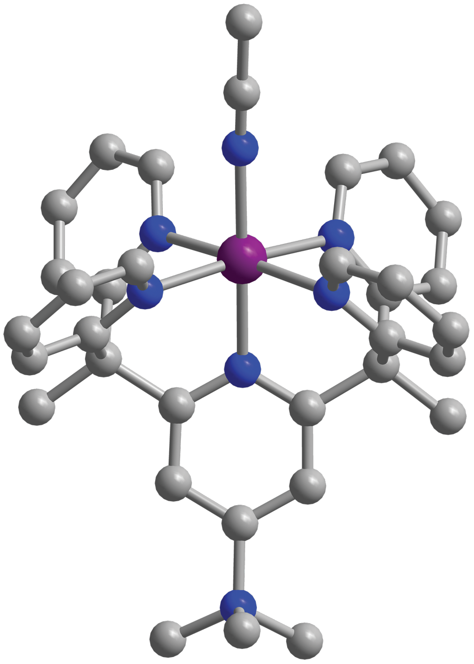

Figure 2.5. Molecular structure of a $[(NMe_3PY5Me_2)Co(CH_3CN)]^{3+}$ ion in compound **2.4**, crystallized from acetonitrile and diethyl ether. Purple, blue, and gray spheres represent Co, N, and C atoms, respectively. H atoms, anions, and solvent molecules are omitted for clarity.

2.3.3. Redox Trends in Polypyridyl M(II) Complexes

Cyclic voltammograms (CVs) of Co(II) complexes **2.1**, **2.2**, and **2.4** were measured in acetonitrile to assess the impact of ligand substitutions upon the electronics of the cobalt ion (Figure 2.6). For all three compounds, two redox events, assigned to Co(III/II) and Co(II/I) redox couples, are observed between +1.0 to −2.0 V (all potentials reported versus $Fe(C_5H_5)_2^{+/0}$). These features occur at similar potentials as those for $[(PY5Me_2)Co(CH_3CN)]^{2+}$, $[(CF_3PY5Me_2)Co(CH_3CN)]^{2+}$, and $[(NMe_2PY5Me_2)Co(CH_3CN)]^{2+}$ (Figure 2.6). The electrochemical data is summarized in Table 2.1.

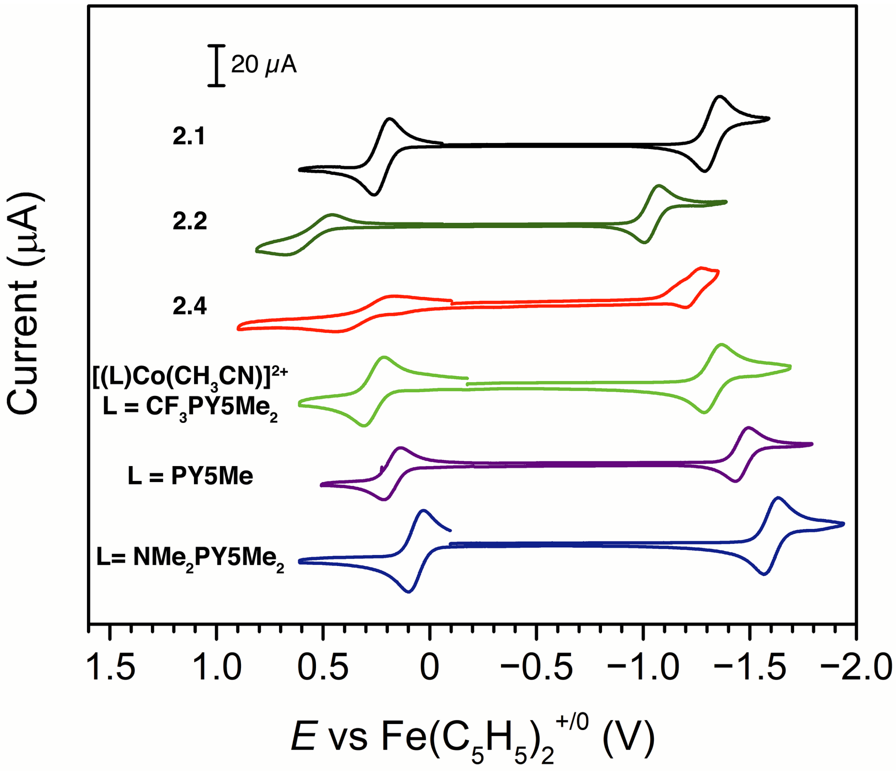

Figure 2.6. CVs showing the Co(III/II) and Co(II/I) redox couples for compounds **2.1**, **2.2**, **2.4**, $[(CF_3PY5Me_2)Co(CH_3CN)]^{2+}$, $[(PY5Me_2)Co(CH_3CN)]^{2+}$, and $[(NMe_2PY5Me_2)Co(CH_3CN)]^{2+}$. CVs were collected with 1 mM solutions of compound in acetonitrile with 0.1 M NBu_4PF_6, under argon. Scan rate = 100 mV/s.

The Co(II/I) couple for compounds **2.1**, **2.2**, and **2.4** occur with half-wave potentials ($E_{1/2}$) at −1.33 V, −1.04 V, and –1.24 V, respectively. Their cathodic and anodic peak potentials (E_{pc} and E_{pa}) do not vary with scan rate (Figure 2.S4–6a), indicating that the Co(II/I) reduction for these compounds are fully reversible. The cathodic and anodic peak currents (i_{pc} and i_{pa}) vary linearly with the square root of scan rate, indicating that electron transfer is diffusion-controlled (Figure 2.S4–6d). The Co(III/II) redox couple for compounds **2.1**, **2.2**, and **2.4** occur at $E_{1/2}$ = 0.22 V, 0.59 V, and 0.32 V, respectively. These redox couples are also diffusion-controlled (Figure 2.S4–6c), but increasing difference between E_{pc} and E_{pa} with increasing scan rate is indicative of quasi-reversible electron transfer (Figure 2.S4–6a). The slow rate of electron transfer is consistent with the large reorganization required between high-spin Co(II) and low-spin Co(III). For a given scan rate, peak-to-peak difference follows the order **2.1** < **2.2** < **2.4**, indicating that the heterogeneous electron transfer rate constant follows the order **2.1** > **2.2** > **2.4**.

The hexafluorophosphate salt **2.1′** displays an identical electrochemical response as **2.1** (Figure 2.S7), confirming that, in acetonitrile solution, the trifluoromethanesulfonate ligand in **2.1** is displaced by acetonitrile. For compound **2.1**, an additional, irreversible reduction is accessible at −2.04 V (Figure 2.S4b). The return wave becomes more peak-shaped at faster scan rates, suggesting that the reduction is coupled to a slow chemical reaction (Figure 2.S4b). The Zn(II) compound **2.3** displays a similar irreversible redox event at approximately −2 V (Figure 2.S7), suggesting that this redox activity is ligand-based. Notably, the $[(PY5Me_2)Zn]^{2+}$ ion is redox inactive,[27] suggesting that the redox activity is engendered by the isoquinoline unit of PY4IqMe$_2$.

The complexes **2.2** and **2.4** also show additional redox behavior at more negative potentials. For **2.2**, an irreversible reduction with current consistent with a one electron event is observed at

−1.93 V, before a multi-electron event. For **2.4**, an irreversible peak occurs at −2.00 V. For the reported complexes, this irreversible reduction at potentials more negative than −2 V was assigned to a Co(I/0) redox event.[27,28] Based on CVs in the presence of weak acids (see below), these redox couples seem to be better assigned as *cobalt(I) / cobalt(II) hydride* redox couples, where, in the time scale of the CV, the generated Co(0) intermediate is intercepted by a proton (from trace water or from acetonitrile solvent) to form a cobalt(II) hydride complex.

Table 2.1. Redox potentials of pentapyridine cobalt complexes.[a]

Compound	$E_{1/2}$ [Co(III/II)] (V)[b]	$E_{1/2}$ [Co(II/I)] (V)	ΔE (V)[c]	$E_{1/2}$ [Co(III/I)] (V)[d]	E_p [Co(I) + e^-]
2.1	0.22	−1.33	1.55	−0.55	−2.04[e]
2.2	0.59	−1.04	1.63	−0.22	−1.93
2.4	0.32	−1.24	1.56	−0.46	−2.00
$[(CF_3PY5Me_2)Co(CH_3CN)]^{2+}$	0.26	−1.33	1.59	−0.53	−2.13
$[(PY5Me_2)Co(CH_3CN)]^{2+}$	0.17	−1.46	1.64	−0.64	−2.27
$[(NMe_2PY5Me_2)Co(CH_3CN)]^{2+}$	0.06	−1.60	1.66	−0.77	−2.36

[a]Potentials referenced against the $Fe(C_5H_5)_2^{+/0}$ couple. [b]Quasi-reversible redox couple. [c]$\Delta E = |E_{1/2}$ [Co(III/II)] − $E_{1/2}$ [Co(II/I)]|. [d]$E_{1/2}$ [Co(III/I)] = ($E_{1/2}$ [Co(III/II)] + $E_{1/2}$ [Co(II/I)])/2. [e]Assigned instead to a ligand-based event.

Overall, the Co(III/II) and Co(II/I) redox couples for this family of pentapyridine complexes track with the substitutions of the peripheral ligand. For the compounds **2.4**, $[(CF_3PY5Me_2)Co(CH_3CN)]^{2+}$, $[(PY5Me_2)Co(CH_3CN)]^{2+}$, and $[(NMe_2PY5Me_2)Co(CH_3CN)]^{2+}$, both redox potentials shift with the σ_p parameter at the 4-position of the axial pyridine (Figure 2.S9). However, these shifts decrease in magnitude as the σ_p becomes more positive, indicating that there are limits to the electronic tuning of the cobalt ion with the ligand periphery.

A similar trend of diminishing returns is observed with the trifluoromethyl groups Between $[(CF_3PY5Me_2)Co(CH_3CN)]^{2+}$ and $[(PY5Me_2)Co(CH_3CN)]^{2+}$, Co(III/II) and Co(II/I) redox couples for the first trifluoromethyl group are +90 mV and +130 mV, respectively. Between **2.2** and $[(CF_3PY5Me_2)Co(CH_3CN)]^{2+}$, the analogous shifts are +230 mV and +290 mV, or +58 mV and +73 mV per trifluoromethyl group.

Of particular interest is the trend in the *difference* between the potentials of the Co(III/II) and Co(II/I) reductions. Most of these complexes have a ~1.65 V different between the two one-electron redox couples. Compound **2.1**, which has the ligand with the most π-accepting character (in the isoquinoline ligand), stabilizes the soft Co(I) oxidation state most. However, the nitrogen lone pair of the isoquinoline is sufficiently Lewis-basic to stabilize the hard Co(III) ion, resulting in the narrowest spread between the two redox couples. Also of note is that, among complexes with substitutions at the axial pyridine, the trimethylammonium group of **2.4** results in the narrowest redox spread. This is because the electron-withdrawing groups affect the redox potential of the Co(II/I) couple more than that of the Co(III/II) couple.

2.3.4. Kinetics of Electrocatalytic Reduction of Dimethylanilinium to Hydrogen

To probe the reactivity of these cobalt complexes, CVs in acetonitrile were performed with varying concentrations of added acid. In this study, the *N*,*N*-dimethylanilinium tetrafluoroborate was chosen as the acid source for several reasons. Firstly, *N*,*N*-dimethylanilinium has a moderate acidity ($\mathrm{p}K_\mathrm{a} = 11.4$ in acetonitrile[50]). Preliminary screens using stronger acids such as *p*-toluenesulfonic acid ($\mathrm{p}K_\mathrm{a} = 8.6$)[51] and *p*-cyanoanilinium ($\mathrm{p}K_\mathrm{a} = 7.0$)[52] indicated direct reaction between the acids and the pentapyridine Co(II) complex, as evidenced by the conversion of the orange color of $[(\mathrm{PY4IqMe_2})\mathrm{Co}(\mathrm{CH_3CN})]^{2+}$ to the pale pink of $[\mathrm{Co}(\mathrm{CH_3CN})_6]^{2+}$. Additionally, the Co(III/II) redox couple decreases with increasing concentrations of acid, suggesting the concentration of the $[(\mathrm{PY4IqMe_2})\mathrm{Co}(\mathrm{CH_3CN})]^{2+}$ ion in solution is diminished by strong acids (Figure 2.S10). This probably arises from the direct protonation of one or more of the pyridine ligands ($\mathrm{p}K_\mathrm{a}$ of pyridinium = 12.5 in acetonitrile)[50]. Thus, weaker acids help mitigate side reactions during the timescale of the experiment. Further, neutral acids, which generate anions that may coordinate to the metal complex (i.e. anation), were previously found to complicate interpretation of the CV data in polypyridyl cobalt complexes.[28] Using cationic acids that generate a neutral conjugate bases can avoid undesirable anation pathways. Given the steric profile surrounding the aniline nitrogen atom and involvement of the nitrogen lone pair with the aromatic π system, we expect minimal association between the dimethylaniline conjugate base and the cobalt ion. Lastly, homoconjugation of the parent acid and its conjugate base can influence the thermodynamic potential of acid reduction[53,54] and manifest several catalytic features.[55] The homoconjugation reaction occurs after an acid HA dissociates to give a solvated proton and the conjugate base A^- (Eq. 2.1). The anion A^- then reacts with HA to form $\mathrm{HA_2}^-$ (Eq. 2.2). The homoconjugation constant, K_f, is defined by Eq. 2.3.

$$\mathrm{HA} \rightleftharpoons \mathrm{H}^+ + \mathrm{A}^- \qquad (2.1)$$

$$\mathrm{A}^- + \mathrm{HA} \rightleftharpoons \mathrm{HA}_2^- \qquad (2.2)$$

$$K_\mathrm{f}(\mathrm{HA}) = \frac{[\mathrm{HA}_2^-]}{[\mathrm{A}^-][\mathrm{HA}]} \qquad (2.3)$$

In acetonitrile, cationic acids exhibit less homoconjugation than their neutral acid counterparts.[30,56] For example, anilinium[50] and trichloroacetic acid[56] have the same acidity (both $\mathrm{p}K_\mathrm{a} = 10.6$), but the former has $K_\mathrm{f} = 3.9$,[30], while the latter has $K_\mathrm{f} = 320$.[56] Direct reduction of *N*,*N*-dimethylanilinium tetrafluoroborate by the glassy carbon electrode onsets at approximately −1.2 V (Figure 2.S11). An oxidation wave on the return sweep at approximately +0.35 V, corresponding to the oxidation of *N*,*N*-dimethylaniline.[57]

The CVs of the compounds **2.1**, **2.2**, $[(\mathrm{CF_3PY5Me_2})\mathrm{Co}(\mathrm{CH_3CN})]^{2+}$, $[(\mathrm{PY5Me_2})\mathrm{Co}(\mathrm{CH_3CN})]^{2+}$, and $[(\mathrm{NMe_2PY5Me_2})\mathrm{Co}(\mathrm{CH_3CN})]^{2+}$ in the presence of 0–10 equivalents of *N*,*N*-dimethylanilinium tetrafluoroborate are shown in Figure 2.S12–16. Notably, addition of acid shifts the Co(II/I) redox couple in the anodic direction by ~150 to 250 mV, indicating that electron transfer triggers an irreversible, non-catalytic chemical reaction (an EC reaction[58]). This feature is assigned to the protonation of an electro-generated Co(I) intermediate to form a Co(III)H complex (first EC steps of Scheme 2.5). After the initial protonation of Co(I), a second, reduction event takes place at more negative potentials, and increases with increasing excess of acid, suggestive of catalytic proton reduction (Figures 2.S12–16). A third reduction strongly overlaps with the reduction wave of *N*,*N*-

dimethylanilinium without any added cobalt complex, indicative of direct reduction at the glassy carbon electrode. Of note, comparing the CV trace of 10 mM *N*,*N*-dimethylanilinium with and without $[(NMe_2PY5Me_2)Co(CH_3CN)]^{2+}$ shows that, Although the Co(III)H complex of $[(NMe_2PY5Me_2)Co(CH_3CN)]^{2+}$ can be formed, the current response with 10 mM *N*,*N*-dimethylanilinium is worse than without any cobalt complex added, demonstrating that, at these conditions, $[(NMe_2PY5Me_2)Co(CH_3CN)]^{2+}$ inhibits catalysis.

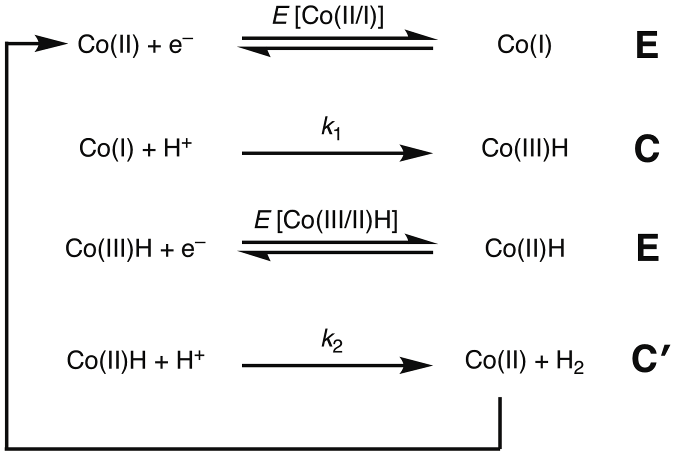

Scheme 2.5. A monometallic ECEC′ scheme for proton reduction by cobalt.

To probe the kinetics of the Co(III)-H formation, CVs of the cobalt complexes with 10 equivalents of *N*,*N*-dimethylanilinium tetrafluoroborate were collected at different scan rates. Their irreversible, one-electron peaks shift cathodically with increasing scan rate (Figure 2.S17–21). For an irreversible EC reaction, the peak potential E_p is expected to shift according to the relation[58-60]:

$$E_p = E_{1/2} - 0.78\frac{RT}{F} + \frac{RT}{2F}\ln\left(\frac{RT}{F}\frac{k}{v}\right) \qquad (2.4)$$

where $E_{1/2}$ is the redox couple underlying the EC step (in this case, the Co(II/I) redox couple), *R* is the ideal gas constant, *T* is the temperature (in Kelvin), *F* is the Faraday constant, *k* is the rate constant of the chemical step (per second), and *v* is the scan rate (in V/s). Rearranging Eq. 2.4 gives:

$$\left(E_p - E_{1/2} + 0.78\frac{RT}{F}\right) = \frac{RT}{2F}\ln\left(\frac{RT}{F}k\right) + \frac{RT}{2F}\ln\frac{1}{v} \qquad (2.5)$$

The plots of ($E_p - E_{1/2} + 0.78\ RT/F$) versus ln(1/*v*) for the first, irreversible step gave good linear fits (Figure 2.S22), from which the rate constant *k* could be solved from the intercept. Substituting in:

$$k = k_1[\mathrm{H}^+] \qquad (2.6)$$

where $[\mathrm{H}^+]$ is the concentration of acid in the bulk solution, the first order rate constant k_1 was determined (Table 2.2). From this data, several salient points stand out. Firstly, protonation of the Co(I) complex of **2.2** is non-existent. This demonstrates that with too many electron-withdrawing trifluoromethyl groups on the ligand, the resulting Co(I) complex is so stabilized that it is not basic enough to react with acids. As one might expect, the rate of protonation k_1 increases with a more negative (i.e. reducing) Co(III/I) redox couple, which provides the driving force for forming Co(III)H (Figure 2.7). For this family of cobalt complexes, k_1 reaches a maximum with complex **2.1**, which has a formal Co(III/I) potential of −0.55 V. At more negative potentials, k_1 *decreases*. This may be an instance of proton transfer between acid and the Co(I) complex displaying inverted region behavior.[61]

Table 2.2. Kinetic parameters of pentapyridine cobalt complexes.

Compound	k_1 (M^{-1} s^{-1})
2.1	1,148,000 ± 7,300
2.2	600 ± 5,000
$[(CF_3PY5Me_2)Co(CH_3CN)]^{2+}$	39,000 ± 4,800
$[(PY5Me_2)Co(CH_3CN)]^{2+}$	790,000 ± 5,300
$[(NMe_2PY5Me_2)Co(CH_3CN)]^{2+}$	270,000 ± 5,300

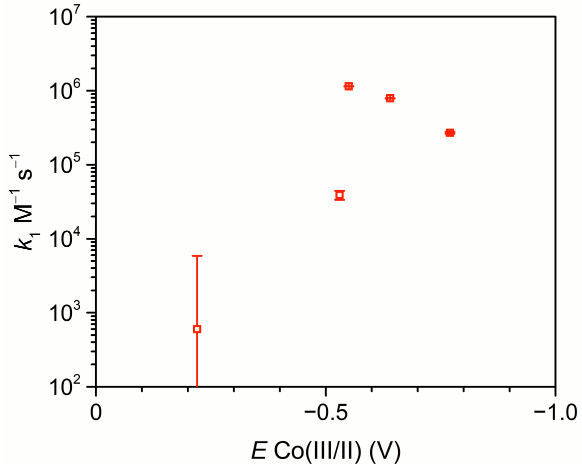

Figure 2.7. Plot of k_1 versus E[Co(III/II)].

That catalysis does not occur immediately from the Co(II/I) redox couple and requires sweeping to more negative potentials is useful mechanistic information. It suggests that further E or C steps from the Co(III)H intermediate are unfavorable or slow. A closer examination of the CVs of $[(NMe_2PY5Me_2)Co(CH_3CN)]^{2+}$ suggest this to be the case (Figure 2.8). As previously discussed, an irreversible redox couple appears with E_{pc} = −2.35 V. The return oxidation wave is well-separated, occurring at E_{pa} = −2.14 V. In the presence of 1 equivalent of *N,N*-dimethylanilinium, and additional reductive wave appears at E_{pc} = −2.21 V. The separation between these two half-waves is 70 mV, close to the ideal ΔE_p of 57 mV of a Nernstian, one-electron redox couple.[62] The fact that this reductive feature only occurs in the presence of acid, together with its potential suggests that it is a quasi-reversible Co(III)H/Co(II)H wave, with $E_{1/2}$ = −2.18 V, a potential 580 mV more negative than the corresponding Co(II/I) couple.

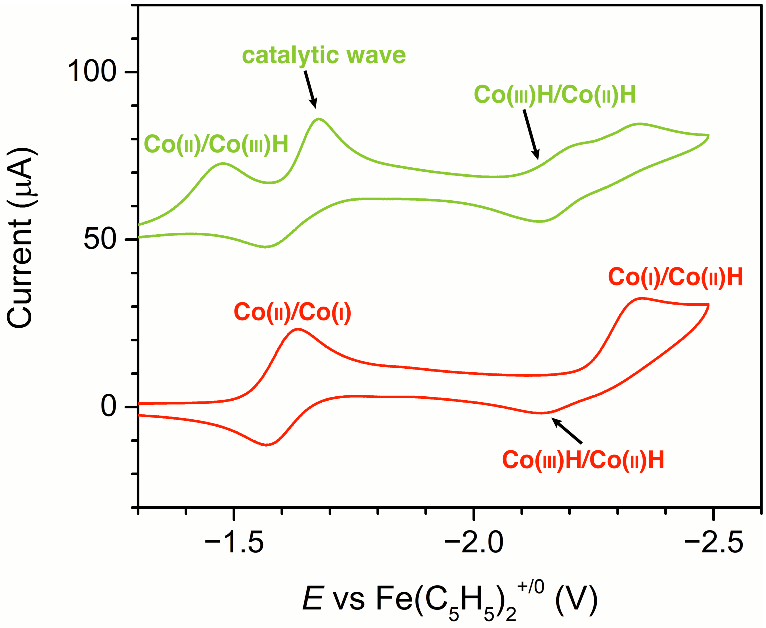

Figure 2.8. CVs of 1 mM $[(NMe_2PY5Me_2)Co(CH_3CN)]^{2+}$, without (red) and with 1 mM *N*,*N*-dimethylanilinium (light green). The addition of acid introduces a reversible redox couple at −2.18 V, which is assigned to the Co(III)H/Co(II)H redox couple.

The prevailing electrochemical characterization suggests that an ECEC′ mechanism is operative wherein the second electron transfer is more difficult than the first.[63,64] This mechanism is also consistent with the pre-features observed before catalysis in aqueous solutions containing $[(PY5Me_2)Co(H_2O)]^{2+}$.[27] Notably, the mechanism of proton reduction in cobalt glyoxime complexes have been identified to be ECEC′, but with the first electron being more difficult.[16,65] Recent reports[66-68] suggest that the glyoxime cobalt(III) hydride undergoes rapid tautomerization in solution by protonating the ligand. Perhaps its structural fluxionality help stabilize and favor the reduction of the formal Co(III)H.

Due to the strong overlap between catalysis by the cobalt complex with the direct reduction of acid at the electrode, we could not confidently quantify k_2. To do so, it may help to use even weaker acids to decrease the extent of acid reduction by the electrode.

2.3.5. Chemical Reduction of Pentapyridine Co(II) Complexes—Isolation of Co(I) Intermediates and Decomposition Products

Given the apparent electrochemical reversibility of the Co(II/I) redox couple for these pentapyridine Co(II) complexes, we sought to prepare and characterize these Co(I) complexes of these ligands. There are few structurally characterized Co(I) complexes in the literature. Among complexes bearing nitrogen donors in a tetragonal ligand field, only four examples have been crystallographically characterized.[16,28,69,70] King and coworkers previously prepared the dark blue pentapyridine Co(I) complex $[(PY5Me_2)Co](BPh_4)$ by metalation of $PY5Me_2$ with tris(triphenylphosphine)cobalt(I) chloride, $(PPh_3)_3CoCl$, followed by metathesis with sodium tetraphenylborate.[28] The crystal structure of $[(PY5Me_2)Co](BPh_4)$,[28] which was obtained from the diffusion of diethyl ether into a solution of the compound in 1,2-difluorobenzene, reveals the Co(I) ion in a pseudo square-pyramidal geometry, with all five pyridines of $PY5Me_2$ coordinated to the metal and a vacant coordination site available at the metal ion (Figure 2.S23). The square pyramidal geometry observed in [(PY5Me$_2$)Co](BPh$_4$) is congruent to those observed in cobalt(I) glyoxime complexes.[16,69] The complex [(PY5Me$_2$)Co](BPh$_4$) was reported to be paramagnetic in CD$_3$CN,[28] which is unusual for its apparent square pyramidal geometry, and suggested that acetonitrile may bind to the cobalt(I) ion in solution.

Extension of this metalation protocol with (PPh$_3$)$_3$CoCl to the ligands PY4IqMe$_2$, (CF$_3$)$_5$PY5Me$_2$, CF$_3$PY5Me$_2$, and NMe$_2$PY5Me$_2$ gave brown, intractable mixtures. We partially attribute difficulties with this protocol to the problematic (PPh$_3$)$_3$CoCl reagent. Several preparations for (PPh$_3$)$_3$CoCl are reported in the literature, utilizing either sodium borohydride[71] or zinc metal[72] to reduce cobalt(II) chloride in the presence of triphenylphosphine. The color of the product has been described as either green[72] or green-brown.[71,73] Krzystek and coworkers[73] have noted difficulty with reproducing some of the literature preparations.

To avoid complications arising from the (PPh$_3$)$_3$CoCl reagent, we sought to isolate the Co(I) complexes using a chemical reductant instead. This is conveniently carried out using potassium cyclopentadienyldicarbonylferrate, K[(C$_5$H$_5$)Fe(CO)$_2$],[31] which has a reduction potential of approximately −1.8 V.[74] The formal reduction potential is ~200 to 760 mV more negative than the Co(II/I) redox couple of the pentapyridine complexes, indicating that a stoichiometric amount of reductant will drive the reaction to > 98% complete.[74] Indeed, the addition of one equivalent of K[(C$_5$H$_5$)Fe(CO)$_2$] to acetonitrile solutions of compounds **2.1**, **2.2**, [(PY5Me$_2$)Co(CH$_3$CN)](CF$_3$SO$_3$)$_2$, [(CF$_3$PY5Me$_2$)Co(CH$_3$CN)](CF$_3$SO$_3$)$_2$, and [(NMe$_2$PY5Me$_2$)Co(CH$_3$CN)](CF$_3$SO$_3$)$_2$ gave dark blue to navy solutions of the corresponding Co(I) complexes, **2.5–9** (Scheme 2.6). Removal of acetonitrile and washing the residue with diethyl ether or hexanes removed the redox byproduct cyclopentadienyliron dicarbonyl dimer, [(C$_5$H$_5$)Fe(CO)$_2$]$_2$. The remaining dark blue to navy solids were, after drying, isolated as analytically pure mixtures of the Co(I) complex with one equivalent of KCF$_3$SO$_3$. Since the solubilities of the Co(I) trifluoromethanesulfonate complexes and KCF$_3$SO$_3$ were similar, attempts to separate the two solids by extraction were not successful.

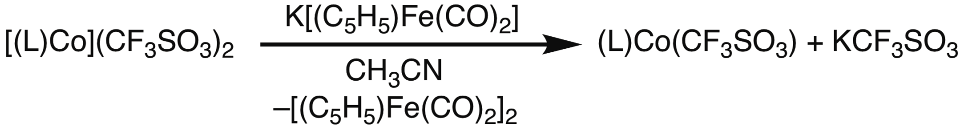

$$[(L)Co](CF_3SO_3)_2 \xrightarrow[\substack{CH_3CN \\ -[(C_5H_5)Fe(CO)_2]_2}]{K[(C_5H_5)Fe(CO)_2]} (L)Co(CF_3SO_3) + KCF_3SO_3$$

Scheme 2.6. Preparation of pentapyridine Co(I) complexes using a chemical reductant.

Slow evaporation of the dark blue acetonitrile solutions of [(PY5Me$_2$)Co(CF$_3$SO$_3$)] (**2.5**) and [((CF$_3$)$_5$PY5Me$_2$)Co(CF$_3$SO$_3$)] (**2.6**) in the presence of excess 18-crown-6 gave dark blue crystals suitable for single-crystal X-ray diffraction analysis. Crystals of **2.5** reveal two crystallographically distinct yet similar molecules of [(PY5Me$_2$)Co(CH$_3$CN)]$^+$ (Figure 2.9), in addition to a molecule of [(18-crown-6)K]$^+$, reside in each asymmetric unit. Three trifluoromethanesulfonate anions are also present. The overall charge balance and the similar metrical distances of the two [(PY5Me$_2$)Co(CH$_3$CN)]$^+$ suggest that they are both monocationic, formally Co(I) ions. Crystals of **2.6** reveal six-coordinate, pseudo-octahedral Co(I) ions of [((CF$_3$)$_5$PY5Me$_2$)Co(CH$_3$CN)]$^+$ (Figure 2.9). Compared with the Co(II) complexes with their respective ligand scaffold, the cobalt-pyridine distances in **2.5** and **2.6** suggest some degree of metal to ligand π back-bonding (Table 2.3). Notably, the shortening is most prominent with the axial pyridine, indicating that the back-bonding interaction is strongest with the axial pyridine.

Table 2.3. Highlighted metal-ligand bond distances in pentapyridine Co(II) and Co(I) complexes.

Bond distance (Å)	$[(PY5Me_2)Co(CH_3CN)]^{2+}$	**2.5**^{a}	**2.2**	**2.6**
Co–N_{ax}	2.095(3)	2.024(2) 2.036(2)	2.122(3)	2.015(2)
Co–N_{eq}^a	2.115(2)	2.115(2) 2.111(2)	2.156(3)	2.144(2)
Co–X	2.123(3)^b	2.112(3)^b 2.134(3)^b	2.066(2)^c	2.121(2)^b

^{a}Bond distances of both crystallographically distinct ions shown. ^{b}X = CH_3CN. ^{c}X = CH_3OH

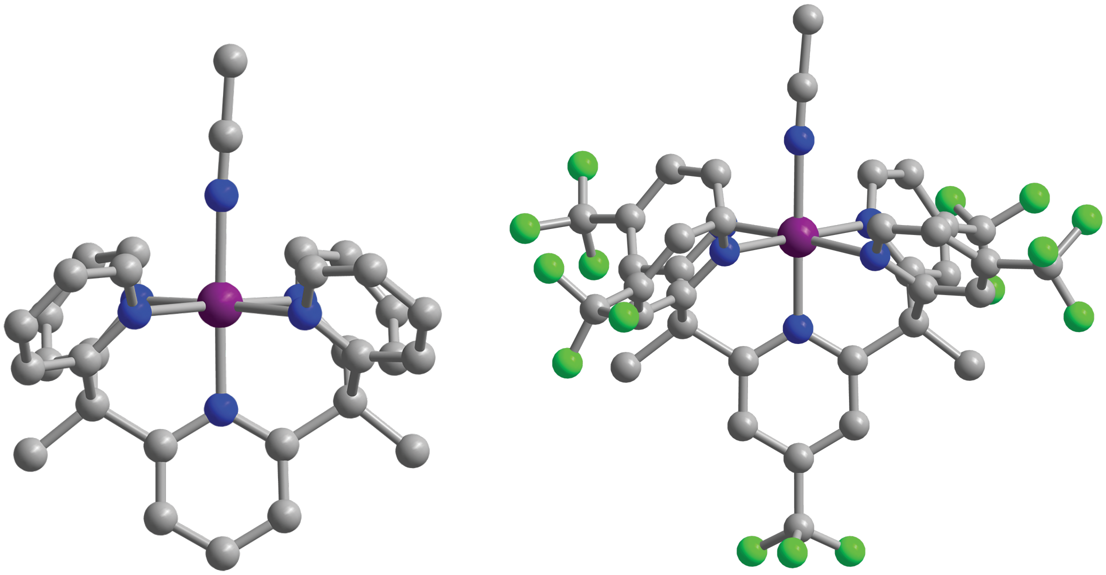

Figure 2.9. Single crystal X-ray structures of the cobalt(I) ions $[(PY5Me_2)Co(CH_3CN)]^+$ (left) and $[((CF_3)_5PY5Me_2)Co(CH_3CN)]^+$ (right) in compounds **2.5** and **2.6**.

Although reductions with $K[(C_5H_5)Fe(CO)_2]$ gave analytically pure Co(I) complexes of a variety of pentapyridine ligands, we found that solutions of **2.7–9** in acetonitrile to be unstable. Even when stored at −35 °C, their dark blue and navy solutions turned brown over 12 h. Some decomposition products from solutions of **2.7** and **2.8** gave crystals suitable for X-ray diffraction analysis, illuminating the fate of those Co(I) complexes. Diffusion of diethyl ether into an acetonitrile solution of **2.7** gave red-orange plates that reveal two $[(CF_3PY5Me_2)Co]$ moieties bridged by an organic ligand (Figure 2.10). The two cobalt atoms and all six non-hydrogen atoms of the bridging ligand rest on a mirror plane. The interatomic distances of the bridging ligand are consistent with being the conjugate base of 3-iminobutanenitrile (Figure 2.S26), which was possibly formed from an aldol-like condensation between two acetonitrile molecules. This leaves the oxidation state of both cobalt ions as Co(II). An alternative possible assignment is a neutral bridging ligand, leaving one Co(II) ion and one Co(I) ion to balance the charge. This assignment seems less plausible, as all ten cobalt-pyridine distances are greater than 2.1 Å, indicating the lack of π back-bonding one would expect from Co(I). Furthermore, the crystals were red-orange rather than the dark blue color that usually arises from Co(I) in a tetragonal ligand field.

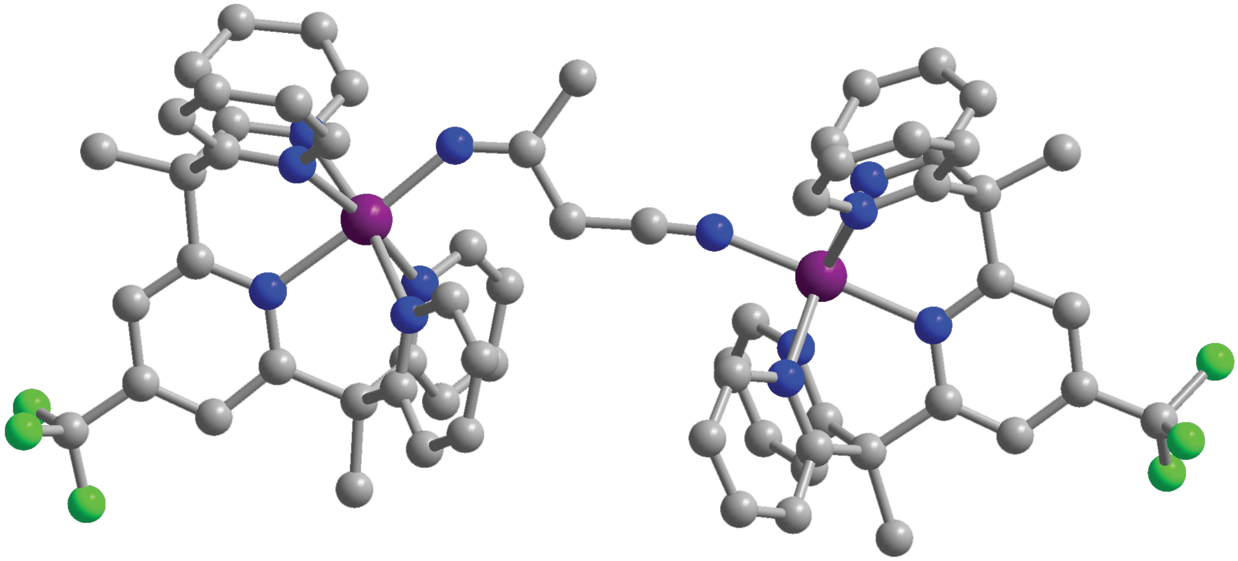

Figure 2.10. Molecular structure of a tricationic decomposition product of compound **2.7**, showing activation and coupling of two acetonitrile molecules. Purple, blue, and gray spheres indicate Co, N, and C atoms, respectively. H atoms and unbound anions are omitted for clarity.

The Co(I) complex of PY4IqMe$_2$ decomposes in an even more surprising manner. Slow evaporation of an acetonitrile solution of **2.8** into toluene under an atmosphere of N$_2$ afforded red crystals. Its X-ray crystal structure reveals a dicobalt dication supported by a PY4IqMe$_2$ ligand that has undergone C–C bond cleavage (Figure 2.11). As a result, a cobalt-aryl bond is formed, and a carbon-carbon bond is formed between the 1,1-bis(pyridyl)ethyl fragment and an acetonitrile molecule. The bridging imine and the isoquinolinyl ligands hold two cobalt centers together at a distance of 2.5910(15) Å. At this stage, the bond order between the two cobalt atoms cannot be unequivocally assigned. The Co–Co bond distance is slightly greater than twice the covalent bond radii of low-spin cobalt (2 × 1.26(3) Å = 2.52(6) Å), and less than those of high-spin cobalt (2 × 1.50(7) Å = 3.00(14) Å)[75]. Since the crystal structure shows only one decomposed PY4IqMe$_2$ ligand for every two cobalt atoms, the fate of an additional PY4IqMe$_2$ is unidentified.

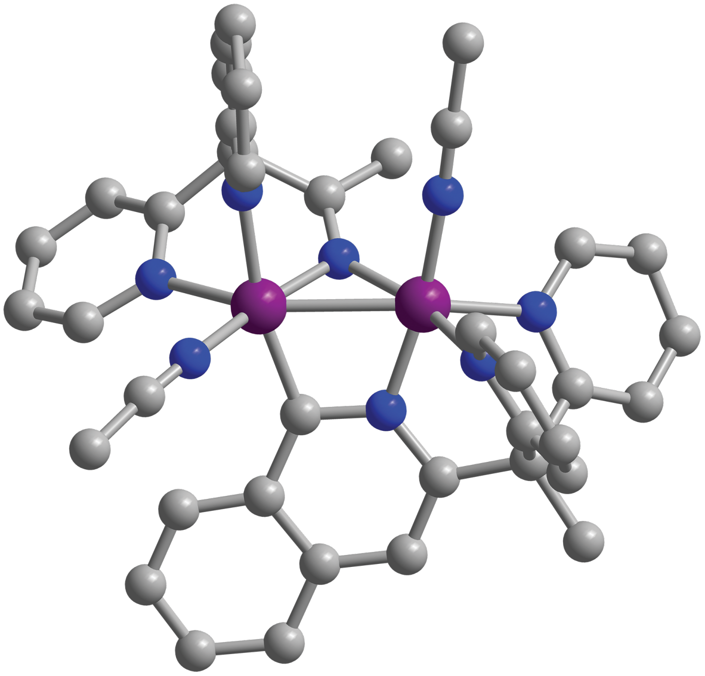

Figure 2.11. Molecular structure of the dicobalt dication deriving from the decomposition of compound **2.8**. Note that a carbon-carbon bond of the PY4IqMe$_2$ ligand has been cleaved. Purple, blue, and gray spheres indicate Co, N, and C atoms, respectively. H atoms and unbound anions are omitted for clarity. Highlighted interatomic distances: *d*(Co–Co) = 2.5910(15) Å.

2.4. Conclusions and Outlook

Three pentadentate polypyridine ligands and their corresponding cobalt(II) complexes were prepared and characterized. Taken together with previously reported ligand scaffolds, this isostructural family of cobalt complexes was analyzed to better understand the effect of ligand electronics on the electrochemical properties of the cobalt ion. In particular, while most ligand substitutions shift both the Co(III/II) and Co(II/I) redox couples by similar degrees, we also pursued the selective stabilization of Co(I)using a π-accepting ligand. The latter strategy was implemented using the isoquinoline ligand of PY4IqMe$_2$, which afforded a cobalt complex with the narrowest spread between the two one-electron redox potentials. Electrochemical titration of the cobalt complexes with acid suggested that catalytic proton reduction operates with an ECEC′ pathway, wherein the second electron transfer is more difficult than the first.

The rate constant k_1, corresponding to the protonation of cobalt(I) to form cobalt(III) hydrides was derived using scan rate-dependent peak shift analysis, and show that protonation is fastest for compound **2.1**, which possesses the narrowest redox spread. Using weaker acids that give more well-separated catalytic plateaus may permit evaluation of protonation kinetics of Co(II)H, k_2, and the global rate constant for catalysis, k_{obs}. Probing the H/D isotope effect upon k_1, k_2, and k_{obs} may also reveal valuable mechanistic information.

Lastly, there is a 0.5 V difference between the Co(II/I) and Co(III)H/Co(II)H redox couples. This suggests that it may be possible to isolate a cobalt(III) hydride complex, and that there is a large potential window in which the Co(III)H can be intercepted to perform useful chemistry other than hydrogen evolution.

2.5. Acknowledgments

This work was funded by NSF grant CHE-146841 and the Joint Center for Artificial Photosynthesis, a DOE Energy Innovation Hub, supported through the Office of Science of the U.S. Department of Energy award DE-SC0004993 to Jeffrey R. Long. The author thanks the National Science Foundation Graduate Research Fellowship program for financial support. Single-crystal X-ray structure determination was supported by the NIH Shared Instrumentation Grant S10-RR027172. The author also thanks Prof. Michael Nippe and Prof. Yogesh Surendranath for helpful discussions.

2.6. Supplementary Information

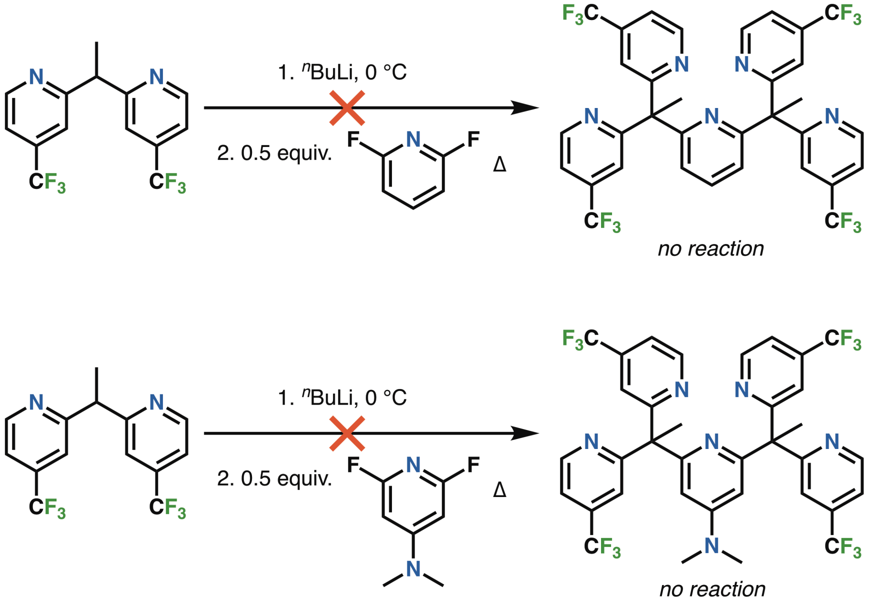

Scheme 2.S1. Attempted syntheses of mixed pentapyridine ligands with electron-poor equatorial pyridines and electron-rich axial pyridines did not give desired products.

Table 2.S1. Crystallographic data for compounds PY4IqMe$_2$, **2.1**, and **2.1′**.[a]

	PY4IqMe$_2$	**2.1**	**2.1′**
formula	$C_{33.5}H_{28}ClN_5$	$C_{37}H_{30}CoF_6N_6O_6S_2$	$C_{37}H_{33}CoF_{12}N_7P_2$
crystal system	monoclinic	triclinic	triclinic
fw, g mol^{-1}	1072.12	891.72	924.57
T, K	100(2)	100(2)	100(2)
space group	$P2_1/c$	$P\bar{1}$	$P\bar{1}$
habit	plate	block	block
color	yellow	red-orange	red-orange
Z	2	2	2
a, Å	19.650(2)	8.9002(13)	10.5856(6)
b, Å	8.6369(10)	12.4762(18)	11.1955(6)
c, Å	16.420(2)	17.113(3)	18.1680(10)
α, °	90	87.491(2)	75.0990(10)
β, °	103.233(2)	77.220(2)	79.2770(10)
γ, °	90	81.117(2)	84.6820(10)
V, Å^3	2712.7(6)	1830.8(5)	2042.1(2)
ρ_{calc}, g cm^{-3}	1.313	1.618	1.504
μ_{calc}, mm^{-1}	0.174	0.671	0.591
2θ range, °	2.13 to 50.886	2.44 to 50.746	3.77 to 50.956
total reflections	39618	35940	50778
data / restr / parameters	4993 / 0 / 363	6684 / 0 / 526	7567 / 0 / 536
$F(000)$	1124	910	938
$T_{\text{min}}/T_{\text{max}}$	0.966	0.780	0.918
crystal size, mm^3	0.3 × 0.2 × 0.1	0.5 × 0.3 × 0.1	0.6 × 0.3 × 0.2
Largest diff. peak/hole / e Å^{-3}	1.12 / −1.33	0.49 / −0.37	0.59 / −0.49
R_1 (wR_2),[b] % [$I > 2\sigma(I)$]	7.58 (17.77)	2.71 (6.73)	3.21 (8.16)
R_1 (wR_2), % (all data)	8.64 (18.38)	2.83 (6.82)	3.50 (8.33)

[a] Obtained with graphite-monochromated Mo Kα (λ = 0.71073 Å) radiation.

[b] $R_1 = \sum||F_o| - |F_c||/\sum|F_o|, wR_2 = \{\sum w(F_o^2 - F_c^2)^2/\sum w(F_o^2)^2\}^{\frac{1}{2}}$

Table 2.S2. Crystallographic data for compounds **2.2**, **2.3**, and **2.4**.[a]

	2.2	**2.3**	**2.4**
formula	$C_{37.6}H_{26.6}CoF_{21}N_5O_{7.6}S_2$	$C_{37}H_{30}F_6N_6O_6S_2Zn$	$C_{39}H_{39}CoF_9N_8O_9S_3$
crystal system	monoclinic	orthorhombic	monoclinic
fw, g mol^{-1}	1193.17	898.16	1089.89
T, K	100(2)	100(2)	100(2)
space group	$P2_1/n$	$P2_12_12_1$	$P2_1$
habit	block	block	block
color	yellow	colorless	orange
Z	4	8	4
a, Å	14.797(9)	10.6560(16)	14.5489(8)
b, Å	17.348(10)	25.470(4)	15.2580(9)
c, Å	18.327(11)	27.846(4)	20.1223(10)
α, °	90	90	90
β, °	104.921(8)	90	91.536(2)
γ, °	90	90	90
V, Å^3	4546(5)	7557.6(19)	4465.3(4)
ρ_{calc}, g cm^{-3}	1.743	1.579	1.621
μ_{calc}, mm^{-1}	0.612	0.846	0.626
2θ range, °	3.17 to 50.388	2.92 to 50.980	2.80 to 50.716
total reflections	100883	156482	39975
data / restr / parameters	8130 / 99 / 783	14031 / 0 / 1052	13833 / 1 / 1314
$F(000)$	2386	3664	2228
T_{min}/T_{max}	0.750	0.740	0.918
crystal size, mm^3	0.6 × 0.4 × 0.4	0.8 × 0.6 × 0.3	0.4 × 0.2 × 0.2
Largest diff. peak/hole / e Å^{-3}	1.35 / −0.53	1.00 / −0.44	0.62 / −0.29
R_1 (wR_2),[b] % [$I > 2\sigma(I)$]	4.68 (12.22)	3.20 (8.26)	3.19 (8.48)
R_1 (wR_2), % (all data)	5.47 (12.91)	3.39 (8.42)	3.30 (8.60)

[a] Obtained with graphite-monochromated Mo Kα (λ = 0.71073 Å) radiation.

[b] $R_1 = \sum||F_o| - |F_c||/\sum|F_o|, wR_2 = \{\sum w(F_o^2 - F_c^2)^2/\sum w(F_o^2)^2\}^{\frac{1}{2}}$

Table 2.S3. Crystallographic data for compounds **2.5** and **2.6**.[a]

	2.5	**2.6**
formula	$C_{40.5}H_{43}CoF_{4.5}K_{0.5}N_7O_{7.5}S_{1.5}$	$C_{39}H_{26}CoF_{18}N_7O_3S$
crystal system	monoclinic	monoclinic
fw, g mol^{-1}	959.89	1073.66
T, K	100(2)	100(2)
space group	$P2_1/c$	$P2_1/n$
habit	plate	plate
color	dark blue	dark blue
Z	4	4
a, Å	9.2735(2)	13.4964(8)
b, Å	24.9844(6)	19.6417(10)
c, Å	36.2712(10)	16.6822(8)
α, °	90	90
β, °	92.8610(10)	107.953(2)
γ, °	90	90
V, Å^3	8393.3(4)	4207.0(4)
ρ_{calc}, g cm^{-3}	1.519	1.695
μ_{calc}, mm^{-1}	0.614	0.586
2θ range, °	2.25 to 50.726	3.30 to 50.758
total reflections	67660	58041
data / restr / parameters	15358 / 1003 / 1199	7683 / 228 / 691
$F(000)$	3968	2152
$T_{\text{min}}/T_{\text{max}}$	0.603	0.656
crystal size, mm^3	0.2 × 0.05 × 0.01	0.5 × 0.05 × 0.02
Largest diff. peak/hole / e Å^{-3}	1.84 / −0.82	0.59 / −0.60
R_1 (wR_2),[b] % [$I > 2\sigma(I)$]	4.62 (11.14)	3.25 (6.92)
R_1 (wR_2), % (all data)	6.64 (12.33)	3.96 (7.25)

[a] Obtained with graphite-monochromated Mo Kα (λ = 0.71073 Å) radiation.

[b] $R_1 = \sum||F_\text{o}| - |F_\text{c}||/\sum|F_\text{o}|, wR_2 = \{\sum w(F_\text{o}^2 - F_\text{c}^2)^2/\sum w(F_\text{o}^2)^2\}^{\frac{1}{2}}$

Table 2.S4. Crystallographic data for compounds **2.7** and **2.8**.[a]

	2.7	**2.8**
formula	$C_{77}H_{72}Co_2F_{15}N_{15}O_{10}S_3$	$C_{42}H_{38.5}Co_2F_6N_8O_{6.25}S_2$
crystal system	monoclinic	monoclinic
fw, g mol^{-1}	1866.53	1051.29
T, K	100(2)	100(2)
space group	$P2_1/m$	$P2_1/c$
habit	plate	needle
color	red orange	dark red
Z	2	8
a, Å	13.0948(4)	13.1713(3)
b, Å	14.7430(4)	29.2404(7)
c, Å	21.5703(6)	26.1527(5)
α, °	90	90
β, °	106.1210(10)	96.148(2)
γ, °	90	90
V, Å^3	4000.5(2)	10014.4(4)
ρ_{calc}, g cm^{-3}	1.550	1.395
μ_{calc}, mm^{-1}	0.597	0.820
2θ range, °	3.24 to 46.622	2.096 to 48.880
total reflections	23696	46059
data / restr / parameters	6044 / 217 / 683	16464 / 626 / 1420
F(000)	1912	4292
T_{min}/T_{max}	0.581	0.649
crystal size, mm^3	0.1 × 0.1 × 0.04	0.15 × 0.04 × 0.04
Largest diff. peak/hole / e Å^{-3}	1.03 / −0.67	2.73 / −1.02
R_1 (wR_2),[b] % [$I > 2\sigma(I)$]	7.23 (18.67)	10.33 (29.69)
R_1 (wR_2), % (all data)	9.75 (20.42)	12.96 (31.59)

[a] Obtained with graphite-monochromated Mo Kα (λ = 0.71073 Å) radiation.

[b] $R_1 = \sum||F_o| - |F_c||/\sum|F_o|, wR_2 = \{\sum w(F_o^2 - F_c^2)^2/\sum w(F_o^2)^2\}^{\frac{1}{2}}$

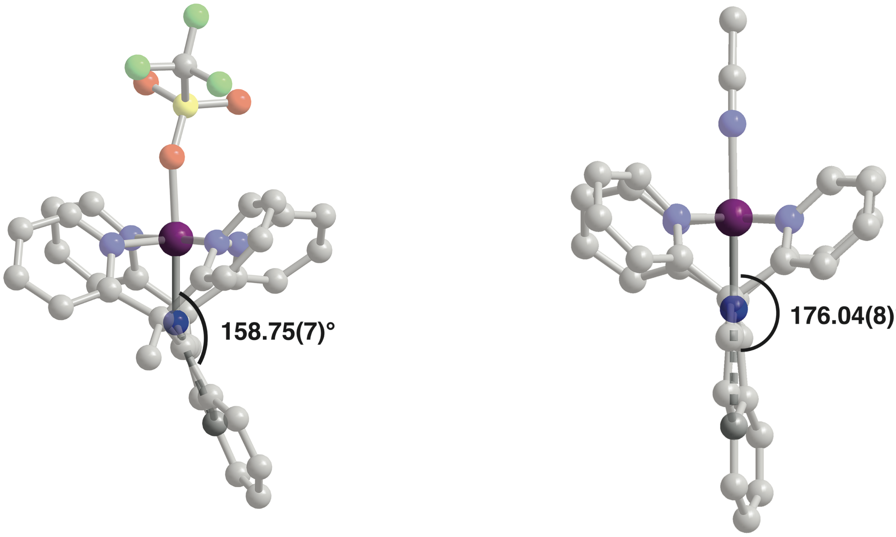

Figure 2.S1. Molecular structures of the $[(\text{PY4IqMe}_2)\text{Co}(\text{CF}_3\text{SO}_3)]^+$ and $[(\text{PY4IqMe}_2)\text{Co}(\text{CH}_3\text{CN})]^{2+}$ ions in compounds **2.1** and **2.1′**. The bond angle highlights the degree of perturbation caused by π-stacking of the isoquinoline fragment in the solid-state.

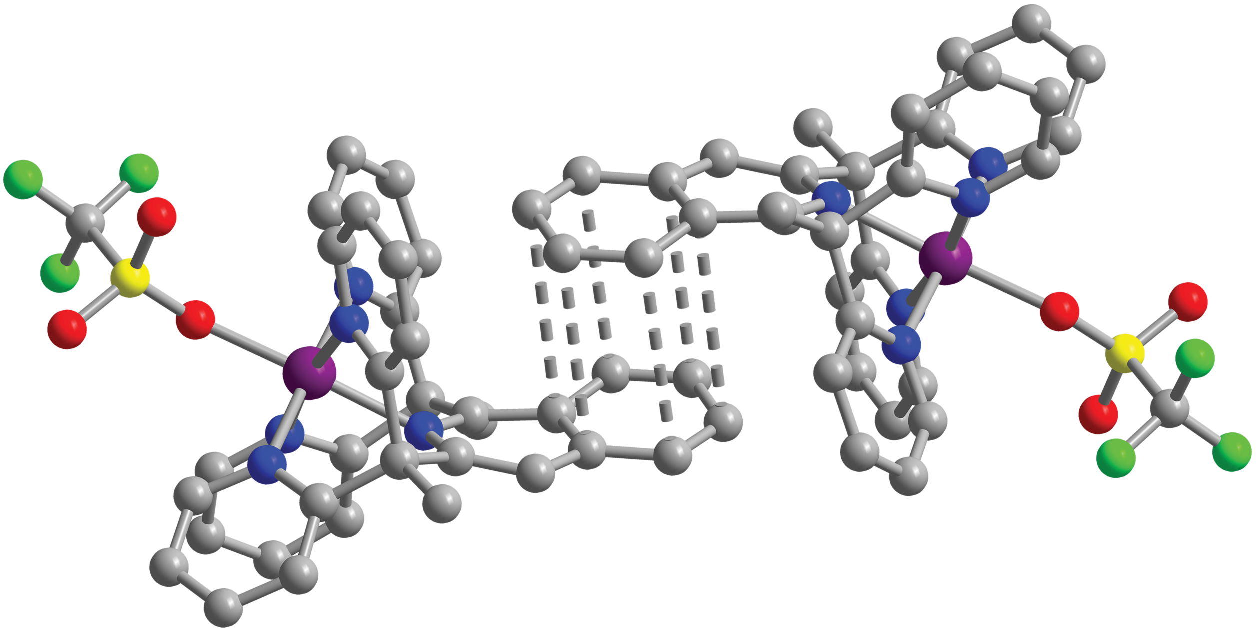

Figure 2.S2. Packing between two $[(\text{PY4IqMe}_2)\text{Co}(\text{CF}_3\text{SO}_3)]^+$ cations, as revealed in the single crystal X-ray analysis of compound **2.1**. Purple, blue, gray, red, yellow, and green spheres represent Co, N, C, O, S, and F atoms, respectively. H atoms, unbound anions, and solvent molecules are omitted for clarity. Dashed gray lines between the isoquinoline moieties indicate a face-to-face π interaction. The centroid-centroid vector is 3.5708(4) Å.

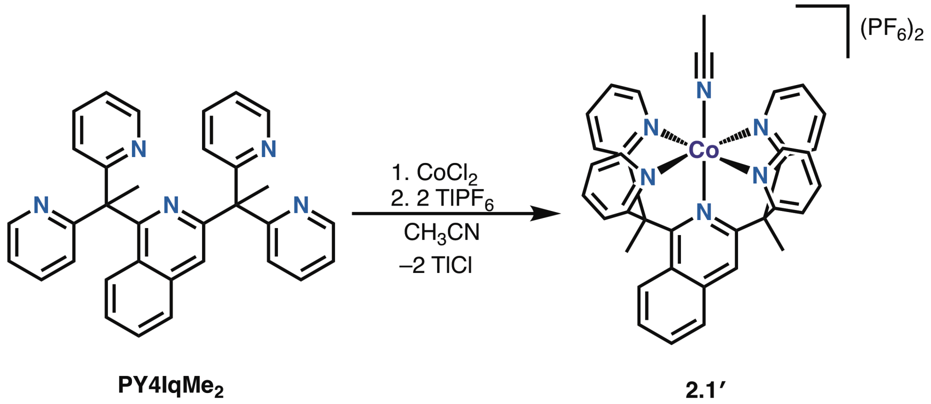

Scheme 2.S2. Preparation of compound **2.1′**.

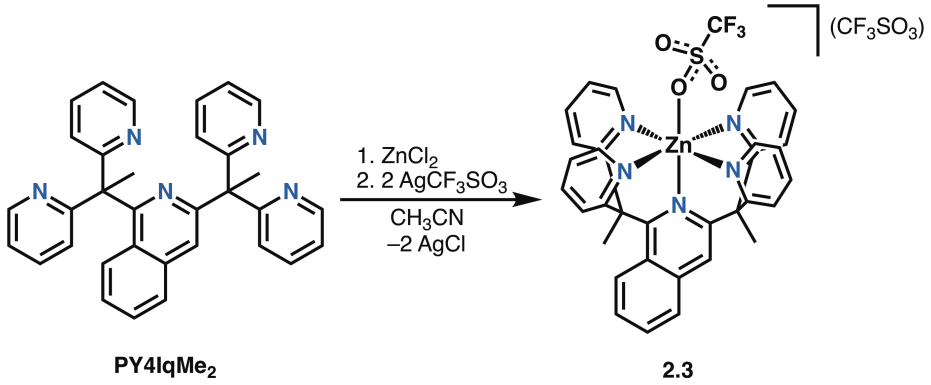

Scheme 2.S3. Preparation of compound **2.3**.

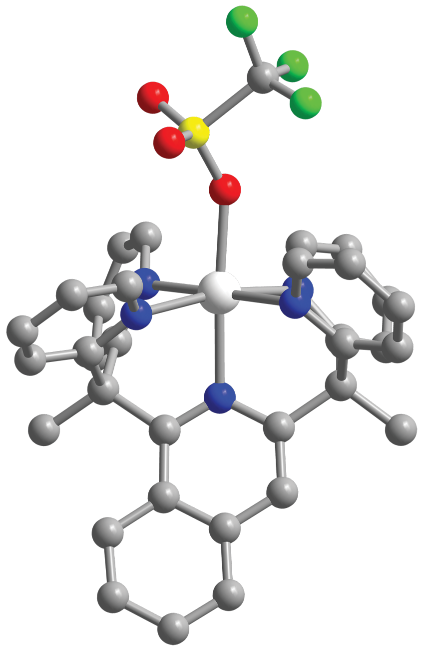

Figure 2.S3. Molecular structure of the $[(PY4IqMe_2)Zn(CF_3SO_3)]^+$ ion in compound **2.3**. White, blue, gray, red, yellow, and green spheres represent Zn, N, C, O, S, and F atoms. H atoms and unbound anions omitted for clarity.

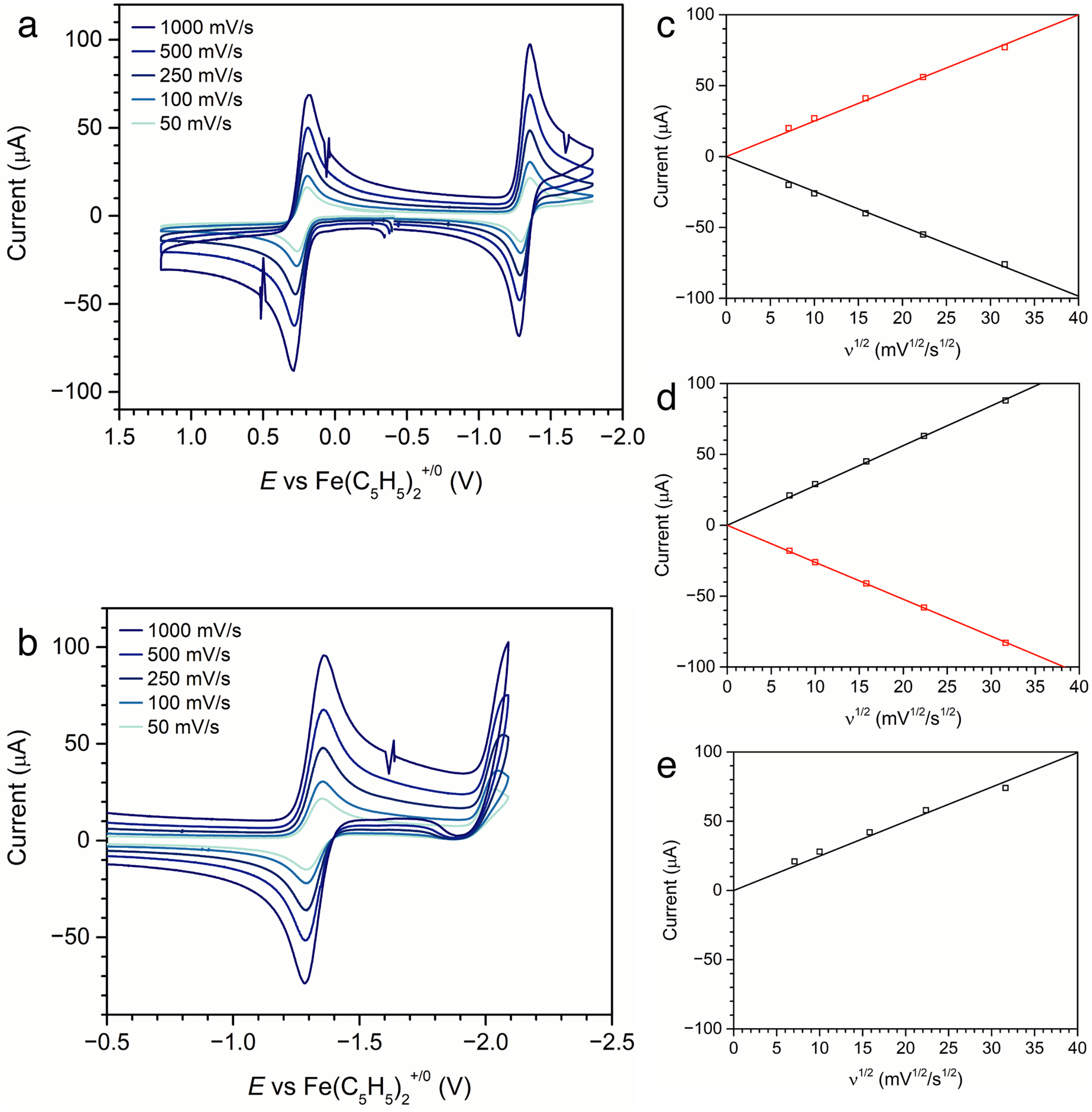

Figure 2.S4. a. CVs of compound **2.1** of the Co(III/II) and Co(II/I) redox couples between scan rates of 50–1000 mV/s. **b.** CVs of compound **2.1** of the Co(II/I) redox couple and an irreversible (ligand-based) reduction between scan rates of 50–1000 mV/s. **c.** Peak currents of the forward (black) and backward (red) scans versus square root of scan rate for the Co(III/II) couple. **d.** Peak currents of the forward (black) and backward (red) scans versus square root of scan rate for the Co(II/I) couple. **e.** Peak currents of the forward scan versus square root of scan rate for the ligand-based reduction.

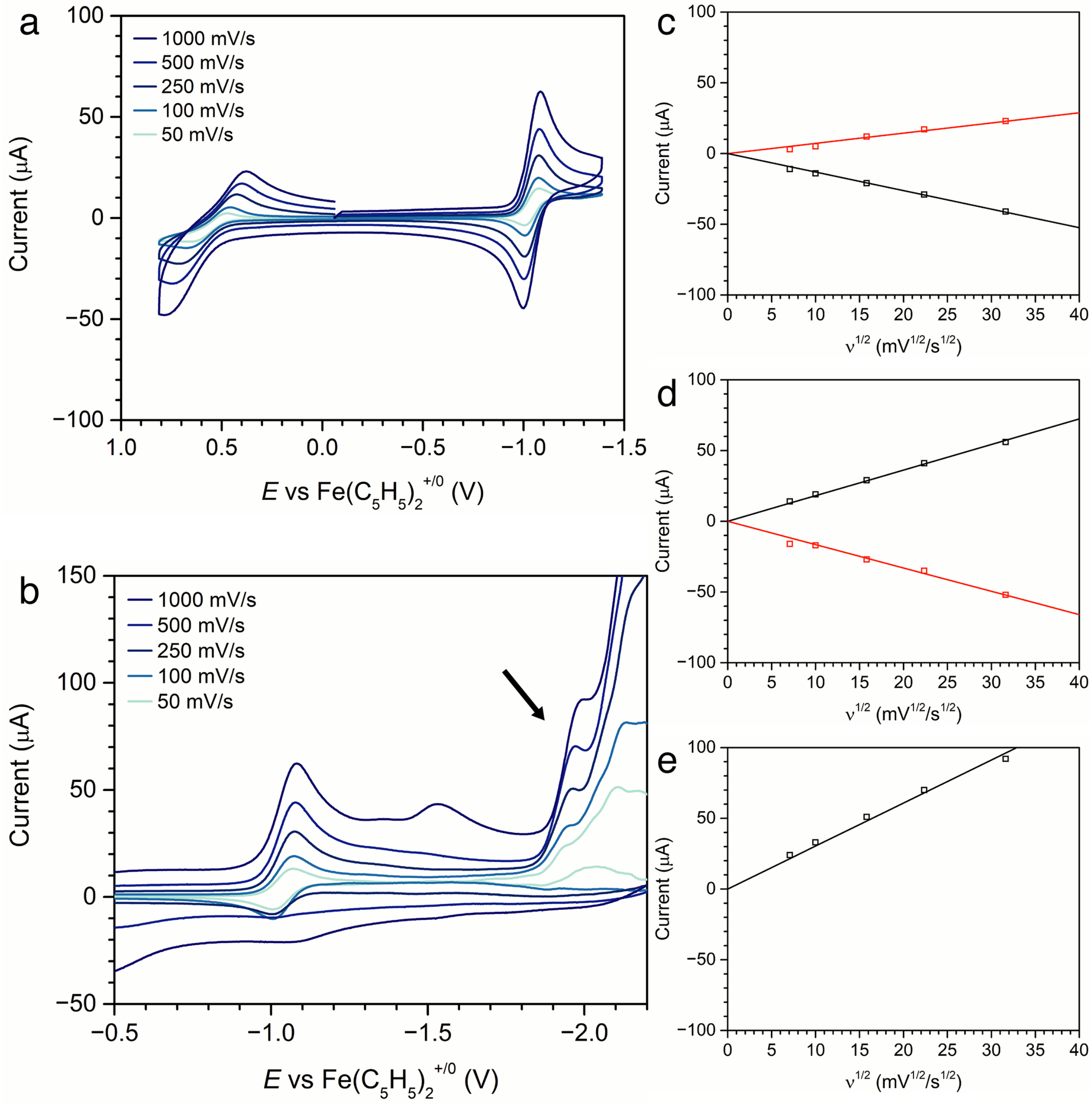

Figure 2.S5. a. CVs of compound **2.2** of the Co(III/II) and Co(II/I) redox couples between scan rates of 50–1000 mV/s. **b.** CVs of compound **2.2** of the Co(II/I) redox couple and an irreversible reduction (black arrow) between scan rates of 50–1000 mV/s. **c.** Peak currents of the forward (black) and backward (red) scans versus square root of scan rate for the Co(III/II) couple. **d.** Peak currents of the forward (black) and backward (red) scans versus square root of scan rate for the Co(II/I) couple. **e.** Peak currents of the forward scan versus square root of scan rate for the third, irreversible redox couple.

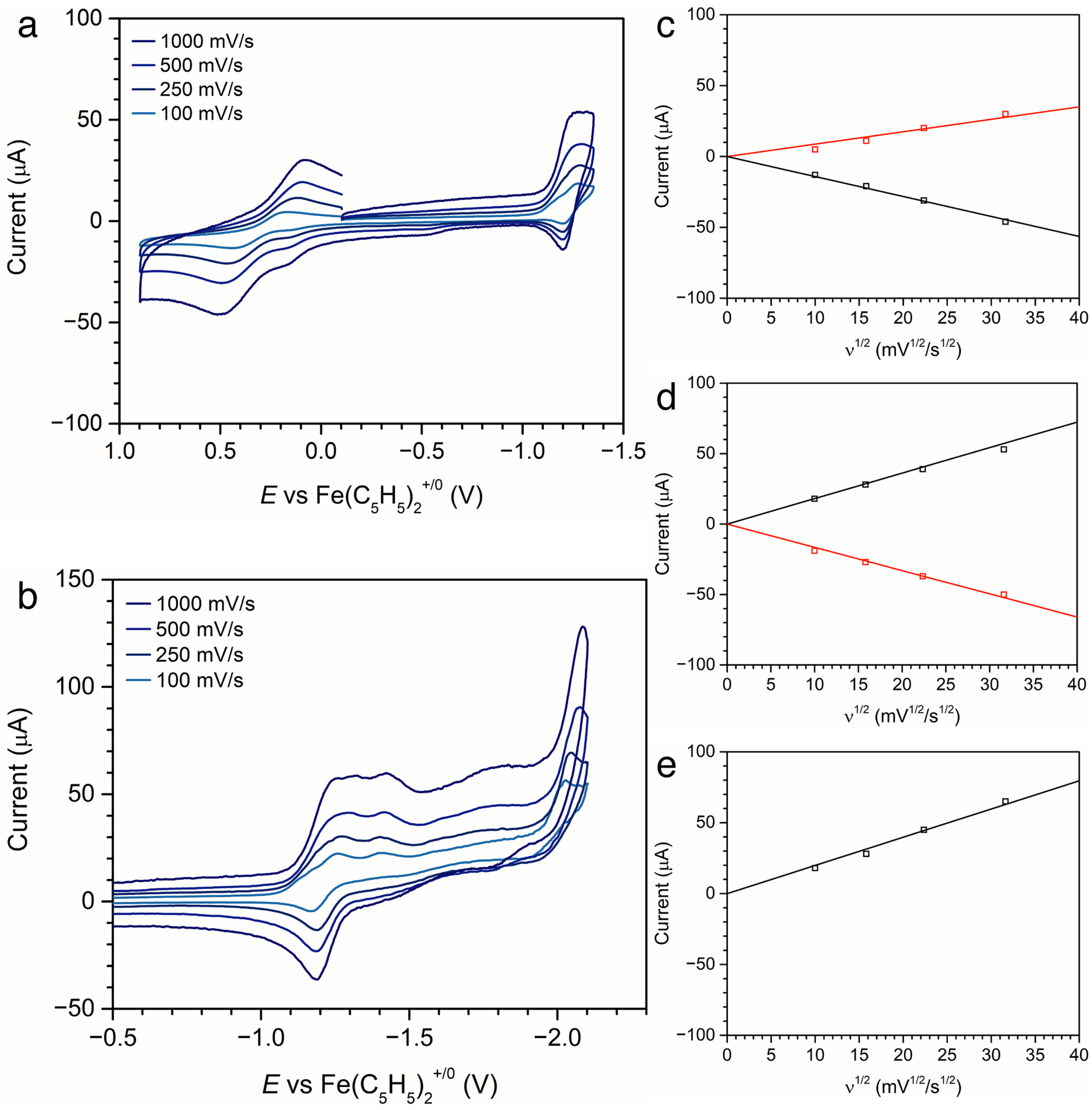

Figure 2.S6. a. CVs of compound **2.4** of the Co(III/II) and Co(II/I) redox couples between scan rates of 100–1000 mV/s. **b.** CVs of compound **2.4** of the Co(II/I) redox couple and an irreversible reduction between scan rates of 100–1000 mV/s. **c.** Peak currents of the forward (black) and backward (red) scans versus square root of scan rate for the Co(III/II) couple. **d.** Peak currents of the forward (black) and backward (red) scans versus square root of scan rate for the Co(II/I) couple. **e.** Peak currents of the forward scan versus square root of scan rate for the third, irreversible redox couple.

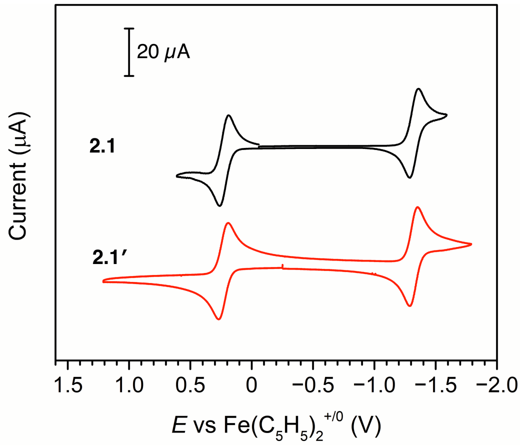

Figure 2.S7. CVs of compounds **2.1** and **2.1′** in acetonitrile. Scan rate = 100 mV/s.

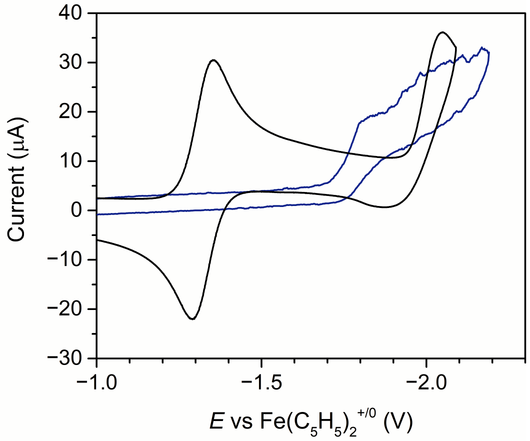

Figure 2.S8. CVs of compounds **2.1** (black) and **2.3** (blue) in acetonitrile. Both compounds show an irreversible reduction at apprxomiately −2.0 V, suggesting that the reduction is ligand based. Scan rate = 100 mV/s.

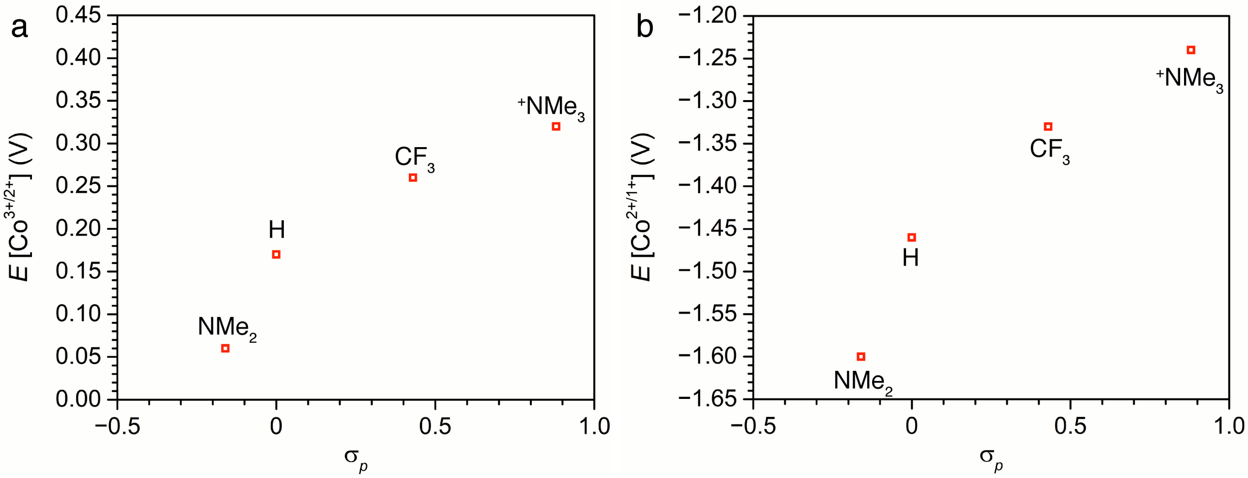

Figure 2.S9. Potentials of **a.** the Co(III/II) and **b.** Co(II/I) redox couples versus the Hammett parameter (σ_p)[39] of the substituent at the 4-position of the axial pyridine for complexes $[(NMe_2PY5Me_2)Co(CH_3CN)]^{2+}$, $[(PY5Me_2)Co(CH_3CN)]^{2+}$, $[(CF_3PY5Me_2)Co(CH_3CN)]^{2+}$, and **2.4**.

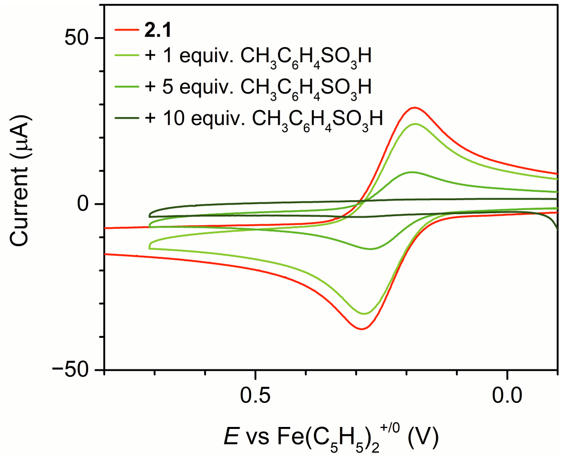

Figure 2.S10. CVs showing the reaction of compound **2.1** with *p*-toluenesulfonic acid. The Co(III/II) redox couple decreases in intensity as more acid is added, suggesting consumption of the $[(PY4IqMe_2)Co(CH_3CN)]^{2+}$ ion.

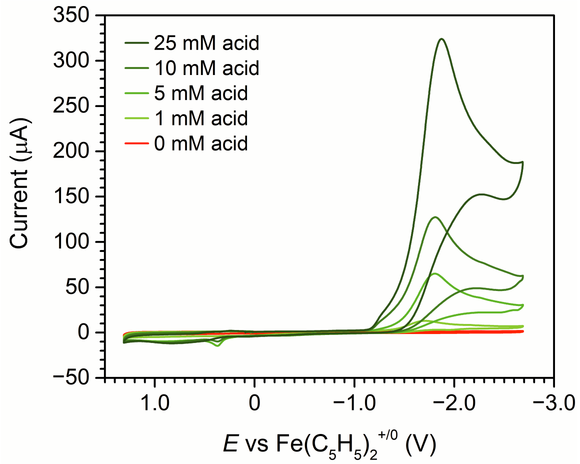

Figure 2.S11. CVs of 0–25 mM *N*,*N*-dimethylanilinium tetrafluoroborate in 0.1 M NBu_4PF_6 acetonitrile solution. A small oxidation feature at +0.35 V is attributed to oxidation of *N*,*N*-dimethylaniline. Scan rate = 100 mV/s.

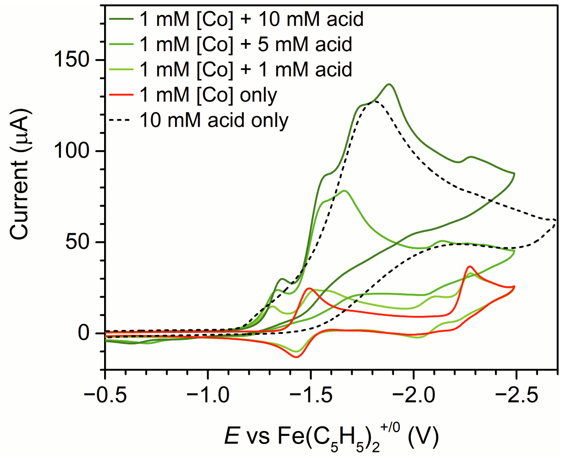

Figure 2.S12. CVs of an acetonitrile solution containing 1 mM $[(PY5Me_2)Co(CH_3CN)]^{2+}$ and 0–10 mM *N*,*N*-dimethylanilinium tetrafluoroborate, versus 10 mM *N*,*N*-dimethylanilinium alone. Scan rate = 100 mV/s.

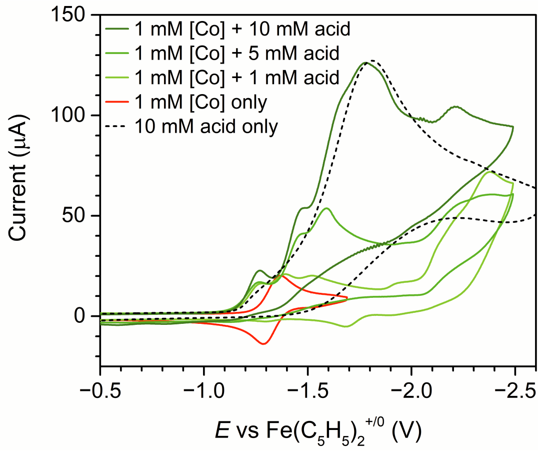

Figure 2.S13. CVs of an acetonitrile solution containing 1 mM $[(CF_3PY5Me_2)Co(CH_3CN)]^{2+}$ and 0–10 mM *N*,*N*-dimethylanilinium tetrafluoroborate, versus 10 mM *N*,*N*-dimethylanilinium alone. Scan rate = 100 mV/s.

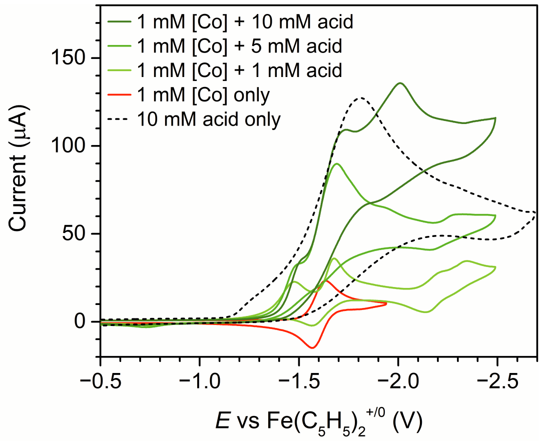

Figure 2.S14. CVs of an acetonitrile solution containing 1 mM $[(NMe_2PY5Me_2)Co(CH_3CN)]^{2+}$ and 0–10 mM *N*,*N*-dimethylanilinium tetrafluoroborate, versus 10 mM *N*,*N*-dimethylanilinium alone. Scan rate = 100 mV/s.

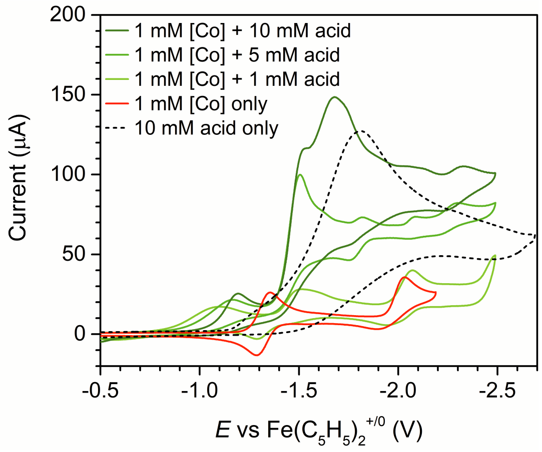

Figure 2.S15. CVs of an acetonitrile solution containing 1 mM of compound **2.1** and 0–10 mM *N*,*N*-dimethylanilinium tetrafluoroborate with M 0.1 M NBu_4PF_6. Scan rate = 100 mV/s.

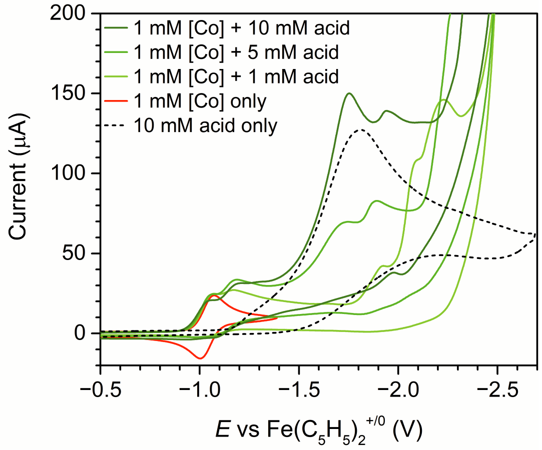

Figure 2.S16. CVs of an acetonitrile solution containing 1 mM of compound **2.2** and 0–10 mM *N*,*N*-dimethylanilinium tetrafluoroborate with M 0.1 M NBu_4PF_6. Scan rate = 100 mV/s.

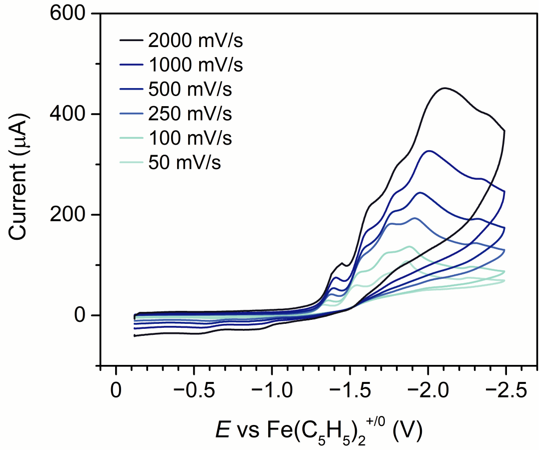

Figure 2.S17. CVs of an acetonitrile solution containing 1 mM $[(PY5Me_2)Co(CH_3CN)]^{2+}$ and 10 mM *N*,*N*-dimethylanilinium tetrafluoroborate with 0.1 M NBu_4PF_6, with scan rates 50–2000 mV/s.

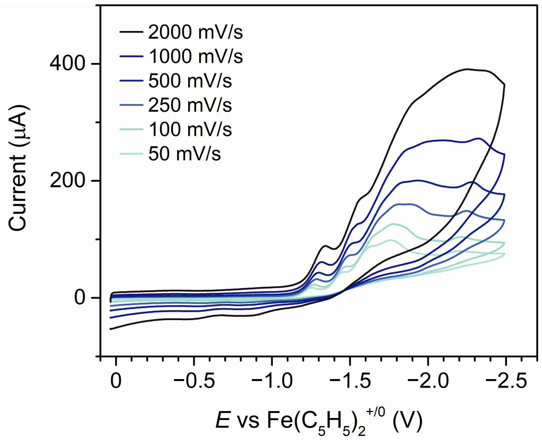

Figure 2.S18. CVs of an acetonitrile solution containing 1 mM $[(CF_3PY5Me_2)Co(CH_3CN)]^{2+}$ and 10 mM *N*,*N*-dimethylanilinium tetrafluoroborate with M 0.1 M NBu_4PF_6, with scan rates 50–2000 mV/s.

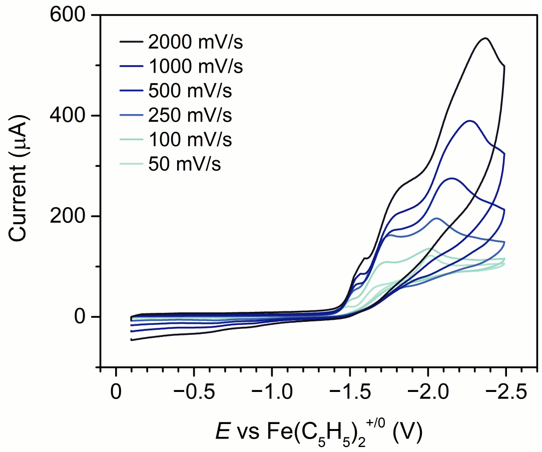

Figure 2.S19. CVs of an acetonitrile solution containing 1 mM $[(NMe_2PY5Me_2)Co(CH_3CN)]^{2+}$ and 10 mM *N*,*N*-dimethylanilinium tetrafluoroborate with 0.1 M NBu_4PF_6, with scan rates 50–2000 mV/s.

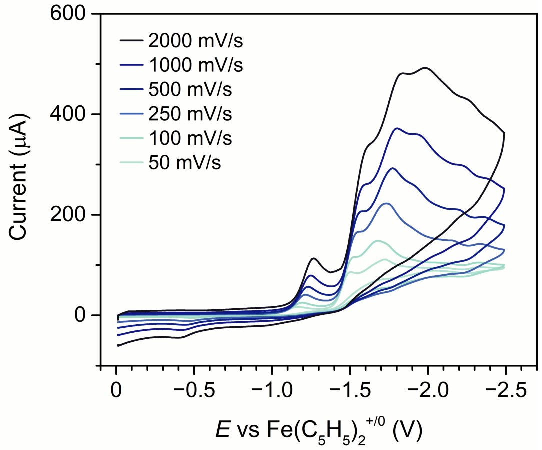

Figure 2.S20. CVs of an acetonitrile solution containing 1 mM of compound **2.1** and 10 mM *N*,*N*-dimethylanilinium tetrafluoroborate with 0.1 M NBu_4PF_6, with scan rates 50–2000 mV/s.

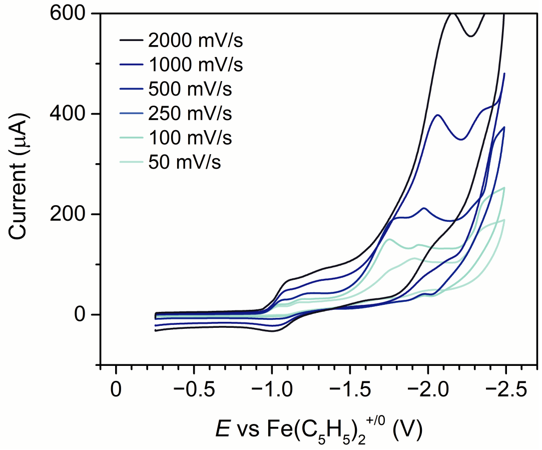

Figure 2.S21. CVs of an acetonitrile solution containing 1 mM of compound **2.2** and 10 mM *N*,*N*-dimethylanilinium tetrafluoroborate with 0.1 M NBu_4PF_6, with scan rates 50–2000 mV/s.

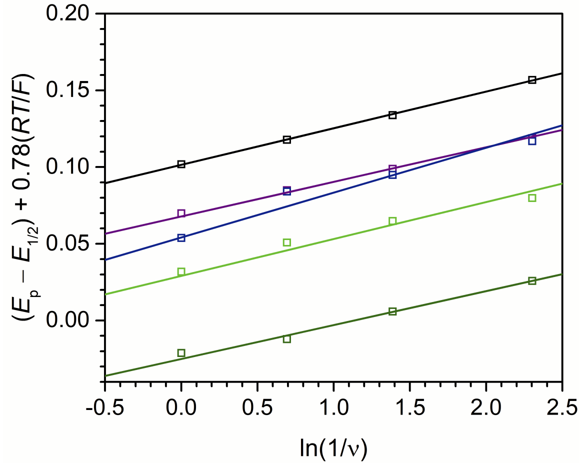

Figure 2.S22. Plot of the peak shift versus ln(1/*ν*) for compounds **2.1** (black), $[(PY5Me_2)Co(CH_3CN)]^{2+}$ (purple), $[(NMe_2PY5Me_2)Co(CH_3CN)]^{2+}$ (blue), $[(CF_3PY5Me_2)Co(CH_3CN)]^{2+}$ (light green), and **2.2** (green).

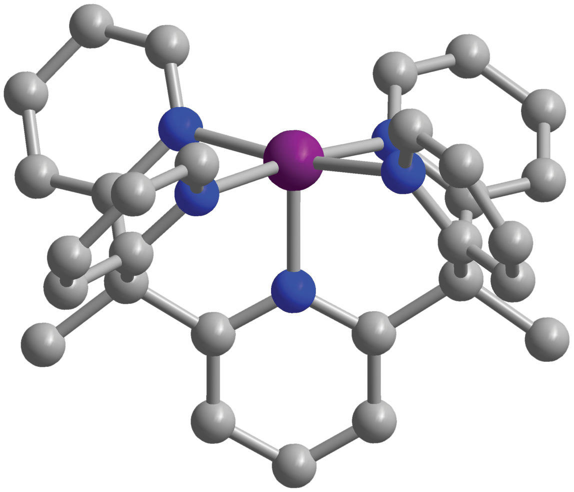

Figure 2.S23. Crystal structure of $[(PY5Me_2)Co]^+$ reported by King and coworkers.[28] Purple, blue, and gray spheres indicate Co, N, and C atoms, respectively. H atoms, unbound anions, and solvent molecules not shown.

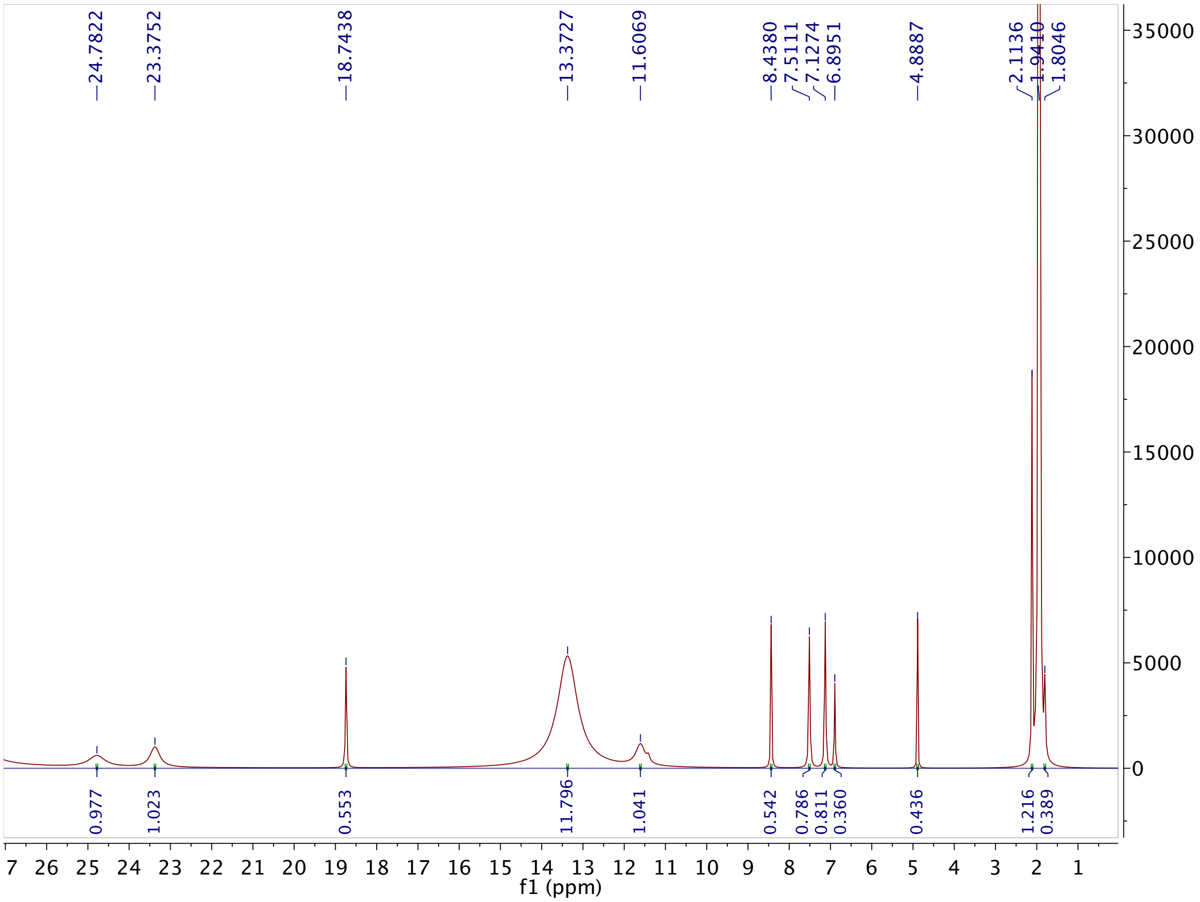

Figure 2.S24. ^1H NMR spectrum of compound **2.5** in CD_3CN.

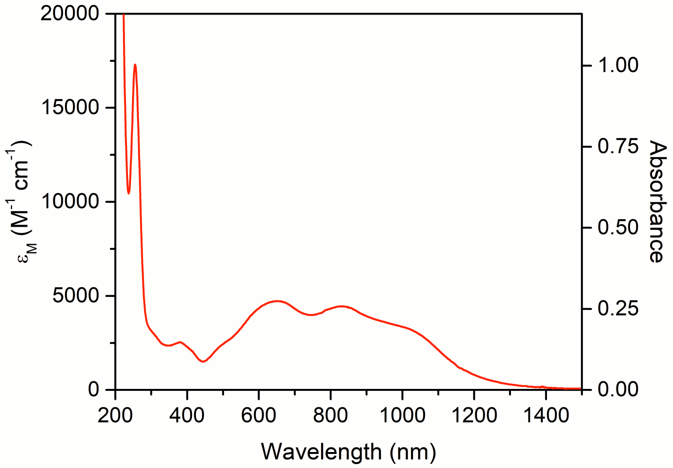

Figure 2.S25. UV-vis spectrum of compound **2.5** in CH_3CN.

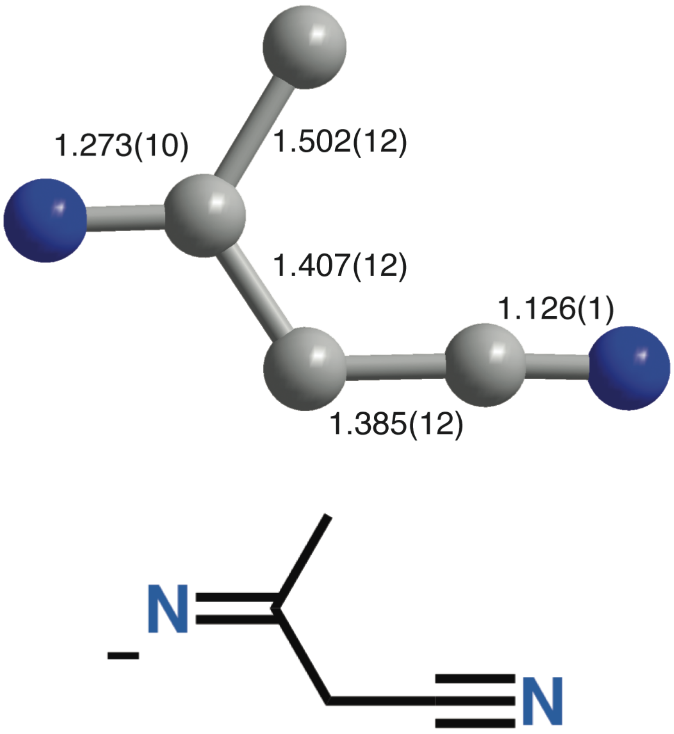

Figure 2.S26. Molecular structure and highlighted bond distances of the bridging ligand in **2.7**.

2.7. References

(1) Lewis, N. S.; Nocera, D. G. Powering the Planet: Chemical Challenges in Solar Energy Utilization. *Proc. Natl. Acad. Sci. U.S.A.* **2006**, *103* (43), 15729–15735.
(2) Turner, J. A. Sustainable Hydrogen Production. *Science* **2004**, *305*, 972–974.
(3) Esswein, A. J.; Nocera, D. G. Hydrogen Production by Molecular Photocatalysis. *Chem. Rev.* **2007**, *107* (10), 4022–4047.
(4) Trasatti, S. Work Function, Electronegativity, and Electrochemical Behaviour of Metals: III. Electrolytic Hydrogen Evolution in Acid Solutions. *J. Electroanal. Chem.* **1972**, *39*, 163–184.
(5) Hinnemann, B.; Moses, P. G.; Bonde, J.; Jørgensen, K. P.; Nielsen, J. H.; Horch, S.; Chorkendorff, I.; Nørskov, J. K. Biomimetic Hydrogen Evolution: MoS_2 Nanoparticles as Catalyst for Hydrogen Evolution. *J. Am. Chem. Soc.* **2005**, *127* (15), 5308–5309.
(6) Gordon, R. B.; Bertram, M.; Graedel, T. E. Metal Stocks and Sustainability. *Proc. Natl. Acad. Sci. U.S.A.* **2006**, *103* (5), 1209–1214.
(7) Artero, V.; Chavarot-Kerlidou, M.; Fontecave, M. Splitting Water with Cobalt. *Angew. Chem. Int. Ed.* **2011**, *50* (32), 7238–7266.
(8) Armstrong, F. Hydrogenases: Active Site Puzzles and Progress. *Curr. Opin. Chem. Biol.* **2004**, *8* (2), 133–140.
(9) Fontecilla-Camps, J. C.; Volbeda, A.; Cavazza, C.; Nicolet, Y. Structure/Function Relationships of [NiFe]- and [FeFe]-Hydrogenases. *Chem. Rev.* **2007**, *107* (10), 4273–4303.
(10) De Lacey, A. L.; Fernández, V. M.; Rousset, M.; Cammack, R. Activation and Inactivation of Hydrogenase Function and the Catalytic Cycle: Spectroelectrochemical

Studies. *Chem. Rev.* **2007**, *107* (10), 4304–4330.

(11) Armstrong, F. A. Recent Developments in Dynamic Electrochemical Studies of Adsorbed Enzymes and Their Active Sites. *Curr. Opin. Chem. Biol.* **2005**, *9* (2), 110–117.

(12) Gutiérrez-Sánchez, C.; Olea, D.; Marques, M.; Fernández, V. M.; Pereira, I. A. C.; Vélez, M.; De Lacey, A. L. Oriented Immobilization of a Membrane-Bound Hydrogenase Onto an Electrode for Direct Electron Transfer. *Langmuir* **2011**, *27* (10), 6449–6457.

(13) Gloaguen, F.; Rauchfuss, T. B. Small Molecule Mimics of Hydrogenases: Hydrides and Redox. *Chem. Soc. Rev.* **2009**, *38* (1), 100–108.

(14) Barton, B. E.; Olsen, M. T.; Rauchfuss, T. B. Artificial Hydrogenases. *Curr. Opin. Biotechnol.* **2010**, *21* (3), 292–297.

(15) Hu, X.; Cossairt, B. M.; Brunschwig, B. S.; Lewis, N. S.; Peters, J. C. Electrocatalytic Hydrogen Evolution by Cobalt Difluoroboryl-Diglyoximate Complexes. *Chem. Commun.* **2005**, No. 37, 4723–4725.

(16) Hu, X.; Brunschwig, B. S.; Peters, J. C. Electrocatalytic Hydrogen Evolution at Low Overpotentials by Cobalt Macrocyclic Glyoxime and Tetraimine Complexes. *J. Am. Chem. Soc.* **2007**, *129* (29), 8988–8998.

(17) Baffert, C.; Artero, V.; Fontecave, M. Cobaloximes as Functional Models for Hydrogenases. 2. Proton Electroreduction Catalyzed by Difluoroborylbis(Dimethylglyoximato)Cobalt(II) Complexes in Organic Media. *Inorg. Chem.* **2007**, *46* (5), 1817–1824.

(18) Bigi, J. P.; Hanna, T. E.; Harman, W. H.; Chang, A.; Chang, C. J. Electrocatalytic Reduction of Protons to Hydrogen by a Water-Compatible Cobalt Polypyridyl Platform. *Chem. Commun.* **2010**, *46* (6), 958–960.

(19) Collin, J.-P.; Jouaiti, A.; Sauvage, J.-P. Electrocatalytic Properties of Ni(Cyclam)$^{2+}$ and Ni_2(biscyclam)$^{4+}$ With Respect to CO_2 and H_2O Reduction. *Inorg. Chem.* **1988**, *27*.

(20) Wilson, A. D.; Newell, R. H.; McNevin, M. J.; Muckerman, J. T.; Rakowski DuBois, M.; DuBois, D. L. Hydrogen Oxidation and Production Using Nickel-Based Molecular Catalysts with Positioned Proton Relays. *J. Am. Chem. Soc.* **2006**, *128* (1), 358–366.

(21) Rakowski DuBois, M.; DuBois, D. L. Development of Molecular Electrocatalysts for CO_2 Reduction and H_2 Production/Oxidation. *Acc. Chem. Res.* **2009**, *42* (12), 1974–1982.

(22) DuBois, M. R.; DuBois, D. L. The Roles of the First and Second Coordination Spheres in the Design of Molecular Catalysts for H_2 Production and Oxidation. *Chem. Soc. Rev.* **2008**, *38* (1), 62–72.

(23) Appel, A. M.; DuBois, D. L.; DuBois, M. R. Molybdenum-Sulfur Dimers as Electrocatalysts for the Production of Hydrogen at Low Overpotentials. *J. Am. Chem. Soc.* **2005**, *127* (36), 12717–12726.

(24) Appel, A. M.; Lee, S.-J.; Franz, J. A.; DuBois, D. L.; DuBois, M. R. Free Energy Landscapes for S-H Bonds in $Cp^*{}_2Mo_2S_4$ Complexes. *J. Am. Chem. Soc.* **2009**, *131* (14), 5224–5232.

(25) Karunadasa, H. I.; Chang, C. J.; Long, J. R. A Molecular Molybdenum-Oxo Catalyst for Generating Hydrogen From Water. *Nature* **2010**, *464* (7293), 1329–1333.

(26) Karunadasa, H. I.; Montalvo, E.; Sun, Y.; Majda, M.; Long, J. R.; Chang, C. J. A Molecular MoS_2 Edge Site Mimic for Catalytic Hydrogen Generation. *Science* **2012**,

335 (6069), 698–702.
(27) Sun, Y.; Bigi, J. P.; Piro, N. A.; Tang, M. L.; Long, J. R.; Chang, C. J. Molecular Cobalt Pentapyridine Catalysts for Generating Hydrogen From Water. *J. Am. Chem. Soc.* **2011**, *133* (24), 9212–9215.
(28) King, A. E.; Surendranath, Y.; Piro, N. A.; Bigi, J. P.; Long, J. R.; Chang, C. J. A Mechanistic Study of Proton Reduction Catalyzed by a Pentapyridine Cobalt Complex: Evidence for Involvement of an Anation-Based Pathway. *Chem. Sci.* **2013**, *4*, 1578–1587.
(29) Bechlars, B.; D'Alessandro, D. M.; Jenkins, D. M.; Iavarone, A. T.; Glover, S. D.; Kubiak, C. P.; Long, J. R. High-Spin Ground States via Electron Delocalization in Mixed-Valence Imidazolate-Bridged Divanadium Complexes. *Nature Chem.* **2010**, *2* (5), 362–368.
(30) McCarthy, B. D.; Martin, D. J.; Rountree, E. S.; Ullman, A. C.; Dempsey, J. L. Electrochemical Reduction of Brønsted Acids by Glassy Carbon in Acetonitrile—Implications for Electrocatalytic Hydrogen Evolution. *Inorg. Chem.* **2014**, *53* (16), 8350–8361.
(31) Plotkin, J. S.; Shore, S. G. Convenient Preparation and Isolation of Pure Potassium Cyclopentadienyldicarbonylferrate, K[(η^5-C_5H_5)Fe$(CO)_2$]. *Inorg. Chem.* **1981**, *20* (1), 284–285.
(32) Hagen, K. S. Iron(II) Triflate Salts as Convenient Substitutes for Perchlorate Salts: Crystal Structures of [Fe$(H_2O)_6$]$(CF_3SO_3)_2$ and Fe$(MeCN)_4(CF_3SO_3)_2$. *Inorg. Chem.* **2000**, *39* (25), 5867–5869.
(33) Ranganathan, S.; Kuo, T.-C.; McCreery, R. L. Facile Preparation of Active Glassy Carbon Electrodes with Activated Carbon and Organic Solvents. *Anal. Chem.* **1999**, *71* (16), 3574–3580.
(34) APEX2. v. 2009; Bruker Analytical X-ray Systems, Inc; Madison, WI, 2009.
(35) Sheldrick, G. M. Version 2.03; Bruker Analytical Systems, Inc.: Madison, WI, 2000.
(36) Sheldrick, G. SHELXT - Integrated Space-Group and Crystal-Structure Determination. *Acta Crystallogr A Found Adv* **2015**, *71* (1), 3–8.
(37) Sheldrick, G. A Short History of SHELX. *Acta Crystallogr A Found Crystallogr* **2008**, *64* (1), 112–122.
(38) Sheldrick, G. Crystal Structure Refinement with SHELXL. *Acta Crystallogr C Struct Chem* **2015**, *71* (1), 3–8.
(39) Hansch, C.; Leo, A.; Taft, R. W. A Survey of Hammett Substituent Constants and Resonance and Field Parameters. *Chem. Rev.* **1991**, *91*, 165–195.
(40) Linnell, R. Notes- Dissociation Constants of 2-Substituted Pyridines. *J. Org. Chem.* **1960**, *25* (2), 290–290.
(41) *Determination of Organic Structures by Physical Methods*; Baude, E. A., Nachod, F. C., Eds.; Academic Press, 1955.
(42) Fürstner, A.; Leitner, A.; Méndez, M.; Krause, H. Iron-Catalyzed Cross-Coupling Reactions. *J. Am. Chem. Soc.* **2002**, *124* (46), 13856–13863.
(43) King, A. E.; Nippe, M.; Atanasov, M.; Chantarojsiri, T.; Wray, C. A.; Bill, E.; Neese, F.; Long, J. R.; Chang, C. J. A Well-Defined Terminal Vanadium(III) Oxo Complex. *Inorg. Chem.* **2014**, *53* (21), 11388–11395.
(44) Falzone, A. J.; Nguyen, J.; Weare, W. W.; Sommer, R. D.; Boyle, P. D. An Unsupported Metal Hydroxide for the Design of Molecular M-Oxo Bridged

Heterobimetallic Complexes. *Chem. Commun.* **2014**, *50* (17), 2139–2141.

(45) Freedman, D. E.; Jenkins, D. M.; Iavarone, A. T.; Long, J. R. A Redox-Switchable Single-Molecule Magnet Incorporating $[Re(CN)_7]^{3-}$. *J. Am. Chem. Soc.* **2008**, *130* (10), 2884–2885.

(46) Wu, X.; Huang, T.; Lekich, T. T.; Sommer, R. D.; Weare, W. W. Synthesis of Unsupported D1–Dx Oxido-Bridged Heterobimetallic Complexes Containing V^{Iv}: A New Direction for Metal-to-Metal Charge Transfer. *Inorg. Chem.* **2015**, *54* (11), 5322–5328.

(47) Chantarojsiri, T.; Sun, Y.; Long, J. R.; Chang, C. J. Water-Soluble Iron(IV)-Oxo Complexes Supported by Pentapyridine Ligands: Axial Ligand Effects on Hydrogen Atom and Oxygen Atom Transfer Reactivity. *Inorg. Chem.* **2015**, *54* (12), 5879–5887.

(48) Zadrozny, J. M.; Freedman, D. E.; Jenkins, D. M.; Harris, T. D.; Iavarone, A. T.; Mathonière, C.; Clérac, R.; Long, J. R. Slow Magnetic Relaxation and Charge-Transfer in Cyano-Bridged Coordination Clusters Incorporating $[Re(CN)_7]^{3-/4-}$. *Inorg. Chem.* **2010**, *49* (19), 8886–8896.

(49) Evans, D. F. The Determination of the Paramagnetic Susceptibility of Substances in Solution by Nuclear Magnetic Resonance. *J. Chem. Soc.* **1959**, 2003–2005.

(50) Kaljurand, I.; Kütt, A.; Sooväli, L.; Rodima, T.; Mäemets, V.; Leito, I.; Koppel, I. A. Extension of the Self-Consistent Spectrophotometric Basicity Scale in Acetonitrile to a Full Span of 28 pK_a Units: Unification of Different Basicity Scales. *J. Org. Chem.* **2005**, *70* (3), 1019–1028.

(51) Kütt, A.; Leito, I.; Kaljurand, I.; Sooväli, L.; Vlasov, V. M.; Yagupolskii, L. M.; Koppel, I. A. A Comprehensive Self-Consistent Spectrophotometric Acidity Scale of Neutral Brønsted Acids in Acetonitrile. *J. Org. Chem.* **2006**, *71* (7), 2829–2838.

(52) Appel, A. M.; Lee, S.-J.; Franz, J. A.; DuBois, D. L.; Rakowski DuBois, M.; Twamley, B. Determination of S−H Bond Strengths in Dimolybdenum Tetrasulfide Complexes. *Organometallics* **2009**, *28* (3), 749–754.

(53) Roberts, J. A. S.; Bullock, R. M. Direct Determination of Equilibrium Potentials for Hydrogen Oxidation/Production by Open Circuit Potential Measurements in Acetonitrile. *Inorg. Chem.* **2013**, *52* (7), 3823–3835.

(54) Appel, A. M.; Helm, M. L. Determining the Overpotential for a Molecular Electrocatalyst. *ACS Catal.* **2014**, *4* (2), 630–633.

(55) Fourmond, V.; Jacques, P.-A.; Fontecave, M.; Artero, V. H_2 Evolution and Molecular Electrocatalysts: Determination of Overpotentials and Effect of Homoconjugation. *Inorg. Chem.* **2010**, *49* (22), 10338–10347.

(56) Izutsu, K. Acid-Base Reactions in Non-Aqueous Solvents. In *Electrochemistry in Nonaqueous Solutions*; Wiley-VCH Verlag GmbH & Co. KGaA: Weinheim, FRG, 2002; pp 59–83.

(57) Hand, R.; Nelson, R. F. The Electrochemical Oxidation of *N*,*N*-Dimethylaniline. *J. Electrochem. Soc.* **1970**, *117* (11), 1353–1355.

(58) Lee, K. J.; Elgrishi, N.; Kandemir, B.; Dempsey, J. L. Electrochemical and Spectroscopic Methods for Evaluating Molecular Electrocatalysts. *Nat. rev. chem.* **2017**, *1* (5), 0039–14.

(59) Nicholson, R. S.; Shain, I. Theory of Stationary Electrode Polarography for a Chemical Reaction Coupled Between Two Charge Transfers. *Anal. Chem.* **1965**, *37* (2), 178–190.

(60) Roubelakis, M. M.; Bediako, D. K.; Dogutan, D. K.; Nocera, D. G. Proton-Coupled Electron Transfer Kinetics for the Hydrogen Evolution Reaction of Hangman Porphyrins. *Energy Environ. Sci.* **2012**, *5* (7), 7737–4.

(61) Andrieux, C. P.; Gamby, J.; Hapiot, P.; Savéant, J.-M. Evidence for Inverted Region Behavior in Proton Transfer to Carbanions. *J. Am. Chem. Soc.* **2003**, *125* (33), 10119–10124.

(62) Elgrishi, N.; Rountree, K. J.; McCarthy, B. D.; Rountree, E. S.; Eisenhart, T. T.; Dempsey, J. L. A Practical Beginner's Guide to Cyclic Voltammetry. *J. Chem. Educ.* **2017**, acs.jchemed.7b00361–10.

(63) Rountree, E. S.; McCarthy, B. D.; Eisenhart, T. T.; Dempsey, J. L. Evaluation of Homogeneous Electrocatalysts by Cyclic Voltammetry. *Inorg. Chem.* **2014**, 140923083950003.

(64) Costentin, C.; Savéant, J.-M. Multielectron, Multistep Molecular Catalysis of Electrochemical Reactions: Benchmarking of Homogeneous Catalysts. *ChemElectroChem* **2014**, *1* (7), 1226–1236.

(65) Rountree, E. S.; Martin, D. J.; McCarthy, B. D.; Dempsey, J. L. Linear Free Energy Relationships in the Hydrogen Evolution Reaction: Kinetic Analysis of a Cobaloxime Catalyst. *ACS Catal.* **2016**, *6* (5), 3326–3335.

(66) Estes, D. P.; Grills, D. C.; Norton, J. R. The Reaction of Cobaloximes with Hydrogen: Products and Thermodynamics. *J. Am. Chem. Soc.* **2014**, *136* (50), 17362–17365.

(67) Li, G.; Han, A.; Pulling, M. E.; Estes, D. P.; Norton, J. R. Evidence for Formation of a Co–H Bond From $(H_2O)_2Co(dmgBF_2)_2$ Under H_2: Application to Radical Cyclizations. *J. Am. Chem. Soc.* **2012**, *134* (36), 14662–14665.

(68) Lacy, D. C.; Roberts, G. M.; Peters, J. C. The Cobalt Hydride That Never Was: Revisiting Schrauzer's "Hydridocobaloxime." *J. Am. Chem. Soc.* **2015**, *137* (14), 4860–4864.

(69) Shi, S.; Daniels, L. M.; Espenson, J. H. Molecular Structure of a Cobalt(I) Complex Lacking a Carbonyl Ligand. a Unique Example of Cobalt-Nitrogen Bond Shortening. *Inorg. Chem.* **1991**, *30* (18), 3407–3410.

(70) de Bruin, B.; Bill, E.; Bothe, E.; Weyhermüller, T.; Wieghardt, K. Molecular and Electronic Structures of Bis(Pyridine-2,6-Diimine)Metal Complexes $[ML_2](PF_6)_n$ (n = 0, 1, 2, 3; M = Mn, Fe, Co, Ni, Cu, Zn)†. *Inorg. Chem.* **2000**, *39* (13), 2936–2947.

(71) Aresta, M.; Rossi, M.; Sacco, A. Tetrahedral Complexes of Cobalt (I). *Inorg. Chim. Acta* **1969**, *3*, 227–231.

(72) Liebeskind, L. S.; Baysdon, S. L.; South, M. S.; Iyer, S.; Leeds, J. P. The Development of an Organotransition Metal Synthesis of Quinones. *Tetrahedron* **1985**, *41* (24), 5839–5853.

(73) Krzystek, J.; Ozarowski, A.; Zvyagin, S. A.; Telser, J. High Spin Co(I): High-Frequency and -Field EPR Spectroscopy of $CoX(PPh_3)_3$ (X = Cl, Br). *Inorg. Chem.* **2012**, *51* (9), 4954–4964.

(74) Connelly, N. G.; Geiger, W. E. Chemical Redox Agents for Organometallic Chemistry. *Chem. Rev.* **1996**, *96* (2), 877–910.

(75) Cordero, B.; Gómez, V.; Platero-Prats, A. E.; Revés, M.; Echeverría, J.; Cremades, E.; Barragán, F.; Alvarez, S. Covalent Radii Revisited. *Dalton Trans.* **2008**, *40* (21), 2832–2837.

Chapter 3. Tuning Second Coordination Sphere Interactions in Polypyridyl–Iron Complexes to Achieve Selective Electrocatalytic Reduction of Carbon Dioxide to Carbon Monoxide

3.1. Introduction

Cost-effective solar-to-chemical conversion requires the identification of efficient electrocatalysts that are built solely from earth-abundant elements.[1-3] Powering the conversion of carbon dioxide (CO_2) via solar-derived potential energy would allow for the regeneration of carbon-based fuels and the utilization of CO_2 as an inexpensive C1 feedstock molecule for industrial applications. Various heterogeneous electrocatalytic CO_2 reduction systems have been reported that utilize non-precious metal surfaces,[4-12] molecularly-inspired covalent[13] and metal-organic frameworks,[14-16] and surface-attached molecular catalysts.[17-23] Designing electrocatalysts with high selectivities for the reduction of CO_2 to carbon monoxide (CO) over the energetically and kinetically more accessible reduction of protons is a major challenge for all CO_2 reduction catalyst systems in aqueous media. It is therefore not surprising that only very few molecular catalysts based on precious metals[24-26] or base metals[21,27-39] have been reported that are chemically compatible with aqueous conditions yet maintain high selectivities for the electrocatalytic production of CO from CO_2.

The identification of new design elements towards the development of next-generation molecular catalysts has recently involved the modulation of the second coordination sphere, with a particular focus on the incorporation of proton relays.[29,30,40-49] These considerations are predominantly inspired by natural catalysts (enzymes), which are able to control substrate selectivity via a plethora of second- and third-coordination sphere functional groups with only a single cofactor. Specifically, functional and structural aspects of the active site of [FeFe]-hydrogenases[50] have previously been exploited for the design of efficient synthetic molecular electrocatalysts for dihydrogen oxidation[40,51-57] as well as proton reduction.[40,51,54,57-66]

We previously reported that the synergistic interplay between redox-active bipyridine (bpy) ligand moieties and first-row transition metal ions, stabilized by polydentate ligand platforms, results in increased electrocatalytic and photocatalytic activity for proton reduction.[67] Herein, we present a bio-inspired expansion of this work to the systematic study of iron-based catalysts in pursuit of systems for selective CO_2 reduction. The new catalysts feature three functional partitions (reactive metal, electron reservoir, second coordination sphere Lewis acidic moiety; see Scheme 3.1), which mimic some of the crucial components of the enzymatic active site in Ni-carbon monoxide dehydrogenase.[68,69] We were especially interested in complexes of iron, because, until very recently,[70,71] selective electrocatalytic CO_2 reduction had only been observed for heme-type Fe-porphyrin molecules.[30-34,42,43,72-74]

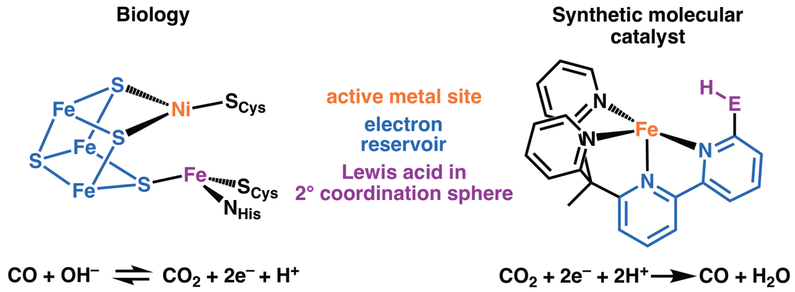

Scheme 3.1. Bio-inspired features in [(bpy^{R}PY2Me)Fe] complexes.

3.2. Experimental

3.2.1. Materials and Methods

Air- and/or moisture-sensitive compounds were synthesized and manipulated under air-free conditions, using either a Vacuum Atmospheres drybox or standard Schlenk techniques under a dry nitrogen or argon atmosphere. Anhydrous solvents were obtained using a commercial solvent purification system from JC Meyer Solvent Systems.

The compounds n-butyllithium, 2,6-dibromopyridine, ethylamine, diethylamine, NaO^{t}Bu, di(1-adamantyl)-2-dimethylaminophenylphosphine (98%), $Pd(PPh_3)_4$, and $[Pd(C_3H_5)Cl]_2$ were purchased from Sigma Aldrich and used without further purification. $Fe(CF_3SO_3)_2$ was purchased from Wako, stored in a nitrogen-filled glovebox, and used without further purification. 2-Chloro-6-(tributylstannyl)pyridine (Oakwood), and 6-fluoro-6′-methoxy-2,2′-bipyridine (Bepharm) were purchased from other sources and used as received. Compounds 1,1-bis(pyridyl)ethane,[21] bpyPY2Me,[75] and $Mn(CF_3SO_3)_2{\cdot}2CH_3CN$[76] were prepared according to literature procedures.

NMR spectra were obtained using a Bruker AVANCE III instrument and referenced relative to tetramethylsilane using residual solvent signals. Deuterated solvents were purchased from Cambridge Isotopes. $CDCl_3$ (99.8% D) was treated with anhydrous K_2CO_3. CD_3CN (99.8% D) was dried over powdered 3 Å molecular sieves for 48 h, separated from the sieves by vacuum transfer, deoxygenated by freeze-pump-thaw cycles, and stored over beads of 3 Å molecular sieves under an inert atmosphere.

Electrospray ionization mass spectrometry (ESI-MS) measurements were performed using an Agilent 6230 time-of-flight mass spectrometer equipped with an Agilent Jet Stream source. Carbon, hydrogen, and nitrogen analyses were obtained from the Microanalytical Laboratory at the University of California, Berkeley. Magnetic susceptibility measurements were made using the Evans' method[77] with an NMR tube containing the paramagnetic compound with one drop of hexamethyldisiloxane in CD_3CN was fitted with an insert containing the same solvent without the paramagnetic compound. The paramagnetic shift of the hexamethyldisiloxane signal was used to calculate the room temperature solution magnetic moment.

3.2.2. Synthesis

bpy^{OMe}PY2Me. A 50 mL Schlenk flask equipped with a stir bar was charged with 1,1-bis(pyridyl)ethane (1.81g, 9.80 mmol) and 50 mL of THF, then cooled to −78 °C. The solution was vigorously stirred while ^{n}BuLi (2.5M in hexanes, 3.9 mL, 9.8 mmol) was added via syringe in a dropwise fashion. The resulting dark red solution was allowed to stir at −78 °C for 1 h, after which a solution of 6-fluoro-6′-methoxy-2,2′-bipyridine (1.00 g, 4.90 mmol) in 10 mL of THF was introduced using a cannula. After the transfer was complete, the reaction was refluxed for 12 h. The reaction was quenched with 100 mL of saturated aqueous NH_4Cl, and the workup was performed in air. The aqueous phase was separated and extracted with 4 × 50 mL of EtOAc. The organics were combined, dried over $MgSO_4$, filtered, and concentrated yielding a brown oil by rotary evaporation. Flash chromatography (silica, 3:1 to 1:1 hexanes:EtOAc, R_f = 0.29 in 1:1 hexanes:EtOAc) followed by recrystallization from hot Et_2O afforded the product as colorless crystals (2.67 g, 74%). ^{1}H NMR (500 MHz, $CDCl_3$) δ 8.60 (ddd, *J* = 4.9, 2.0, 0.9 Hz, 2H), 8.25 (dd, *J* = 7.8, 1.0 Hz, 1H), 7.79 (dd, *J* = 7.5, 0.9 Hz, 1H), 7.71 (t, *J* = 7.8 Hz, 1H), 7.62 – 7.53 (m, 3H), 7.17 – 7.07 (m, 5H), 6.71 (dd, *J* = 8.2, 0.8 Hz, 1H), 4.02 (s, 3H), 2.41 (s, 3H). ^{13}C NMR (126 MHz, $CDCl_3$) δ 166.4, 164.8, 163.5, 154.7, 154.0, 148.9, 139.3, 136.9, 135.9, 123.8, 123.5, 121.3, 118.4, 114.1, 110.8, 60.5, 53.3, 27.4. ESI-MS *m/z* for $[C_{23}H_{20}N_4O + H]^+$ requires 369.1710, found 369.1732. Anal. Calcd. for $C_{23}H_{20}N_4O$: C, 74.98; H, 5.47; N, 15.21. Found: C, 74.74; H, 5.58; N, 15.12.

bpy^{OH}PY2Me. A 100 mL round-bottomed flask was charged with bpy^{OMe}PY2Me (906 mg, 2.47 mmol), HBr (12 mL), and acetic acid (12 mL), then heated to reflux for 4 h, resulting in a clear, tan-colored solution. The reaction was allowed to cool to room temperature, then quenched with excess saturated aqueous $NaHCO_3$ solution (100 mL) and excess Na_2CO_3 until the pH reached ~9. The aqueous phase was extracted with 3 × 100 mL of CH_2Cl_2. The organic extracts were combined, dried over $MgSO_4$, filtered, and concentrated to yield a yellow oil by rotary evaporation. The oil was triturated with ~30 mL of hexanes and dried under reduced pressure first via rotary evaporation followed by high vacuum to give an off-white, powdery solid (828 mg, 95%). ^{1}H NMR (600 MHz, CD_3OD) δ 8.52 (d, *J* = 4.7 Hz, 2H), 7.96 (d, *J* = 7.9 Hz, 1H), 7.88 (t, *J* = 7.9 Hz, 1H), 7.77 (t, *J* = 7.8 Hz, 2H), 7.73 – 7.67 (m, 1H), 7.38 – 7.27 (m, 3H), 7.18 (d, *J* = 8.1 Hz, 3H), 6.59 (d, *J* = 9.1 Hz, 1H), 2.39 (s, 3H). ^{13}C NMR (151 MHz, CD_3OD) δ 166.5, 166.4, 165.0, 149.7, 147.7, 143.8, 143.6, 139.3, 138.2, 126.6, 125.0, 123.2, 121.3, 119.5, 106.0, 61.3, 27.6. ESI-MS *m/z* for $[C_{22}H_{18}N_4O + H]^+$ requires 355.1553, found 355.1552. Anal. Calcd. for $C_{22}H_{18}N_4O$: C, 74.56; H, 5.12; N, 15.81. Found: C, 74.71; H, 5.22; N, 15.43.

2,2′-(1-(6-Bromopyridin-2-yl)ethane-1,1-diyl)dipyridine. This compound was previously prepared using a two-step, one-pot reaction starting from 2-fluoropyridine.[78] A 100 mL Schenk flask equipped with a stir bar was charged with 1,1-bis(pyridyl)ethane (3.73 g, 20.2 mmol) and 50 mL of THF, then cooled to −78 °C. The solution was vigorously stirred while ^{n}BuLi (2.5M in hexanes, 8.1 mL, 20 mmol) was added via syringe in a dropwise fashion. The resulting dark red solution was allowed to stir at −78 °C for 1 h, after which it was transferred via cannula into a solution of 2,6-dibromopyridine (9.57 g, 40.4 mmol) in 100 mL of THF cooled to −78 °C. After the transfer was complete, the reaction was allowed to warm to room temperature and stirred for 24 h. The reaction was subsequently quenched with 100 mL of saturated aqueous NH_4Cl, and the workup was performed in air. The aqueous phase was separated and extracted with 4 × 50 mL of EtOAc. The organics were combined, dried over $MgSO_4$, filtered, and concentrated to a brown oil by rotary evaporation. The product was obtained as an orange oil after flash chromatography (silica, 1:1 hexanes:EtOAc, $R_f = 0.25$) and solvent removal under reduced pressure. The oil was then triturated with hexanes, stored at −30 °C for 1.5 h, and dried under high vacuum at room temperature to yield the product as an off-white solid (5.32 g, 77%). ^{1}H NMR (500 MHz, $CDCl_3$) δ 8.58 (d, *J* = 4.6 Hz, 2H), 7.60 (t, *J* = 7.8 Hz, 2H), 7.42 (t, *J* = 7.8 Hz, 1H), 7.31 (d, *J* = 7.9 Hz, 1H), 7.14 (t, *J* = 6.2 Hz, 2H), 7.10 – 7.03 (m, 3H), 2.30 (s, 3H). ^{13}C NMR (126 MHz, $CDCl_3$) δ 167.1, 165.5, 149.0, 141.0, 138.2, 136.3, 125.9, 123.5, 123.1, 121.6, 60.2, 27.3. ESI-MS *m/z* for $[C_{17}H_{14}BrN_3 + H]^+$ requires 340.0444, found 340.0449. Anal. Calcd. for $C_{17}H_{14}BrN_3$: C, 60.02; H, 4.15; N, 12.35. Found: C, 60.15; H, 4.20; N, 12.13.

bpy^{Cl}PY2Me. A 100 mL Schlenk flask equipped with a stir bar was charged with 2,2′-(1-(6-bromopyridin-2-yl)ethane-1,1-diyl)dipyridine (2.11 g, 6.21 mmol), 2-chloro-6-(tributylstannyl)pyridine (3.00 g, 7.45 mmol), $Pd(PPh_3)_4$ (359 mg, 310 μmol) and *m*-xylene (60 mL). The reaction mixture was refluxed for 30 h, then allowed to cool to room temperature before quenching with 200 mL of 10% (w/w) aqueous KF. Subsequent workup was performed in air. The aqueous phase was extracted with 3 × 150 mL of EtOAc. The combined organic phases were dried over $MgSO_4$, filtered, and concentrated to a yellow oil by rotary evaporation. Purification by flash chromatography (silica, 1:1 hexanes:EtOAc, $R_f = 0.23$) followed by rotary evaporation and drying under high vacuum at 40 °C for 8 h afforded the product as an off-white, sticky solid (1.12 g, 55%).

^{1}H NMR (500 MHz, $CDCl_3$) δ 8.61 (d, *J* = 4.8 Hz, 2H), 8.26 (d, *J* = 7.7 Hz, 1H), 8.10 (d, *J* = 7.7 Hz, 1H), 7.72 (t, *J* = 7.8 Hz, 1H), 7.61 (dt, *J* = 31.4, 7.6 Hz, 3H), 7.28 (s, 1H), 7.21 – 7.06 (m, 6H), 2.41 (s, 3H). ^{13}C NMR (126 MHz, $CDCl_3$) δ 166.1, 165.1, 157.4, 153.2, 150.8, 148.9, 139.4, 137.2, 136.1, 124.4, 124.0, 123.7, 121.4, 119.7, 118.9, 60.5, 27.4. ESI-MS *m/z* for $[C_{22}H_{17}ClN_4 + H]^+$ requires 373.1215, found 373.1216. Anal. Calcd. for $C_{22}H_{17}ClN_4$: C, 70.87; H, 4.60; N, 15.03. Found: C, 71.13; H, 4.87; N, 14.64.

bpy^{NHEt}PY2Me. A 50 mL Schlenk flask equipped with a stir bar was charged with bpy^{Cl}PY2Me (899 mg, 2.41mmol), NaO^{t}Bu (348 mg, 3.63 mmol), $[Pd(C_3H_5)Cl]_2$ (4.4 mg, 12 μmol), di(1-adamantyl)-2-dimethylaminophenylphosphine (10. mg, 24 μmol), and toluene (10 mL). Ethylamine was condensed into a separate Schlenk tube cooled with liquid N_2, then ~4 mL of diethylamine (~70 mmol) was transferred to the reaction mixture via cannula. The reaction was heated to 100 °C for 12 h, then allowed to cool to room temperature before quenching with 100 mL of aqueous 1 M HCl. Subsequent workup was conducted in air. The aqueous phase was first extracted with 3 × 100 mL of CH_2Cl_2 to remove unwanted byproducts and excess reagents. The aqueous phase was basified with KOH until the pH was ~10 and then extracted with 3 × 100 mL of Et_2O. The combined organics were dried over $MgSO_4$, filtered, and concentrated to ~50 mL by rotary evaporation. Addition of hexanes (200 mL) and storage at −30 °C for 8 h afforded colorless crystals, which were isolated and dried under high vacuum at 40 °C for 8 h to give the product as a white, crystalline solid (651 mg, 71%). ^{1}H NMR (500 MHz, $CDCl_3$) δ 8.59 (d, *J* = 4.9 Hz, 2H), 8.19 (d, *J* = 7.9 Hz, 1H), 7.68 (t, *J* = 7.8 Hz, 1H), 7.56 (t, *J* = 7.8 Hz, 2H), 7.52 – 7.42 (m, 2H), 7.11 (dt, *J* = 11.6, 6.6 Hz, 5H), 6.37 (d, *J* = 8.0 Hz, 1H), 4.49 (br, 1H), 3.41 – 3.34 (m, 2H), 2.41 (s, 3H), 1.28 (t, *J* = 7.1 Hz, 3H). ^{13}C NMR (126 MHz, $CDCl_3$) δ 166.5, 164.5, 148.8, 138.3, 136.8, 135.9, 123.9, 123.2, 121.2, 118.3, 110.5, 106.8, 100.1, 60.4, 37.1, 27.3, 15.1. ESI-MS *m/z* for $[C_{24}H_{23}N_5 + H]^+$ requires 382.2026, found 382.2032. Anal. Calcd. for $C_{24}H_{23}N_5$: C, 75.56; H, 6.08; N, 18.36. Found: C, 75.51; H, 5.84; N, 18.02.

bpy^{NEt2}PY2Me. A 25 mL Schlenk flask was charged with bpy^{Cl}PY2Me (225 mg, 603 μmol), NaO^{t}Bu (87 mg, 910 μmol), $[Pd(C_3H_5)Cl]_2$ (1 mg, 3 μmol), di(1-adamantyl)-2-dimethylaminophenylphosphine (3 mg, 6 μmol), and toluene (3 mL). Diethylamine (~1 mL, ~10 mmol) was condensed into a Schlenk tube cooled with liquid N_2, then transferred to the reaction mixture via cannula. The reaction was heated to 100 °C for 12 hours, then allowed to cool to room temperature before quenching with 50 mL of aqueous 1 M HCl. Subsequent workup was conducted in air. The aqueous phase was first extracted with 3 × 50 mL of CH_2Cl_2 to remove unwanted byproducts and excess reagents. The aqueous phase was basified with KOH until the pH was ~14 and then extracted with 3 × 50 mL of EtOAc. The combined organics were dried over $MgSO_4$, filtered, and concentrated by rotary evaporation, then further dried at 60 °C for 12 h to afford the product as an oily 0.2 EtOAc solvate as determined by ^{1}H NMR and elemental analysis (228 mg, 88%). ^{1}H NMR (500 MHz, $CDCl_3$) δ 8.61 (d, *J* = 4.9 Hz, 2H), 8.23 (d, *J* = 7.9 Hz, 1H), 7.69 (t, *J* = 7.8 Hz, 1H), 7.58 (t, *J* = 7.7 Hz, 2H), 7.43 (s, 1H), 7.13 (q, *J* = 7.4, 6.8 Hz, 6H), 6.46 (d, *J* = 7.6 Hz, 1H), 4.12 (EtOAc), 3.58 (q, *J* = 7.1 Hz, 4H), 2.43 (s, 3H), 2.05 (EtOAc), 1.25 (EtOAc), 1.21 (t, *J* = 7.1 Hz, 6H). ^{13}C NMR (126 MHz, $CDCl_3$) δ 166.3, 164.0, 156.9, 155.9, 154.3, 148.6, 137.9, 136.9, 136.2, 124.1, 122.8, 121.3, 118.3, 108.4, 105.8, 60.3, 42.8, 27.3, 13.1. ESI-MS *m/z* for $[C_{26}H_{27}N_5 + H]^+$ requires 410.2339, found 410.2342. Anal. Calcd. for $C_{26}H_{27}N_5 \cdot 0.2C_4H_8O$: C, 75.36; H, 6.75; N, 16.40. Found: C, 75.78; H, 6.74; N, 15.97.

General synthetic procedure for iron complexes. Equimolar quantities of $Fe(CF_3SO_3)_2$ and ligand were vigorously stirred in ~5 mL of acetonitrile for 12 h, affording dark red (**1**-**3**) or orange (**4** and **5**) solutions. The solutions were subsequently filtered through diatomaceous earth (Celite®

545). Layering of the filtrate with ~15 mL of diethyl ether afforded crystals of the iron complex, which were washed with three ~3-mL aliquots of diethyl ether and dried under reduced pressure until a constant weight was achieved.

[(bpyPY2Me)Fe(CH$_3$CN)$_2$](CF$_3$SO$_3$)$_2$ (3.1). bpyPY2Me (300 mg, 887 μmol) and Fe(CF$_3$SO$_3$)$_2$ (314 mg, 887 μmol) afforded red crystals, which became a red powder after drying (663 mg, 97%). ^{1}H NMR (600 MHz, CD$_3$CN) δ 9.53 (d, *J* = 5.6 Hz, 1H), 9.22 (d, *J* = 5.7 Hz, 2H), 8.37 (d, *J* = 8.0 Hz, 1H), 8.23 (d, *J* = 7.9 Hz, 1H), 8.17 (dtd, *J* = 7.8, 4.8, 2.5 Hz, 2H), 8.01 – 7.85 (m, 5H), 7.80 – 7.72 (m, 1H), 7.37 (s, 2H), 2.76 (s, 3H). ESI-MS *m*/*z* for [(bpyPY2Me)Fe]$^{2+}$ requires 196.0458, found 196.0450. Anal. Calcd. for $C_{28}H_{24}F_6FeN_6O_6S_2$: C, 43.42; H, 3.12; N, 10.85. Found: C, 43.47; H, 2.89; N, 10.85. UV-vis (CH$_3$CN): λ_{max} (ε_M, M^{-1} cm^{-1}) 250 (2.4×10^3), 303 (2.2×10^3), 394 (4800), 483 (3500) nm.

[(bpy^{OH}PY2Me)Fe(CH$_3$CN)$_2$](CF$_3$SO$_3$)$_2$ (3.2). bpy^{OH}PY2Me (150 mg, 423 μmol) and Fe(CF$_3$SO$_3$)$_2$ (150 mg, 423 μmol) afforded dark brown crystals, which gave a red powder after drying (230 mg, 69%). ^{1}H NMR (600 MHz, CD$_3$CN) δ 10.38 (s, 1H), 9.52 (s, 2H), 8.27 (d, *J* = 7.9 Hz, 1H), 8.16 (t, *J* = 7.9 Hz, 1H), 8.07 – 8.01 (m, 2H), 7.99 (d, *J* = 8.2 Hz, 2H), 7.96 – 7.85 (m, 3H), 7.42 (t, *J* = 6.6 Hz, 2H), 7.19 (d, *J* = 8.4 Hz, 1H), 2.79 (s, 3H). ESI-MS *m*/*z* for [(bpy^{OH}PY2Me)Fe]$^{2+}$ requires 204.0433, found 204.0417. Anal. Calcd. for $C_{28}H_{24}F_6FeN_6O_7S_2$: C, 42.54; H, 3.06; N, 10.63. Found: C, 42.59; H, 2.90; N, 10.41. UV-vis (CH$_3$CN): λ_{max} (ε_M, M^{-1} cm^{-1}) 320 (2.4×10^3), 350 (5100), 400 (4000), 471 (3000) nm.

[(bpy^{OMe}PY2Me)Fe(CH$_3$CN)$_2$](CF$_3$SO$_3$)$_2$ (3.3). bpy^{OMe}PY2Me (150 mg, 407 μmol) and Fe(CF$_3$SO$_3$)$_2$ (144 mg, 407 μmol) afforded dark red crystals, which became a red powder after drying (272 mg, 83%). ^{1}H NMR (600 MHz, CD$_3$CN) δ 9.58 (s, 2H), 8.43 (d, *J* = 7.8 Hz, 1H), 8.23 – 8.13 (m, 3H), 8.08 (t, *J* = 7.8 Hz, 3H), 7.88 (t, *J* = 7.8 Hz, 2H), 7.48 (t, *J* = 6.5 Hz, 2H), 7.39 (d, *J* = 8.6 Hz, 1H), 4.31 (s, 3H), 2.82 (s, 3H). ESI-MS *m*/*z* for [(bpy^{OMe}PY2Me)Fe]$^{2+}$ requires 211.0511, found 211.0501. Anal. Calcd. for $C_{29}H_{26}F_6FeN_6O_7S_2$: C, 43.30; H, 3.26; N, 10.45. Found: C, 42.89; H, 2.99; N, 9.93. UV-vis (CH$_3$CN): λ_{max} (ε_M, M^{-1} cm^{-1}) 318 (2.3×10^3), 350 (5000), 399 (4100), 473 (3200) nm.

[(bpy^{NHEt}PY2Me)Fe(CF$_3$SO$_3$)$_2$] (3.4). bpy^{NHEt}PY2Me (153 mg, 401 μmol) and Fe(CF$_3$SO$_3$)$_2$ (142 mg, 401 μmol) initially afforded brown crystals, which gave an orange powder after drying (282 mg, 96%). ESI-MS *m*/*z* for [(bpy^{NHEt}PY2Me)Fe(CH$_3$CN)]$^{2+}$ requires 238.0804, found 238.0802. Anal. Calcd. for $C_{26}H_{23}F_6FeN_5O_6S_2$: C, 42.46; H, 3.15; N, 9.52. Found: C, 42.67; H, 3.11; N, 9.49. Effective magnetic moment (CD$_3$CN, 298 K): μ_{eff} = 1.4 μ_B. UV-vis (CH$_3$CN): λ_{max} (ε_M, M^{-1} cm^{-1}) 223 (4.4×10^3), 250 (2.3×10^3), 351 (1.2×10^3), 359 (1.1×10^3), 418 (3800), 460 (3300) nm.

[(bpy^{NEt2}PY2Me)Fe(CF$_3$SO$_3$)$_2$] (3.5). bpy^{NEt2}PY2Me (199 mg, 486 μmol) and Fe(CF$_3$SO$_3$)$_2$ (172 mg, 486 μmol) afforded yellow-orange crystals. Drying under vacuum at 80°C for two hours afforded an orange powder that is the product as a 0.25 CH$_3$CN, 0.25 Et$_2$O solvate (337 mg, 88%). ESI-MS *m*/*z* for [(bpy^{NEt2}PY2Me)Fe]$^{2+}$ requires 232.5843, found 232.5826. Anal. Calcd. for $C_{28}H_{27}F_6FeN_5O_6S_2 \cdot 0.25C_2H_3N \cdot 0.25C_4H_{10}O$: C, 44.72; H, 3.85; N, 9.28. Found: C, 44.58; H, 3.58; N, 9.54. Effective magnetic moment (CD$_3$CN, 298 K): μ_{eff} = 5.1 μ_B. UV-vis (CH$_3$CN): λ_{max} (ε_M, M^{-1} cm^{-1}) 230 (3.0×10^3), 258 (2.2×10^3), 377 (7000), 490 (750) nm.

[(bpy^{NHEt}PY2Me)Mn(CF$_3$SO$_3$)$_2$] (3.6). A 20 mL vial equipped with a stir bar was charged with bpy^{NHEt}PY2Me (136 mg, 357 μmol), Mn(CF$_3$SO$_3$)$_2$·2CH$_3$CN (155 mg, 357 μmol), and CH$_3$CN (4 mL). The reaction mixture was stirred at room temperature for 12 h to give a clear yellow solution, which was then filtered through Celite. The Celite was washed with 3 × 1 mL of CH$_3$CN. The combined filtrate was concentrated to ~4 mL, layered with ~16 mL of Et$_2$O, then allowed to stand at room temperature for three days to afford yellow crystals. The crystals were separated from the mother liquor, washed with 3 × 3 mL of Et_2O, and dried under vacuum at 80 °C for 2 h to afford the titular compound as a yellow powder (208 mg, 79%). ESI-MS *m/z* for $[(bpy^{NHEt}PY2Me)Mn]^{2+}$ requires 218.0661, found 218.0659. Anal. Calcd. for $C_{26}H_{23}F_6MnN_5O_6S_2$: C, 42.51; H, 3.16; N, 9.53. Found: C, 42.66; H, 2.86; N, 9.51. Yellow block-shaped crystals suitable for X-ray diffraction analysis were obtained from a slow diffusion of Et_2O into a CH_3CN solution of the title compound. Effective magnetic moment (CD_3CN, 298 K): $\mu_{eff} = 5.8\ \mu_B$. UV-vis (CH_3CN): λ_{max} (ε_M, $M^{-1}\ cm^{-1}$) 263 (1.4×10^3), 367 (8600) nm.

3.2.3. Crystal Structure Determinations

Slow diffusion of diethyl ether into acetonitrile solutions of compounds **3.1**–**6** afforded single crystals suitable for X-ray diffraction analysis. Data collection was performed on single crystals coated with Paratone-N oil and mounted on Kaptan loops. The crystals of **3.1**–**5** were cooled under a stream of N_2 (100 K; Oxford Cryostream 700) during measurements. Data collection for **3.6** was performed at 250 K because its crystals fractured when cooled to 100 K. Data were collected using a Bruker APEX II QUAZAR diffractometer equipped with a Microfocus Sealed Source (Incoatec IμS; Mo-K_α $\lambda = 0.71073$ Å) and APEX-II detector. Raw data were integrated and corrected for Lorentz and polarization effects using Bruker APEX2.[79] Absorption corrections were applied using SADABS.[80] Space group assignments were determined by examination of systematic absences, E-statistics, and successive refinement of the structures. Structures were solved using SHELXT[81] and all non-hydrogen atoms were refined anisotropically by full-matrix least-squares (SHELXL).[82,83] Carbon-bound hydrogen atoms were inserted at idealized positions and refined isotropically using a riding model with the appropriate HFIX command in SHELXL.

In the structure of **3.5**, the coordinated trifluoromethanesulfonate anion was found to be disordered over two orientations, with an occupancy ratio of 73/27. Bond distances of the trifluoromethanesulfonate were restrained with the SADI command. The anisotropic refinement of the disordered trifluoromethanesulfonate anions were restrained using the RIGU and SIMU commands. In addition, electron density was located near an edge of the unit cell. This was attributed to disordered solvent. Attempts to model the disorder were unsuccessful. As such, a solvent mask was applied to account for the unassigned electron density.[84]

In the structure of **3.6**, the ethyl group of the complex was disordered over two positions, with an occupancy ratio of 64/36. Also, one of the coordinated trifluoromethanesulfonate anions was found to be disordered over two orientations, with an occupancy ratio of 75/25. The disorder was addressed in a similar fashion as described above, using SADI, RIGU, and SIMU restraints. In addition, the higher collection temperature for **3.6** necessitated a RIGU restraint on the bipyridine ring.

The phenolic hydrogen atom in the structure of **3.2** was inserted with the HFIX 147 command. The nitrogen-bound hydrogen atoms in the structures of **3.4** and **3.6** were located in the Fourier difference map and refined freely.

3.2.4. Electrochemical Methods

Electrochemical measurements were performed with acetonitrile (EMD Millipore, OmniSolv Gradient grade) and water (18.2 MΩ·cm, Milli-Q Millipore). NBu_4PF_6 (Oakwood Chemical) was recrystallized from ethanol/water and dried under vacuum at 100°C for 24 hours before use. Cyclic voltammetry measurements were obtained with 1 mM of complex in anhydrous CH_3CN using a glassy carbon disk (3.0 mm dia.) working electrode, a Ag/AgNO$_3$ (0.1 mM) reference electrode, and a graphite counter electrode with 0.1 M NBu$_4$PF$_6$ as supporting electrolyte.

Controlled-potential electrolyses were performed in a custom H-cell (Adams and Chittenden). The working electrode was glassy carbon plate (Tokai) with an area of ~6 cm^2, and the auxiliary electrode was a carbon cloth (Fuel Cell Earth) cut to ~225 cm^2. Electrical contact between the electrodes and wires were made using silver epoxy (Chemtronics CW2400), which was then sealed into a borosilicate glass tube with epoxy (Agilent TorrSeal) to avoid exposure of the underlying conductive epoxy or bare wire. A Ag/AgNO$_3$ (0.1 mM) nonaqueous reference electrode was used, which was referenced against the Fe(C$_5$H$_5$)$_2^{+/0}$ couple after every experiment (E[Fe(C$_5$H$_5$)$_2^{+/0}$] = +0.16(1) V versus Ag/AgNO$_3$). The cathodic and anodic compartments of the H-cell were separated with a glass frit, and each filled with 70 mL of a 0.1 M NBu$_4$PF$_6$ solution of acetonitrile with 11 M of added water. The electrolyte was deaerated by sparging CO$_2$ (4.8 grade, Praxair), after which a 2 mL aliquot of stock solution (8.75 mM) of catalyst was introduced via a gas-tight syringe to attain a final catalyst concentration of 240 µM. The cell was then sealed to allow a constant infusion of gaseous CO$_2$ into the liquid electrolyte. The headspace was permitted to flow into a mass-flow controller at 10 ± 0.1 sccm, and subsequently into an Agilent 490 MicroGC for analysis. The MicroGC was calibrated for simultaneous detection of H$_2$, CO, and CH$_4$. Aqueous electrolyses were performed in a similar manner, with 0.1 M KCl$_{(aq)}$ (Fisher, 99.5%), 0.1 M KPF$_{6(aq)}$ (Alfa Aesar, 99%), or 0.1 M K$_2$CO$_{3(aq)}$ (Sigma 99.995%), solutions as the electrolyte, a Ag/AgCl reference electrode, and a Selemion anion exchange membrane as the separator. Each electrolysis experiment was performed in quadruplicate.

3.2.5. ^{1}H NMR Analysis of Electrolysis Solutions

Our protocol for ^{1}H NMR analysis of liquid CO$_2$ reduction products in the electrolyte solution derives from one used by Kang and coworkers.[85] After electrolysis, a 1500 µL aliquot of the electrolyte solution was taken and to it was added 750 µL of CD$_3$CN and 25 µL of concentrated aqueous HCl (38% by weight). The acid was added to liberate any formate from the Fe ion that may have formed during electrolysis. In all cases, no resonances attributable to formic acid, formaldehyde, or methanol were observed in the ^{1}H NMR. Resonances were observed for the $^+$NBu$_4$ cation, as well as polypyridine resonances resulting from the acidic workup.

3.2.6. Electrochemical Characterization of Electrode Post-Electrolysis

After a 12 h electrolysis of **3.4** in CO$_2$-saturated acetonitrile with 11 M water, the electrolyte solution in the working electrode compartment was removed using a cannula, while keeping the electrolysis cell under an atmosphere of argon. The working electrode and cell chamber were washed with anhydrous, deaerated acetonitrile (3 × ~70 mL) to remove traces of the original electrolyte solution. Electrochemical characterization of the electrode was subsequently performed on a fresh batch of degassed electrolyte solution, which was introduced with a cannula.

3.2.7. SEM and EDX Analysis of Electrode Post-Electrolysis

After a 12 h electrolysis of **3.4** in CO$_2$-saturated acetonitrile with 11 M water, the electrolysis cell was disassembled. The glassy carbon working electrode was gently rinsed with 3 × ~1 mL of CH$_3$CN and then imaged by scanning electron microscopy (SEM). SEM images were taken using a Zeiss Ultra 55 SEM at 15 kV. Chemical characterization of the surface was performed using energy-dispersive X-ray spectroscopy (EDX) using a Bruker Nano XFlash Detector 5030.

3.3. Results and Discussion

3.3.1. Design Elements and Synthesis of Functionalized Ligand Set

We previously demonstrated the utility of multidentate, polypyridine ligand scaffolds in stabilizing highly active and water-compatible electrocatalysts for proton reduction using earth-abundant transition metal elements such as molybdenum[86-89] and cobalt.[67,75,90-94] For the current study, we were particularly interested in the functionalization of complexes stabilized by the tetradentate ligand 6-(1,1-di(pyridin-2-yl)ethyl)-2,2′-bipyridine (bpyPY2Me), because of the reported favorable electrochemical potentials of metal-centered reduction events[75] and the presence of the bpy-based redox-reservoir. To incorporate an acidic proton into the second coordination sphere, we synthesized the ligand $\text{bpy}^{\text{OH}}\text{PY2Me}$, which features an OH group in 6-position of the bipyridine moiety. Because the oxygen lone pair is partially delocalized into the bipyridine rings, this ligand is more electron-rich than the bpyPY2Me parent ligand. Thus, to control for electronic effects in the first coordination sphere, we also synthesized $\text{bpy}^{\text{OMe}}\text{PY2Me}$, which is devoid of the phenolic proton. Of relevance here are the Hammett constants, σ_p, of the OMe and OH groups are −0.27 and −0.37, versus 0.00 for H.[95] Finally, as a means of evaluating the effect of proton acidity on catalysis we synthesized $\text{bpy}^{\text{NHEt}}\text{PY2Me}$, which features a less acidic N–H proton in place of the O–H proton in $\text{bpy}^{\text{OH}}\text{PY2Me}$**.** For reference the pK_a values of 2-aminopyridine and 2-pyridone in dimethylsulfoxide are 27.7 and 17.0, respectively.[96] For use in control experiments, we also synthesized the reference ligand $\text{bpy}^{\text{NEt2}}\text{PY2Me}$, wherein the aniline proton of $\text{bpy}^{\text{NHEt}}\text{PY2Me}$ is replaced with a second ethyl group. Here, the σ_p constants for the shorter alkylamine derivatives NHMe and NMe_2 are −0.70 and −0.83, respectively.[95]

3.3.2. Synthesis and Characterization of Tetrapyridyl Complexes

Metalation of this series of ligands proceeds smoothly with use of $Fe(CF_3SO_3)_2$ in acetonitrile (Scheme 3.2). Adding it to solutions of ligands resulted in a rapid color change from pale yellow to dark red or orange. The resulting solutions were purified via filtration through a short Celite® column and subsequently layered with diethyl ether. Diffusion of the ether into the acetonitrile solutions over the course of 1 to 2 days afforded crystalline forms of $[(\text{bpyPY2Me})\text{Fe}(CH_3CN)_2](CF_3SO_3)_2$ (**3.1**), $[(\text{bpy}^{\text{OH}}\text{PY2Me})\text{Fe}(CH_3CN)_2](CF_3SO_3)_2$ (**3.2**), $[(\text{bpy}^{\text{OMe}}\text{PY2Me})\text{Fe}(CH_3CN)_2](CF_3SO_3)_2$ (**3.3**), $[(\text{bpy}^{\text{NHEt}}\text{PY2Me})\text{Fe}(CF_3SO_3)_2]$ (**3.4**), and $[(\text{bpy}^{\text{NEt2}}\text{PY2Me})\text{Fe}(CF_3SO_3)_2]$ (**3.5**). To probe the critical role of the Fe center in **4** during catalysis (see below), while maintaining the same charge state for the overall complex, we also synthesized a crystalline form of $[(\text{bpy}^{\text{NHEt}}\text{PY2Me})\text{Mn}(CF_3SO_3)_2]$ (**3.6**) by following the same general preparation outlined in Scheme 2.2, starting from $Mn(CF_3SO_3)_2$.

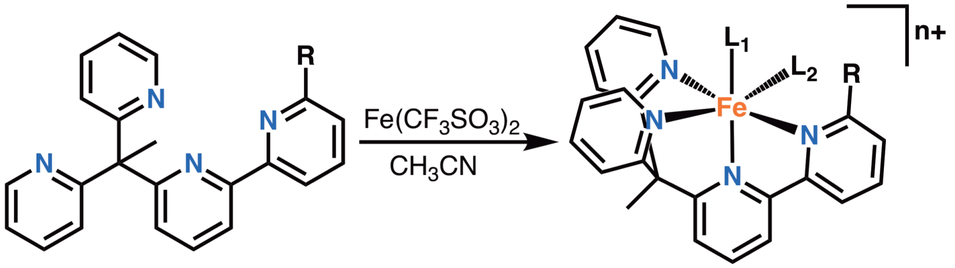

bpyPY2Me R = H
bpy^{OH}PY2Me R = OH
bpy^{OMe}PY2Me R = OMe
bpy^{NHEt}PY2Me R = NHEt
bpy^{NEt2}PY2Me R = NEt_2

1 R = H, $L_1 = L_2 = CH_3CN$, n = 2
2 R = OH, $L_1 = L_2 = CH_3CN$, n = 2
3 R = OMe, $L_1 = L_2 = CH_3CN$, n = 2
4 R = NHEt, $L_1 = L_2 = CF_3SO_3^-$, n = 0
5 R = NEt_2, $L_1 = CH_3CN$, $L_2 = CF_3SO_3^-$, n = 1

Scheme 3.2. Synthesis of [(bpy^{R}PY2Me)Fe(II)]$^{n+}$ complexes. Outer-sphere $CF_3SO_3^-$ anions not shown.

The solid-state structures of compounds **3.1**–**6** were established using single crystal X-ray diffraction analyses (Figures 3.1 and 3.S1, Table 3.S1–2). The divalent metal centers in all six complexes display pseudo-octahedral coordination geometries, wherein four coordination sites are occupied by the tetrapyridyl ligand, thus leaving two open *cis* sites available for coordination by exogenous ligands. Notably, in the cases of **3.4** and **3.6**, which bear the bpy^{NHEt}PY2Me ligand, two of the metal coordination sites are occupied by $CF_3SO_3^-$ anions. For both complexes, the NH protons were located in the Fourier difference map. Their positions suggest the presence of intramolecular hydrogen bonding between the ligand and one of the $CF_3SO_3^-$ anions. This observation showcases the ability of the bpy^{NHEt}PY2Me ligand to stabilize a coordinated anion. For the complexes in **3.1**–**3**, the similar Fe-ligand distances (ranging from 1.903(1) to 2.053(2) Å, see Table **3.**S3) indicate strong similarities of the first coordination spheres in these complexes. Notably, these metal-ligand distances lengthen in **3.4** and **3.5**, ranging from 2.087(1) to 2.249(4) Å, perhaps due to the weaker ligand field imposed by the $CF_3SO_3^-$ anions (versus the coordinated acetonitrile molecules in **3.1**–**3**) and the steric bulk of the pendant alkyl aniline moieties.

To probe the electronic impact of the second coordination sphere functionality on the ferrous ion, we measured the room temperature magnetic susceptibility of each complex in acetonitrile using the Evans method.[77] While compounds **3.1**–**3** are diamagnetic in acetonitrile, the corresponding solution magnetic moment for **3.5** ($\mu_{\mathrm{eff}} = 5.1\ \mu_B$) is consistent with an $S = 2$ ground state. Notably, a much lower value of $\mu_{\mathrm{eff}} = 1.4\ \mu_B$ was obtained for **3.4** and suggests a possible spin transition near room temperature. The solution magnetic moment of $\mu_{\mathrm{eff}} = 5.8\ \mu_B$ for **3.6** is consistent with an $S = 5/2$ Mn(II) center.

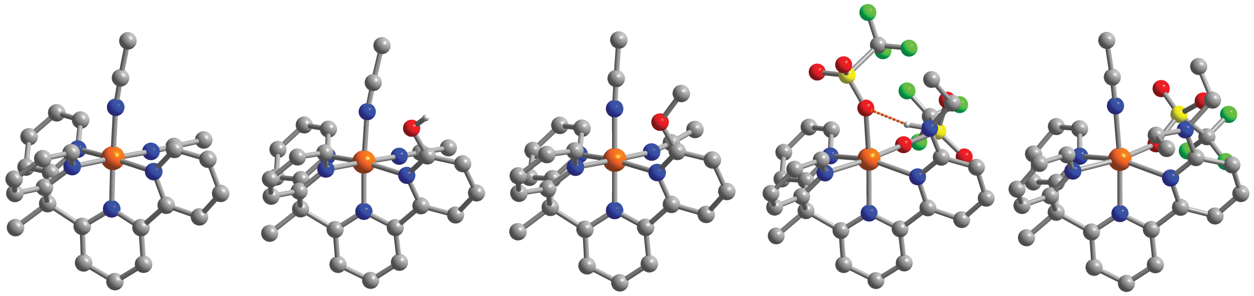

3.1 **3.2** **3.3** **3.4** **3.5**

Figure 3.1. Single crystal X-ray structures of Fe-containing complexes in **3.1**–**5**. Orange, blue, gray, red, yellow, green, and white spheres represent Fe, N, C, O, S, F, and H atoms, respectively. H atoms, except those in the hydroxyl and aniline moieties, are omitted for clarity. Unbound solvent and $CF_3SO_3^-$ molecules are also not shown. The dashed orange line in 3.**4** depicts an intramolecular hydrogen bond.

3.3.3. Cyclic Voltammetry

Cyclic voltammograms (CVs) of compounds **3.1**–**6** were measured under an argon atmosphere in anhydrous acetonitrile to further probe the electronic effects of varying substituents on the bipyridine unit (Figure 3.2). Due to the presence of Fe and a redox-active bipyridyl ligand, the complexes in **3.1**–**5** display rich electrochemistry. For complex **3.1**, which features the parent bipyridine moiety, three redox events are observed between +1.3 V and −2.3 V versus $Fe(C_5H_5)_2^{+/0}$. These redox events are centered at $E_{1/2}$ = +0.81 V, −1.71 V, and –1.86 V. For scan rates (ν) of 50 mV/s to 1000 mV/s, the peak potentials (E_p) of these redox processes are invariant, indicative of fast, reversible electron transfer (Figure 3.S2). Furthermore, the forward and reverse currents display a linear dependence on $\nu^{1/2}$, suggesting these redox processes are diffusion-controlled processes. We attribute the oxidation feature to a metal-centered oxidation from Fe(II) to Fe(III), while the first reductive process is tentatively assigned to arising from predominantly metal-centered reduction of Fe(II) to Fe(I), followed by a second ligand-based reduction from bpy^0 to $bpy^{\bullet-}$ (see below).

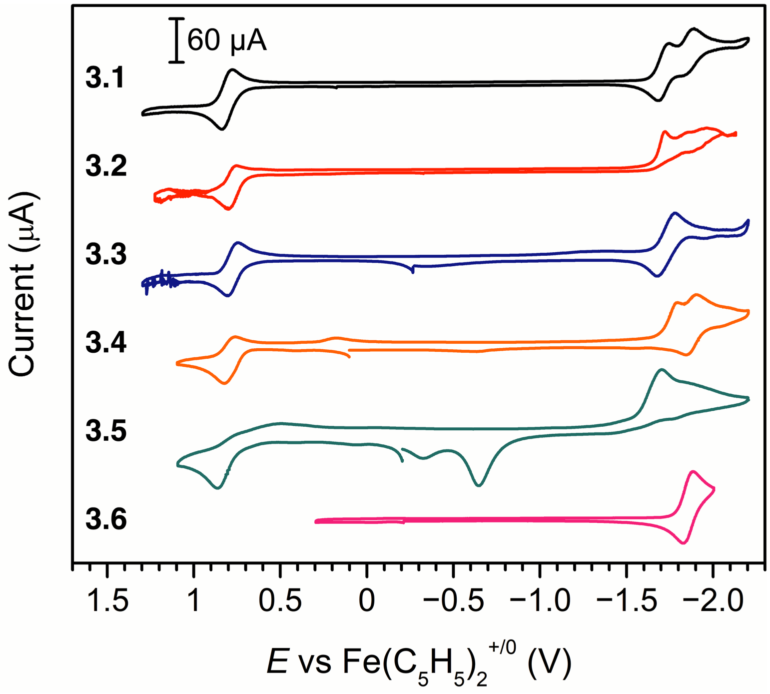

Figure 3.2. Cyclic voltammograms of complexes **3.1**–**6** in argon-saturated acetonitrile solutions with 0.1 M NBu_4PF_6 as supporting electrolyte. All scans were performed at 0.1 V/s.

Incorporation of electron-donating groups at the 6-position of the bipyridine introduces slight cathodic shifts to the potentials of the redox processes and substantially impacts the electrochemical reversibility of those processes. Oxidation waves are observed at +0.78, +0.78, and +0.80 V versus $Fe(C_5H_5)_2^{+/}$ for complexes **3.2**–**4** (Figure 3.2). Of note, the oxidation wave of complex **3.3** appears reversible and diffusion-controlled across all measured scan rates (Figure S4). The oxidation waves of complexes **3.2** and **3.4**, while still diffusion-controlled, exhibit quasi-reversibility involving a slow chemical step, suggesting that the second coordination sphere proton may be chemically involved upon oxidation (Figures 3.S3 and 3.S5).

The impact of substitutions on the reductive processes in this family of compounds is still more complicated. For complexes **3.2** and **3.3**, which both possess substituents containing oxygen atoms, only one reduction feature is apparent at slower scan rates ($\nu \leq 100$ mV/s), occurring at $E_p = -1.72$ V and $E_{1/2} = -1.71$ V, respectively (Figure 3.S3–4). Since this process is irreversible in complex **3.2** and reversible in **3.3**, the OH moiety is again likely to be chemically labile under reducing conditions. An additional broad, quasi-reversible feature centered at −1.87 V is observable when CVs of **3.2** are swept at 250 mV/s $\leq \nu \leq$ 1000 mV/s (Figure S3). At $\nu \geq 250$ mV/s, CVs of **3.3** also display a broad feature apparent at 0 V $\leq E \leq -1$ V (Figure S4) with peak currents that vary linearly with ν, and an increasing peak-to-peak separation at higher scan rates, suggestive of an irreversible, adsorptive process.

Like that of complex **3.1**, the CV of **3.4** at $\nu = 0.1$ V/s exhibit two one-electron reduction events within a narrow 0.2-V window, at −1.79 V and −1.87 V versus $Fe(C_5H_5)_2^{+/0}$ (Figure 3.2). The first reduction event is irreversible, again highlighting the chemical lability of protic groups under reducing potentials. The second reduction process is reversible (Figure 3.S5) and occurs at a potential similar the lone reversible reduction event at −1.85 V observed for **3.6** (Figure 3.2 and 3.S7), which features the bpy$^{\mathrm{NHEt}}$PY2Me ligand and a Mn(II) ion. On this basis, we assign the reduction wave at −1.87 V/−1.85 V for complexes **3.4** and **3.6** to be predominantly ligand-based.

At $\nu \geq 500$ mV/s, CVs of **3.4** show several small features between +0.5 and –0.5 V, which we attribute to possible electroactive intermediates arising from the irreversible oxidation and reduction of **3.4**. In the CV of complex **3.5**, a diffusion-controlled, irreversible oxidation feature is observed at E_{p} = +0.87 V. Return waves are observable at $\nu \geq 500$ mV/s, and occurs at ~+0.7 and ~+0.5 V (Figure 3.S6). Since the peak potentials of the forward and backwards processes are insensitive to changes in scan rate, the irreversibility is chemical in nature. Similar to **3.4**, the first reduction feature of complex **3.5** is diffusion-controlled and irreversible, occurring at −1.71 V. A second irreversible reduction feature occurs at ~−1.9 V is apparent at $\nu \geq 500$ mV/s.

Following this electrochemical characterization in acetonitrile, we sought to evaluate the compatibility of all complexes with the presence of high concentrations of water. The base electrochemical response of compounds **3.1–5** to water was evaluated by collecting CVs under a N_2 atmosphere using an 11 M solution of water in acetonitrile. The complexes exhibited little current buildup at potentials as far negative as −2.2 V versus $Fe(C_5H_5)_2^{+/0}$ (Figure 3.S8), suggesting negligible background reactivity with water under a N_2 atmosphere. Of note, the oxidation waves of complexes **3.1–4** now occur at $E_{1/2}$ = +0.41 V, +0.21 V, +0.35 V, and +0.12 V versus $Fe(C_5H_5)_2^{+/0}$, which are shifted negatively by 0.4 to 0.7 V relative those in pure acetonitrile. This suggests that water has displaced acetonitrile at one or both of the open coordination sites of the Fe(II) ion.

To probe the reactivity towards CO_2, CVs were subsequently recorded after saturating electrolyte solutions with 1 atm of CO_2. For the complexes in **3.1** and **3.3**, which lack acidic protons, reductive current enhancements are observed at onset potentials of approximately −1.6 V versus $Fe(C_5H_5)_2^{+/0}$ (Figures 3.S9 and 3.S10, red traces). The resulting peak currents are approximately five-fold greater than the corresponding one-electron event (Figures 3.S9 and 3.S10, black traces), suggesting a multi-electron process and possibly CO_2 reduction catalysis. Curve crossing occurs in the catalytic CVs of complexes **3.1** and **3.3**. Notably, the presence of CO_2 induces an even greater twelve-fold current enhancement for **4** at −1.91 V versus $Fe(C_5H_5)_2^{+/0}$ (Figure 3.3). The rise in reductive current that occurs for these complexes upon introduction of CO_2 suggests the onset of an electrocatalytic reaction, while the greater current exhibited by **3.4** suggests that the corresponding reaction rate is greater than that of **3.1** or **3.3**. Of note, a small pre-wave at ~−1.6 V precedes the main catalytic wave, suggesting that an electrochemical process occurs prior to the turnover-limiting electrochemical and/or chemical steps. Upon sweeping to more negative potentials, a separate multi-electron wave is observed for complexes **3.1**, **3.3**, and **3.4**, likely due to competing side reactions. In stark contrast to these results, the CV of **3.2** reveals little sensitivity to the presence of CO_2 (Figure 3.S11). Although there is a catalytic wave, it strongly overlaps with the multi-electron feature already observed under N_2, suggesting that the complex may be participating in CO_2-promoted water reduction.[97] Notably, the CV of the tertiary amine-functionalized complex **3.5** exhibits no apparent electrocatalytic activity (Figure 3.S12), further highlighting the importance of the N-H moiety in **3.4** during catalysis.

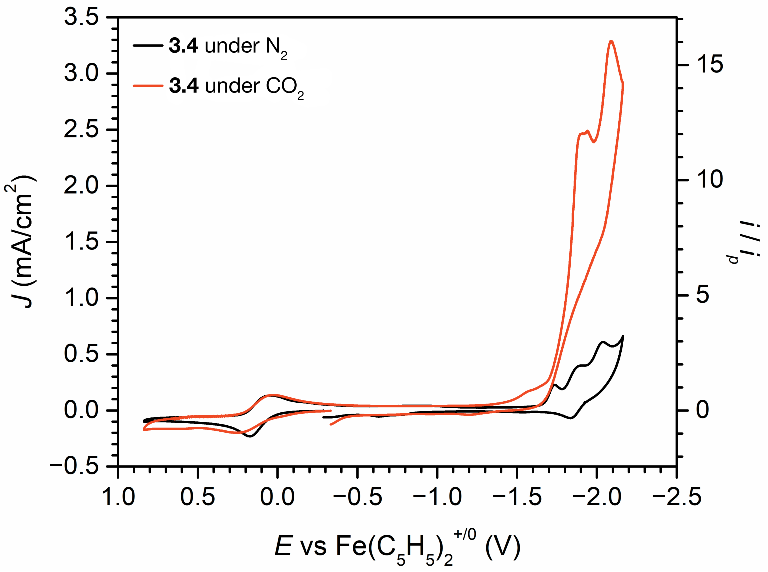

Figure 3.3. CVs of a 1 mM solution of **3.4** in CH_3CN with 11 M H_2O, saturated with 1 atm of N_2 (black) or CO_2 (red). Scans were performed at 0.1 V/s. For i/i_p, the currents are normalized to the peak current i_p of the Fe(III/II) couple.

3.3.4. Controlled-Potential Electrolyses in CO_2-Saturated Wet Acetonitrile

To establish whether the observed current enhancements for **3.1**, **3.3**, and **3.4** could be sustained over multiple catalytic cycles, we next performed controlled-potential electrolysis. Over the course of these experiments, we also used gas chromatography via a flow-cell set up to continuously monitor the composition of the reaction vessel headspace for electrocatalysis products. During catalysis, the cathodic chamber of the two-compartment electrolysis cell was purged with a constant stream of CO_2 and the chamber headspace was directly plumbed into a gas chromatograph and sampled at 10-min intervals. To avoid interference from the second reductive wave while maximizing current densities, electrolyses were performed at a constant potential of −1.91 V versus $Fe(C_5H_5)_2^{+/0}$ for 3 h, corresponding to the peak of the first multi-electron feature of **3.4**. Using a 240 µM solution of **3.4** in acetonitrile, with 11 M of added water, a sustained charge buildup of 37 ± 7 C was observed more than the background reaction from the glassy carbon electrode (Figure 3.4). In contrast, electrolyses in the presence of **3.1** or **3.3** under identical experimental conditions only passed 14.17 ± 0.04 C and 7 ± 1 C, respectively. Furthermore, over the course of the 3-h experiment, the charge accumulation for the latter two complexes slowed dramatically. These findings contrast the CO_2-induced reactivity observed previously on the shorter voltammetry timescale, and underscores the importance of preparative electrolytic data. Unsurprisingly, electrolysis of **3.2**, which did not display CO_2 reduction activity in its CV, accumulated only 5 ± 2 C. The foregoing results demonstrate that the N-H functionalized complex in **3.4** alone can sustain reductive currents at high rates. Complexes lacking an acidic proton, such as in **3.1** and **3.3**, or with a proton that is too acidic, such as in **3.2**, do not catalyze the reduction of CO_2.

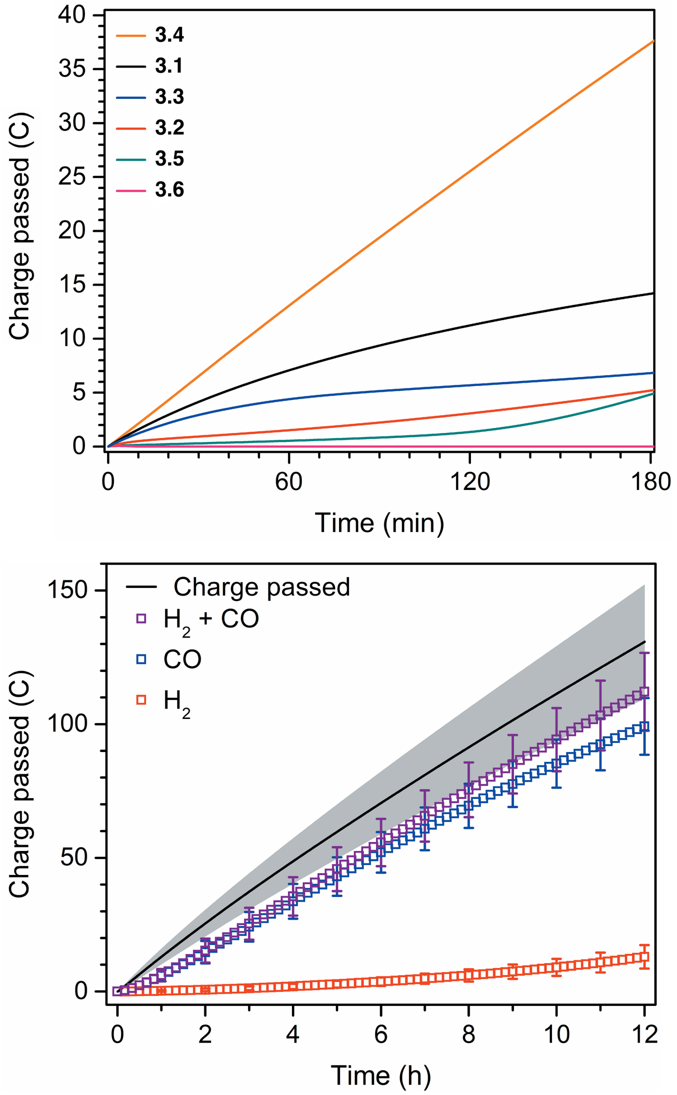

Figure 3.4. Top: Charge buildup during controlled-potential electrolyses of various complexes in CO_2-saturated CH_3CN/H_2O at −1.91 V versus $Fe(C_5H_5)_2^{+/0}$, with 240 µM of catalyst. Bottom: The solid black line and its surrounding gray area indicate the charge passed during electrolysis for **3.4** and the standard deviation. The red, blue, and purple squares correspond to the charge equivalents of GC-detected H_2, CO, and their combined total. Standard deviations for gas detection were calculated at each measurement, but plotted at hourly intervals here for clarity. The activity of the bare glassy carbon electrode has been subtracted from the plotted data.

Importantly, the electrolytic performance of **3.4** is also superior when compared to several control experiments. Compound **3.5**, in which the bipyridine unit of the ligand bears the dialkyl aniline motif, passes only 5 ± 2 C over 3 h. This observation also eliminates the possibility that CO_2 reduction is catalyzed by a protonated anilinium complex of **3.4**. Electrolysis of a solution containing the simple salt $Fe(CF_3SO_3)_2$ under identical conditions displays no charge buildup, indicating that solvated Fe(II) centers without the ligand scaffold, is incapable of catalyzing CO_2 reduction under these conditions (Figure 3.S3). Furthermore, electrolysis of the Mn(II) complex in **3.6**, which possesses the same ligand as **3.4** and similar $bpy^{0/\bullet-}$ redox potentials but lacks the metal-based redox activity, reveals no catalytic activity. Altogether, these results indicate that a conflux of at least two factors is required for catalysis—the redox-active Fe center, ligated by the tetradentate ligand, and the second coordination sphere N-H functional group.

Notably, the electrocatalytic activity of **3.4** could be reproducibly sustained for at least 12 h, and the average charge passed over four trials was found to be 130 ± 21 C (Figure 3.4, bottom). During this period, H_2 and CO were the only gaseous products observed by chromatography, with total faradaic efficiencies of 11 ± 3% and 81 ± 11%, respectively, as determined from the four trials. Over the course of catalysis, the faradaic efficiency of the two gases combined is 92 ± 11%. ^{1}H NMR spectra of the electrolyte solution after acidic workup showed no detectable traces of formic acid, formaldehyde, or methanol. Although the performance of **3.4** was quite good after 12 h, we did not run electrolyses for longer durations because, by this stage, most of the acetonitrile in the bubblers (used to help maintain solvent composition and volume) had evaporated. For this family of iron complexes, complex **3.4** is the most selective for CO_2 reduction to CO (Figure 3.5). Notably, for compound **3.2**, in which the iron complex possesses the more acidic phenol proton in the second coordination sphere, more of the consumed charge is directed towards hydrogen evolution (Figure 3.5).

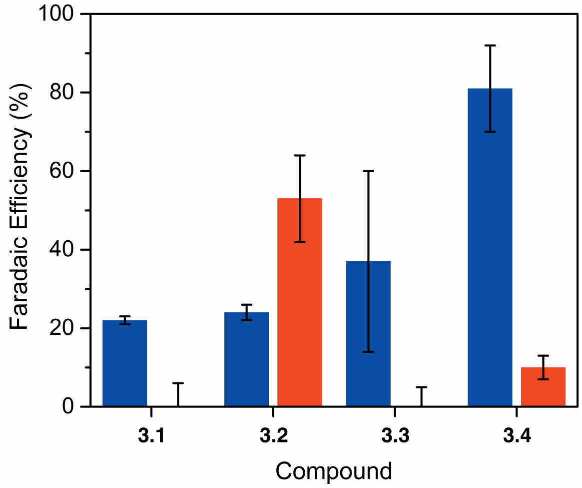

Figure 3.5. Faradaic efficiencies for CO_2 to CO (blue) and water to H_2 (red) conversion obtained during 12-h electrolyses at $E = -1.91$ V for compounds **3.1**–**4**.

To date, **3.4** is the non-heme electrocatalyst that displays the highest selectivity for the reduction of CO_2 to CO. The faradaic efficiencies of various Fe-containing electrocatalysts for CO_2 reduction are summarized in Table 3.S3. The few reported examples of non-heme electrocatalysts for CO_2 reduction typically favor the production of formate (rather than CO). A phenanthroline-based Fe complex was reported to electrocatalytically reduce CO_2 in organic solvents in the presence of weak Brønsted acids in dimethylformamide and dimethylsulfoxide solutions.[98] These systems yield mixtures of CO and formate in a ~1:2 ratio. Two recently reported non-heme Fe electrocatalysts display higher selectivities for producing formate.[70,71] An Fe complex supported by a macrocyclic pyridine-diimine ligand was reported to produce only formate under electrocatalytic conditions in dimethylformamide, albeit in the absence of a proton source.[71] A tetrairon carbonyl cluster produces formate with faradaic efficiencies of up to 96% in aqueous solutions at near neutral pH.[70] In contrast to these non-heme examples, the preference of **3.4** for the production of CO (rather than formate) resembles the reactivities reported for Fe porphyrin electrocatalysts.[30-33,43] Notably, the CO/H_2 selectivity of **3.4** in the presence of a high water content/proton activity compares favorably with those reported for most Fe porphyrin catalysts (Table 3.1).

Table 3.1. Faradaic efficiencies of Fe-containing electrocatalysts for CO_2 reduction.

compound	electrolysis conditions[a]	applied potential (V)	Faradaic efficiency (%) CO	 $HCOO^-$	 $C_2O_4^{2-}$	 H_2	ref
4	11 M H_2O in CH_3CN	−1.91 V vs $[Fe(C_5H_5)_2]^{+/0}$	81 ± 11	0	–[b]	11 ± 3	this work
FeTPP[c]	1 M CF_3CH_2OH in DMF	−2.15 V[d] vs $[Fe(C_5H_5)_2]^{+/0}$	100	0	0	0	31
FeTPP[c]	1 M PhOH in DMF	−2.15 V[d] vs $[Fe(C_5H_5)_2]^{+/0}$	94	0	0	0	31
FeTPP[c]	0.1 M AcOH	−2.15 V[d] vs $[Fe(C_5H_5)_2]^{+/0}$	31	0	0	0	31
FeTDHPP[e]	2 M H_2O in DMF	−1.85 V[d] vs $[Fe(C_5H_5)_2]^{+/0}$	94	–[b]	–[b]	6	30
Fe(*p*-$NMe_3)_4$TPP[f]	pH 6.7 unbuffered aqueous solution	−0.97 V vs SHE	90	0.7	0.5	7	32
Fe(*p*-$NMe_3)_4$TPP[f]	pH 6.7 unbuffered aqueous solution	−0.86 V vs SHE	98–100	–[b]	–[b]	–[b]	32
Fe(*p*-$NMe_3)_4$TPP[f]	pH 6.7 phosphate buffer	−0.86 V vs SHE	50	–[b]	–[b]	50	32
$Fe(C_6F_5)_2$DHDPP[g]	3 M PhOH in DMF	−1.77 V[d] vs $[Fe(C_5H_5)_2]^{+/0}$	100 ± 10	–[b]	–[b]	<1	43
Fe(*o*-$NMe_3)_4$TPP[h]	0.1 M H_2O and 3 M PhOH in DMF	−1.65 V[d] vs $[Fe(C_5H_5)_2]^{+/0}$	93	–[b]	–[b]	0	33
$Fe(dophen)(MeIm)_2$[i]	1.23 M CH_3OH in DMF	−2.00 V vs $[Fe(C_5H_5)_2]^{+/0}$	30	52	11	0	98
$Fe(dophen)(MeIm)_2$[i]	1.23 M CF_3CH_2OH in DMF	−2.00 V vs $[Fe(C_5H_5)_2]^{+/0}$	31	53	9	0	98
$Fe(dophen)(MeIm)_2$[i]	1.23 M CH_3OH in DMSO	−2.00 V vs $[Fe(C_5H_5)_2]^{+/0}$	26	66	6	0	98
$Fe(dophen)(MeIm)_2$[i]	1.23 M CF_3CH_2OH in DMSO	−2.00 V vs $[Fe(C_5H_5)_2]^{+/0}$	30	65	3	0	98
$[Fe(L)Cl_2]^+$[j]	DMF[k]	−1.70 V[l] vs $[Fe(C_5H_5)_2]^{+/0}$	0	75–80%	–	0	71
$[Fe_4N(CO)_{12}]^-$	pH 6.5 $KHCO_3$ buffer	−1.44 V vs SHE	0	96 ± 2	0	2 ± 1	70

[a] performed under 1 atm of CO_2. [b] –, not determined or reported. [c] H_2TPP = (5,10,15,20-tetraphenylporphyrin). [d] converted from SHE by first referencing against saturated calomel electrode (SCE = 0.24 V vs SHE)[99], then referencing against the $[Fe(C_5H_5)_2]^{+/0}$ redox couple ($[Fe(C_5H_5)_2]^{+/0}$ = 0.45 V vs SCE in DMF solution[100]). [e] H_2TDHPP = 2,2′,2″,2‴-(porphyrin-5,10,15,20-tetrayl)tetrakis(benzene-1,3-diol). [f] H_2(*p*-$NMe_3)_4$TPP = 4,4′,4″,4‴-(porphyrin-5,10,15,20-tetrayl)tetrakis(*N*,*N*,*N*-trimethylbenzenaminium). [g] $H_2(C_6F_5)_2$DHDPP = 2,2′-(10,20-bis(perfluorophenyl)porphyrin-5,15-diyl)bis(benzene-1,3-diol). [h] H_2(*o*-$NMe_3)_4$TPP = 2,2′,2″,2‴-(porphyrin-5,10,15,20-tetrayl)tetrakis(*N*,*N*,*N*-trimethylbenzenaminium). [i] H_2dophen = 2,9-bis(2-hydroxyphenyl)-1,10-phenanthroline; MeIm = 1-methylimidazole. [j] L = (2*E*,12*E*)-2,13-dimethyl-3,6,9,12-tetraaza-1(2,6)-pyridinacyclotridecaphane-2,12-diene. [k] no acid was added. [l] converted from SCE by referencing against the $[Fe(C_5H_5)_2]^{+/0}$ redox couple ($[Fe(C_5H_5)_2]^{+/0}$ = 0.45 V vs SCE in DMF solution[100]).

We performed further experiments to ascertain whether CO_2 reduction catalysis arises from a molecular species or a heterogeneous adsorbate. After performing a 12-h electrolysis of a solution of **3.4** under CO_2, the glassy carbon electrode was rinsed with anhydrous, deaerated acetonitrile under an atmosphere of Ar. Electrolysis was subsequently performed using a fresh, iron-free electrolyte, after which the rinsed electrode displayed electrochemical characteristics identical to a bare glassy carbon electrode (Figure 3.S14). After the 12-h electrolysis with **3.4**, the resulting electrode was also characterized using scanning electron microscopy (SEM) and energy-dispersive X-ray spectroscopy (EDX). SEM revealed that the electrode surface is slightly roughened following electrolysis, although no Fe K_α or K_β features were observed in the EDX spectrum, suggesting that the active catalyst does not form iron-containing adsorbates on the electrode surface (Figure 3.S15).

3.3.5. Catalytic Role of the Second Coordination Sphere Aniline

While the voltammetric and electrolytic data show that the protic aniline group in the second coordination sphere of **4** is crucial to catalysis, its precise catalytic role is not known. One possibility is that the N-H proton behaves as a local proton source, which stabilizes transition states with significant metallacarboxylate character and assists in CO_2 binding or C-O bond cleavage (Scheme 3.3, Pathway A). This type of role was invoked in iron porphyrin[30,42] and macrocyclic nickel[38] CO_2 reduction catalysts. A second possibility is that amine ligand participates in CO_2 capture, and the resulting metal-bound carbamate/carbamic acid complex is then reduced to release CO (Scheme 3.3, Pathway B). Relevantly, CO_2 fixation has been described in an iridium(III)-stabilized amidopyridine complex[101], and in a zinc(II) complex with aminopyridine ligands.[102] Current evidence suggests that, without electrons, the Fe(II) complex of **3.4** does not directly interact with CO_2, since the oxidation wave in **3.4** is largely unaffected by the presence of CO_2 (Figure 3.3). However, the aniline N–H bond may be weakened upon reduction of **3.4**, thereby facilitating CO_2 insertion. In fact, this may be the origin of the pre-wave at ~−1.6 V in Figure 3.3. The selectivity of complex **3.2** for producing hydrogen may be rationalized by the increased acidity of the second coordination sphere phenol, which promotes the formation of a Fe hydride and is protonated more quickly than CO_2 can bind and be reduced. Ongoing studies are aimed at elucidating the catalytic mechanism of complex **3.4** and the role of its ligand scaffold.

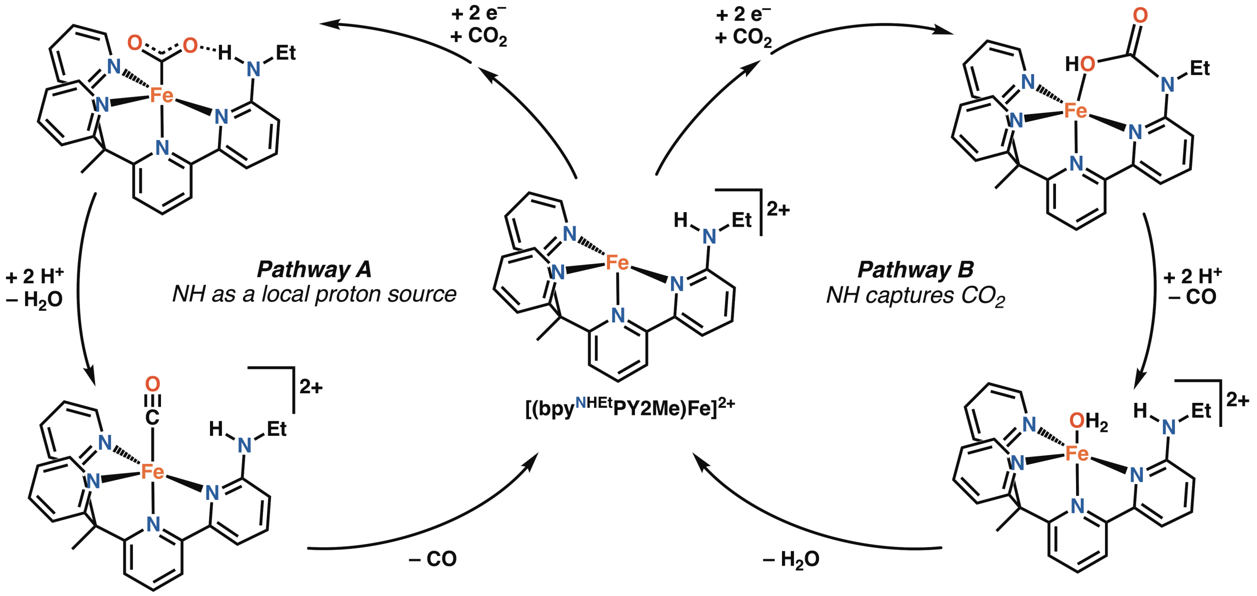

Scheme 3.3. Two possible catalytic pathways for the catalytic reduction of CO_2 to CO by complex **3.4**. In pathway A, the second coordination sphere amine stabilizes CO_2 binding to the iron center. In pathway B, the amine participates in CO_2 fixation to give metal-bound carbamic acid (or carbamate), which is reduced to give CO and a metal-aquo complex.

3.3.6. Controlled-Potential Electrolyses in CO_2-Saturated Water

Encouraged by the catalytic activity of the $[bpy^{NHEt}PY2Me]Fe]^{2+}$ complex of **3.4** in organic solvents in the presence of water, we sought to further explore its performance in fully aqueous solutions. Gratifyingly, compound **3.4** readily dissolves in water and is stable to electrochemical analysis. CVs of pH-adjusted (pH 4 or 7) aqueous solutions of **3.4** under CO_2 displayed large variations in reductive currents, depending on the nature of the anion comprising the electrolyte (Figures 3.S16–18). In each of these CVs, a multi-electron feature precedes a second, more rapid process at more negative potentials. We focused our investigations on the first reductive feature. For instance, compound **3.4** generates a ~10-fold enhancement of current in a 0.1 M aqueous KPF_6 solution relative to the ~8-fold enhancement observed for **3.4** in 0.1 M aqueous KCl, despite the same pH of 4 for both solutions. In a more alkaline pH = 7 $KHCO_3$ solution, **3.4** displays a feature with an overall ~20-fold current enhancement over the bicarbonate solution alone (Figure 3.S18).

To better understand the nature of these multi-electron processes, we performed electrolyses of **3.4** under the same solution conditions. As expected from the current response from the voltammetry experiment, the compound was the least catalytically active in pH 4 KCl solutions. Interestingly, in contrast to the results obtained from measurements in wet acetonitrile, H_2 was the only detectable gas produced over the course of a 2 h experiment, at a Faradaic efficiency of 76 ± 11% (Figure 3.S19). Compound **3.4** was more active in pH 7 $KHCO_3$ solution, reflecting the higher currents observed in the CV experiments. However, again H_2 was the only gaseous product observed, at a slightly higher Faradaic efficiency of 88 ±6% (Figure S20). In contrast, using KPF_6 as the electrolyte, which contains non-coordinating PF_6^- anions, allows the iron complex in **3.4** to exhibit an intermediate charge accumulation (Figure 6), and importantly, an optimal CO_2 reduction performance with a faradaic efficiency of 21 ± 3% for CO formation. Notably, the electrolysis experiments of **3.4** in pure water pass less charge than in wet acetonitrile.

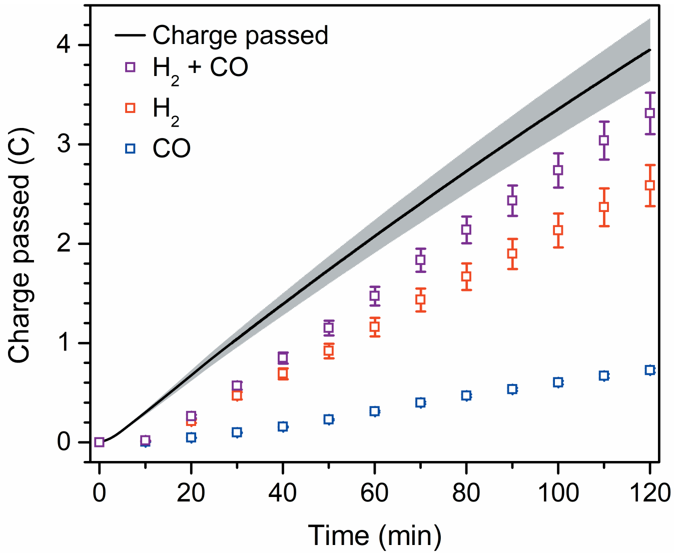

Figure 3.6. Controlled-potential electrolysis of a 240 µM solution of **3.4** in 0.1 M aqueous KPF_6 at −1.71 V (versus SHE). The solid black line and its surrounding gray area indicate the charge passed and its standard deviation. The red, blue, and purple squares correspond to the charge equivalents of H_2, CO, and their combined total detected charge. The activity of the bare glassy carbon electrode has been subtracted from the data.

The foregoing results highlight the sensitivity of catalytic metrics to experimental conditions. The more complex catalytic behavior of **3.4** in aqueous solutions can be ascribed to two factors. First, while the compound is selective for the reduction of CO_2 in wet acetonitrile, this selectivity is overwhelmed in pure aqueous solutions. Since CO_2 is less soluble in water than in acetonitrile (0.033 M/atm versus 0.28 M/atm at 298 K)[103,104], the activity of dissolved CO_2 is dwarfed by the much higher activity of water. Secondly, the electrocatalytic performance of **3.4** in pH 4 aqueous KPF_6 versus pH 4 aqueous KCl solutions suggests that introduction of coordinating anions can significantly alter the catalytic pathway(s). We postulate that coordinating anions such as Cl^- and HCO_3^- compete with the substrate binding necessary for CO_2 reduction catalysis.

3.4. Conclusions

We have designed and synthesized a new family of non-heme iron complexes and shown that the incorporation of functional groups featuring protic groups of varying acidity can enhance electrocatalytic activity towards CO_2. With the appropriate protic group in the second coordination sphere, the $[(bpy^{NHEt}PY2Me)Fe]^{2+}$ complex in compound **3.4** is able to utilize water as the proton source for CO_2 to CO conversion with high activity, selectivity, and stability. Notably, catalyst **3.4** represents a rare example of a non-heme iron CO_2 electro-reduction catalyst, and is the first example that selectively generates CO. Furthermore, **3.4** is devoid of strongly light-absorbing moieties such as porphyrins, rendering it a potentially attractive new candidate for the functionalization of semiconductor surfaces for photocatalytic CO_2 reduction.[21] Finally, the foregoing results suggest the myriad of still yet untapped areas wherein fine synthetic molecular control can be harnessed in the design of improved molecular electrocatalysts.

3.5. Acknowledgments

This Chapter includes work from: Zee, D. Z.; Nippe, M.; King, A. E.; Chang, C. J.; Long, J. R. Tuning Second Coordination Sphere Interactions in Polypyridyl–Iron Complexes to Achieve Selective Electrocatalytic Reduction of Carbon Dioxide to Carbon Monoxide. *In preparation.* This work was funded by DOE/LBNL Grant 101528-002 (M.N. and C.J.C), NSF grant CHE-146841 (D.Z.Z. and J.R.L.), and the Joint Center for Artificial Photosynthesis, a DOE Energy Innovation Hub, supported through the Office of Science of the U.S. Department of Energy award DE-SC0004993 (D.Z.Z. and J.R.L.). D.Z.Z. thanks the National Science Foundation Graduate Research Fellowship program for support. C.J.C. is an Investigator with the Howard Hughes Medical Institute and a CIFAR Senior Fellow. Single-crystal X-ray structure determination was supported by the NIH Shared Instrumentation Grant S10-RR027172. The authors are grateful to Dr. Lena Trotochaud for assistance with SEM and EDX imaging, and to Matthew J. Singleton for help automating extraction of GC data.

3.6. Supplementary Information

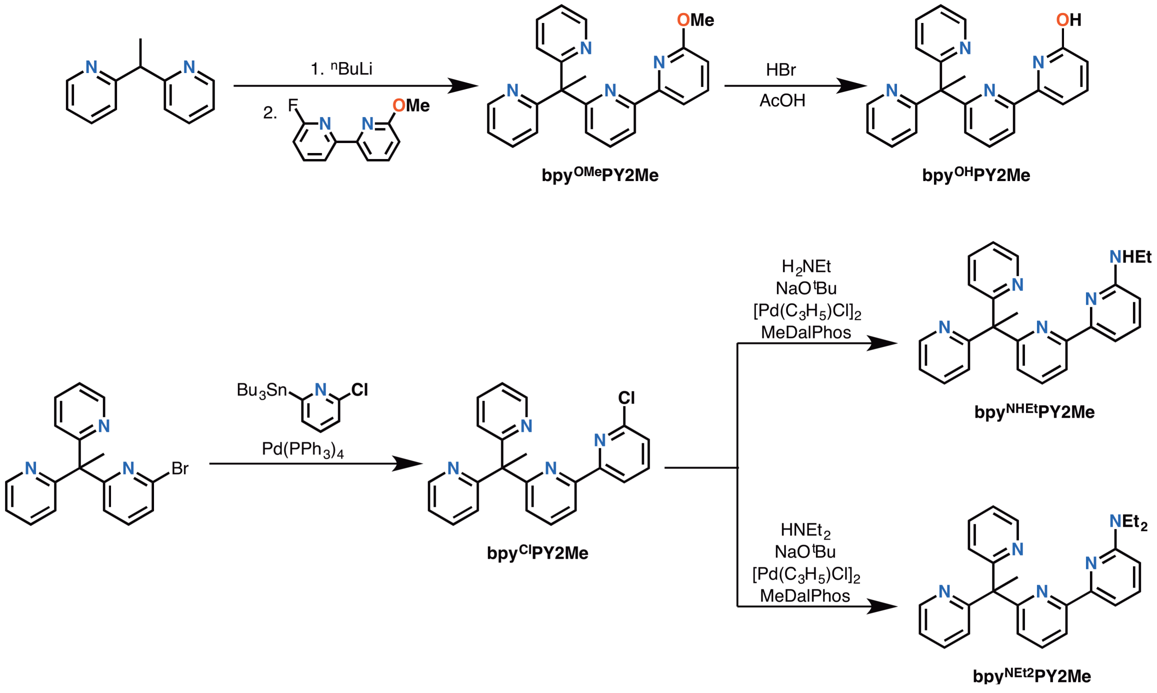

Scheme 3.S1. Synthetic scheme for the ligands bpy^{OMe}PY2Me, bpy^{OH}PY2Me, bpy^{NHEt}PY2Me, and bpy^{NEt2}PY2Me.

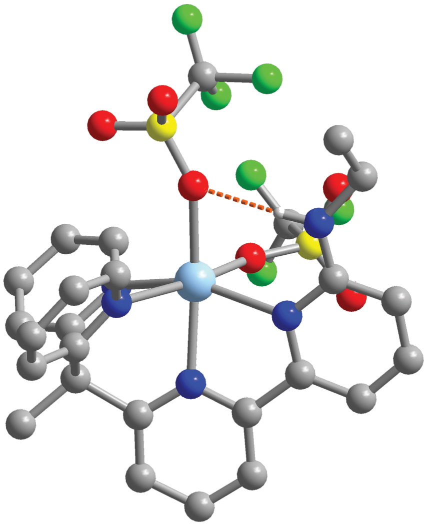

Figure 3.S1. Single Crystal X-ray structure of complex **3.6**. Light blue, blue, gray, red, yellow, green, and white spheres represent Mn, N, C, O S, F, and H atoms, respectively. Hydrocarbon H atoms and unbound solvent molecules are not shown. The ethyl group and the coordinated trifluoromethanesulfonate anion at the top of the figure are disordered over two positions; only one orientation is shown for each.

Table 3.S1. Crystallographic data for complexes **3.1–3**.[a]

	3.1	**3.2**	**3.3**
formula	$C_{30}H_{27}F_6FeN_7O_6S_2$	$C_{28}H_{24}F_6FeN_6O_7S_2$	$C_{33}H_{32}F_6FeN_8O_7S_2$
crystal system	monoclinic	triclinic	triclinic
fw, g mol^{-1}	815.55	790.50	886.63
T, K	100(2)	100(2)	100(2)
space group	$P2_1/c$	$P\bar{1}$	$P\bar{1}$
habit	block	block	block
color	red	brown	red
Z	4	2	2
a, Å	12.1919(4)	10.5333(8)	12.5851(7)
b, Å	12.1059(5)	13.0119(9)	12.6151(7)
c, Å	22.5920(8)	13.0285(10)	14.8628(8)
α, °	90	104.106(4)	113.007(2)
β, °	94.560(2)	113.539(4)	93.593(3)
γ, °	90	94.581(4)	116.284(2)
V, Å^3	3323.9(2)	1555.9(2)	1866.26(18)
ρ_{calc}, g cm^{-3}	1.63	1.687	1.578
μ_{calc}, mm^{-1}	0.669	0.713	0.605
2θ range, °	3.352 to 50.73	3.294 to 50.796	3.106 to 50.836
total reflections	27407	24996	46480
data / restr / parameters	6097 / 0 / 473	5691 / 0 / 458	6816 / 0 / 520
F(000)	1664	804	908
T_{min}/T_{max}	0.886	0.916	0.923
crystal size, mm^3	0.14 × 0.1 × 0.08	0.23 × 0.21 × 0.18	0.34 × 0.31 × 0.23
Largest diff. peak/hole / e Å^{-3}	0.49 / −0.37	1.04 / −0.44	0.61 / −0.47
R_1 (wR_2),[b] % [$I > 2\sigma(I)$]	3.44 (9.16)	4.35 (8.66)	3.68 (8.47)
R_1 (wR_2), % (all data)	3.85 (9.41)	6.82 (9.67)	4.57 (8.89)

[a] Obtained with graphite-monochromated Mo Kα (λ = 0.71073 Å) radiation.

[b] $R_1 = \sum\left||F_o| - |F_c|\right|/\sum|F_o|, wR_2 = \{\sum w(F_o^2 - F_c^2)^2/\sum w(F_o^2)^2\}^{\frac{1}{2}}$

Table 3.S2. Crystallographic data for complexes **3.4–6**.[a]

	3.4	3.5[c]	3.6
formula	$C_{26}H_{23}F_6FeN_5O_6S_2$	$C_{30}H_{30}F_6FeN_6O_6S_2$	$C_{26}H_{23}F_6MnN_5O_6S_2$
crystal system	monoclinic	triclinic	monoclinic
fw, g mol^{-1}	735.46	804.57	734.55
T, K	100(2)	100(2)	250(2)
space group	$P2_1/c$	$P\bar{1}$	$P2_1/c$
habit	block	block	block
color	brown	yellow-orange	yellow
Z	4	2	4
a, Å	15.4307(6)	12.2693(6)	15.7289(16)
b, Å	11.1704(4)	13.0429(7)	11.2251(11)
c, Å	18.2742(7)	13.4976(6)	18.4618(19)
α, °	90	107.264(2)	90
β, °	110.4350(10)	113.727(2)	109.666(2)
γ, °	90	101.057(2)	90
V, Å^3	2951.64(19)	1764.63(15)	3069.5(5)
ρ_{calc}, g cm^{-3}	1.655	1.514	1.59
μ_{calc}, mm^{-1}	0.741	0.628	0.651
2θ range, °	2.816 to 50.732	3.5 to 50.746	2.75 to 50.762
total reflections	46906	29803	35531
data / restr / parameters	5404 / 0 / 421	6422 / 242 / 528	5625 / 274 / 505
$F(000)$	1496	824	1492
$T_{\text{min}}/T_{\text{max}}$	0.904	0.935	0.872
crystal size, mm^3	0.38 × 0.3 × 0.21	0.08 × 0.06 × 0.06	0.6 × 0.3 × 0.3
Largest diff. peak/hole / e Å^{-3}	0.41 / −0.33	1.48 / −0.95	0.48 / −0.33
R_1 (wR_2),[b] % [$I > 2\sigma(I)$]	2.36 (6.01)	5.91 (14.83)	4.19 (10.36)
R_1 (wR_2), % (all data)	2.57 (6.16)	6.61 (15.37)	5.14 (11.11)

[a] Obtained with graphite-monochromated Mo Kα (λ = 0.71073 Å) radiation.

[b] $R_1 = \sum||F_o| - |F_c||/\sum|F_o|, wR_2 = \{\sum w(F_o^2 - F_c^2)^2/\sum w(F_o^2)^2\}^{\frac{1}{2}}$

[c] The empirical formula and formula weight of **5** does not include unidentified, disordered solvent.

Table 3.S3. Highlighted crystallographic bond distances for complexes **3.1–6**.

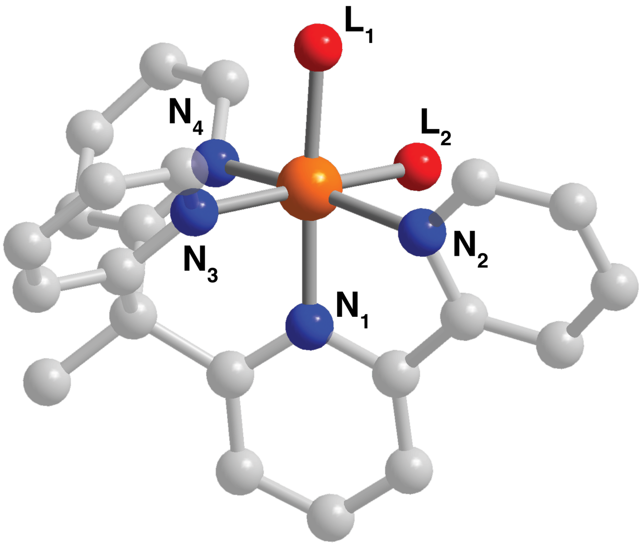

Bond, Å	Complex					
	3.1	**3.2**	**3.3**	**3.4**	**3.5**	**3.6**
M–N$_1$	1.903(1)	1.905(3)	1.905(1)	2.109(1)	2.106(2)	2.192(3)
M–N$_2$	1.992(1)	2.053(2)	2.043(3)	2.204(1)	2.249(4)	2.253(3)
M–N$_3$	1.952(2)	1.955(3)	1.942(2)	2.169(1)	2.184(4)	2.261(3)
M–N$_4$	1.970(2)	1.974(3)	1.970(3)	2.138(1)	2.175(3)	2.203(3)
M–L$_1$[a]	1.953(2)	1.949(3)	1.942(2)	2.087(1)	2.108(3)	2.135(3)
M–L$_2$[b]	1.945(2)	1.958(3)	1.951(2)	2.167(1)	2.182(3)	2.172(3)

[a] L$_1$ = CH_3CN for **3.1**, **3.2**, **3.3**, and **3.5**; L$_1$ = $CF_3SO_3^-$ for **3.4** and **3.6**.

[b] L$_2$ = CH_3CN for **3.1–3**. L$_2$ = $CF_3SO_3^-$ for **3.4–6**.

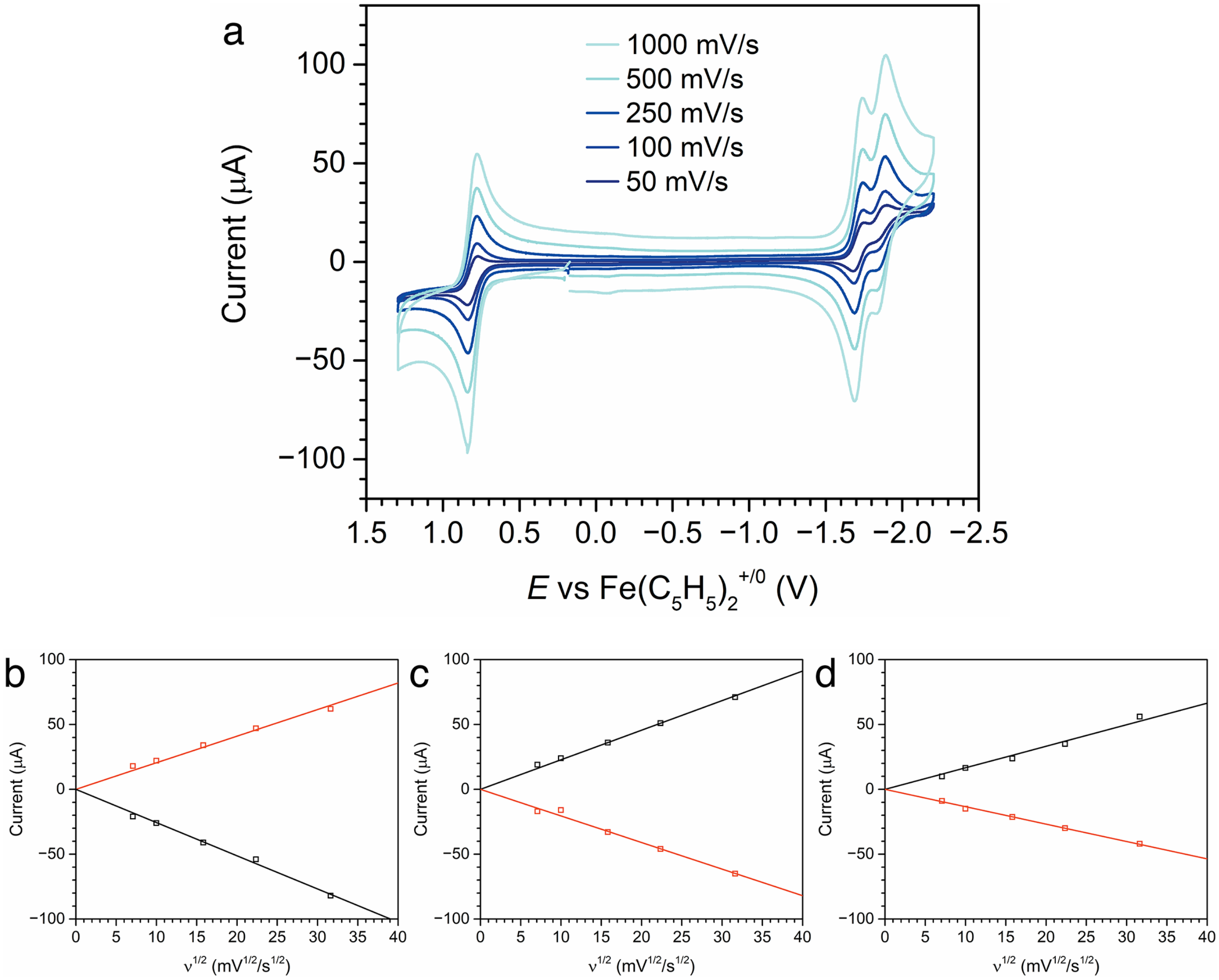

Figure 3.S2. (a) CVs of complex **3.1** in argon-saturated acetonitrile solution with 0.1 M NBu_4PF_6 supporting electrolyte, with scan rates of 50 mV/s to 1000 mV/s. Plots of peak current versus square root of scan rate for forward (black squares) and reverse (red squares) sweeps of the redox couple centered at (b) +0.81 V, (c) −1.71 V, and (d) −1.86 V. Black and red lines are the corresponding linear fits.

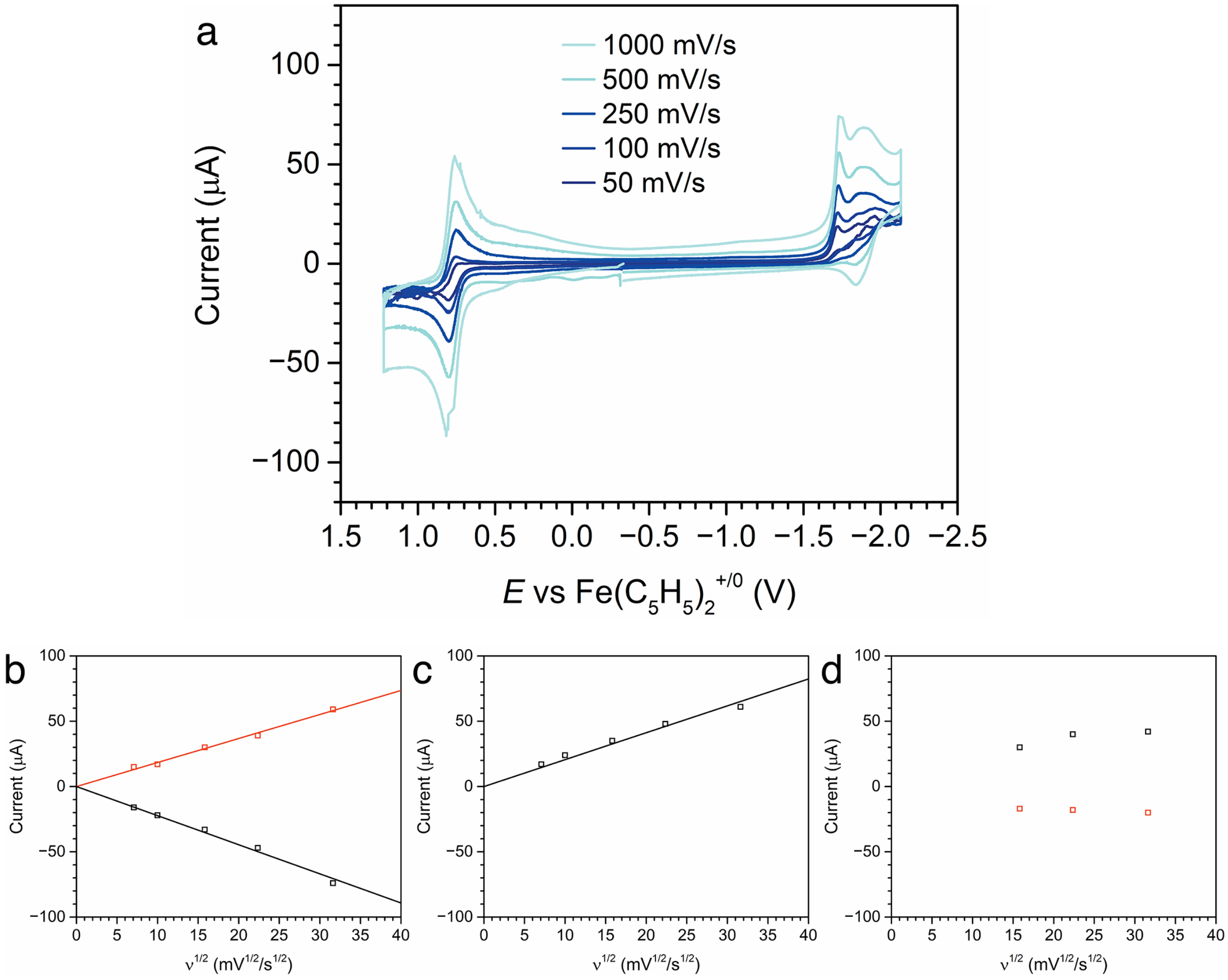

Figure 3.S3. (a) CVs of complex **3.2** in argon-saturated acetonitrile solution with 0.1 M NBu$_4$PF$_6$ supporting electrolyte, with scan rates of 50 mV/s to 1000 mV/s. (b) Plot of peak current versus square root of scan rate for forward (black squares) and reverse (red squares) sweeps of the redox couple centered at +0.78 V. (c) Plot of peak current versus square root of scan rate for the forward sweep of the redox couple with E_p = −1.72 V. (d) Plot of peak current versus square root of scan rate for the forward (black squares) and reverse (red squares) sweeps of the broad feature at approximately −1.87 V. Black and red lines are the corresponding linear fits.

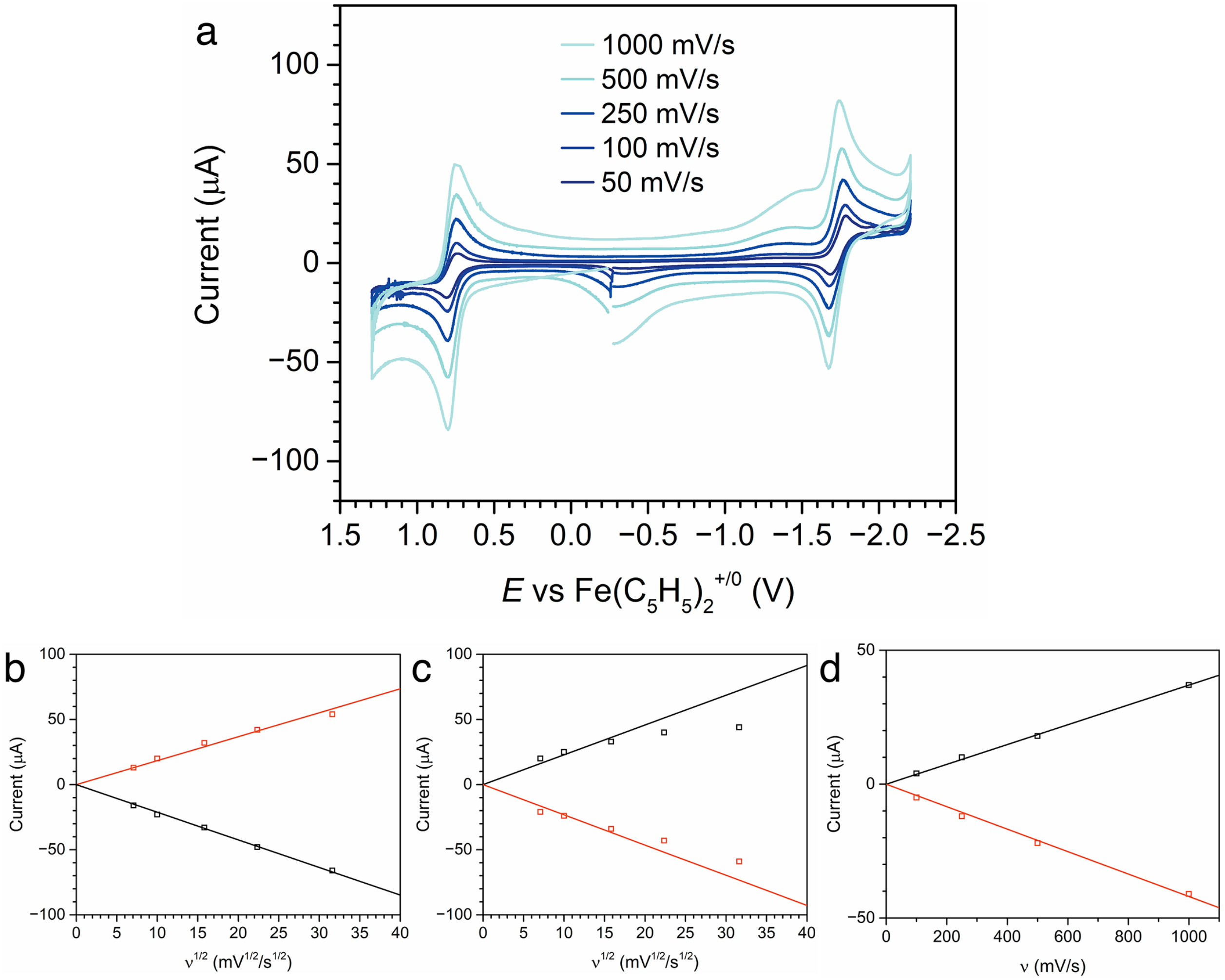

Figure 3.S4. (a) CVs of complex **3.3** in argon-saturated acetonitrile solution with 0.1 M NBu_4PF_6 supporting electrolyte, with scan rates of 50 mV/s to 1000 mV/s. Plots of peak current versus square root of scan rate for forward (black squares) and reverse (red squares) sweeps of the redox couple centered at (b) +0.78 V and (c) −1.72 V. We attribute the deviation of from ideal behavior predicted by the Cottrell equation due to interference from a broad, preceding feature apparent at $\nu \geq 250$ mV/s. (d) Plot of peak current versus scan rate for the forward (black squares) and reverse (red squares) sweeps of the broad features occurring at $E_{pc} \approx -1.2$ V and $E_{pa} \approx -0.2$ V. Black and red lines are the corresponding linear fits.

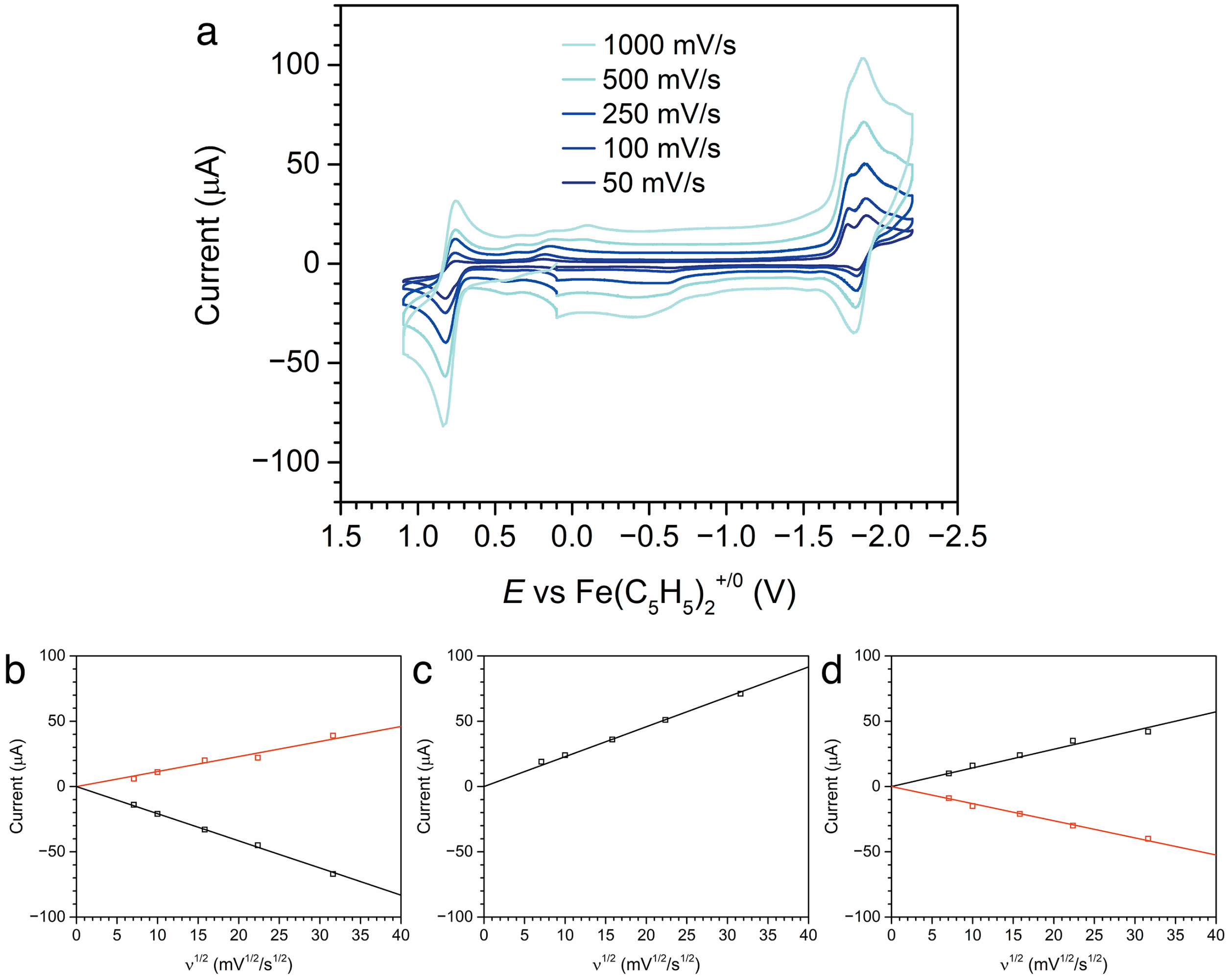

Figure 3.S5. (a) CVs of complex **3.4** in argon-saturated acetonitrile solution with 0.1 M NBu_4PF_6 supporting electrolyte, with scan rates of 50 mV/s to 1000 mV/s. Plots of peak current versus square root of scan rate for forward (black squares) and reverse (red squares) sweeps of the redox couples with (b) $E_{1/2} = +0.80$ V, (c) $E_{pc} = -1.79$ V, and (d) $E_{1/2} = -1.87$ V. Black and red lines are the corresponding linear fits.

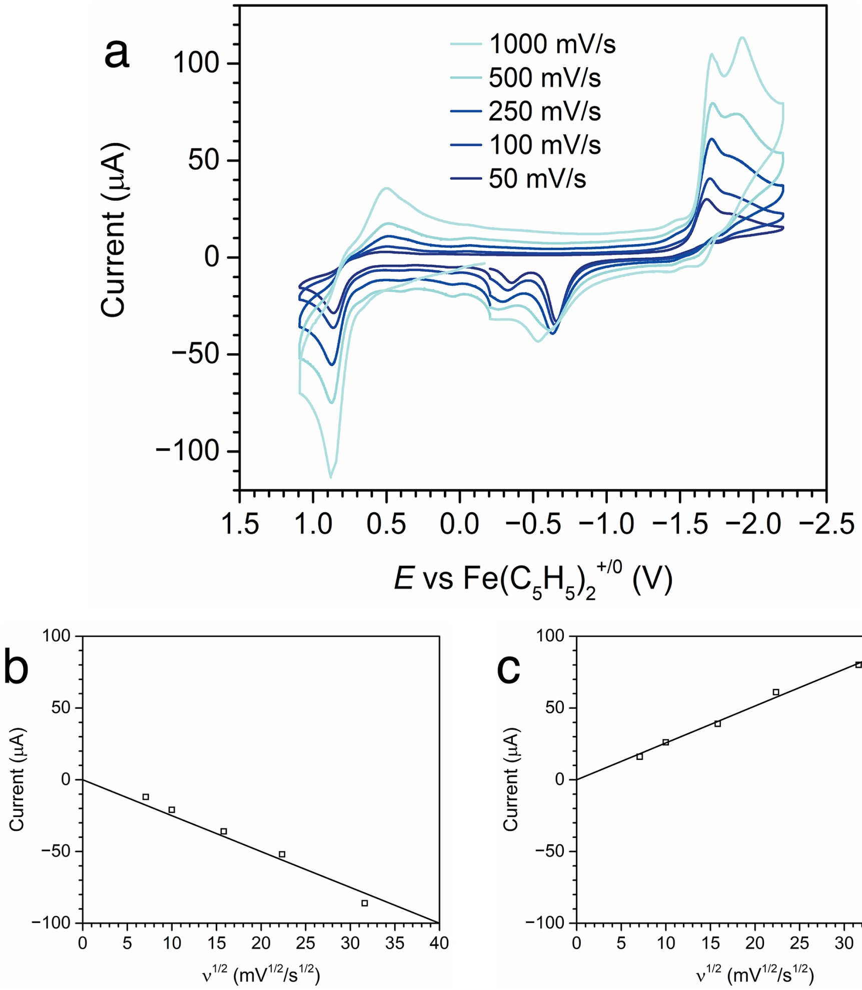

Figure 3.S6. (a) CVs of complex **3.5** in argon-saturated acetonitrile solution with 0.1 M NBu_4PF_6 supporting electrolyte, with scan rates of 50 mV/s to 1000 mV/s. Plots of peak current versus square root of scan rate for forward sweeps of the redox couples with (b) E_{pa} = +0.87 V, and (c) E_{pc} = −1.71 V. Black lines are the corresponding linear fits.

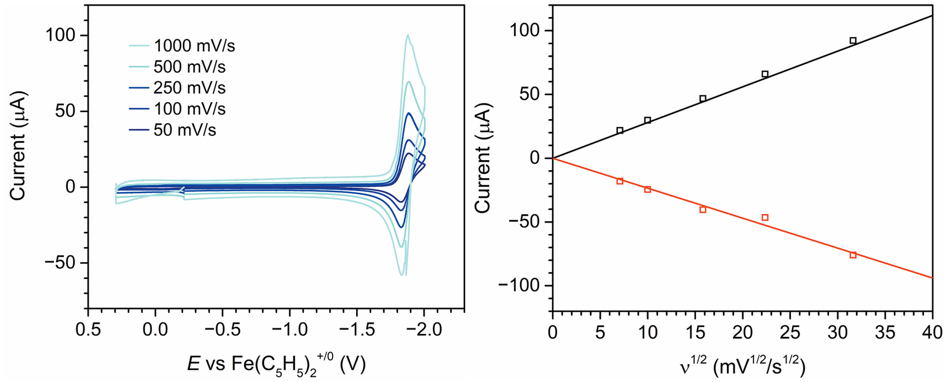

Figure 3.S7. Left: CVs of complex **3.6** in argon-saturated acetonitrile solution with 0.1 M NBu_4PF_6 supporting electrolyte, with scan rates of 50 mV/s to 1000 mV/s. Right: Plot of peak current versus square root of scan rate for forward (black squares) and reverse (red squares) sweeps of the redox couple with $E_{1/2}$ = −1.85 V. Black and red lines are the corresponding linear fits.

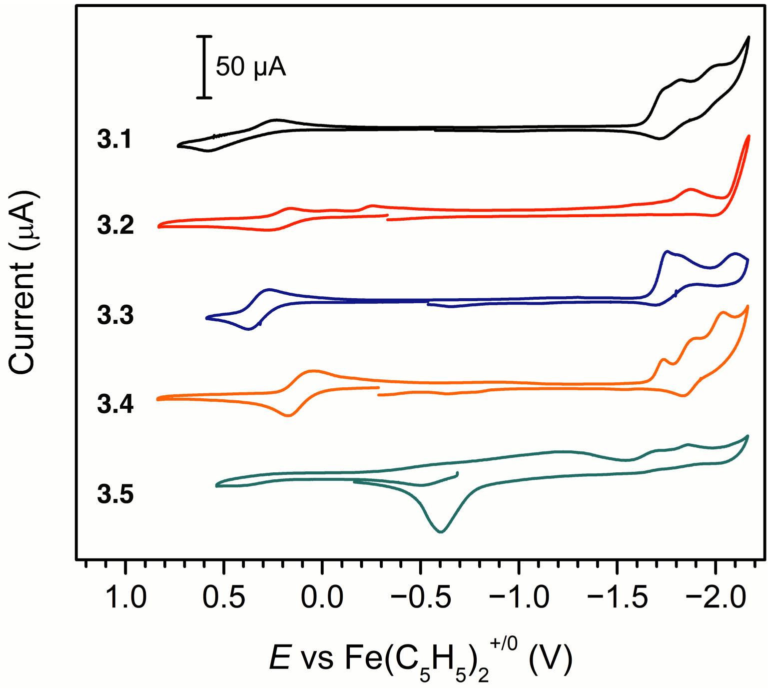

Figure 3.S8. CVs of complexes **3.1**–**5** in N_2-saturated CH_3CN solutions with 11 M H_2O and 0.1 M NBu_4PF_6 as the supporting electrolyte. All scans were performed at 0.1 V s^{-1}.

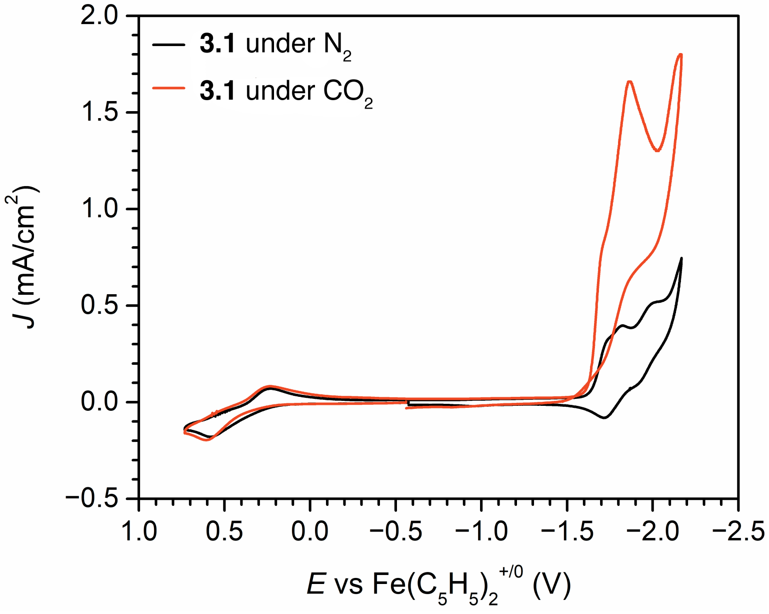

Figure 3.S9. CVs of **3.1** in N_2-saturated (black) and CO_2-saturated CH_3CN/H_2O (red) collected at a scan rate of 0.1 V/s. Data was obtained using a glassy carbon disk (3 mm dia.) working electrode, an $Ag/AgNO_3$ reference electrode, and a graphite counter electrode with 0.1 M NBu_4PF_6 as supporting electrolyte.

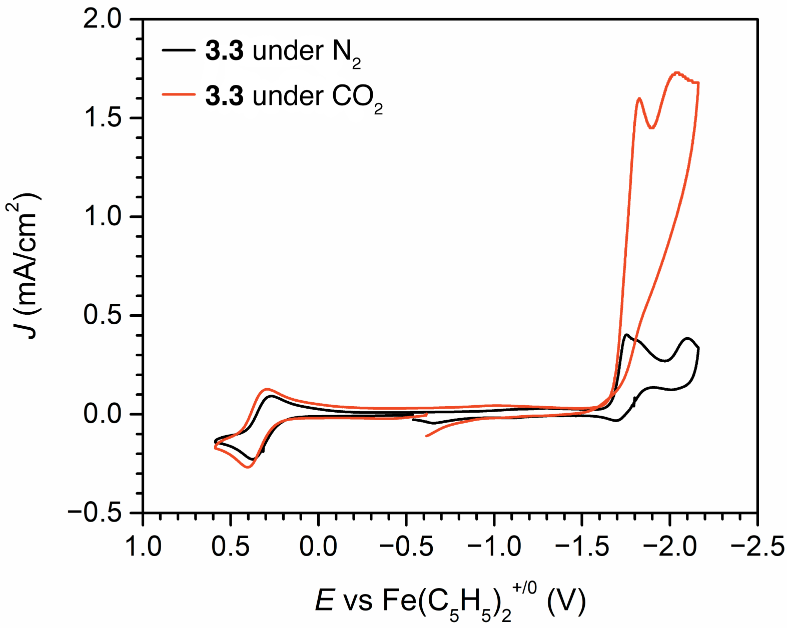

Figure 3.S10. CVs of **3.3** in N_2-saturated (black) and CO_2-saturated CH_3CN/H_2O (red) collected at a scan rate of 0.1 V/s. Data was obtained using a glassy carbon disk (3 mm dia.) working electrode, an $Ag/AgNO_3$ reference electrode, and a graphite counter electrode with 0.1 M NBu_4PF_6 as supporting electrolyte.

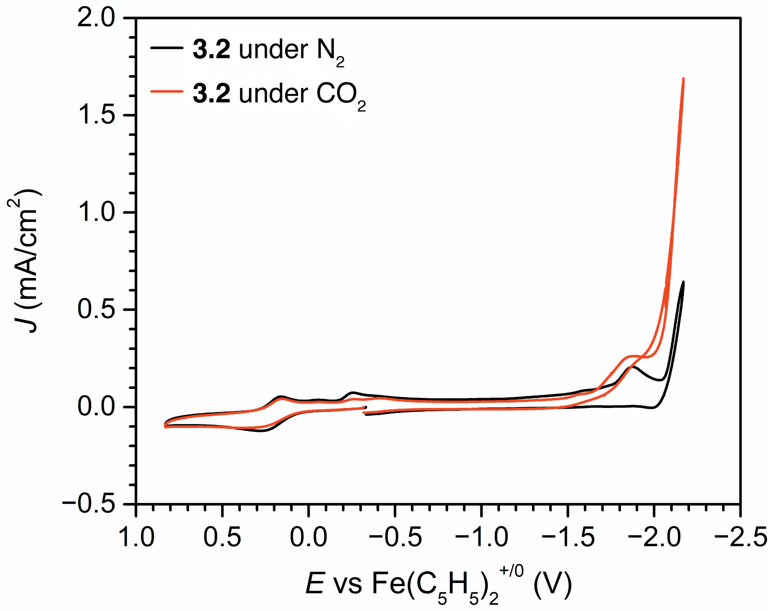

Figure 3.S11. CVs of **3.2** in N_2-saturated (black) and CO_2-saturated CH_3CN/H_2O (red) collected at a scan rate of 0.1 V/s. Data was obtained using a glassy carbon disk (3 mm dia.) working electrode, an $Ag/AgNO_3$ reference electrode, and a graphite counter electrode with 0.1 M NBu_4PF_6 as supporting electrolyte.

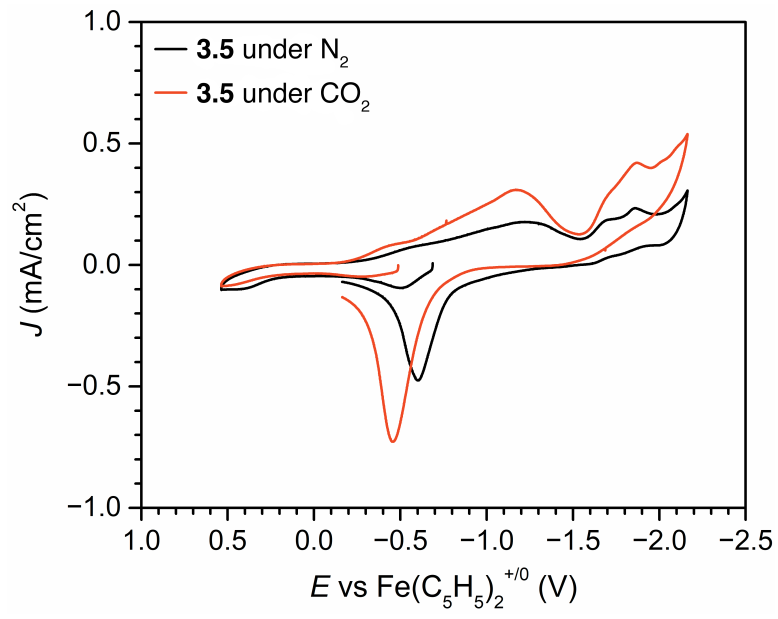

Figure 3.S12. CVs of **3.5** in N_2-saturated (black) and CO_2-saturated CH_3CN/H_2O (red) collected at a scan rate of 0.1 V/s. Data was obtained using a glassy carbon disk (3 mm dia.) working electrode, an $Ag/AgNO_3$ reference electrode, and a graphite counter electrode with 0.1 M NBu_4PF_6 as supporting electrolyte.

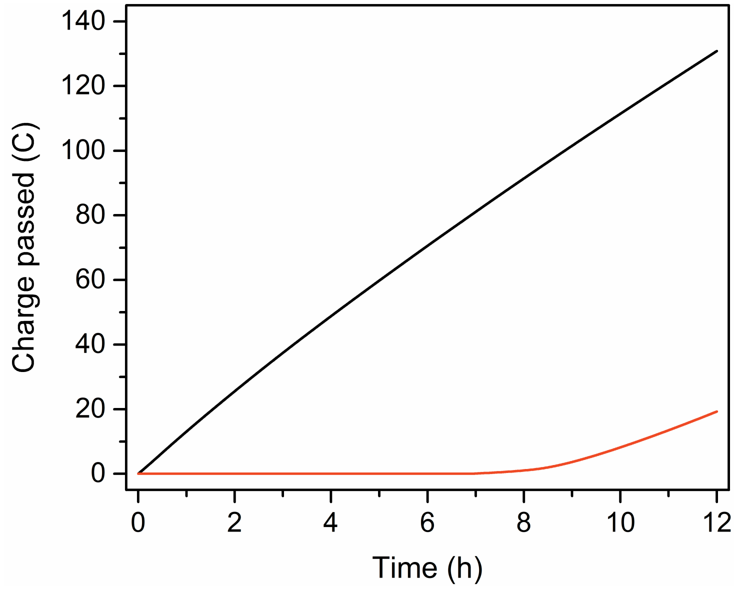

Figure 3.S13. Charge buildup during controlled-potential electrolyses at −1.91 V versus $Fe(C_5H_5)_2^{+/0}$, with 240 µM of **3.4** (black) or 240 µM of $Fe(CF_3SO_3)_2$ (red). The activity of the bare glassy carbon electrode has been subtracted from the plotted data.

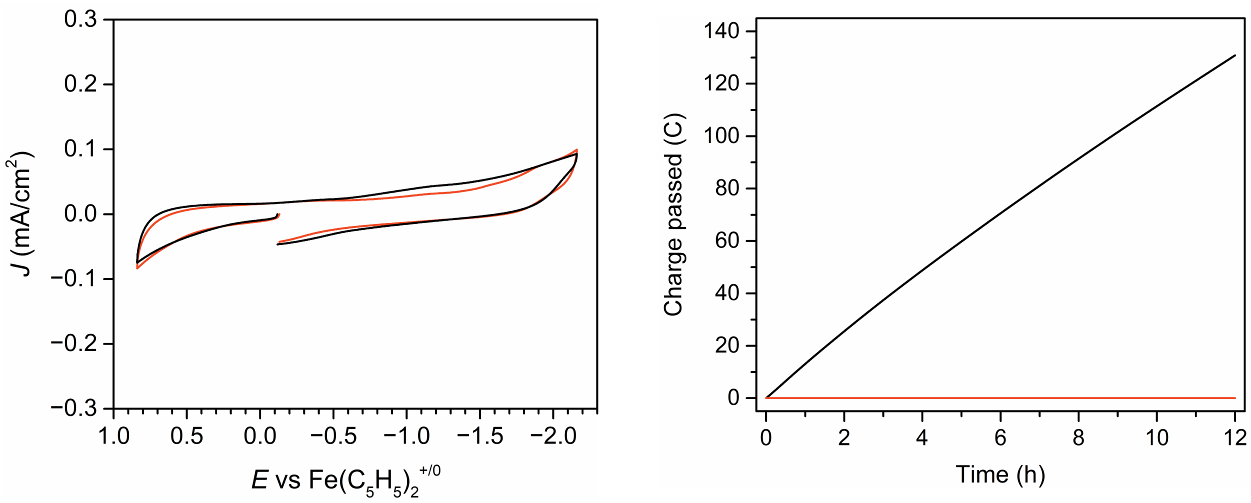

Figure 3.S14. Left: CVs in CO$_2$-saturated CH$_3$CN/H$_2$O of a polished glassy carbon electrode (black) and of a rinsed electrode (red) after a 12-h electrolysis with **3.4**. Right: Charge buildup during controlled-potential electrolysis of at −1.91 V versus Fe(C$_5$H$_5$)$_2^{+/0}$, with 240 µM of **3.4** (black). The electrode was rinsed, then another electrolysis experiment was performed on fresh electrolyte (red). The activity of the bare glassy carbon electrode was subtracted from the plotted data.

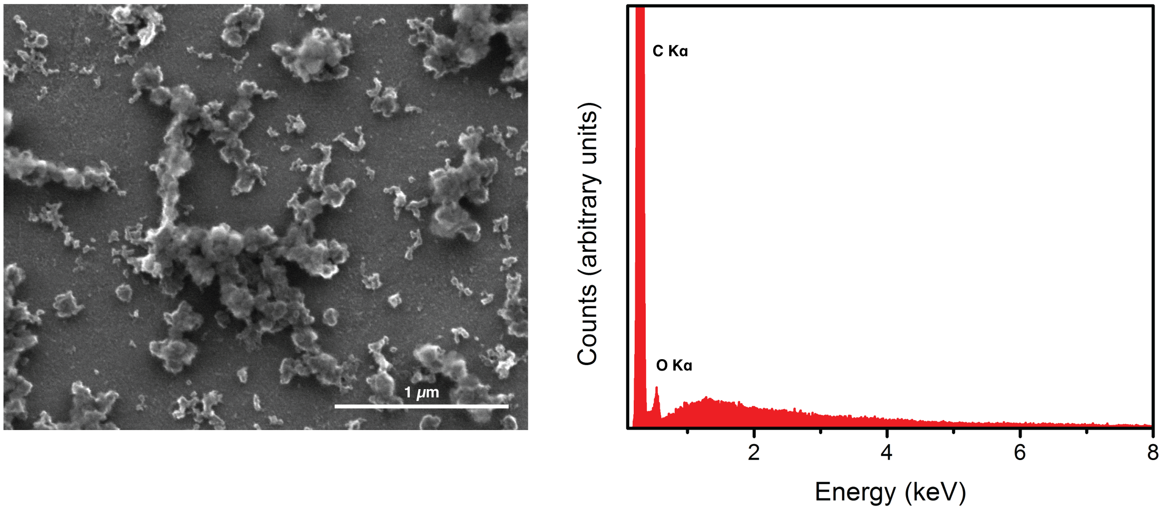

Figure 3.S15. SEM (left) and EDX spectrum (right) of a glassy carbon electrode after a 12-h electrolysis with **3.4** in CH$_3$CN with 11 M H$_2$O. The absence of Fe K$_\alpha$ (*ca.* 6.4 keV) and K$_\beta$ (*ca.* 7.1 keV) lines suggests the lack of Fe-containing adsorbates on the electrode.

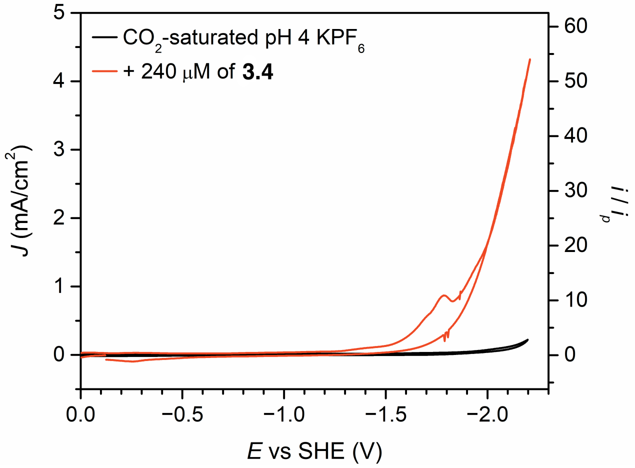

Figure 3.S16. Cyclic voltammogram of **3.4** in a CO_2-saturated (red) 0.1 M potassium hexafluorophosphate solution, collected at a scan rate of 0.1 V/s.

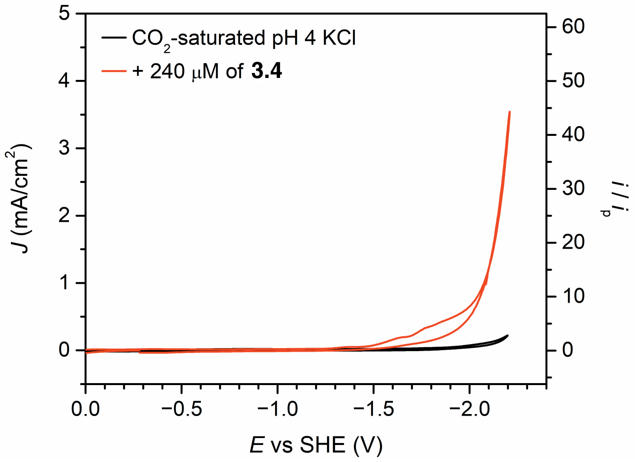

Figure 3.S17. Cyclic voltammogram of **3.4** in a CO_2-saturated (red) 0.1 M potassium chloride solution, collected at a scan rate of 0.1 V/s.

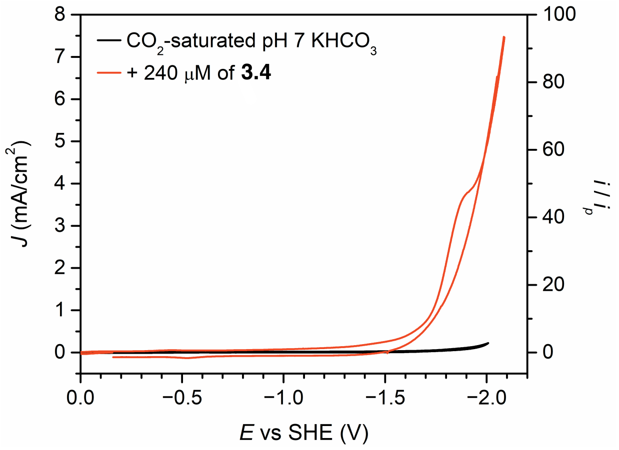

Figure 3.S18. Cyclic voltammogram of **3.4** in a CO_2-saturated (red) 0.1 M potassium bicarbonate solution, collected at a scan rate of 0.1 V/s.

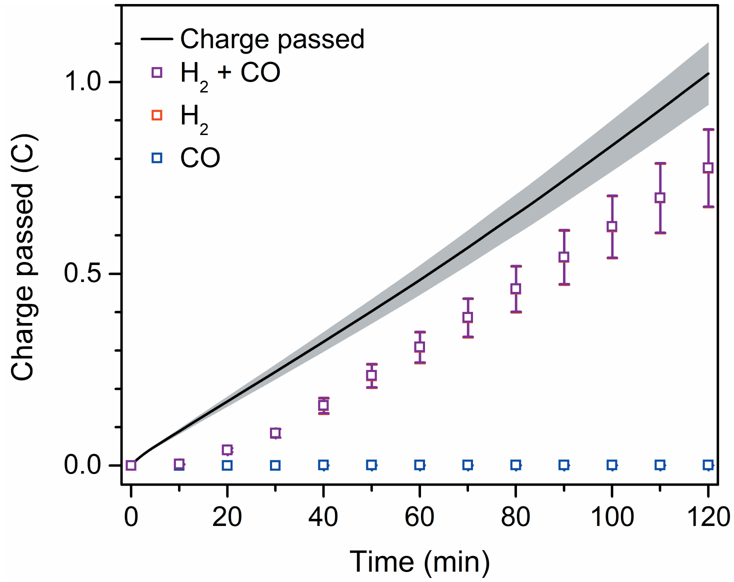

Figure 3.S19. Controlled-potential electrolysis of **3.4** in a CO_2-saturated (red) 0.1 M potassium chloride solution with a pH of 4 at −1.71 V versus SHE.

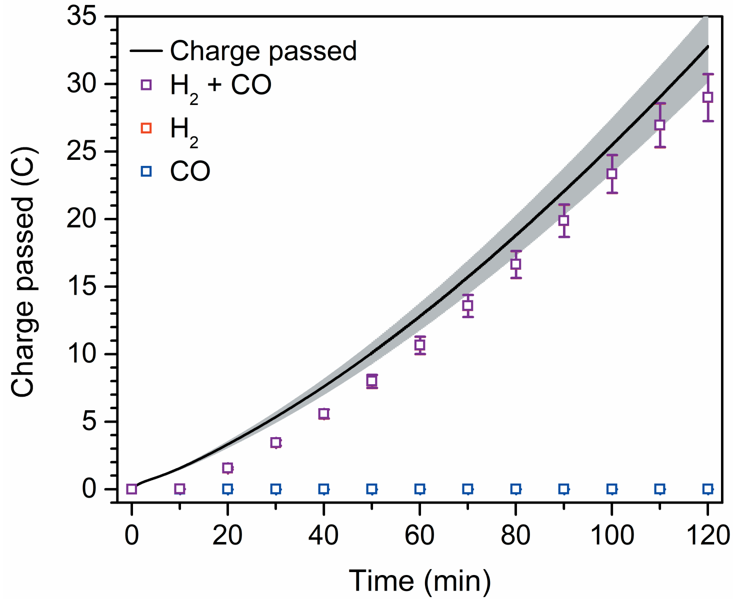

Figure 3.S20. Controlled-potential electrolysis of **3.4** in a CO_2-saturated (red) 0.1 M potassium bicarbonate solution with a pH of 7 at −1.88 V versus SHE.

3.7. References

(1) Thoi, V. S.; Sun, Y.; Long, J. R.; Chang, C. J. Complexes of Earth-Abundant Metals for Catalytic Electrochemical Hydrogen Generation Under Aqueous Conditions. *Chem. Soc. Rev.* **2013**, *42* (6), 2388–2400.

(2) Zee, D. Z.; Chantarojsiri, T.; Long, J. R.; Chang, C. J. Metal–Polypyridyl Catalysts for Electro- and Photochemical Reduction of Water to Hydrogen. *Acc. Chem. Res.* **2015**, *48* (7), 2027–2036.

(3) Elgrishi, N.; Chambers, M. B.; Wang, X.; Fontecave, M. Molecular Polypyridine-Based Metal Complexes as Catalysts for the Reduction of CO_2. *Chem. Soc. Rev.* **2017**, *46*, 761–796.

(4) Hori, Y. Electrochemical CO_2 Reduction on Metal Electrodes. In *Modern Aspects of Electrochemistry*; Vayenas, C. G., White, R. E., Gamboa-Aldeco, M. E., Eds.; Modern Aspects of Electrochemistry; Springer New York: New York, NY, 2008; Vol. 42, pp 89–189.

(5) Chen, Y.; Kanan, M. W. Tin Oxide Dependence of the CO_2 Reduction Efficiency on Tin Electrodes and Enhanced Activity for Tin/Tin Oxide Thin-Film Catalysts. *J. Am. Chem. Soc.* **2012**, *134* (4), 1986–1989.

(6) Li, C. W.; Kanan, M. W. CO_2 Reduction at Low Overpotential on Cu Electrodes Resulting From the Reduction of Thick Cu_2O Films. *J. Am. Chem. Soc.* **2012**, *134* (17), 7231–7234.

(7) Lee, C. H.; Kanan, M. W. Controlling H+ vs CO_2 Reduction Selectivity on Pb Electrodes. *ACS Catal.* **2015**, *5* (1), 465–469.

(8) Kuhl, K. P.; Cave, E. R.; Abram, D. N.; Jaramillo, T. F. New Insights Into the Electrochemical Reduction of Carbon Dioxide on Metallic Copper Surfaces. *Energy Environ. Sci.* **2012**, *5* (5), 7050–7059.

(9) Kuhl, K. P.; Hatsukade, T.; Cave, E. R.; Abram, D. N.; Kibsgaard, J.; Jaramillo, T. F. Electrocatalytic Conversion of Carbon Dioxide to Methane and Methanol on Transition Metal Surfaces. *J. Am. Chem. Soc.* **2014**, *136* (40), 14107–14113.

(10) DiMeglio, J. L.; Rosenthal, J. Selective Conversion of CO_2 To CO with High Efficiency Using an Inexpensive Bismuth-Based Electrocatalyst. *J. Am. Chem. Soc.* **2013**, *135* (24), 8798–8801.

(11) Medina-Ramos, J.; DiMeglio, J. L.; Rosenthal, J. Efficient Reduction of CO_2 To CO with High Current Density Using in Situ or Ex Situ Prepared Bi-Based Materials. *J. Am. Chem. Soc.* **2014**, *136* (23), 8361–8367.

(12) Medina-Ramos, J.; Pupillo, R. C.; Keane, T. P.; DiMeglio, J. L.; Rosenthal, J. Efficient Conversion of CO_2 To CO Using Tin and Other Inexpensive and Easily Prepared Post-Transition Metal Catalysts. *J. Am. Chem. Soc.* **2015**, *137* (15), 5021–5027.

(13) Lin, S.; Diercks, C. S.; Zhang, Y.-B.; Kornienko, N.; Nichols, E. M.; Zhao, Y.; Paris, A. R.; Kim, D.; Yang, P.; Yaghi, O. M.; Chang, C. J. Covalent Organic Frameworks Comprising Cobalt Porphyrins for Catalytic CO_2 Reduction in Water. *Science* **2015**, *349* (6253), 1208–1213.

(14) Hod, I.; Sampson, M. D.; Deria, P.; Kubiak, C. P.; Farha, O. K.; Hupp, J. T. Fe-Porphyrin-Based Metal–Organic Framework Films as High-Surface Concentration, Heterogeneous Catalysts for Electrochemical Reduction of CO_2. *ACS Catal.* **2015**, *5* (11), 6302–6309.

(15) Xu, H.-Q.; Hu, J.; Wang, D.; Li, Z.; Zhang, Q.; Luo, Y.; Yu, S.-H.; Jiang, H.-L. Visible-Light Photoreduction of CO_2 In a Metal–Organic Framework: Boosting Electron–Hole Separation via Electron Trap States. *J. Am. Chem. Soc.* **2015**, *137* (42), 13440–13443.

(16) Kornienko, N.; Zhao, Y.; Kley, C. S.; Zhu, C.; Kim, D.; Lin, S.; Chang, C. J.; Yaghi, O. M.; Yang, P. Metal–Organic Frameworks for Electrocatalytic Reduction of Carbon Dioxide. *J. Am. Chem. Soc.* **2015**, *137* (44), 14129–14135.

(17) Sende, J. R.; Arana, C. R.; Hernandez, L. Electrocatalysis of CO_2 Reduction in Aqueous Media at Electrodes Modified with Electropolymerized Films of Vinylterpyridine Complexes of Transition Metals. *Inorg. Chem.* **1995**, *34* (12), 3339–3348.

(18) Yao, S. A.; Ruther, R. E.; Zhang, L.; Franking, R. A.; Hamers, R. J.; Berry, J. F. Covalent Attachment of Catalyst Molecules to Conductive Diamond: CO_2 Reduction Using “Smart” Electrodes. *J. Am. Chem. Soc.* **2012**, *134* (38), 15632–15635.

(19) Liu, C.; Dubois, K. D.; Louis, M. E.; Vorushilov, A. S.; Li, G. Photocatalytic CO2 Reduction and Surface Immobilization of a Tricarbonyl Re(I) Compound Modified with Amide Groups. *ACS Catal.* **2013**, *3* (4), 655–662.

(20) Kang, P.; Zhang, S.; Meyer, T. J.; Brookhart, M. Rapid Selective Electrocatalytic Reduction of Carbon Dioxide to Formate by an Iridium Pincer Catalyst Immobilized on Carbon Nanotube Electrodes. *Angew. Chem. Int. Ed.* **2014**, *53* (33), 8709–8713.

(21) Neri, G.; Walsh, J. J.; Wilson, C.; Reynal, A.; Lim, J. Y. C.; Li, X.; White, A. J. P.; Long, N. J.; Durrant, J. R.; Cowan, A. J. A Functionalised Nickel Cyclam Catalyst for CO_2 Reduction: Electrocatalysis, Semiconductor Surface Immobilisation and Light-Driven Electron Transfer. *Phys. Chem. Chem. Phys.* **2014**, *17*, 1562–1566.

(22) Elgrishi, N.; Griveau, S.; Chambers, M. B.; Bedioui, F.; Fontecave, M. Versatile Functionalization of Carbon Electrodes with a Polypyridine Ligand: Metallation and Electrocatalytic H+ and CO_2 Reduction. *Chem. Commun.* **2015**, *51* (14), 2995–2998.

(23) Oh, S.; Gallagher, J. R.; Miller, J. T.; Surendranath, Y. Graphite-Conjugated Rhenium Catalysts for Carbon Dioxide Reduction. *J. Am. Chem. Soc.* **2016**, *138* (6), 1820–1823.

(24) Hawecker, J.; Lehn, J.-M.; Ziessel, R. Photochemical and Electrochemical Reduction of Carbon Dioxide to Carbon Monoxide Mediated by (2,2′-Bipyridine)Tricarbonylchlororhenium(I) and Related Complexes as Homogeneous Catalysts. *Helv. Chim. Acta* **1986**, *69* (8), 1990–2012.

(25) Kang, P.; Chen, Z.; Nayak, A.; Zhang, S.; Meyer, T. J. Single Catalyst Electrocatalytic Reduction of CO_2 In Water to H_2+CO Syngas Mixtures with Water Oxidation to O_2. *Energy Environ. Sci.* **2014**, *7*, 4007–4012.

(26) Sypaseuth, F. D.; Matlachowski, C.; Weber, M.; Schwalbe, M.; Tzschucke, C. C. Electrocatalytic Carbon Dioxide Reduction by Using Cationic Pentamethylcyclopentadienyl–Iridium Complexes with Unsymmetrically Substituted Bipyridine Ligands. *Chem. Eur. J.* **2015**, *21* (17), 6564–6571.

(27) Agarwal, J.; Shaw, T. W.; Stanton, C. J.; Majetich, G. F.; Bocarsly, A. B.; Schaefer, H. F. NHC-Containing Manganese(I) Electrocatalysts for the Two-Electron Reduction of CO_2. *Angew. Chem. Int. Ed. Engl.* **2014**, *53* (20), 5152–5155.

(28) Agarwal, J.; Shaw, T. W.; Schaefer, H. F.; Bocarsly, A. B. Design of a Catalytic Active Site for Electrochemical CO_2 Reduction with Mn(I)-Tricarbonyl Species. *Inorg. Chem.* **2015**, *54* (11), 5285–5294.

(29) Ngo, K. T.; McKinnon, M.; Mahanti, B.; Narayanan, R.; Grills, D. C.; Ertem, M. Z.; Rochford, J. Turning on the Protonation-First Pathway for Electrocatalytic CO_2 Reduction by Manganese Bipyridyl Tricarbonyl Complexes. *J. Am. Chem. Soc.* **2017**, *139* (7), 2604–2618.

(30) Costentin, C.; Drouet, S.; Robert, M.; Saveant, J. M. A Local Proton Source Enhances CO_2 Electroreduction to CO by a Molecular Fe Catalyst. *Science* **2012**, *338* (6103), 90–94.

(31) Costentin, C.; Drouet, S.; Passard, G.; Robert, M.; Savéant, J.-M. Proton-Coupled Electron Transfer Cleavage of Heavy-Atom Bonds in Electrocatalytic Processes. Cleavage of a C–O Bond in the Catalyzed Electrochemical Reduction of CO_2. *J. Am. Chem. Soc.* **2013**, *135* (24), 9023–9031.

(32) Costentin, C.; Robert, M.; Savéant, J.-M.; Tatin, A. Efficient and Selective Molecular Catalyst for the CO_2-To-CO Electrochemical Conversion in Water. *Proc. Natl. Acad. Sci. U.S.A.* **2015**, *112* (22), 6882–6886.

(33) Azcarate, I.; Costentin, C.; Robert, M.; Savéant, J.-M. Through-Space Charge Interaction Substituent Effects in Molecular Catalysis Leading to the Design of the Most Efficient Catalyst of CO_2-To-CO Electrochemical Conversion. *J. Am. Chem. Soc.* **2016**, *138* (51), 16639–16644.

(34) Azcarate, I.; Costentin, C.; Robert, M.; Savéant, J.-M. Dissection of Electronic Substituent Effects in Multielectron–Multistep Molecular Catalysis. Electrochemical CO_2-To-CO Conversion Catalyzed by Iron Porphyrins. *J. Phys. Chem. C* **2016**, *120* (51), 28951–28960.

(35) Lacy, D. C.; McCrory, C. C. L.; Peters, J. C. Studies of Cobalt-Mediated Electrocatalytic CO_2 Reduction Using a Redox-Active Ligand. *Inorg. Chem.* **2014**, *53* (10), 4980–4988.

(36) Fisher, B. J.; Eisenberg, R. Electrocatalytic Reduction of Carbon Dioxide by Using Macrocycles of Nickel and Cobalt. *J. Am. Chem. Soc.* **1980**, *102* (24), 7361–7363.

(37) Saravanakumar, D.; Song, J.; Jung, N.; Jirimali, H.; Shin, W. Reduction of CO_2 To CO at Low Overpotential in Neutral Aqueous Solution by a Ni(Cyclam) Complex Attached to Poly(Allylamine). *ChemSusChem* **2012**, *5* (4), 634–636.

(38) Froehlich, J. D.; Kubiak, C. P. Homogeneous CO_2 Reduction by Ni(Cyclam) at a Glassy Carbon Electrode. *Inorg. Chem.* **2012**, *51* (7), 3932–3934.

(39) Neri, G.; Aldous, I. M.; Walsh, J. J.; Hardwick, L. J.; Cowan, A. J. A Highly Active Nickel Electrocatalyst Shows Excellent Selectivity for CO_2 Reduction in Acidic Media. *Chem. Sci.* **2016**, *7* (2), 1521–1526.

(40) DuBois, M. R.; DuBois, D. L. The Roles of the First and Second Coordination Spheres in the Design of Molecular Catalysts for H_2 Production and Oxidation. *Chem. Soc. Rev.* **2008**, *38* (1), 62–72.

(41) Costentin, C.; Drouet, S.; Robert, M.; Savéant, J.-M. Turnover Numbers, Turnover Frequencies, and Overpotential in Molecular Catalysis of Electrochemical Reactions. Cyclic Voltammetry and Preparative-Scale Electrolysis. *J. Am. Chem. Soc.* **2012**, *134* (27), 11235–11242.

(42) Costentin, C.; Passard, G.; Robert, M.; Savéant, J.-M. Pendant Acid–Base Groups in Molecular Catalysts: H-Bond Promoters or Proton Relays? Mechanisms of the Conversion of CO_2 To CO by Electrogenerated Iron(0)Porphyrins Bearing Prepositioned Phenol Functionalities. *J. Am. Chem. Soc.* **2014**, *136* (33), 11821–11829.

(43) Costentin, C.; Passard, G.; Robert, M.; Saveant, J. M. Ultraefficient Homogeneous Catalyst for the CO_2-To-CO Electrochemical Conversion. *Proc. Natl. Acad. Sci. U.S.A.* **2014**, *111* (42), 14990–14994.

(44) Ahn, S. T.; Bielinski, E. A.; Lane, E. M.; Chen, Y.; Bernskoetter, W. H.; Hazari, N.; Palmore, G. T. R. Enhanced CO_2 Electroreduction Efficiency Through Secondary Coordination Effects on a Pincer Iridium Catalyst. *Chem. Commun.* **2015**, *51* (27), 5947–5950.

(45) Schmeier, T. J.; Dobereiner, G. E.; Crabtree, R. H.; Hazari, N. Secondary Coordination Sphere Interactions Facilitate the Insertion Step in an Iridium(III) CO_2 Reduction Catalyst. *J. Am. Chem. Soc.* **2011**, *133* (24), 9274–9277.

(46) Hull, J. F.; Himeda, Y.; Wang, W.-H.; Hashiguchi, B.; Periana, R.; Szalda, D. J.; Muckerman, J. T.; Fujita, E. Reversible Hydrogen Storage Using CO_2 And a Proton-Switchable Iridium Catalyst in Aqueous Media Under Mild Temperatures and Pressures. *Nature Chem.* **2012**, *4* (5), 383–388.

(47) Badiei, Y. M.; Wang, W.-H.; Hull, J. F.; Szalda, D. J.; Muckerman, J. T.; Himeda, Y.; Fujita, E. Cp*Co(III) Catalysts with Proton-Responsive Ligands for Carbon Dioxide Hydrogenation in Aqueous Media. *Inorg. Chem.* **2013**, *52* (21), 12576–12586.

(48) Onishi, N.; Xu, S.; Manaka, Y.; Suna, Y.; Wang, W.-H.; Muckerman, J. T.; Fujita, E.; Himeda, Y. Co_2 Hydrogenation Catalyzed by Iridium Complexes with a Proton-Responsive Ligand. *Inorg. Chem.* **2015**, *54* (11), 5114–5123.

(49) Chapovetsky, A.; Do, T. H.; Haiges, R.; Takase, M. K.; Marinescu, S. C. Proton-Assisted Reduction of CO_2 By Cobalt Aminopyridine Macrocycles. *J. Am. Chem. Soc.* **2016**, *138* (18), 5765–5768.

(50) Lubitz, W.; Ogata, H.; Rüdiger, O.; Reijerse, E. Hydrogenases. *Chem. Rev.* **2014**, *114* (8), 4081–4148.

(51) Wilson, A. D.; Newell, R. H.; McNevin, M. J.; Muckerman, J. T.; Rakowski DuBois, M.; DuBois, D. L. Hydrogen Oxidation and Production Using Nickel-Based Molecular Catalysts with Positioned Proton Relays. *J. Am. Chem. Soc.* **2006**, *128* (1), 358–366.

(52) Yang, J. Y.; Bullock, R. M.; Shaw, W. J.; Twamley, B.; Fraze, K.; DuBois, M. R.; DuBois, D. L. Mechanistic Insights Into Catalytic H_2 Oxidation by Ni Complexes Containing a Diphosphine Ligand with a Positioned Amine Base. *J. Am. Chem. Soc.* **2009**, *131* (16), 5935–5945.

(53) Yang, J. Y.; Chen, S.; Dougherty, W. G.; Kassel, W. S.; Bullock, R. M.; DuBois, D. L.; Raugei, S.; Rousseau, R.; Dupuis, M.; DuBois, M. R. Hydrogen Oxidation Catalysis by a Nickel Diphosphine Complex with Pendant Tert-Butyl Amines. *Chem. Commun.* **2010**, *46* (45), 8618.

(54) Smith, S. E.; Yang, J. Y.; DuBois, D. L.; Bullock, R. M. Reversible Electrocatalytic Production and Oxidation of Hydrogen at Low Overpotentials by a Functional Hydrogenase Mimic. *Angew. Chem. Int. Ed. Engl.* **2012**, *51* (13), 3152–3155.

(55) Liu, T.; DuBois, D. L.; Bullock, R. M. An Iron Complex with Pendent Amines as a Molecular Electrocatalyst for Oxidation of Hydrogen. *Nature Chem.* **2013**, *5* (3), 228–233.

(56) Yang, J. Y.; Smith, S. E.; Liu, T.; Dougherty, W. G.; Hoffert, W. A.; Kassel, W. S.; DuBois, M. R.; DuBois, D. L.; Bullock, R. M. Two Pathways for Electrocatalytic Oxidation of Hydrogen by a Nickel Bis(Diphosphine) Complex with Pendant Amines in the Second Coordination Sphere. *J. Am. Chem. Soc.* **2013**, *135* (26), 9700–9712.

(57) Dutta, A.; DuBois, D. L.; Roberts, J. A. S.; Shaw, W. J. Amino Acid Modified Ni Catalyst Exhibits Reversible H 2oxidation/Production Over a Broad pH Range at Elevated Temperatures. *Proc. Natl. Acad. Sci. U.S.A.* **2014**, *111* (46), 16286–16291.

(58) Wiese, S.; Kilgore, U. J.; Ho, M.-H.; Raugei, S.; DuBois, D. L.; Bullock, R. M.; Helm, M. L. Hydrogen Production Using Nickel Electrocatalysts with Pendant Amines: Ligand Effects on Rates and Overpotentials. *ACS Catal.* **2013**, 2527–2535.

(59) Kilgore, U. J.; Stewart, M. P.; Helm, M. L.; Dougherty, W. G.; Kassel, W. S.; DuBois, M. R.; DuBois, D. L.; Bullock, R. M. Studies of a Series of $[Ni(PR_2NPh_2)_2(CH_3CN)]^{2+}$ Complexes as Electrocatalysts for H_2 Production: Substituent Variation at the Phosphorus Atom of the P_2N_2 Ligand. *Inorg. Chem.* **2011**, *50* (21), 10908–10918.

(60) Wiedner, E. S.; Appel, A. M.; DuBois, D. L.; Bullock, R. M. Thermochemical and Mechanistic Studies of Electrocatalytic Hydrogen Production by Cobalt Complexes Containing Pendant Amines. *Inorg. Chem.* **2013**, *52* (24), 14391–14403.

(61) Kilgore, U. J.; Roberts, J. A. S.; Pool, D. H.; Appel, A. M.; Stewart, M. P.; DuBois, M. R.; Dougherty, W. G.; Kassel, W. S.; Bullock, R. M.; DuBois, D. L. $[Ni(PPh_2NC_6H_4X_2)_2]^{2+}$ Complexes as Electrocatalysts for H_2 Production: Effect of Substituents, Acids, and Water on Catalytic Rates. *J. Am. Chem. Soc.* **2011**, *133* (15), 5861–5872.

(62) Pool, D. H.; DuBois, D. L. $[Ni(PPh_2NAr_2)_2(NCMe)][BF_4]_2$ As an Electrocatalyst for H_2 Production: PPh_2NAr_2=1,5-(Di(4-(Thiophene-3-yl)Phenyl)-3,7-Diphenyl-1,5-Diaza-3,7-Diphosphacyclooctane). *J. Organomet. Chem.* **2009**, *694* (17), 2858–2865.

(63) Wiedner, E. S.; Yang, J. Y.; Dougherty, W. G.; Kassel, W. S.; Bullock, R. M.; DuBois, M. R.; DuBois, D. L. Comparison of Cobalt and Nickel Complexes with Sterically Demanding Cyclic Diphosphine Ligands: Electrocatalytic H_2 Production by $[Co(P^{tBu}{}_2N^{Ph}{}_2)(CH_3CN)_3](BF_4)_2$. *Organometallics* **2010**, *29* (21), 5390–5401.

(64) Fang, M.; Wiedner, E. S.; Dougherty, W. G.; Kassel, W. S.; Liu, T.; DuBois, D. L.; Bullock, R. M. Cobalt Complexes Containing Pendant Amines in the Second Coordination Sphere as Electrocatalysts for H_2 Production. *Organometallics* **2014**, *33* (20), 5820–5833.

(65) Wilson, A. D.; Shoemaker, R. K.; Miedaner, A.; Muckerman, J. T.; DuBois, D. L.; DuBois, M. R. Coordination Chemistry of Saturated Molecules Special Feature: Nature of Hydrogen Interactions with Ni(II) Complexes Containing Cyclic Phosphine Ligands with Pendant Nitrogen Bases. *Proc. Natl. Acad. Sci. U.S.A.* **2007**, *104* (17), 6951–6956.

(66) Helm, M. L.; Stewart, M. P.; Bullock, R. M.; DuBois, M. R.; DuBois, D. L. A Synthetic Nickel Electrocatalyst with a Turnover Frequency Above 100,000 S^{-1} for H_2 Production. *Science* **2011**, *333* (6044), 863–866.

(67) Nippe, M.; Khnayzer, R. S.; Panetier, J. A.; Zee, D. Z.; Olaiya, B. S.; Head-Gordon, M.; Chang, C. J.; Castellano, F. N.; Long, J. R. Catalytic Proton Reduction with Transition Metal Complexes of the Redox-Active Ligand bpy2PYMe. *Chem. Sci.* **2013**, *4* (10), 3934–3945.

(68) Armstrong, F. A.; Hirst, J. Reversibility and Efficiency in Electrocatalytic Energy Conversion and Lessons From Enzymes. *Proc. Natl. Acad. Sci. U.S.A.* **2011**, *108* (34), 14049–14054.

(69) Can, M.; Armstrong, F. A.; Ragsdale, S. W. Structure, Function, and Mechanism of the Nickel Metalloenzymes, CO Dehydrogenase, and Acetyl-CoA Synthase. *Chem. Rev.*

2014, *114* (8), 4149–4174.
(70) Taheri, A.; Thompson, E. J.; Fettinger, J. C.; Berben, L. A. An Iron Electrocatalyst for Selective Reduction of CO_2 To Formate in Water: Including Thermochemical Insights. *ACS Catal.* **2015**, 7140–7151.
(71) Chen, L.; Guo, Z.; Wei, X.-G.; Gallenkamp, C.; Bonin, J.; Anxolabéhère-Mallart, E.; Lau, K.-C.; Lau, T.-C.; Robert, M. Molecular Catalysis of the Electrochemical and Photochemical Reduction of CO_2 With Earth-Abundant Metal Complexes. Selective Production of CO vs HCOOH by Switching of the Metal Center. *J. Am. Chem. Soc.* **2015**, *137* (34), 10918–10921.
(72) Bhugun, I.; Lexa, D.; Savéant, J.-M. Ultraefficient Selective Homogeneous Catalysis of the Electrochemical Reduction of Carbon Dioxide by an Iron(0) Porphyrin Associated with a Weak Brönsted Acid Cocatalyst. *J. Am. Chem. Soc.* **1994**, *116* (11), 5015–5016.
(73) Bhugun, I.; Lexa, D.; Savéant, J.-M. Catalysis of the Electrochemical Reduction of Carbon Dioxide by Iron(0) Porphyrins: Synergystic Effect of Weak Brönsted Acids. *J. Am. Chem. Soc.* **1996**, *118* (7), 1769–1776.
(74) Bhugun, I.; Lexa, D.; Savéant, J.-M. Catalysis of the Electrochemical Reduction of Carbon Dioxide by Iron(0) Porphyrins. Synergistic Effect of Lewis Acid Cations. *J. Phys. Chem.* **1996**, *100* (51), 19981–19985.
(75) Khnayzer, R. S.; Thoi, V. S.; Nippe, M.; King, A. E.; Jurss, J. W.; Roz, El, K. A.; Long, J. R.; Chang, C. J.; Castellano, F. N. Towards a Comprehensive Understanding of Visible-Light Photogeneration of Hydrogen From Water Using Cobalt(II) Polypyridyl Catalysts. *Energy Environ. Sci.* **2014**, *7*, 1477–1488.
(76) Riedel, P. J.; Arulsamy, N.; Mehn, M. P. Facile Routes to Manganese(II) Triflate Complexes. *Inorg. Chem. Commun.* **2011**, *14* (5), 734–737.
(77) Evans, D. F. The Determination of the Paramagnetic Susceptibility of Substances in Solution by Nuclear Magnetic Resonance. *J. Chem. Soc.* **1959**, 2003–2005.
(78) Ünal, E. A.; Wiedemann, D.; Seiffert, J.; Boyd, J. P.; Grohmann, A. Efficient Synthesis of Pentakis- and Tris(Pyridine) Ligands. *Tet. Lett.* **2012**, *53* (1), 54–55.
(79) APEX2. v. 2009; Bruker Analytical X-ray Systems, Inc; Madison, WI, 2009.
(80) Sheldrick, G. M. Version 2.03; Bruker Analytical Systems, Inc.: Madison, WI, 2000.
(81) Sheldrick, G. SHELXT - Integrated Space-Group and Crystal-Structure Determination. *Acta Crystallogr A Found Adv* **2015**, *71* (1), 3–8.
(82) Sheldrick, G. A Short History of SHELX. *Acta Crystallogr A Found Crystallogr* **2008**, *64* (1), 112–122.
(83) Sheldrick, G. Crystal Structure Refinement with SHELXL. *Acta Crystallogr C Struct Chem* **2015**, *71* (1), 3–8.
(84) van der Sluis, P.; Spek, A. L. BYPASS: an Effective Method for the Refinement of Crystal Structures Containing Disordered Solvent Regions. *Acta Crystallogr A Found Crystallogr* **1990**, *46* (3), 194–201.
(85) Kang, P.; Cheng, C.; Chen, Z.; Schauer, C. K.; Meyer, T. J.; Brookhart, M. Selective Electrocatalytic Reduction of CO_2 To Formate by Water-Stable Iridium Dihydride Pincer Complexes. *J. Am. Chem. Soc.* **2012**, *134* (12), 5500–5503.
(86) Karunadasa, H. I.; Chang, C. J.; Long, J. R. A Molecular Molybdenum-Oxo Catalyst for Generating Hydrogen From Water. *Nature* **2010**, *464* (7293), 1329–1333.
(87) Karunadasa, H. I.; Montalvo, E.; Sun, Y.; Majda, M.; Long, J. R.; Chang, C. J. A

Molecular MoS_2 Edge Site Mimic for Catalytic Hydrogen Generation. *Science* **2012**, *335* (6069), 698–702.

(88) Sundstrom, E. J.; Yang, X.; Thoi, V. S.; Karunadasa, H. I.; Chang, C. J.; Long, J. R.; Head-Gordon, M. Computational and Experimental Study of the Mechanism of Hydrogen Generation From Water by a Molecular Molybdenum-Oxo Electrocatalyst. *J. Am. Chem. Soc.* **2012**, *134* (11), 5233–5242.

(89) Thoi, V. S.; Karunadasa, H. I.; Surendranath, Y.; Long, J. R.; Chang, C. J. Electrochemical Generation of Hydrogen From Acetic Acid Using a Molecular Molybdenum–Oxo Catalyst. *Energy Environ. Sci.* **2012**, *5* (7), 7762–7770.

(90) Bigi, J. P.; Hanna, T. E.; Harman, W. H.; Chang, A.; Chang, C. J. Electrocatalytic Reduction of Protons to Hydrogen by a Water-Compatible Cobalt Polypyridyl Platform. *Chem. Commun.* **2010**, *46* (6), 958–960.

(91) Sun, Y.; Bigi, J. P.; Piro, N. A.; Tang, M. L.; Long, J. R.; Chang, C. J. Molecular Cobalt Pentapyridine Catalysts for Generating Hydrogen From Water. *J. Am. Chem. Soc.* **2011**, *133* (24), 9212–9215.

(92) King, A. E.; Surendranath, Y.; Piro, N. A.; Bigi, J. P.; Long, J. R.; Chang, C. J. A Mechanistic Study of Proton Reduction Catalyzed by a Pentapyridine Cobalt Complex: Evidence for Involvement of an Anation-Based Pathway. *Chem. Sci.* **2013**, *4*, 1578–1587.

(93) Sun, Y.; Sun, J.; Long, J. R.; Yang, P.; Chang, C. J. Photocatalytic Generation of Hydrogen From Water Using a Cobalt Pentapyridine Complex in Combination with Molecular and Semiconductor Nanowire Photosensitizers. *Chem. Sci.* **2013**, *4* (1), 118–124.

(94) Jurss, J. W.; Khnayzer, R. S.; Panetier, J. A.; Roz, El, K. A.; Nichols, E. M.; Head-Gordon, M.; Long, J. R.; Castellano, F. N.; Chang, C. J. Bioinspired Design of Redox-Active Ligands for Multielectron Catalysis: Effects of Positioning Pyrazine Reservoirs on Cobalt for Electro- and Photocatalytic Generation of Hydrogen From Water. *Chem. Sci.* **2015**, *6* (8), 4954–4972.

(95) Hansch, C.; Leo, A.; Taft, R. W. A Survey of Hammett Substituent Constants and Resonance and Field Parameters. *Chem. Rev.* **1991**, *91*, 165–195.

(96) Bordwell, F. G. Equilibrium Acidities in Dimethyl Sulfoxide Solution. *Acc. Chem. Res.* **1988**, *21* (12), 456–463.

(97) Mukhopadhyay, T. K.; MacLean, N. L.; Gan, L.; Ashley, D. C.; Groy, T. L.; Baik, M.-H.; Jones, A. K.; Trovitch, R. J. Carbon Dioxide Promoted H+ Reduction Using a Bis(Imino)Pyridine Manganese Electrocatalyst. *Inorg. Chem.* **2015**, *54* (9), 4475–4482.

(98) Pun, S.-N.; Chung, W.-H.; Lam, K.-M.; Guo, P.; Chan, P.-H.; Wong, K.-Y.; Che, C.-M.; Chen, T.-Y.; Peng, S.-M. Iron(I) Complexes of 2,9-Bis(2-Hydroxyphenyl)-1,10-Phenanthroline (H_2Dophen) as Electrocatalysts for Carbon Dioxide Reduction. X-Ray Crystal Structures of $[Fe(Dophen)Cl]_2 \cdot 2HCON(CH_3)_2$ And $[Fe(Dophen)(N\text{-}MeIm)_2]ClO_4$ (*N*-MeIm = 1-Methylimidazole). *J. Chem. Soc., Dalton Trans.* **2002**, *291* (4), 575–579.

(99) Sawyer, D. T.; Sobkowiak, A.; Roberts, J. L. *Electrochemistry for Chemists*, 2nd ed.; John Wiley and Sons, Inc., 1995.

(100) Connelly, N. G.; Geiger, W. E. Chemical Redox Agents for Organometallic Chemistry. *Chem. Rev.* **1996**, *96* (2), 877–910.

(101) Dobereiner, G. E.; Wu, J.; Manas, M. G.; Schley, N. D.; Takase, M. K.; Crabtree, R.

H.; Hazari, N.; Maseras, F.; Nova, A. Mild, Reversible Reaction of Iridium(III) Amido Complexes with Carbon Dioxide. *Inorg. Chem.* **2012**, *51* (18), 9683–9693.

(102) Yamaguchi, S.; Takahashi, T.; Wada, A.; Funahashi, Y.; Ozawa, T.; Jitsukawa, K.; Masuda, H. Fixation of CO_2 By Hydroxozinc(II) Complex with Pyridylamino Type Ligand. *Chem. Lett.* **2007**, *36* (7), 842–843.

(103) Sander, R. Compilation of Henry's Law Constants (Version 4.0) for Water as Solvent. *Atmos. Chem. Phys.* **2015**, *15* (8), 4399–4981.

(104) Gennaro, A.; Isse, A. A.; Vianello, E. Solubility and Electrochemical Determination of CO_2 In Some Dipolar Aprotic Solvents. *J. Electroanal. Chem.* **1990**, *289* (1–2), 203–215.

Chapter 4. Towards Coordinatively-Unsaturated First-Row Transition Metal Pentapyridine Complexes with Tetrakis(3,5-(Trifluoromethyl)phenyl)borate Anions

4.1. Introduction

Prior work by the Long and Chang groups and as detailed in the preceding Chapters have together demonstrated the utility of neutral, semi-rigid polypyridine ligand scaffolds towards supporting cationic transition metal electrocatalysts for proton[1-6] and carbon dioxide reduction (Chapter 3). In particular, the neutral, weak-field polypyridine ligands afford metal complexes that are sufficiently electrophilic and easy to reduce. The coordinative unsaturation of the metal complex permits reactivity. In the case of Co-based proton reduction, a low-valent Co(I) center acts as a nucleophile towards H^+.[6] In $[(PY5Me_2)Mo]^{2+}$, the vacant site allows coordination of water and subsequent oxidative addition of an O–H bond.[2,7]

For the majority of work involving transition metal complexes of polypyridine ligands, attention was focused on their trifluoromethanesulfonate salts.[1-6] As such their chemistries were predominantly explored in strongly coordinating solvents such as acetonitrile, water, and methanol, all of which are good donor solvents[8] that can outcompete binding by small, nonpolar molecules such as H_2, N_2, and CO_2.

Owing to their large size and delocalized negative charge, the development of weakly coordinating anions[9-11] enabled the isolation and characterization of reactive cations and novel, unusual coordination complexes. In particular, cationic, coordinatively unsaturated metal centers have been demonstrated to trap very weak σ donors. In a seminal study, Brookhart and coworkers protonated a rhodium(I) methyl complex with the oxonium acid $[H(OEt_2)_2][B(C_6H_3(CF_3)_2)_4]$ to generate and characterize a transient rhodium(I) σ-methane complex.[12] Extension of this work led to the isolation of Rh(I)-$ClCH_2Cl$ and Rh(I)-N_2 complexes.[13] Protonation of a trigonal bipyramidal Ni(II) alkyl complex afforded a cationic Ni(II)-N_2 complex that shows minimal π back-bonding and activation.[14] Interestingly, substitutions of the ligand scaffold of the nickel complex show that the metal–N_2 binding affinity increases with the N_2 stretching frequency, attesting to the fact that the Ni(II)-N_2 interaction is predominantly an electrophilic σ interaction. Overall, these systems share the commonality that they are cationic, electrophilic centers that interact with substrates in a predominantly σ fashion, and the electrophilicity is directed towards the substrate of interest using weakly coordinating anions and robust, weakly coordinating solvents.

Thus, given the affinity the $PY5Me_2$ ligand for divalent transition metal ions, this semi-rigid neutral ligand scaffold provides an opportunity to generate dicationic, coordinatively-unsaturated metal centers. The work in this Chapter explores the synthetic methods and challenges for such electrophilic complexes. The ligand binding at these metal centers are explored, with an eye on very weakly σ-donating π-acids N_2, CO, ethylene, where the interplay of empty σ-accepting orbitals and filled π-donating orbitals at the metal will be particularly critical.

4.2. Experimental

4.2.1. Materials and Methods

Air- and/or moisture-sensitive compounds were synthesized and manipulated under air-free conditions, using either a Vacuum Atmospheres glovebox or standard Schlenk techniques under a dry nitrogen or argon atmosphere. Anhydrous tetrahydrofuran (THF), diethyl ether (Et_2O), acetonitrile, hexanes, toluene, 1,2-difluorobenzene (DFB), and 1,4-dioxane were dried and deoxygenated with a commercial solvent purification system from JC Meyer Solvent Systems, then stored under an inert atmosphere over beads of 3 Å molecular sieves. 1,2-Dimethoxyethane (DME) was dried over Na-benzophenone ketyl for 24 h, distilled, and stored over 3 Å molecular sieves.

The compounds $CuCl_2$, $ZnCl_2$, and trimethylsilyltrifluoromethanesulfonate were purchased from Sigma Aldrich and used as received. Anhydrous $TiCl_2$ and VCl_2 were purchased from American Elements and used as received. Celite® 545 (Sigma Aldrich) was dried under vacuum at 120 °C for 12 h prior to use.

The compounds $PY5Me_2$,[15] potassium tetrakis(3,5-bis(trifluoromethyl)phenyl)borate,[16] thallium tetrakis(3,5-bis(trifluoromethyl)phenyl)borate,[16] $NiCl_2(DME)$,[17] $VCl_2(tmeda)_2$,[18] potassium graphite[19] and hexakis(acetonitrile)vanadium(II) bis(trifluoromethanesulfonate)[15] were prepared according to literature methods. The metal chloride tetrahydrofuran complexes $TiCl_4(THF)_2$, $VCl_3(THF)_3$, $CrCl_2(THF)$, $FeCl_2(THF)_{1.5}$, and $CoCl_2(THF)_{1.2}$ were prepared by treatment of the anhydrous metal chloride with tetrahydrofuran according to a literature procedure,[20] and their tetrahydrofuran contents were confirmed by elemental analysis. The compound $TiCl_3(THF)_3$ was prepared by extraction of $3TiCl_3 \cdot AlCl_3$ (Alfa Aesar), according to a published procedure.[21]

The oxonium acid $[H(OEt_2)_2][B(C_6H_3(CF_3)_2)_4]$ was prepared with adjustments from a literature procedure[22]—commercial hydrogen chloride (2.0 M in diethyl ether, Sigma Aldrich) was used instead of gaseous hydrogen chloride, and the glassware used for the preparation was silanized (see below) before use. The $[H(OEt_2)_2][B(C_6H_3(CF_3)_2)_4]$ product was judged to be free of water based on the chemical shift of oxonium proton at δ 16.5 ppm[23] and elemental analysis.

The compounds methylmagnesium chloride (3.0 M in tetrahydrofuran) and phenylmagnesium chloride (2.0 M in tetrahydrofuran) were purchased from Sigma Aldrich and diluted with anhydrous tetrahydrofuran to give stock solutions. Their concentrations were determined using a No-D ^1H NMR technique described by Hoye and coworkers[24] or by colorimetric titration.[25]

NMR spectra were obtained using a Bruker AVANCE III instrument and referenced relative to tetramethylsilane using residual solvent signals. Deuterated solvents were purchased from Cambridge Isotopes. CD_3CN (99.8% D) and CD_2Cl_2 (99.8% D) were dried over powdered 3 Å molecular sieves for 48 h, separated from the sieves by vacuum transfer, deoxygenated by freeze-pump-thaw cycles, and stored over beads of 3 Å molecular sieves under an inert atmosphere.

Electrospray ionization mass spectrometry (ESI-MS) measurements were performed using an Agilent 6230 time-of-flight mass spectrometer equipped with an Agilent Jet Stream source. Carbon, hydrogen, and nitrogen analyses were obtained from the Microanalytical Laboratory at the University of California, Berkeley.

4.2.2. Silanization of Glassware

Due to the high electrophilicity in coordinatively-unsaturated dicationic metal complexes, glassware involved with their preparation and characterization were silylated using a procedure adapted from the literature.[26,27] Vials and J. Young tubes were charged with ~100 μL of *N*,*O*-bis(trimethylsilyl)acetamide (Oakwood Chemicals), sealed, then heated to 120 °C for at least 2 h. The glassware was cooled to room temperature, then thoroughly rinsed with acetone. Successful passivation of glassware was checked by observing whether water formed convex beads on the glass surface. The cleaned glassware was heated in an oven at 165 °C for at least 2 h, then cycled into a glovebox while hot.

4.2.3. Synthesis

General synthetic procedure for divalent [(PY5Me$_2$)MCl][B(C$_6$H$_3$(CF$_3$)$_2$)$_4$] complexes (M = Cr, Fe, Co, Ni, Cu, Zn). In a N$_2$-filled glovebox, equimolar quantities of PY5Me$_2$, metal dichloride tetrahydrofuran complex, and K[B(C$_6$H$_3$(CF$_3$)$_2$)$_4$] were vigorously stirred in ~5 mL of DFB or DME for 12 h. During this time, the reagents dissolved to give, except for the zinc complex, colored solutions and colorless precipitates of KCl. The KCl was removed from the solution by vacuum filtration through a fine glass frit packed with ~1 inch of Celite®. The Celite® was washed with additional DFB (3 × ~1 mL) until the washes were colorless. The combined filtrate was reduced to ~5 mL in volume under vacuum. Addition of hexanes (~15 mL) to this solution precipitated microcrystalline solids. The crystals were isolated from the mother liquor, washed with aliquots of hexanes (3 × ~3 mL), and dried under high vacuum at room temperature until constant weight was achieved.

[(PY5Me$_2$)CrCl][B(C$_6$H$_3$(CF$_3$)$_2$)$_4$] (4.1Cl). The compounds PY5Me$_2$ (150 mg, 338 μmol), CrCl$_2$(THF) (65.9 mg, 338 μmol), and K[B(C$_6$H$_3$(CF$_3$)$_2$)$_4$] (305 mg, 338 μmol) afforded dark green, microcrystalline needles, which was a DFB solvate. Yield: 494 mg (90%). ESI-MS *m*/*z* for [(PY5Me$_2$)CrCl]$^+$ requires 530.1198, found 530.1202. Anal. Calcd. for C$_{73}$H$_{45}$BClCrF$_{28}$N$_5$ (**4.1Cl**·2DFB): C, 54.04; H, 2.80; N, 4.32. Found: C, 53.74; H, 2.59; N, 4.21.

[(PY5Me$_2$)FeCl][B(C$_6$H$_3$(CF$_3$)$_2$)$_4$] (4.2Cl). The compounds PY5Me$_2$ (110 mg, 255 μmol), FeCl$_2$(THF)$_{1.5}$ (59.8 mg, 255 μmol), and K[B(C$_6$H$_3$(CF$_3$)$_2$)$_4$] (230 mg, 255 μmol) afforded yellow-brown crystals. Yield: 292 mg (82%). ESI-MS *m*/*z* for [(PY5Me$_2$)FeCl]$^+$ requires 534.1142, found 534.1146. Anal. Calcd. for C$_{61}$H$_{37}$BClFeF$_{24}$N$_5$: C, 52.41; H, 2.67; N, 5.01. Found: C, 52.08; H, 2.36; N, 4.82.

[(PY5Me$_2$)CoCl][B(C$_6$H$_3$(CF$_3$)$_2$)$_4$] (4.3Cl). The compounds PY5Me$_2$ (150 mg, 338 μmol), CoCl$_2$(THF)$_{1.2}$ (80.4 mg, 340 μmol), and K[B(C$_6$H$_3$(CF$_3$)$_2$)$_4$] (305 mg, 340 μmol) afforded pale orange crystalline solids. Yield: 407 mg (86%). ESI-MS *m*/*z* for [(PY5Me$_2$)CoCl]$^+$ requires 537.1125, found 537.1141. Anal. Calcd. for C$_{61}$H$_{37}$BClCoF$_{24}$N$_5$: C, 52.29; H, 2.66; N, 5.00. Found: C, 52.09; H, 2.27; N, 5.31.

[(PY5Me$_2$)NiCl][B(C$_6$H$_3$(CF$_3$)$_2$)$_4$] (4.4Cl). The compounds PY5Me$_2$ (150 mg, 338 μmol), NiCl$_2$(DME) (74.3 mg, 338 μmol), and K[B(C$_6$H$_3$(CF$_3$)$_2$)$_4$] (305 mg, 338 μmol) gave lavender microcrystalline needles. Yield: 419 mg (88%). ESI-MS *m*/*z* for [(PY5Me$_2$)NiCl]$^+$ requires 536.1146, found 536.1139. Anal. Calcd. for C$_{61}$H$_{37}$BClNiF$_{24}$N$_5$: C, 52.29; H, 2.66; N, 5.00. Found: C, 52.09; H, 2.27; N, 5.31.

[(κ^4-PY5Me$_2$)CuCl][B(C$_6$H$_3$(CF$_3$)$_2$)$_4$] (4.5Cl). The compounds PY5Me$_2$ (150 mg, 338 μmol), CuCl$_2$ (45.4 mg, 338 μmol), and K[B(C$_6$H$_3$(CF$_3$)$_2$)$_4$] (305 mg, 338 μmol) afforded blue, microcrystalline solids. Yield = 409 mg (86%). ESI-MS *m*/*z* for [(PY5Me$_2$)CuCl]$^+$ requires 541.1089, found 541.1092. Anal. Calcd. for C$_{61}$H$_{37}$BClCuF$_{24}$N$_5$: C, 52.12; H, 2.65; N, 4.98. Found: C, 52.91; H, 2.64; N, 4.61.

[(PY5Me$_2$)ZnCl][B(C$_6$H$_3$(CF$_3$)$_2$)$_4$] (4.6Cl). The compounds PY5Me$_2$ (150 mg, 338 μmol), ZnCl$_2$ (46.1 mg, 338 μmol), and K[B(C$_6$H$_3$(CF$_3$)$_2$)$_4$] (305 mg, 338 μmol) gave a white, free-flowing powder. Yield: 423 mg (89%). ESI-MS *m*/*z* for [(PY5Me$_2$)ZnCl]$^+$ requires 542.1084, found 542.1077. Anal Calcd. for C$_{61}$H$_{37}$BClF$_{24}$N$_5$Zn: C, 52.05; H, 2.65; N, 4.98. Found: C, 52.24; H, 2.64; N, 4.61.

[(PY5Me$_2$)TiCl][B(C$_6$H$_3$(CF$_3$)$_2$)$_4$]$_2$ (4.7Cl). From TiCl$_3$(THF)$_3$: In a N$_2$-filled glovebox, PY5Me$_2$ (100 mg, 225 μmol), TiCl$_3$(THF)$_3$ (83.4 mg, 225 μmol), and K[B(C$_6$H$_3$(CF$_3$)$_2$)$_4$] (406 mg, 450 μmol) were weighed into a 20 mL scintillation vial and stirred in ~5 mL of DFB for 8 h to give an orange solution with colorless precipitates of KCl. The solution was filtered through a fine-fritted filter padded with Celite®. The Celite® was washed with additional DFB (3 × ~1 mL) until the washes were colorless. The combined orange filtrate was concentrated to ~5 mL, and addition of hexanes (~15 mL) afforded orange, microcrystalline solids. The crystals were isolated, washed with three 1 mL portions of hexanes, and dried under vacuum at room temperature until its weight was constant. Yield: 456 mg (90%). ESI-MS *m*/*z* for $[(PY5Me_2)TiCl]^{2+}$ requires 263.0633, found 263.0633. Anal. Calcd. for $C_{93}H_{49}B_2ClF_{48}N_5Ti$: C, 49.57; H, 2.19; N, 3.11. Found: C, 49.67; H, 2.06; N, 2.82.

4.7Cl from $TiCl_4(THF)_2$: In a N_2-filled glovebox, PY5Me$_2$ (150 mg, 338 μmol) and $TiCl_4(THF)_2$ (112 mg, 338 μmol) were weighed into a 20 mL scintillation vial and stirred in ~3 mL of DFB for 30 min to give a yellow slurry. A solution of $K[B(C_6H_3(CF_3)_2)_4]$ (895 mg, 1.01 mmol) in ~5 mL DFB was added to the reaction, affording immediately an orange solution with colorless precipitates. The reaction was stirred at room temperature for an additional 8 h, after which the orange solution was filtered through a fine-fritted filter padded with Celite® to remove KCl. The Celite® was washed with additional DFB (3 × ~1 mL) until the washes were colorless. Concentration of the filtrate to ~8 mL and addition of hexanes (~12 mL) afforded orange, microcrystalline solids in a faint yellow solution. The crystals were isolated, washed with portions of hexanes (3 × ~2 mL), and dried under vacuum at room temperature. Yield = 615 mg (81%).

$[(PY5Me_2)VCl][B(C_6H_3(CF_3)_2)_4]_2$ (4.8Cl). In a N_2-filled glovebox, PY5Me$_2$ (120 mg, 270 μmol), $VCl_3(THF)_3$ (100 mg, 270 μmol), and $K[B(C_6H_3(CF_3)_2)_4]$ (487 mg, 540 μmol) were weighed into a 20 mL scintillation vial and stirred in ~5 mL of DFB for 8 h to give a pink-purple solution with colorless precipitates of KCl. The reaction was stirred at room temperature for an additional 8 h, after which the purple solution was filtered through a fine-fritted filter padded with Celite® to remove KCl. The Celite® was washed with additional DFB (3 × ~1 mL) until the washes were colorless. The filtrate was combined and concentrated to ~5 mL, and addition of hexanes (~15 mL) afforded red crystals in a pink solution. The crystals were isolated, washed with portions of hexanes (3 × ~1 mL), and dried under vacuum at room temperature to afford a red solid. Yield = 389 mg (64%). ESI-MS *m*/*z* for $[(PY5Me_2)VCl]^{2+}$ requires 264.5614, found 264.5608. Anal. Calcd. for $C_{93}H_{49}B_2ClF_{48}N_5V$: C, 49.50; H, 2.19; N, 3.10. Found: C, 49.87; H, 1.93; N, 2.99.

$[(PY5Me_2)TiCl][B(C_6H_3(CF_3)_2)_4]$ (4.9Cl). In a N_2-filled glovebox, PY5Me$_2$ (100 mg, 225 μmol), $TCl_3(THF)_3$ (83.5 mg, 225 μmol), and $K[B(C_6H_3(CF_3)_2)_4]$ (203 mg, 225 μmol) were weighed into a 20 mL scintillation vial and stirred in ~5 mL of DME at 60 °C for 1 h to give an orange solution with colorless precipitate. The reaction was cooled to room temperature, then KC_8 (30.4 mg, 225 μmol) was added in one portion. The color of the reaction immediately turned dark, inky blue. The solution was stirred at room temperature for an additional 30 min, then the solvent was removed to give a dark solid. The solid was dissolved into ~5 mL of DFB to give a dark blue solution, which was filtered through Celite® to remove graphite and KCl. The Celite® was washed with additional portions of DFB (3 × ~1 mL) until the washes were colorless. The combined filtrate was reduced to ~5 mL in volume. Addition of hexanes (~15 mL) precipitated the product as small, dark blue crystals in a light green supernatant. The crystals were isolated, washed with hexanes (3 × ~1 mL), and dried under vacuum at constant weight to afford a dark blue, crystalline powder. Yield = 109 mg (69%). Elemental analyses for this compound were inconsistent. Anal. Calcd. for $C_{61}H_{37}BClF_{24}N_5Ti$: C, 52.71; H, 2.68; N, 5.04. Found (for three trials): C, 50.52–53.42; H, 2.75–3.11; N, 4.01–5.13. This compound is best stored at −35 °C in a glovebox.

$[(PY5Me_2)VCl][B(C_6H_3(CF_3)_2)_4]$ (4.10Cl). In a N_2-filled glovebox, PY5Me$_2$ (100 mg, 225 μmol), $VCl_3(THF)_3$ (84.1 mg, 225 μmol), and $K[B(C_6H_3(CF_3)_2)_4]$ (203 mg, 225 μmol) were weighed into a 20 mL scintillation vial and stirred in ~5 mL of DME at 60 °C for 1 h to give a lavender solution with colorless precipitate. The reaction was cooled to room temperature, then KC_8 (30.4 mg, 225 µmol) was added in one portion. The color of the reaction immediately turned dark, inky purple. The reaction was stirred at room temperature for an additional 30 min, then the solvent was removed under vacuum to give a dark solid. The solid was dissolved into ~5 mL DFB to give a dark purple solution, which was filtered through Celite® to remove graphite and KCl. The Celite® was washed with additional portions of DFB (3 × ~1 mL) until the washes were colorless. The combined filtrate was reduced to ~5 mL in volume. Addition of hexanes (~15 mL) precipitated the product as small, dark purple crystals. The crystals were isolated, washed with hexanes (3 × ~1 mL), and dried under vacuum at constant weight to afford a dark purple, crystalline powder. Yield = 142 mg (90%). ESI-MS *m*/*z* for $[(PY5Me_2)VCl]^+$ requires 529.1233, found 529.1236. Anal. Calcd. for $C_{61}H_{37}BClF_{24}N_5V$: C, 52.59; H, 2.68; N, 5.03. Found: C, 52.50; H, 2.98; N, 4.85.

$[(PY5Me_2)CrCH_3][B(C_6H_3(CF_3)_2)_4]$ (4.1CH$_3$). In a N_2-filled glovebox, the compound **4.1Cl** (249 mg, 153 µmol) was dissolved into 2 mL of THF and 2 mL of 1,4-dioxane to give a dark green solution. Methylmagnesium chloride (510 µL of a 300(8) µM solution, 153 µmol) was added in one portion, giving a slight color change to dark olive and precipitation of colorless solids. The reaction was stirred at room temperature for 8 h, after which the solvent was removed to give a dark green solid. The solid was dissolved into ~2 mL of DFB and filtered through a fine-fritted filter padded with Celite® to remove $MgCl_2$(dioxane). The Celite® was washed with additional portions of DFB (3 × ~1 mL) until the washes were colorless. The combined filtrate was reduced to ~4 mL in volume. Addition of hexanes (~16 mL) induced immediate formation of dark green crystals, which were isolated, rinsed with hexanes (3 × ~2mL), and dried under vacuum at room temperature. Yield = 186 mg (76%). ESI-MS *m*/*z* for $[(PY5Me_2)CrCH_3]^+$ requires 508.1800, found 508.1797. Anal. Calcd. for $C_{74}H_{48}BCrF_{28}N_5$ (**4.1CH$_3$**·2DFB): C, 55.48; H, 3.02; N, 4.37. Found: C, 55.46; H, 3.08; N, 4.62.

$[(PY5Me_2)FeCH_3][B(C_6H_3(CF_3)_2)_4]$ (4.2CH$_3$). In a N_2-filled glovebox, the compound **4.2Cl** (198 mg, 142 µmol) was dissolved into 2 mL of THF and 2 mL of 1,4-dioxane to give a yellow solution. Methylmagnesium chloride (470 µL of a 300(8) µM solution, 142 µmol) was added in one portion, giving a color change to dark purple. The reaction was stirred at room temperature for 8 h, after which the solvent was removed. The purple solid was dissolved into ~3 mL of DFB and filtered through a fine frit padded with Celite® to remove $MgCl_2$(dioxane). The Celite® was washed with additional portions of DFB (3 × ~1 mL) until the washes were colorless. The combined filtrate was reduced to ~4 mL in volume. Addition of hexanes (~16 mL) precipitated dark purple crystals, which were isolated, rinsed with hexanes (3 × ~2mL), and dried under vacuum at room temperature. Yield = 168 mg (86%). ESI-MS *m*/*z* for $[(PY5Me_2)FeCH_3]^+$ requires 512.1733, found 512.1735. Combustion analyses reproducibly gives high carbon content. Anal. Calcd. for $C_{62}H_{40}BF_{24}FeN_5$: C, 54.05; H, 2.93; N, 5.08. Found (two trials): C, 55.28–55.61; H, 2.64–2.95; N, 5.10–5.39.

$[(\kappa^4\text{-}PY5Me_2)CoCH_3][B(C_6H_3(CF_3)_2)_4]$ (4.3CH$_3$). In a N_2-filled glovebox, the compound **4.3Cl** (210 mg, 150 µmol) was dissolved into 2 mL of THF and 2 mL of 1,4-dioxane to give an orange solution. Methylmagnesium chloride (500 µL of a 300(8) µM solution, 150 µmol) was added in one portion, giving a color change to brick red with formation of a colorless precipitate. The reaction was stirred at room temperature for 8 h, after which the solvent was removed. The red solid was dissolved into ~2 mL of DFB and filtered through a fine frit padded with Celite® to remove $MgCl_2$(dioxane). The Celite® was washed with additional portions of DFB (3 × ~1 mL) until the washes were colorless. The combined filtrate was reduced to ~3 mL in volume. Hexanes

(~17 mL) was added, and storage at −35 °C for 72 h afforded red crystals. The mother liquor was decanted, and the crystals were washed with portions of hexanes (3 × ~2 mL), and dried under vacuum at room temperature for 2 h. Yield = 175 mg (84%). ESI-MS *m*/*z* for $[(PY5Me_2)CoCH_3]^+$ requires 517.1671, found 517.1681. Anal. Calcd. for $C_{62}H_{40}BCoF_{24}N_5$: C, 53.93; H, 2.92; N, 5.07. Found: C, 53.68; H, 2.78; N, 5.10.

$[(\kappa^3\text{-}PY5Me_2)NiCH_3][B(C_6H_3(CF_3)_2)_4]$ (4.4CH₃). In a N_2-filled glovebox, the compound **4.4Cl** (194 mg, 138 μmol) was dissolved into 2 mL of THF and 2 mL of 1,4-dioxane to give a lavender solution. Methylmagnesium chloride (460 μL of a 300(8) μM solution, 138 μmol) was added in one portion, giving a color change to bright yellow with formation of a colorless precipitate. The reaction was stirred at room temperature for 8 h, after which the solvent was removed. The yellow residue was dissolved into ~5 mL of toluene and filtered through a fine frit padded with Celite® to remove $MgCl_2$(dioxane). The Celite® was washed with additional portions of toluene (5 × ~1 mL) until the washes were colorless. Hexanes (~10 mL) was added to the combined filtrate to precipitate yellow microcrystals. The crystals were isolated, washed with hexanes (3 × ~2mL), and dried under vacuum at room temperature for 2 h. Yield = 156 mg (77%). ^{1}H NMR (500 MHz, CD_2Cl_2) δ 8.33 (d, *J* = 5.0 Hz, 2H), 8.03 (t, *J* = 8.0 Hz, 1H), 7.87 (t, *J* = 8.0 Hz, 2H), 7.75 – 7.69 (m, 16H), 7.55 (s, 4H), 7.38 (dd, *J* = 7.5, 4.9 Hz, 2H), 7.29 (d, *J* = 5.6 Hz, 2H), 7.24 (t, *J* = 7.6 Hz, 2H), 7.14 (dt, *J* = 21.1, 7.0 Hz, 5H), 6.75 (d, *J* = 8.0 Hz, 2H), 2.34 (s, 3H, $PhC\underline{H}_3$), 2.28 (s, 6H), −0.88 (s, 3H, $NiC\underline{H}_3$). ESI-MS *m*/*z* for $[(PY5Me_2)NiCH_3]^+$ requires 516.1693, found 516.1693. Anal. Calcd. for $C_{69}H_{48}BF_{24}N_5Ni$ (**4.4CH₃**·toluene): C, 53.93; H, 2.92; N, 5.07. Found: C, 53.68; H, 2.78; N, 5.10.

$[(PY5Me_2)Fe(C_6H_5)][B(C_6H_3(CF_3)_2)_4]$ (4.2Ph). In a N_2-filled glovebox, the compound **4.2Cl** (100 mg, 72 μmol) was dissolved into 2 mL of THF and 2 mL of 1,4-dioxane to give a yellow solution. Phenylmagnesium chloride (64 μL of a 1.17(4) M solution, 75 μmol) was added in one portion, giving a color change to dark red. The reaction was stirred at room temperature for 8 h, then filtered through Celite®. The solvent was removed to afford a dark red solid, which was dissolved into ~4 mL of DFB. Addition of hexanes (~16 mL) and storage at −35 °C afforded dark red needles, which were isolated, rinsed with hexanes (3 × ~2mL), and dried under vacuum at room temperature. Yield = 82 mg (73%). ^{1}H NMR (600 MHz, CD_2Cl_2) δ 8.67 (d, J = 6.1 Hz, 4H), 7.96 (q, J = 5.7 Hz, 3H), 7.72 (d, J = 7.4 Hz, 13H), 7.63 – 7.58 (m, 4H), 7.55 (s, 4H), 7.08 (d, J = 6.9 Hz, 1H), 7.04 (t, J = 7.2 Hz, 2H), 6.98 (t, J = 7.0 Hz, 4H), 6.78 (d, J = 7.2 Hz, 2H), 2.81 (s, 6H). Anal. Calcd. for $C_{73}H_{46}BF_{26}FeN_5$ (**4.2Ph**·DFB): C, 56.43; H, 2.98; N, 4.48. Found (two trials): C, 56.54; H, 3.26; N, 4.51.

Protonolysis of metal alkyl and metal aryl complexes. In a N_2-filled glovebox, ~10 mg of the metal alkyl or metal aryl complex and an equimolar quantity of $[H(OEt_2)_2][B(C_6H_3(CF_3)_2)_4]$ were weighed into a silanized Durham tube, then dissolved into ~300 μL of 1,2-difluorobenzene or ~300 μL of a 1:1 (v/v) mixture of 1,2-difluorobenzene with dioxane or ether. The solutions stood at room temperature for ~10 min, then layered with ~1 mL of hexanes. After approximately 1 to 2 d, crystals formed and were characterized by single crystal X-ray crystallography. The yields of these reactions were not determined.

$[(PY5Me_2)V(\mu\text{-}Cl)V(PY5Me_2)][B(C_6H_3(CF_3)_2)_4]_3$ (4.10(*μ*-Cl)). In a N_2-filled glovebox, the compound **4.10Cl** (10 mg, 7.2 μmol) and $Tl[B(C_6H_3(CF_3)_2)_4]$ (7.7 mg, 7.2 μmol) were dissolved into ~1 mL of 1,2-difluorobenzene to give a dark red purple solution. After 1.5 h at room temperature, the solution was red, with formation of an off-white precipitate. The solid was removed by filtering through a pipette packed with Celite®. Diffusion of hexanes into the 1,2-difluorobenzene solution afforded crystals of **4.10(*μ*-Cl)**, as well as colorless prisms of presumably

$Tl[B(C_6H_3(CF_3)_2)_4]$.

$Ti(CF_3SO_3)_3(THF)_2$. In a N_2-filled glovebox, $TiCl_3(THF)_3$ (108 mg, 294 μmol) was dissolved into ~2 mL of CH_2Cl_2 to give a light blue-green solution. A solution of trimethylsilyltrifluoromethanesulfonate (216 mg, 970 μmol) in ~1 mL of CH_2Cl_2 was added in one portion, giving instantly a color change to blue-purple. The reaction stood at room temperature for 15 min, then the solvent was removed under vacuum to afford a light blue-purple, microcrystalline powder. The solid was redissolved into ~4 mL of CH_2Cl_2, filtered through Celite®, and layered with hexanes (~16 mL). After 48 h, diffusion of hexanes into the CH_2Cl_2 solution afforded purple crystals, which were isolated, washed with aliquots of hexanes (~3 × 1 mL), and dried under vacuum to give a purple crystalline solid. Yield = 115 mg (62%). Anal. Calcd. for $C_{11}H_{16}F_9O_{11}S_3Ti$: C, 20.67; H, 2.52; N, 0.00. Found: C, 20.80; H, 2.55; N, <0.20. Notably, these crystals immediately decomposed in Paratone oil to give a red-brown oil.

$[(PY5Me_2)Ti(CF_3SO_3)][B(C_6H_3(CF_3)_2)_4]_2$ (4.7CF$_3$SO$_3$). In a N_2-filled glovebox, $PY5Me_2$ (19 mg, 42 μmol), $Ti(CF_3SO_3)_3(THF)_2$ (27 mg, 42 μmol), and $K[B(C_6H_3(CF_3)_2)_4]$ (76 mg, 84 μmol) were weighed into a 20 mL scintillation vial and stirred in ~2 mL of 1,2-difluorobenzene for 4 h to afford a golden orange solution with colorless precipitate of KCF_3SO_3. The solution was filtered through a pipette packed with Celite®, then diluted with ~10 mL of hexanes to give yellow-orange crystals. The crystals were isolated from the mother liquor, washed with hexanes (3 × ~1 mL), and dried under vacuum at 80 °C for 1 h. Yield = 59 mg (60%). Anal. Calcd. for $C_{94}H_{49}B_2F_{51}N_5O_3STi$: C, 47.70; H, 2.09; N, 2.96. Found: C, 47.38; H, 2.07; N, 2.78.

4.2.4. Crystal Structure Determinations

Crystals suitable for single crystal X-ray diffraction analysis were grown by layering hexanes over solutions of metal complex (~5 mg) in ~0.5 mL of benzene (**4.4CH$_3$**) or 1,2-difluorobenzene solvent (all other compounds) and allowing the solutions to diffuse over 2 to 4 days at room temperature. Data collection was performed on single crystals coated with Paratone-N oil and mounted on Kapton loops. The crystals were cooled under a stream of N_2 (100 K; Oxford Cryostream 700) during measurements. Data were collected using a Bruker APEX II QUAZAR diffractometer equipped with a Microfocus Sealed Source (Incoatec IμS; Mo-K$_\alpha$ $\lambda = 0.71073$ Å) or using monochromated X-ray radiation generated by a synchrotron. Raw data were integrated and corrected for Lorentz and polarization effects using Bruker APEX2.[28] Absorption corrections were applied using SADABS.[29] Space group assignments were determined by examination of systematic absences, E-statistics, and successive refinement of the structures. Structures were solved using SHELXT[30] and all non-hydrogen atoms were refined anisotropically by full-matrix least-squares (SHELXL).[31,32] Carbon-bound hydrogen atoms were inserted at idealized positions and refined isotropically using a riding model with the appropriate HFIX command in SHELXL. Occasionally, the trifluoromethyl groups of the $[B(C_6H_3(CF_3)_2)_4]^-$ anions exhibited positional disorder, which was addressed using SADI, RIGU, and SIMU commands.[33]

4.3. Results and Discussion

4.3.1. Cationic First-Row Transition Metal Chloride Complexes

The monocationic, pentapyridine metal(II) chloride complexes $[(\mathrm{PY5Me_2})\mathrm{MCl}]^+$ of Cr(II) through Zn(II) are conveniently prepared by treating $\mathrm{PY5Me_2}$ ligand with one equivalent of the appropriate tetrahydrofuran metal dichloride complex and one equivalent of $\mathrm{K[B(C_6H_3(CF_3)_2)_4]}$ in 1,2-difluorobenzene (Scheme 4.1). The potassium chloride byproduct precipitates from solution and is removed by filtration. Due to the highly fluorous nature of the $\mathrm{[B(C_6H_3(CF_3)_2)_4]^-}$ anion, layering of concentrated solutions of metal complexes (>100 mg/mL) with alkane solvents tends to produce oils instead of crystalline material. Thus, the bulk materials were purified by adding hexanes to the filtered solutions (at concentrations of ~30 mg/mL to 50 mg/mL), which afforded microcrystalline, analytically pure forms of $\mathrm{[(PY5Me_2)CrCl][B(C_6H_3(CF_3)_2)_4]}$ (**4.1Cl**, green solid), $\mathrm{[(PY5Me_2)FeCl][B(C_6H_3(CF_3)_2)_4]}$ (**4.2Cl**, yellow-brown), $\mathrm{[(PY5Me_2)CoCl][B(C_6H_3(CF_3)_2)_4]}$ (**4.3Cl**, pale orange), $\mathrm{[(PY5Me_2)NiCl][B(C_6H_3(CF_3)_2)_4]}$ (**4.4Cl**, lavender), $[(\kappa^4\text{-}\mathrm{PY5Me_2})\mathrm{CuCl}][\mathrm{B(C_6H_3(CF_3)_2)_4}]$ (**4.5Cl**, blue), and $\mathrm{[(PY5Me_2)ZnCl][B(C_6H_3(CF_3)_2)_4]}$ (**4.6Cl**, white). The presence of the $[(\mathrm{PY5Me_2})\mathrm{MCl}]^+$ cations was confirmed by ESI-MS. Notably, this protocol does not afford the analogous manganous chloride complex.

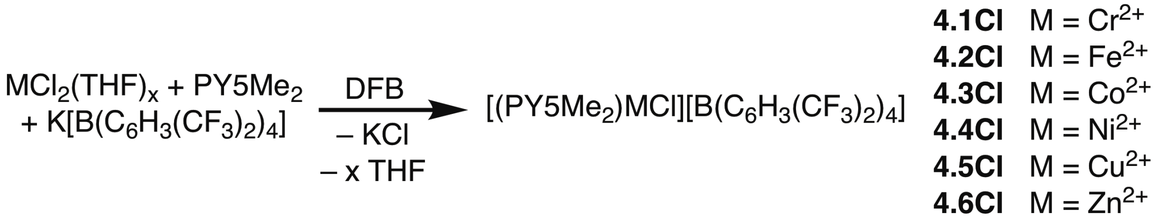

$$\mathrm{MCl_2(THF)_x + PY5Me_2 + K[B(C_6H_3(CF_3)_2)_4]} \xrightarrow[-\,\mathrm{KCl}\ \ -\,\mathrm{x\,THF}]{\mathrm{DFB}} \mathrm{[(PY5Me_2)MCl][B(C_6H_3(CF_3)_2)_4]}$$

4.1Cl M = $\mathrm{Cr^{2+}}$
4.2Cl M = $\mathrm{Fe^{2+}}$
4.3Cl M = $\mathrm{Co^{2+}}$
4.4Cl M = $\mathrm{Ni^{2+}}$
4.5Cl M = $\mathrm{Cu^{2+}}$
4.6Cl M = $\mathrm{Zn^{2+}}$

Scheme 4.1. Preparation of divalent $\mathrm{[(PY5Me_2)MCl][B(C_6H_3(CF_3)_2)_4]}$ complexes of Cr, Fe, Co, Ni, Cu, and Zn.

In contrast to the corresponding pentapyridine metal trifluoromethanesulfonate salts, these $\mathrm{[(PY5Me_2)MCl][B(C_6H_3(CF_3)_2)_4]}$ compounds are highly soluble in weakly donating solvents such as tetrahydrofuran and dimethoxyethane, as well as non-coordinating, polar solvents such as 1,2-difluorobenzene and dichloromethane.

For these compounds, single crystals suitable for X-ray diffraction analysis are best obtained by layering of hexanes over dilute (~10 mg/mL) solutions of metal complex in 1,2-difluorobenzene. As expected, the solid-state structures of compounds **4.1**–**6** reveal monocationic complexes of the $[\mathrm{M–Cl}]^+$ unit coordinated by the $\mathrm{PY5Me_2}$ ligand (Figure 4.1, Tables 4.S1–2). The complexes **4.1**–**4** and **4.6** display isostructural, pseudo-octahedral coordination geometries. In complex **4.5**, one of the equatorial pyridine ligands does not coordinate to the Cu(II) ion, instead blocking the open coordination site (Cu–centroid distance = 3.5721 (9) Å) to give a characteristic square pyramidal, d^9 Cu(II) ion.

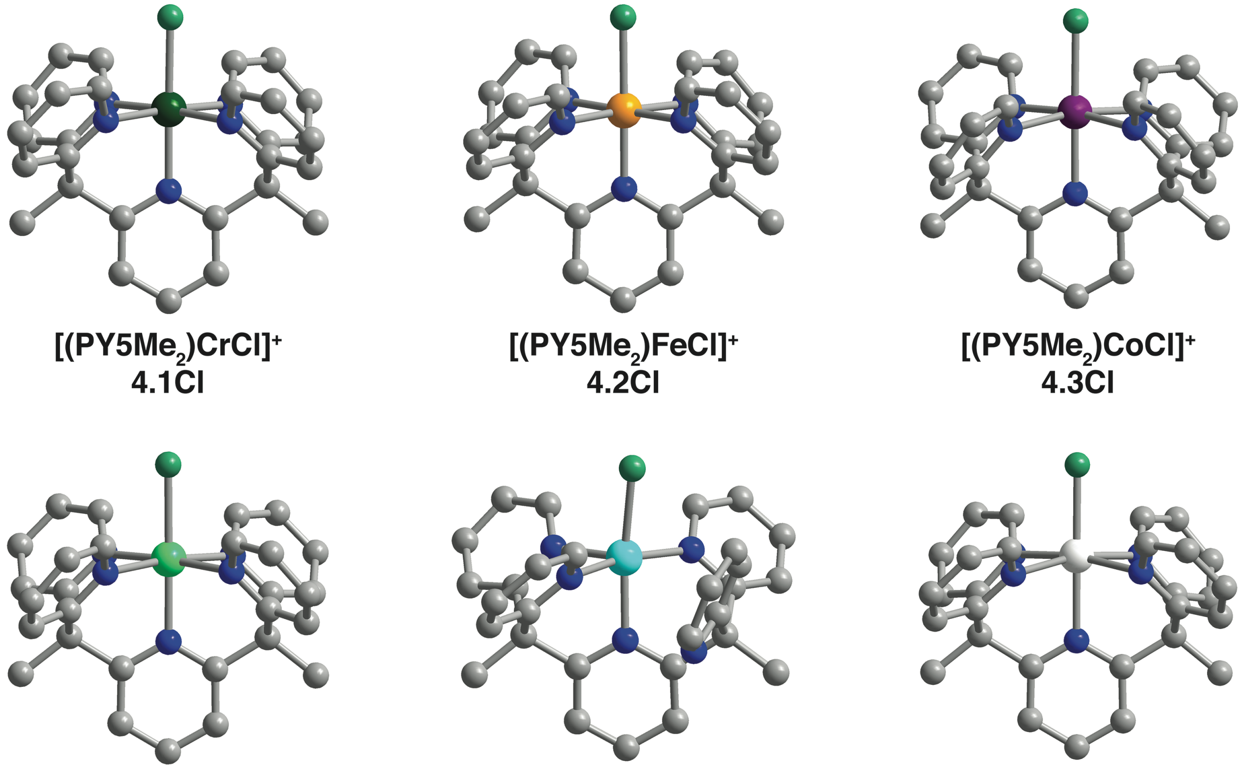

$[(PY5Me_2)CrCl]^+$
4.1Cl

$[(PY5Me_2)FeCl]^+$
4.2Cl

$[(PY5Me_2)CoCl]^+$
4.3Cl

$[(PY5Me_2)NiCl]^+$
4.4Cl

$[(PY5Me_2)CuCl]^+$
4.5Cl

$[(PY5Me_2)ZnCl]^+$
4.6Cl

Figure 4.1. Crystal structures of the monocationic complexes in compounds **4.1Cl**, **4.2Cl**, **4.3Cl**, **4.4Cl**, **4.5Cl**, and **4.6Cl**. Dark green, orange, purple, green, aqua, white, blue-green, blue, and gray spheres represent Cr, Fe, Co, Ni, Cu, Zn, Cl, N, and C atoms, respectively. H atoms, $B(C_6H_3(CF_3)_2)_4^-$ anions, and solvent are not shown for clarity.

The analogous Ti(II) and V(II) complexes, being early transition metals and thus stronger reductants, would be promising candidates for N_2 activation and reduction. We initially explored metalation conditions using the commercially available compounds $TiCl_2$ and VCl_2, as well as the complex $VCl_2(tmeda)_2$ (tmeda = *N*, *N*, *N′*, *N′*-tetramethylethylenediamine).[34] We found the solubilities of $TiCl_2$ and VCl_2 in solvents such as THF, dimethoxyethane, diglyme, and 1,2-difluorobenzene to be too low for metalation to proceed smoothly. Metalation of $PY5Me_2$ with $VCl_2(tmeda)_2$ in the presence of one equivalent of $K[B(C_6H_3(CF_3)_2)_4]$ affords a mixture of purple and colorless crystals of the same habit and similar unit cell parameters. Mass spectrometry displayed signals with *m*/*z* consistent with the ions $[(PY5Me_2)VCl]^+$ and $[(PY5Me_2)ZnCl]^+$, with abundances at a ratio of ~10:1. We surmised that the purple crystals were the desired V(II) complex, and the colorless crystals a Zn(II) contaminant. As $VCl_2(tmeda)_2$ is prepared by reduction of $VCl_3(THF)_3$ with zinc metal,[18] it seems likely that the $VCl_2(tmeda)_2$ precursor is contaminated with a $ZnCl_2$ complex.

In light of these synthetic challenges, we elected to use the precursors $TiCl_3(THF)_3$ and $VCl_3(THF)_3$ instead. Stirring equimolar quantities of the $PY5Me_2$ ligand and $TiCl_3(THF)_3$ or $VCl_3(THF)_3$ with two equivalents of $K[B(C_6H_3(CF_3)_2)_4]$ in 1,2-difluorobenzene rapidly afforded orange (for Ti(III)) and lavender (for V(III)) solutions (Scheme 4.2). Filtration of the solutions and addition of hexanes furnishes the trivalent compounds $[(PY5Me_2)TiCl][B(C_6H_3(CF_3)_2)_4]_2$ (**4.7Cl**) and $[(PY5Me_2)VCl][B(C_6H_3(CF_3)_2)_4]_2$ (**4.8Cl**). Single-crystal X-ray crystallography and ESI-MS both confirm that the $PY5Me_2$ ligand displaces two of the three chloride ligands to give $[(PY5Me_2)MCl]^{2+}$ dications (Figure 4.2). Compound **4.7Cl** can also be prepared from $TiCl_4(THF)_2$ (Scheme 4.S1). Apparently the Ti(IV)-$PY5Me_2$ adduct is so oxidizing that it decomposes the $[B(C_6H_3(CF_3)_2)_4]$ anion to make the Ti(III) complex and biphenyl. Given this finding, it seems that the $PY5Me_2$ ligand alone cannot stabilize tetravalent metal ions, and requires good π donating ligands (e.g. oxo, nitrido, etc) as well.

$$\begin{array}{c}\mathrm{MCl_3(THF)_3 + PY5Me_2}\\ \mathrm{+\ 2\ K[B(C_6H_3(CF_3)_2)_4]}\end{array} \xrightarrow[\substack{-\ 2\ \mathrm{KCl}\\ -\ 3\ \mathrm{THF}}]{\mathrm{DFB}} \mathrm{[(PY5Me_2)MCl][B(C_6H_3(CF_3)_2)_4]_2} \quad \begin{array}{ll}\textbf{4.7Cl} & \mathrm{M = Ti^{3+}}\\ \textbf{4.8Cl} & \mathrm{M = V^{3+}}\end{array}$$

Scheme 4.2. Metalation of $PY5Me_2$ to afford compounds **4.7Cl** and **4.8Cl**.

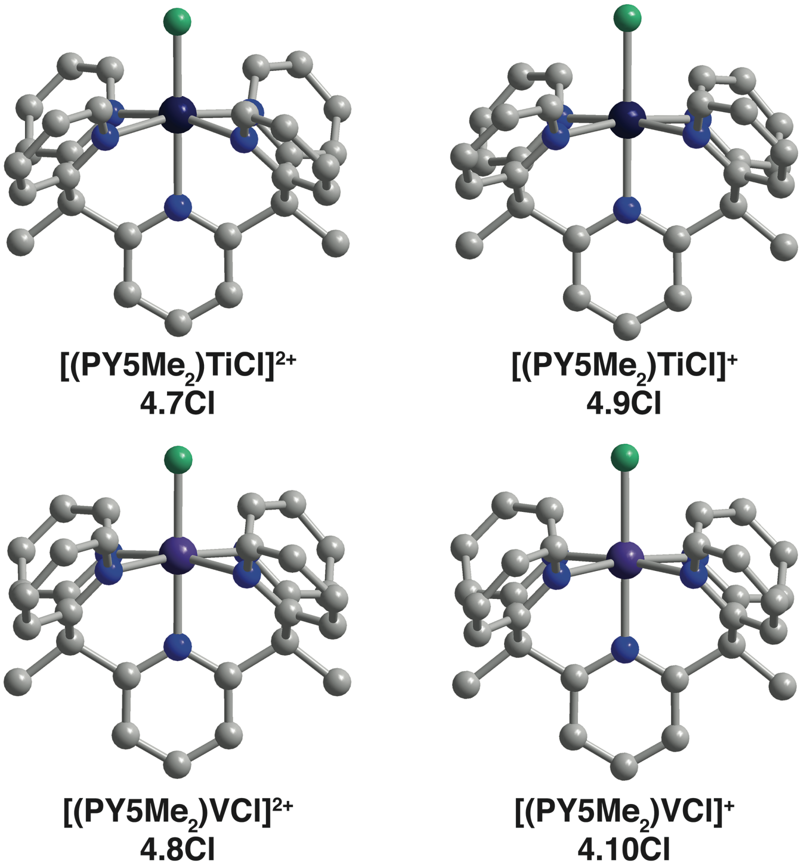
$[(PY5Me_2)TiCl]^{2+}$
4.7Cl

$[(PY5Me_2)TiCl]^{+}$
4.9Cl

$[(PY5Me_2)VCl]^{2+}$
4.8Cl

$[(PY5Me_2)VCl]^{+}$
4.10Cl

Figure 4.2. Crystal structures of the dicationic complexes in compounds **4.7Cl** and **4.8Cl**, and the monocations in **4.9Cl** and **4.10Cl**. Dark blue, dark purple, blue-green, blue, and gray spheres represent Ti, V, Cl, N, and C atoms, respectively. H atoms, $B(C_6H_3(CF_3)_2)_4^-$ anions, and solvent are not shown for clarity.

In view of the successful preparation of trivalent early transition metal complexes **4.7Cl** and **4.8Cl**, we conjectured that *in situ* reduction during metalation would afford the corresponding divalent compounds. Indeed, treating the $PY5Me_2$ ligand with one equivalent of $MCl_3(THF)_3$, one equivalent of $K[B(C_6H_3(CF_3)_2)_4]$, and one equivalent of potassium graphite in dimethoxyethane gives dark, inky solutions that, upon workup, afford dark blue $[(PY5Me_2)TiCl][B(C_6H_3(CF_3)_2)_4]$ (**4.9Cl**) and dark purple $[(PY5Me_2)VCl][B(C_6H_3(CF_3)_2)_4]$ (**4.10Cl**) (Scheme 4.3). Samples of

4.10Cl obtained with this protocol were found to be analytically pure. However, elemental analyses of **4.9Cl** yielded variable and unsatisfactory results. We attribute this to the reactive nature of the low-valent Ti(II) species. Nevertheless, the chemical composition of **4.9Cl** is confirmed by crystallography. Slow diffusion of hexanes into dilute 1,2-difluorobenzene solutions of **4.9Cl** and **4.10Cl** afforded single crystals from which their molecular structures were determined (Figure 4.2). The Ti–Cl bond distance lengthens from 2.218(2) Å in **4.7Cl** to 2.405(2) Å in **4.9Cl**. This is attributed to the expansion of the ionic radius from Ti(III) to Ti(II), or equivalently, a weakened electrostatic interaction between the titanium and chloride ions. The V–Cl bond lengthens by a similar magnitude (by ~0.19 Å) between **4.8Cl** (2.2335(8) Å) and **4.10Cl** (2.4252(12) Å).

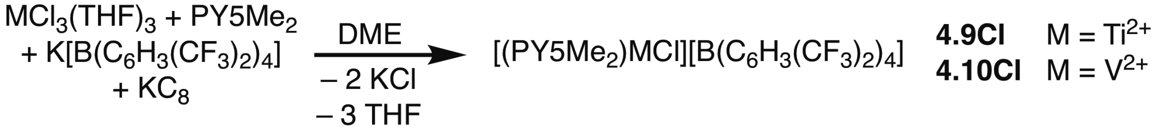

$$\begin{array}{c} MCl_3(THF)_3 + PY5Me_2 \\ + K[B(C_6H_3(CF_3)_2)_4] \\ + KC_8 \end{array} \xrightarrow[\begin{array}{c}-\ 2\ KCl \\ -\ 3\ THF\end{array}]{DME} [(PY5Me_2)MCl][B(C_6H_3(CF_3)_2)_4] \quad \begin{array}{ll} \textbf{4.9Cl} & M = Ti^{2+} \\ \textbf{4.10Cl} & M = V^{2+} \end{array}$$

Scheme 4.3. Synthesis of the divalent Ti(II) and V(II) complexes **4.9Cl** and **4.10Cl**.

There are notably few structurally characterized examples of mononuclear Ti(II) complexes without π-acidic ligands. Two structures comparable to **4.9Cl** are the complexes *trans*-$TiCl_2(tmeda)_2$ and *trans*-$TiCl_2(pyridine)_4$,[18,35,36] both of which possess nitrogen donors in an approximately tetragonal ligand field. Owing to the overall cationic charge of the complex and the lack of a π-donating *trans*-chloride ligand, the Ti–Cl bond distance of 2.405(2) Å in **4.9Cl** is ~0.07 to 0.09 Å shorter than those of *trans*-$TiCl_2(tmeda)_2$ (2.477(2) Å)[18] and *trans*-$TiCl_2(pyridine)_4$ (2.497(1) Å).[35]

As a periodic series, the metal–pyridine and metal–chloride bond distances of the divalent metal chloride complexes are summarized in Table 4.1. The relatively short metal–pyridine distances of the complexes in compounds **4.1Cl** and **4.2Cl** suggest that they are low-spin Cr(II) and Fe(II) complexes at 100 K, whereas the bond distances of the complex in compound **4.3Cl** are consistent with high-spin Co(II).

Table 4.1. Selected bond distances of $[(PY5Me_2)MCl][B(C_6H_3(CF_3)_2)_4]$ complexes.

compound	metal	*d*(M–N_{eq}, average) (Å)	*d*(M–N_{ax}) (Å)	*d*(M–Cl) (Å)
4.9Cl	Ti(II)	2.168(4)	2.129(4)	2.405(2)
4.10Cl	V(II)	2.139(3)	2.106(3)	2.425(2)
4.1Cl	Cr(II)	2.059(2)	2.064(2)	2.333(1)
4.2Cl	Fe(II)	2.011(3)	1.969(3)	2.345(1)
4.3Cl	Co(II)	2.145(2)	2.141(2)	2.379(1)
4.4Cl	Ni(II)	2.103(2)	2.077(2)	2.392(1)
4.5Cl[a]	Cu(II)	2.020(3)	2.169(3)[b]	2.264(1)
4.6Cl	Zn(II)	2.168(3)	2.195(3)	2.3508(10)

[a] The $PY5Me_2$ ligand exhibits κ^4 coordination.

[b] Distance for the Cu–N_{py} bond *trans* to the unbound pyridine.

4.3.2. Cationic Metal Alkyl and Aryl Complexes

The chloride ligands of the divalent complexes in the compound $[(PY5Me_2)MCl][B(C_6H_3(CF_3)_2)_4]$ were exchanged with methyl ligands using methylmagnesium chloride. For the Cr(II), Fe (II), Co(II), and Ni(II) complexes, the halide/alkyl exchange reactions proceed readily to afford [(PY5Me$_2$)MCH$_3$][B(C$_6$H$_3$(CF$_3$)$_2$)$_4$] (**4.1–4CH$_3$**, Scheme 4.4).

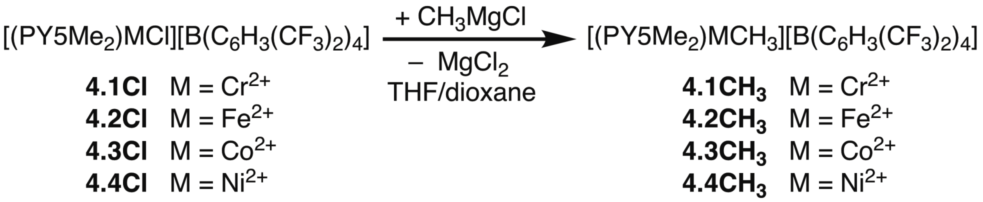

Scheme 4.4. Halide/methyl exchange in [(PY5Me$_2$)MCl][B(C$_6$H$_3$(CF$_3$)$_2$)$_4$] complexes.

The molecular structures of **4.1CH$_3$** and **4.2CH$_3$** show octahedral [(PY5Me$_2$)MCH$_3$]$^+$ ions (Figure 4.3). Notably, there is substitutional disorder of the Cl$^-$ versus CH$_3^-$ ligands in both complexes (Figure 4.S1). For compound **4.1CH$_3$**, the occupancies of Cl$^-$ versus CH$_3^-$ ligands are 13% and 87%. For compound **4.2CH$_3$**, the occupancies of Cl$^-$ versus CH$_3^-$ ligands are 37% and 63%. The ESI-MS spectra of **4.1CH$_3$** and **4.2CH$_3$** show the metal-methyl complexes as the major product at their expected *m*/*z* values (Figure 4.S2 and S3). The metal chloride cations are also present, and the relative ion intensities suggest the contamination to be only 3–10% (Figures 4.S2 and S3). Taking into account the satisfactory elemental analysis of **4.1CH$_3$** and the higher than expected carbon content in **4.2CH$_3$**, we think the extent of chloride contamination may be overstated by the crystallographic analysis.

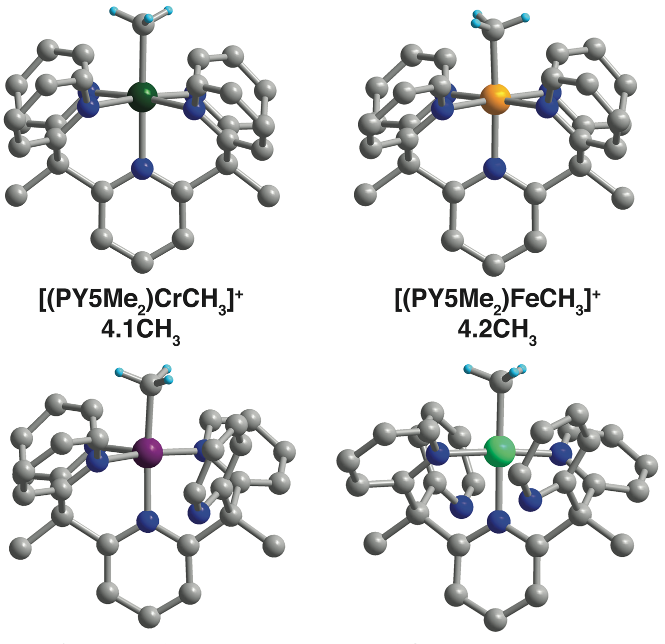
[(PY5Me$_2$)CrCH$_3$]$^+$
4.1CH$_3$
[(PY5Me$_2$)FeCH$_3$]$^+$
4.2CH$_3$
[(κ^4-PY5Me$_2$)CoCH$_3$]$^+$
4.3CH$_3$
[(κ^3-PY5Me$_2$)NiCH$_3$]$^+$
4.4CH$_3$

Figure 4.3. Crystal structures of the monocationic metal alkyl complexes **4.1CH$_3$**, **4.2CH$_3$**, **4.3CH$_3$**, and **4.4CH$_3$**. Dark green, orange, purple, green, blue, gray, and light blue spheres represent Cr, Fe, Co, Ni, N, C, and H atoms, respectively. H atoms (except for those of the M–CH$_3$ group), B(C$_6$H$_3$(CF$_3$)$_2$)$_4^-$ anions, and solvent are omitted for clarity.

The cobalt and nickel methyl complexes in **4.3CH$_3$** and **4.4CH$_3$** exhibit markedly different solubility properties compared to other cationic PY5Me$_2$-metal complexes. The compound **4.3CH$_3$**

required cooling to −35 °C to induce crystallization in 1,2-difluorobenzene/hexanes. The nickel complex salt **4.4CH$_3$** is uniquely soluble in arene solvents; single crystals of **4.4CH$_3$** can be obtained via layering of hexanes over its benzene solutions. The molecular structures of **4.3CH$_3$** and **4.4CH$_3$** show the PY5Me$_2$ binding to Co and Ni in κ^4- and κ^3- modes. This is due to the stronger ligand field of the methyl donor, which encourages the square pyramidal and square planar coordination geometries for the d^7 and d^8 metal ions in compounds **4.3CH$_3$** and **4.4CH$_3$**, respectively. The exposed van der Waals surface area of the unbound pyridine ligands, in turn, impart the greater solubilities of **4.3CH$_3$** and **4.4CH$_3$** in less polar solvents. As expected from its square planar geometry, the complex **4.4CH$_3$** is diamagnetic. The ^{1}H resonance of the nickel–methyl ligand appears at −0.88 ppm.

Highlighted bond distances for complexes **4.1–4CH$_3$** are presented in Table 4.2.

Table 4.2. Selected bond distances of [(PY5Me$_2$)MCH$_3$][B(C$_6$H$_3$(CF$_3$)$_2$)$_4$] complexes.

compound	metal	d(M–N$_{py}$, average) (Å)	d(M–CH$_3$) (Å)
4.1CH$_3$	Cr(II)	2.079(2)	2.14(2)
4.2CH$_3$	Fe(II)	2.000(2)	2.01(2)
4.3CH$_3$[a]	Co(II)	1.993(2)	1.982(2)
4.4CH$_3$[b]	Ni(II)	1.915(2)	1.915(2)

[a] The PY5Me$_2$ ligand exhibits κ^4 coordination.

[b] The PY5Me$_2$ ligand exhibits κ^3 coordination.

The methylmagnesium chloride protocol described in Scheme 4.4 fails to afford methyl complexes of titanium(II) and vanadium(II). Analogous conditions using methyllithium were also attempted. In all cases, the starting materials **4.9Cl** and **4.10Cl** were recovered. At the time of writing, it is not clear whether the inertness of the chloride ligands in **4.9Cl** and **4.10Cl** is a kinetic effect (arising from a lack of *d* electrons in the anti-bonding manifold) or a thermodynamic effect reasons (arising from smaller differences in electronegativities of Mg versus Ti and V).

Interestingly, dark purple solutions of **4.2CH$_3$** in 1,2-difluorobenzene turned red over a period of three days. The ESI-MS of this red solution no longer shows the peaks at m/z = 514.17 Da expected for the [(PY5Me$_2$)FeCH$_3$]$^+$ ion. Instead, a new set of peaks appears at m/z = 612.17 Da, consistent with the ion [(PY5Me$_2$)Fe(C$_6$H$_3$F$_2$)]$^+$ (Figure 4.S4). We speculate that the Fe–CH$_3$ unit of **4.2CH$_3$** slowly reacts with the aryl C–H bond of 1,2-difluorobenzene, affording a new iron(II)-aryl bond and eliminating methane.

In light of the reactivity and chloride contamination issue of **4.2CH$_3$**, we also synthesized the iron(II) phenyl complex salt [(PY5Me$_2$)Fe(C$_6$H$_5$)][B(C$_6$H$_3$(CF$_3$)$_2$)$_4$] (**4.2Ph**). Addition of phenylmagnesium chloride to a solution of **4.2CH$_3$** in THF/dioxane gives a color change from yellow-orange to red (Scheme 4.5). Filtration and workup affords **4.2Ph** as a red solid. The molecular structure of **4.2CH$_3$** reveals the pseudo-octahedral complex [(PY5Me$_2$)Fe(C$_6$H$_5$)]$^+$, with a Fe–C bond distance of 1.994(2) Å (Figure 4.4) Owing to the distinct shapes and solubilities of **4.2Cl** versus **4.2Ph**, substitutional disorder of Cl$^-$ versus C$_6$H$_5$$^-$ is not observed.

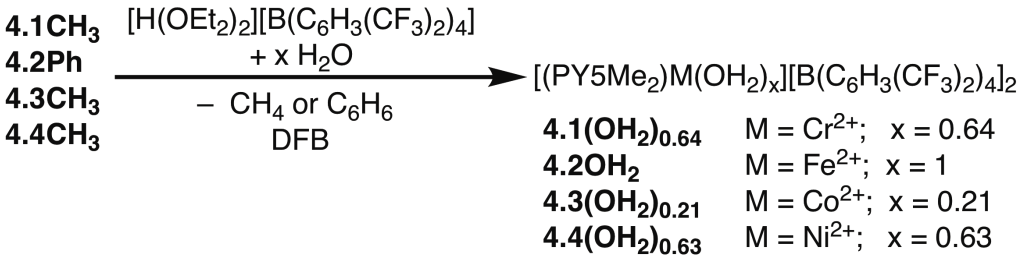

Scheme 4.5. Synthesis of **4.2Ph**.

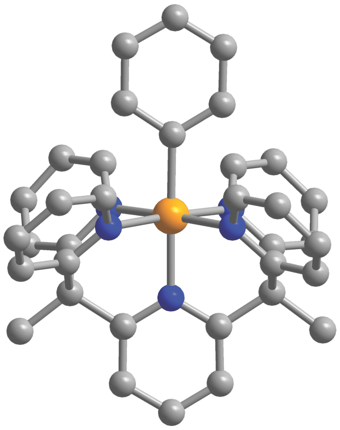

Figure 4.4. Crystal structure of the cation in **4.2Ph**. Orange, blue, and gray spheres represent Fe, N, and C atoms, respectively. H atoms, $B(C_6H_3(CF_3)_2)_4^-$ anions, and solvent molecules are omitted for clarity.

4.3.3. Coordinatively-Unsaturated Pentapyridine Metal Dications

Protonolysis of metal alkyl and metal aryl complexes generate dicationic metal complexes, each with a vacant coordination site at which a weakly donating ligand can bind. Since these dications are highly Lewis-acidic, their syntheses were performed exclusively with silanized glassware. The compounds **4.1CH$_3$**, **4.3CH$_3$**, **4.4CH$_3$**, and **4.2Ph** do not react with lutidinium tetrakis(3,5-bis(trifluoromethyl)phenyl)borate and $[HNEt_3][B(C_6H_3(CF_3)_2)_4]$ after 12 h at room temperature. Monitoring protonolysis by ^1H NMR spectroscopy in CD_2Cl_2, showed that treating **4.2Ph** with one equivalent of the more acidic oxonium acid $[H(OEt_2)_2][B(C_6H_3(CF_3)_2)_4]$ quantitatively forms C_6H_6 within ~3 min, and the resonances attributed to **4.2Ph** disappear. Broad resonances appear between +126 and −10 ppm, indicating the formation of a paramagnetic Fe(II) species. Performing the reaction in 1,2-difluorobenzene (Scheme 4.6) and layering with hexanes affords green crystals of $[(PY5Me_2)Fe(OH_2)][B(C_6H_3(CF_3)_2)_4]$ (**4.2OH$_2$**) suitable for X-ray crystallography (Figure 4.5). Similarly, protonation **4.1CH$_3$**, **4.3CH$_3$**, and **4.4CH$_3$** with $[H(OEt_2)_2][B(C_6H_3(CF_3)_2)_4]$ give single crystals that are, based on the metal-ligand distances and the residual electron density surrounding the oxygen atom, formulated as $[(PY5Me_2)Cr(OH_2)_{0.64}][B(C_6H_3(CF_3)_2)_4]$ (**4.1(OH$_2$)$_{0.64}$**), $[(PY5Me_2)Co(OH_2)_{0.21}][B(C_6H_3(CF_3)_2)_4]$ (**4.3(OH$_2$)$_{0.21}$**), and $[(PY5Me_2)Ni(OH_2)_{0.63}][B(C_6H_3(CF_3)_2)_4]$ (**4.4(OH$_2$)$_{0.63}$**). Their molecular structures are presented in Figure 4.5, and additional refinement parameters can be found in Tables 4.S6–7.

$$\begin{array}{l}\mathbf{4.1CH_3}\\ \mathbf{4.2Ph}\\ \mathbf{4.3CH_3}\\ \mathbf{4.4CH_3}\end{array}\ \xrightarrow[\substack{-\ \mathrm{CH_4}\text{ or }\mathrm{C_6H_6}\\ \mathrm{DFB}}]{\substack{[\mathrm{H(OEt_2)_2}][\mathrm{B(C_6H_3(CF_3)_2)_4}]\\ +\ x\ \mathrm{H_2O}}}\ \begin{array}{ll}\multicolumn{2}{l}{[\mathrm{(PY5Me_2)M(OH_2)_x}][\mathrm{B(C_6H_3(CF_3)_2)_4}]_2}\\ \mathbf{4.1(OH_2)_{0.64}} & \mathrm{M = Cr^{2+};\ x = 0.64}\\ \mathbf{4.2OH_2} & \mathrm{M = Fe^{2+};\ x = 1}\\ \mathbf{4.3(OH_2)_{0.21}} & \mathrm{M = Co^{2+};\ x = 0.21}\\ \mathbf{4.4(OH_2)_{0.63}} & \mathrm{M = Ni^{2+};\ x = 0.63}\end{array}$$

Scheme 4.6. Protonolyses of $[(PY5Me_2)MCH_3]^+$ and $[(PY5Me_2)M(C_6H_5)]^+$ complexes.

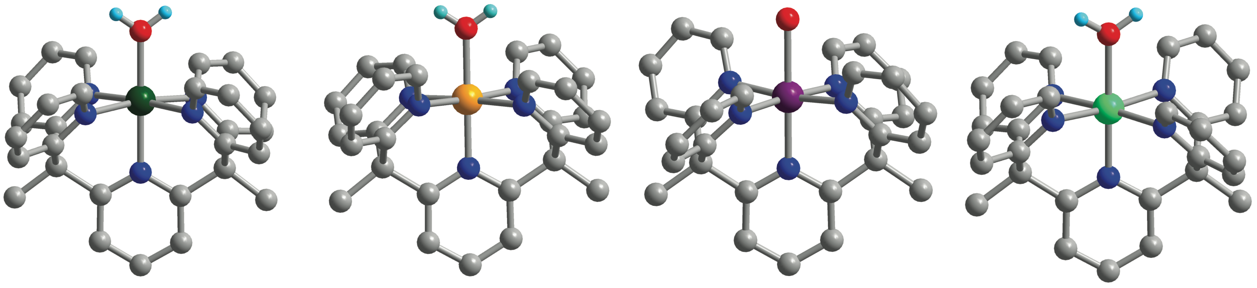

4.1(OH$_2$)$_{0.64}$ **4.2OH$_2$** **4.3(OH$_2$)$_{0.21}$** **4.4(OH$_2$)$_{0.63}$**

Figure 4.5. Crystal structures of **4.1(OH$_2$)$_{0.64}$**, **4.2OH$_2$**, **4.3(OH$_2$)$_{0.21}$**, and **4.4(OH$_2$)$_{0.63}$**. Dark green, orange, purple, green, blue, gray, and light blue spheres represent Cr, Fe, Co, Ni, N, C, and H atoms, respectively. H atoms (except those of the aquo ligand), $B(C_6H_3(CF_3)_2)_4^-$ anions, and solvent are omitted for clarity. Due to the low occupancy of the aquo ligand in **4.3(OH$_2$)$_{0.21}$**, the H atoms of the aquo ligand could not be located.

Despite our best efforts, the dicationic complexes scavenge trace water to form aquo complexes. Furthermore, the partial occupancies of the aquo ligand in **4.1(OH$_2$)$_{0.64}$**, **4.3(OH$_2$)$_{0.21}$**, and **4.4(OH$_2$)$_{0.63}$** suggest that if water is not present, the electronic configurations of Cr(II), Co(II), and Ni(II) encourage the metal ions to take square pyramidal geometries over binding N_2.

Considering the large affinity of coordinatively-unsaturated mid- and late transition metal dications for ligands with oxygen donors, we attempted to outcompete water with ethereal co-solvents. Protonolysis of **4.2Ph** in 1:1 (v/v) 1,2-difluorobenzene/dioxane affords single crystals of $[(PY5Me_2)Fe(C_4H_8O_2)][B(C_6H_3(CF_3)_2)_4]_2$ (**4.2C$_4$H$_8$O$_2$**), in which the oxygen atom of 1,4-dioxane is coordinated to the Fe(II) center (Figure 4.6). The Fe–O bond distances in **4.2C$_4$H$_8$O$_2$** and **4.2OH$_2$** are identical within error (2.023(7) Å and 2.017(3) Å, respectively), thus suggesting comparable interaction strengths between Fe(II) and 1,4-dioxane versus Fe(II) and water, and underscoring the capacity of 1,4-dioxane to displace water. Protonolysis of **4.2Ph** in 1:1 (v/v) 1,2-difluorobenzene/diethyl ether instead affords single crystals of $[(PY5Me_2)Fe(OH_2)_{0.75}(OEt_2)_{0.25}][B(C_6H_3(CF_3)_2)_4]_2$ (**4.2(OH$_2$)$_{0.75}$(OEt$_2$)$_{0.25}$**), in which the electron density adjacent to the Fe(II) center is best modeled as a bound aquo ligand at 75% occupancy, and a coordinated diethyl ether molecule at 25% occupancy. Due to the steric clashes between the diethyl ether ligand and the PY5Me$_2$ ligand, the interaction between Et_2O and the Fe(II) center is much weaker. The molecular structure of the $[(PY5Me_2)Fe(OEt_2)]^{2+}$ ion presents a Fe–O bond length of 2.494(2) Å (Figure 4.6).

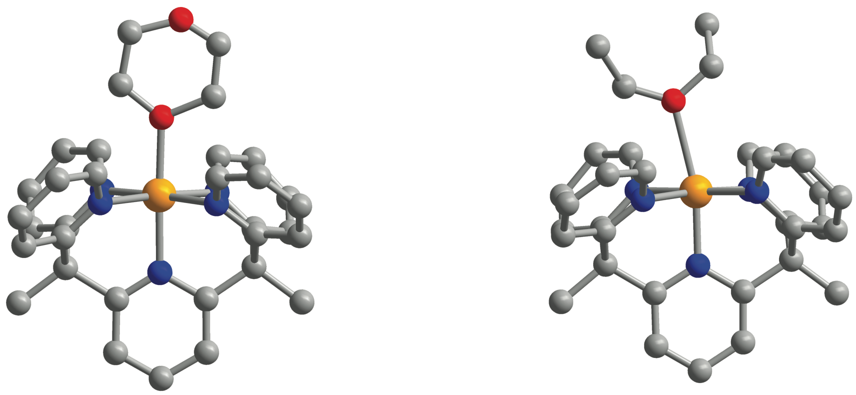

Figure 4.S1. Crystal structures of the dications in **4.2C$_4$H$_8$O$_2$** (left) and **4.2(OH$_2$)$_{0.75}$(OEt$_2$)$_{0.25}$**, (right, only the Et$_2$O-bound complex shown). Orange, red, blue, and gray spheres represent Fe, O, N, and C atoms, respectively. H atoms, $B(C_6H_3(CF_3)_2)_4^-$ anions, and solvent are omitted for clarity.

4.3.4. Chloride Abstraction Reactions

Owing to the inertness of the M–Cl bond in **4.9Cl** and **4.10Cl** towards chloride/alkyl exchange with organometallic reagents, we explored whether chloride abstraction routes could generate vacant coordination sites at Ti(II) and V(II). These attempts were largely unsuccessful. Addition of $Tl[B(C_6H_3(CF_3)_2)_4]$ to a dark purple solution of **4.10Cl** in 1,2-difluorobenzene affords, over 1.5 h, a color change to dark red and precipitation of TlCl. After filtration and workup, dark red crystals of $[(PY5Me_2)V(\mu\text{-}Cl)V(PY5Me_2)][B(C_6H_3(CF_3)_2)_4]_3$ (**4.10(*μ*-Cl)**) were identified by crystallography. Evidently, the chloride ligand of one molecule of **4.10Cl** is abstracted by Tl^+, thereby creating an open metal site at V(II). In 1,2-difluorobenzene, the best ligand is a second molecule of **4.10Cl**, thus forming a bridging chloride between two vanadium ions. The two V–Cl bonds are crystallographically distinct but identical within error (2.457(3) Å and 2.461(3) Å) (Figure 4.7). The V–Cl–V angle is almost linear, at 179.92(13)°.

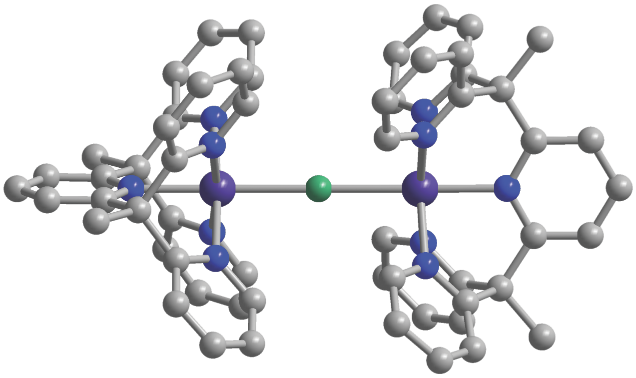

Figure 4.6. Molecular structure of the $[(PY5Me_2)V(\mu\text{-}Cl)V(PY5Me_2)]^{3+}$ ion in **4.10(*μ*-Cl)**. Dark purple, blue-green, blue, and gray spheres represent V, Cl, N, and C atoms, respectively. H atoms, $[B(C_6H_3(CF_3)_2)_4]^-$ anions, and solvent are omitted for clarity.

In the case of Ti(II), chloride abstraction fails because the Ti(II) ion is more reducing than Tl^+. Addition of one equivalent of $Tl[B(C_6H_3(CF_3)_2)_4]$ to a solution of **4.9Cl** in 1,2-difluorobenzene results in an immediate color change form dark blue to orange, with concomitant formation of a gray residue that is likely thallium metal. The Ti-containing product was identified by crystallography to be the Ti(III) complex **4.7Cl**.

4.3.5. Coordinated Trifluoromethanesulfonate Complexes of Vanadium and Titanium

As the M–Cl bonds in **4.9Cl** and **4.10Cl** are exceedingly inert, it is challenging to establish well-defined open coordination site that could leverage the latent reducing power of Ti(II) and V(II). Consequently, we sought alternative, more labile and less nucleophilic pseudohalides to facilitate ligand exchange and dissociation. The trifluoromethanesulfonate anion was identified as a particularly attractive candidate because it is an excellent leaving group.[37-39] Furthermore, the trifluoromethanesulfonate anion possesses strong sulfur-oxygen bonds that, in principle, should be robust towards the oxophilic titanium and vanadium ions. The metalation of PY5Me$_2$ with [V(CH$_3$CN)$_6$](CF$_3$SO$_3$)$_2$ with one equivalent of K[B(C$_6$H$_3$(CF$_3$)$_2$)$_4$] affords the V(II) complex salt [(PY5Me$_2$)V(CF$_3$SO$_3$)][B(C$_6$H$_3$(CF$_3$)$_2$)$_4$] (**4.10CF$_3$SO$_3$**, Scheme 4.7). As potassium trifluoromethanesulfonate is insoluble in 1,2-difluorobenzene, it is conveniently removed by filtration. The molecular structure of **4.10CF$_3$SO$_3$** confirms a coordinated trifluoromethanesulfonate anion, with a V–O bond distance of 2.109(2) Å (Figure 4.8).

$$\begin{array}{c}[V(CH_3CN)_6](CF_3SO_3)_2\\ +\ PY5Me_2\\ +\ K[B(C_6H_3(CF_3)_2)_4]\end{array} \xrightarrow[\begin{array}{c}-\ KCF_3SO_3\\ -\ 6\ CH_3CN\end{array}]{DFB} \begin{array}{c}[(PY5Me_2)V(CF_3SO_3)][B(C_6H_3(CF_3)_2)_4]\\ \mathbf{4.10CF_3SO_3}\end{array}$$

Scheme 4.7. Preparation of **4.10CF$_3$SO$_3$**.

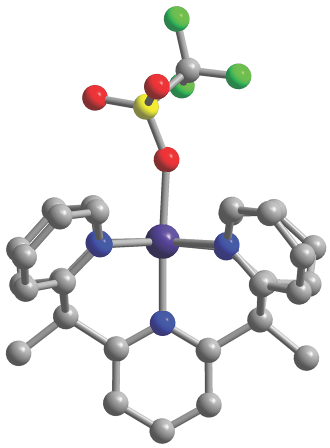

Figure 4.7. Molecular structure of the cation in **4.10CF$_3$SO$_3$**. Dark purple, yellow, red, green, blue, and gray spheres represent V, S, O, F, N, and C atoms, respectively. H atoms, [B(C$_6$H$_3$(CF$_3$)$_2$)$_4$]$^-$ anions, and solvent are omitted for clarity.

Since there are no reported simple trifluoromethanesulfonate salts of Ti(III) or Ti(II), initial efforts centered on substituting the Cl$^-$ ligand for CF$_3$SO$_3$$^-$ using trimethylsilyltrifluoromethanesulfonate. Heating solutions of **4.7Cl** with excess (CH$_3$)$_3$SiCF$_3$SO$_3$ in CD$_2$Cl$_2$ shows no reaction, judging by the ^{1}H NMR resonances of the trimethylsilyl group. We conjecture that, due to the dicationic complex of **4.7Cl**, the coordinated chloride ligand is insufficiently nucleophilic towards (CH$_3$)$_3$SiCF$_3$SO$_3$. Thus, the neutral TiCl$_3$(THF)$_3$ complex is treated with a slight excess of $(CH_3)_3SiCF_3SO_3$ in dichloromethane, giving an instant color change from blue-green to purple (Scheme 4.8). Solvent removal and recrystallization in CH_2Cl_2/hexanes affords a purple crystalline solid having a composition consistent with $Ti(CF_3SO_3)_3(THF)_2$. Adding $Ti(CF_3SO_3)_3(THF)_2$ to $PY5Me_2$ and two equivalents of $K[B(C_6H_3(CF_3)_2)_4]$ in 1,2-difluorobenzene affords the coordination complex $[(PY5Me_2)Ti(CF_3SO_3)][B(C_6H_3(CF_3)_2)_4]_2$ (**4.7$\mathbf{CF_3SO_3}$**, Scheme 4.9). It is expected that reduction of **4.7$\mathbf{CF_3SO_3}$** will give the corresponding Ti(II) trifluoromethanesulfonate complex, which will hopefully be labile towards ligand substitution chemistry, and permit an open coordination site at Ti(II).

$$\mathrm{TiCl_3(THF)_3 + 3\ (CH_3)_3SiCF_3SO_3 \xrightarrow[\substack{CH_2Cl_2,\ rt,\ 15\ min\\ -\ 3\ (CH_3)_3SiCl\\ -\ THF}]{} Ti(CF_3SO_3)_3(THF)_2}$$

Scheme 4.8. Preparation of titanium tris(trifluoromethanesulfonate) bis(tetrahydrofuran).

$$\begin{array}{c}\mathrm{Ti(CF_3SO_3)_3(THF)_2 + PY5Me_2}\\ \mathrm{+\ 2\ K[B(C_6H_3(CF_3)_2)_4]}\end{array} \xrightarrow[\substack{-\ 2\ KCF_3SO_3\\ -\ 2\ THF}]{\mathrm{DFB}} \underset{\mathbf{4.7CF_3SO_3}}{\mathrm{[(PY5Me_2)Ti(CF_3SO_3)][B(C_6H_3(CF_3)_2)_4]_2}}$$

Scheme 4.9. Preparation of **4.7$\mathbf{CF_3SO_3}$** with $Ti(CF_3SO_3)_3(THF)_2$.

4.4. Conclusions and Outlook

With the exception of Mn(II), the mononuclear divalent first-row transition metal chloride complexes of $PY5Me_2$ were synthesized and characterized. Relevantly, the compound **4.9Cl** represents a rare example of a well-defined Ti(II) complex without π-acidic ligands. The alkyl complexes of Cr(II), Fe(II), Co(II), and Ni(II), and the aryl complex of Fe(II) were also synthesized. Protonolysis of the metal-carbon bonds in 1,2-difluorobenzene creates electrophilic, coordinatively unsaturated metal ions that rapidly scavenge water. The electronic configurations of the Cr(II), Co(II), and Ni(II) ions stabilize the square pyramidal geometry, thus resulting in only partial occupancies of the water ligand. Depending on crystallization conditions, the sixth ligand at Fe(II) can be water, 1,4-dioxane, or diethyl ether, but ligand occupancy at the axial site always totals 100%. Thermogravimetric analyses should be performed to determine whether the sixth ligand can be removed by heating. Additionally, protonolyses could be performed in the presence of other σ donors such as H_2, CO, or ethylene to determine whether they have an affinity for the dicationic metal complexes.

Halide abstraction experiments in 1,2-difluorobenzene suggest that the $[M–Cl–M]^{3+}$ moiety is at least a kinetic trap. It may also prove to be a thermodynamic trap, but this could potentially be sidestepped deliberately adding a weak donor ligand to compete with the formation of the $[M–Cl–M]^{3+}$ unit.

Given the similar electronegativities of carbon and hydrogen, the stability of $PY5Me_2$ metal alkyl complexes indicates that, with the appropriate reagents, the metal-hydride complexes may be accessible. One potential route is to test the reactivity of metal alkyl complexes towards H_2. Another is to transmetallate from the appropriate metal hydride source.

As a final note, although N_2 coordination was not observed, it may yet be possible at open metal sites of the more reducing Ti(II) and V(II) centers. In this vein, the vanadium and titanium trifluoromethanesulfonate complexes should be further explored. Owing to their expanded *d* orbitals, second and third row transition metals may be more promising platforms for N_2 coordination and activation.

4.5. Acknowledgments

This work was funded by NSF grant CHE-146841 to Jeffrey R. Long. This research used resources of the Advanced Light Source, which is supported by the Director, Office of Science, Office of Basic Energy Sciences, of the U.S. Department of Energy under Contract No. DE-AC02-05CH11231. Miguel C. I. Gonzalez is acknowledged for collecting the crystal structures of **4.2OH$_2$**, **4.2(OH$_2$)$_{0.75}$(OEt$_2$)$_{0.25}$**, and **4.10(μ-Cl)**. D.Z.Z. thanks the National Science Foundation Graduate Research Fellowship program for support.

4.6. Supplementary Information

Table 4.S1. Crystallographic details for complexes **4.1Cl**, **4.2Cl**, and **4.3Cl**.[a]

	4.1Cl	**4.2Cl**	**4.3Cl**
formula	$C_{73}H_{45}BClCrF_{28}N_5$	$C_{64}H_{39}BClF_{25}FeN_5$	$C_{64}H_{39}BClCoF_{25}N_5$
crystal system	monoclinic	triclinic	triclinic
fw, g mol^{-1}	1622.40	1455.11	1458.19
T, K	100(2)	100(2)	100(2)
space group	$P2_1/n$	$P\bar{1}$	$P\bar{1}$
habit	plate	block	block
color	dark green	yellow	orange
Z (Z′)	4 (1)	4 (2)	4 (2)
a, Å	11.9068(4)	17.1001(5)	17.1651(9)
b, Å	16.7508(5)	19.0915(6)	19.1653(10)
c, Å	33.1934(11)	22.3740(6)	22.4105(12)
α, °	90	99.7460(10)	99.331(3)
β, °	94.9606(17)	110.4620(10)	110.542(3)
γ, °	90	109.2950(10)	109.311(3)
V, Å^3	6595.6(4)	6114.9(3)	6184.0(6)
ρ_{calc}, g cm^{-3}	1.634	1.581	1.566
μ_{calc}, mm^{-1}	0.344	0.413	0.442
2θ range, °	2.464 to 50.748	2.6 to 50.784	2.598 to 50.716
total reflections	75615	112754	50778
data / restr / parameters	12084 / 25 / 1051	22469 / 0 / 1751	7567 / 0 / 536
F(000)	3264	2924	2928
$T_{\text{min}}/T_{\text{max}}$	0.776	0.926	0.648
crystal size, mm^3	0.15 × 0.1 × 0.06	0.2 × 0.18 × 0.1	0.24 × 0.1 × 0.1
Largest diff. peak/hole / e Å^{-3}	0.99 / −0.58	2.14 / −1.82	0.99 / −0.49
R_1 (wR_2),[b] % [$I > 2\sigma(I)$]	4.44 (11.26)	6.52 (16.07)	4.62 (10.85)
R_1 (wR_2), % (all data)	5.54 (12.05)	7.38 (16.80)	6.12 (11.80)

[a] Obtained with graphite-monochromated Mo Kα (λ = 0.71073 Å) radiation.

[b] $R_1 = \sum\left||F_o| - |F_c|\right|/\sum|F_o|, wR_2 = \{\sum w(F_o^2 - F_c^2)^2/\sum w(F_o^2)^2\}^{\frac{1}{2}}$

Table 4.S2. Crystallographic details for complexes **4.4Cl**, **4.5Cl**, and **4.6Cl**.[a]

	4.4Cl	**4.5Cl**	**4.6Cl**
formula	$C_{64}H_{39}BClF_{25}N_5Ni$	$C_{61}H_{36}BN_5F_{24}ClCu$	$C_{64}H_{39}BClF_{25}N_5Zn$
crystal system	triclinic	triclinic	triclinic
fw, g mol^{-1}	1457.97	1404.75	1464.65
T, K	100(2)	100(2)	100(2)
space group	$P\bar{1}$	$P\bar{1}$	$P\bar{1}$
habit	block	block	block
color	light violet	blue	colorless
Z (Z')	4 (2)	2 (1)	4 (2)
a, Å	17.1357(5)	13.136(5)	17.1736(5)
b, Å	19.1142(5)	14.727(5)	19.1517(6)
c, Å	22.3931(6)	16.407(6)	22.4522(6)
α, °	99.4190(10)	102.304(7)	99.3150(10)
β, °	110.5500(10)	99.261(7)	110.6780(10)
γ, °	109.2090(10)	92.800(7)	109.2550(10)
V, Å^3	6153.8(3)	3049.4(18)	6190.1(3)
ρ_{calc}, g cm^{-3}	1.574	1.530	1.510
μ_{calc}, mm^{-1}	0.481	0.520	0.556
2θ range, °	2.65 to 50.718	2.58 to 51.024	2.042 to 50.782
total reflections	107380	54960	121464
data / restr / parameters	22445 / 36 / 1918	11278 / 0 / 877	7567 / 0 / 536
$F(000)$	2932	1408	2824
T_{min}/T_{max}	0.749	0.823	0.726
crystal size, mm^3	0.3 × 0.2 × 0.15	0.15 × 0.09 × 0.04	0.6 × 0.3 × 0.2
Largest diff. peak/hole / e Å^{-3}	1.05 / −0.67	2.68 / −1.31	2.32 / −1.13
R_1 (wR_2),[b] % [$I > 2\sigma(I)$]	4.20 (10.71)	6.57 (22.78)	6.25 (17.40)
R_1 (wR_2), % (all data)	4.98 (11.31)	7.07 (23.99)	6.95 (18.15)

[a] Obtained with graphite-monochromated Mo Kα (λ = 0.71073 Å) radiation.

[b] $R_1 = \sum||F_o| - |F_c||/\sum|F_o|$, $wR_2 = \{\sum w(F_o^2 - F_c^2)^2/\sum w(F_o^2)^2\}^{\frac{1}{2}}$

Table 4.S3. Crystallographic details for complexes **4.7Cl**, **4.8Cl**, and **4.9Cl**.[a]

	4.7Cl	**4.8Cl**	**4.9Cl**
formula	$C_{93}H_{49}B_2ClF_{48}N_5Ti$	$C_{93}H_{49}B_2ClF_{48}N_5V$	$C_{64}H_{39}BClF_{25}N_5Ti$
crystal system	monoclinic	monoclinic	triclinic
fw, g mol^{-1}	2253.34	2256.38	1447.16
T, K	100(2)	100(2)	100(2)
space group	$C2/c$	$C2/c$	$P\bar{1}$
habit	block	block	plate
color	orange	light violet	dark blue
Z (Z')	4 (1)	4 (1)	4 (2)
a, Å	19.3485(13)	19.3010(12)	17.2085(16)
b, Å	17.4653(12)	17.4099(11)	19.2541(18)
c, Å	27.7715(18)	27.8312(17)	22.417(2)
α, °	90	90	99.234(2)
β, °	102.484(4)	102.370(3)	110.715(2)
γ, °	90	90	109.465(2)
V, Å^3	9162.9(11)	9135.0(10)	6215.5(10)
ρ_{calc}, g cm^{-3}	1.633	1.641	1.546
μ_{calc}, mm^{-1}	0.272	0.287	0.302
2θ range, °	3.004 to 50.778	2.996 to 50.786	2.046 to 50.732
total reflections	82642	83982	31377
data / restr / parameters	8427 / 0 / 679	8397 / 0 / 745	21479 / 0 / 1751
$F(000)$	4492	4496	2908
T_{min}/T_{max}	0.936	0.828	0.669
crystal size, mm^3	0.25 × 0.15 × 0.15	0.3 × 0.15 × 0.15	0.15 × 0.02 × 0.01
Largest diff. peak/hole / e Å^{-3}	1.94 / −1.28	0.58 / −0.57	1.17 / −1.06
R_1 (wR_2),[b] % [$I > 2\sigma(I)$]	6.31 (16.11)	3.85 (0.915)	7.71 (18.84)
R_1 (wR_2), % (all data)	6.90 (16.66)	4.07 (9.33)	15.13 (22.67)

[a] Obtained with graphite-monochromated Mo Kα ($\lambda = 0.71073$ Å) radiation.

[b] $R_1 = \sum\left||F_o| - |F_c|\right|/\sum|F_o|, wR_2 = \{\sum w(F_o^2 - F_c^2)^2/\sum w(F_o^2)^2\}^{\frac{1}{2}}$

Table 4.S4. Crystallographic details for complexes **4.10Cl**, **4.1CH$_3$**, and **4.2CH$_3$**.[a]

	4.10Cl	**4.1CH$_3$**	**4.2CH$_3$**
formula	$C_{64}H_{39}BClF_{25}N_5V$	$C_{73.87}H_{43.97}BCl_{0.13}CrF_{28}N_5$	$C_{73.63}H_{42.88}BCl_{0.37}F_{28}FeN_5$
crystal system	triclinic	monoclinic	monoclinic
fw, g mol^{-1}	1450.20	1600.97	1609.35
T, K	100(2)	100(2)	100(2)
space group	$P\bar{1}$	$P2_1/m$	$P2_1/m$
habit	block	plate	plate
color	dark purple	dark green	dark purple
Z (Z')	4 (2)	2 (0.5)	2 (0.5)
a, Å	17.1619(5)	11.8747(10)	11.7907(8)
b, Å	19.1610(6)	16.7645(12)	16.7802(10)
c, Å	22.3865(7)	17.2841(14)	17.2464(11)
α, °	99.2780(10)	90	90
β, °	110.5610(10)	105.475(4)	105.514(3)
γ, °	109.2580(10)	90	90
V, Å^3	6179.0(3)	3316.1(5)	3287.9(4)
ρ_{calc}, g cm^{-3}	1.559	1.603	1.626
μ_{calc}, mm^{-1}	0.326	0.307	0.375
2θ range, °	2.602 to 50.744	3.446 to 50.762	3.45 to 50.786
total reflections	100926	23094	45219
data / restr / parameters	22639 / 0 / 1751	6248 / 0 / 551	6243 / 6 / 545
F(000)	2912	1611	1618
$T_{\text{min}}/T_{\text{max}}$	0.912	0.713	0.640
crystal size, mm^3	0.15 × 0.06 × 0.02	0.30 × 0.08 × 0.04	0.16 × 0.1 × 0.02
Largest diff. peak/hole / e Å^{-3}	1.69 / −1.44	0.74 / −0.44	0.93 / −0.58
R_1 (wR_2),[b] % [$I > 2\sigma(I)$]	6.90 (16.64)	4.99 (10.91)	4.90 (11.64)
R_1 (wR_2), % (all data)	10.68 (18.97)	6.81 (12.03)	6.50 (12.69)

[a] Obtained with graphite-monochromated Mo Kα (λ = 0.71073 Å) radiation.

[b] $R_1 = \sum\left||F_o| - |F_c|\right|/\sum|F_o|, wR_2 = \{\sum w(F_o^2 - F_c^2)^2/\sum w(F_o^2)^2\}^{\frac{1}{2}}$

Table 4.S5. Crystallographic details for complexes **4.3CH$_3$**, **4.4CH$_3$**, and **4.2Ph**.[a]

	4.3CH$_3$	**4.4CH$_3$**	**4.2Ph**
formula	$C_{62}H_{40}BCoF_{24}N_5$	$C_{68}H_{48.77}BF_{24}N_5Ni$	$C_{73}H_{46}BF_{26}FeN_5$
crystal system	monoclinic	monoclinic	triclinic
fw, g mol^{-1}	1380.73	1461.41	1553.81
T, K	100(2)	100(2)	100(2)
space group	$P2_1/n$	$P2_1/c$	$P\bar{1}$
habit	block	plate	block
color	red orange	yellow	dark red
Z (Z′)	4 (1)	4 (1)	2 (1)
a, Å	14.8894(6)	19.2144(8)	13.4871(6)
b, Å	21.1078(9)	18.8339(6)	13.6084(7)
c, Å	18.3813(8)	18.0480(7)	18.0332(9)
α, °	90	90	93.268(2)
β, °	93.559(2)	100.4444(14)	94.909(2)
γ, °	90	90	95.437(2)
V, Å^3	5765.8(4)	6423.0(4)	3275.7(3)
ρ_{calc}, g cm^{-3}	1.591	1.511	1.575
μ_{calc}, mm^{-1}	0.422	0.419	0.354
2θ range, °	3.352 to 50.722	3.054 to 50.754	2.272 to 50.8
total reflections	56975	89258	108060
data / restr / parameters	10522 / 37 / 898	11756 / 12 / 946	11960 / 0 / 957
F(000)	2780	2963	1568
$T_{\text{min}}/T_{\text{max}}$	0.898	0.744	0.926
crystal size, mm^3	0.2 × 0.08 × 0.05	0.2 × 0.08 × 0.03	0.24 × 0.2 × 0.1
Largest diff. peak/hole / e Å^{-3}	0.91 / −0.47	1.06 / −0.72	1.06 / −0.63
R_1 (wR_2),[b] % [$I > 2\sigma(I)$]	3.41 (8.15)	5.33 (12.22)	3.96 (9.89)
R_1 (wR_2), % (all data)	4.05 (8.53)	7.00 (13.24)	4.22 (10.11)

[a] Obtained with graphite-monochromated Mo Kα ($\lambda = 0.71073$ Å) radiation.

[b] $R_1 = \sum||F_o| - |F_c||/\sum|F_o|, wR_2 = \{\sum w(F_o^2 - F_c^2)^2/\sum w(F_o^2)^2\}^{\frac{1}{2}}$

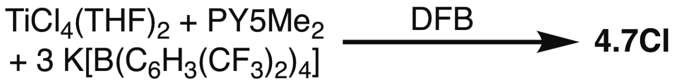

Scheme 4.S1. Alternate preparation of **4.7Cl** from $TiCl_4(THF)_2$.

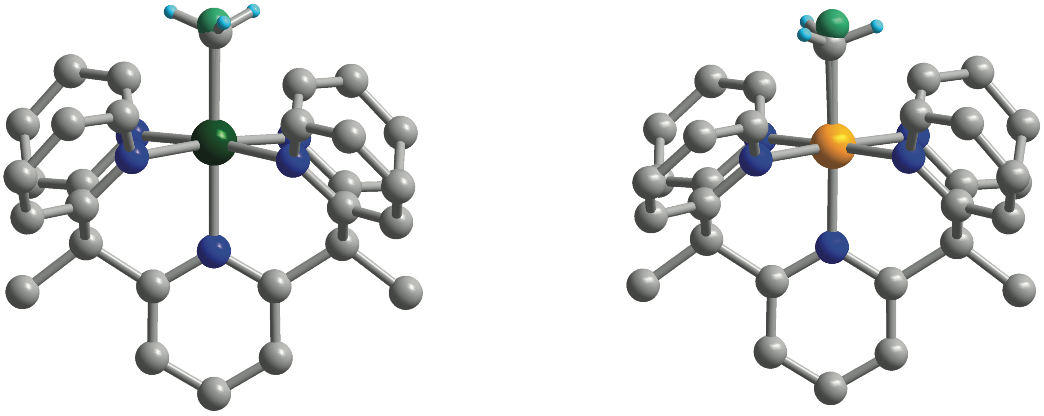

Figure 4.S1. Molecular structures of the cations in **4.1CH$_3$** (left) and **4.2CH$_3$** (right), highlighting the substitutional disorder of methyl versus chloride ligands. The crystallographically determined CH_3^-/Cl^- ratios are 87/13 and 63/37 for **4.1CH$_3$** and **4.2CH$_3$**, respectively. Dark green, orange, blue-green, blue, gray, and light blue spheres represent Cr, Fe, Cl, N, C, and H atoms, respectively. H atoms (except for those of the M–CH_3 group), uncoordinated anions, and solvent are omitted for clarity.

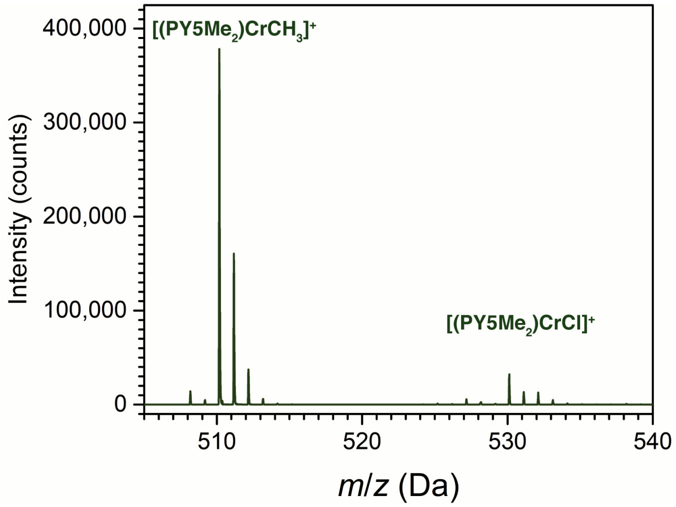

Figure 4.S2. ESI-MS of a DFB solution of **4.1CH$_3$**, showing the primary signal for the $[(PY5Me_2)CrCH_3]^+$ cation (m/z = 510.17 Da) and the secondary signal for the $[(PY5Me_2)CrCl]^+$ impurity (m/z = 530.12 Da).

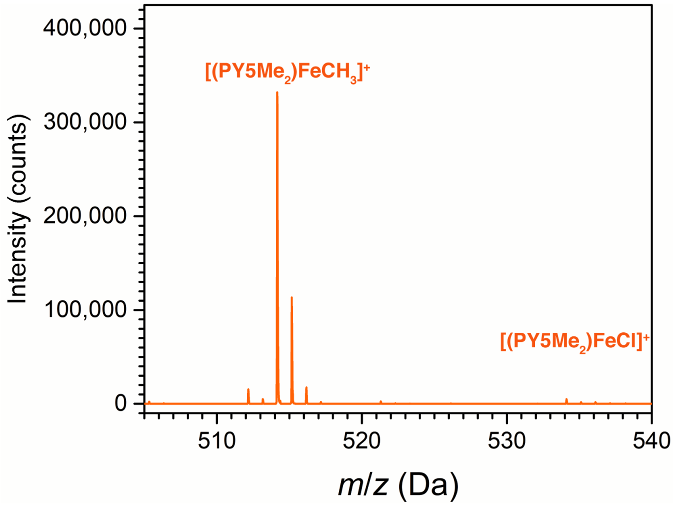

Figure 4.S3. ESI-MS of a DFB solution of **4.2CH$_3$**, showing the main signal for the $[(PY5Me_2)FeCH_3]^+$ cation (*m*/*z* = 514.17 Da) and the minor signal for the $[(PY5Me_2)FeCl]^+$ impurity (*m*/*z* = 534.11 Da).

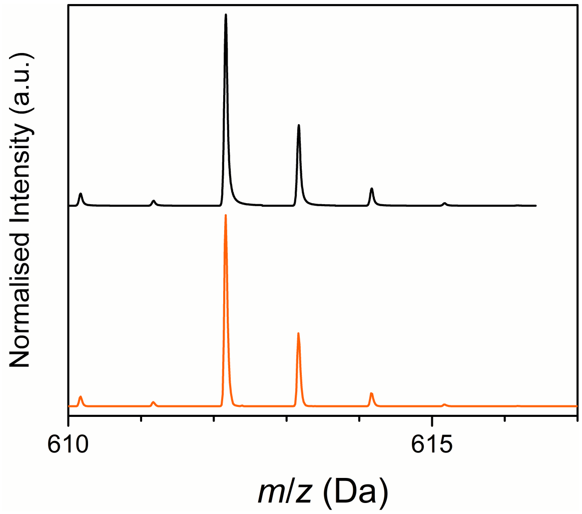

Figure 4.S4. ESI-MS of a **4.2CH$_3$** after standing in DFB for three days, showing the calculated (black) and experimental (orange) spectra, corresponding to the $[(PY5Me_2)Fe(C_6H_3F_2)]^+$ cation (*m*/*z* = 612.17 Da).

Table 4.S6. Crystallographic details for complexes **$4.1(OH_2)_{0.64}$**, **$4.2OH_2$**, and **$4.3(OH_2)_{0.21}$**.

	$4.1(OH_2)_{0.64}$ [a]	**$4.2OH_2$** [c]	**$4.3(OH_2)_{0.21}$** [a]
formula	$C_{99}H_{64.88}B_2CrF_{48}N_5O_{0.64}$	$C_{99}H_{65}B_2F_{48}FeN_5O$	$C_{99}H_{63}B_2CoF_{48}N_5O_{0.21}$
crystal system	monoclinic	triclinic	monoclinic
fw, g mol^{-1}	2320.41	2330.03	2318.43
T, K	100(2)	273(2)	100(2)
space group	$C2/c$	$P\bar{1}$	$C2/c$
habit	block	block	block
color	green	yellow green	orange
Z (Z')	4 (1)	2 (1)	4 (1)
a, Å	19.8036(8)	12.821(4)	19.7066(12)
b, Å	16.8341(6)	12.959(4)	16.7703(11)
c, Å	28.8474(11)	29.091(9)	28.7223(18)
α, °	90	89.739(12)	90
β, °	90.199(2)	89.036(18)	90.883(3)
γ, °	90	80.245(18)	90
V, Å^3	9617.0(6)	4763(3)	9491.2(10)
ρ_{calc}, g cm^{-3}	1.603	1.625	1.622
μ_{calc}, mm^{-1}	0.265	0.551	0.328
2θ range, °	2.824 to 50.79	3.49 to 69.178	2.836 to 50.766
total reflections	52456	51780	84516
data / restr / parameters	8845 / 540 / 739	20301 /4 / 1415	8724 / 38 / 786
$F(000)$	4660	2340	4651
$T_{\text{min}}/T_{\text{max}}$	0.766	0.811	0.913
crystal size, mm^3	0.3 × 0.1 × 0.1	0.35 × 0.06 × 0.04	0.22 × 0.15 × 0.15
Largest diff. peak/hole / e Å^{-3}	1.11 / −0.70	1.84 / −0.84	0.88 / −0.58
R_1 (wR_2),[b] % [$I > 2\sigma(I)$]	6.18 (16.54)	7.46 (18.51)	4.45 (10.64)
R_1 (wR_2), % (all data)	7.17 (17.40)	9.65 (19.87)	4.71 (10.82)

[a] Obtained with graphite-monochromated Mo Kα (λ = 0.71073 Å) radiation.

[b] $R_1 = \sum\left||F_o| - |F_c|\right|/\sum|F_o|$, $wR_2 = \{\sum w(F_o^2 - F_c^2)^2/\sum w(F_o^2)^2\}^{\frac{1}{2}}$

[c] Obtained with synchrotron (λ = 0.8856 Å) radiation.

Table 4.S7. Crystallographic details for complexes **4.4(OH$_2$)$_{0.63}$**, **4.2C$_4$H$_8$O$_2$**, and **4.2(OH$_2$)$_{0.75}$(OEt$_2$)$_{0.25}$**.

	4.4(OH$_2$)$_{0.63}$ [a]	**4.2C$_4$H$_8$O$_2$** [a]	**4.2(OH$_2$)$_{0.75}$(OEt$_2$)$_{0.25}$** [c]
formula	$C_{99}H_{63.63}B_2F_{48}N_5NiO_{0.63}$	$C_{97}H_{50}B_2F_{48}FeN_5O_2$	$C_{97.51}H_{55.03}B_2F_{48}FeN_4O_{1.75}$
crystal system	monoclinic	monoclinic	monoclinic
fw, g mol^{-1}	2325.63	2306.91	2300.16
T, K	100(2)	100(2)	273(2)
space group	$C2/c$	$P2_1$	$P2_1$
habit	block	block	block
color	purple	green	yellow green
Z (Z')	4 (1)	2 (1)	2 (1)
a, Å	19.8115(6)	13.3755(6)	13.2864(9)
b, Å	16.7312(5)	18.3853(8)	18.3152(11)
c, Å	28.8161(8)	20.2974(9)	20.4674(14)
α, °	90	90	90
β, °	90.9614(19)	108.681(2)	108.94
γ, °	90	90	90
V, Å^3	9550.3(5)	4728.4(4)	4710.9(5)
ρ_{calc}, g cm^{-3}	1.617	1.620	1.622
μ_{calc}, mm^{-1}	0.350	0.307	0.556
2θ range, °	3.186 to 50.79	3.064 to 50.78	2.622 to 65.59
total reflections	54195	91378	56173
data / restr / parameters	8778 / 0 / 740	17172 / 1 / 1368	17445 / 1 / 1424
F(000)	2780	2302	2300
$T_{\text{min}}/T_{\text{max}}$	0.908	0.906	0.954
crystal size, mm^3	0.3 × 0.2 × 0.2	0.2 × 0.18 × 0.14	0.2 × 0.18 × 0.13
Largest diff. peak/hole / e Å^{-3}	0.66 / −0.43	2.45 / −0.67	0.86 / −0.65
R_1 (wR_2),[b] % [$I > 2\sigma(I)$]	4.57 (9.57)	7.38 (20.48)	9.49 (20.07)
R_1 (wR_2), % (all data)	6.92 (10.70)	8.19 (21.14)	11.89 (21.14)

[a] Obtained with graphite-monochromated Mo Kα (λ = 0.71073 Å) radiation.

[b] $R_1 = \sum||F_o| - |F_c||/\sum|F_o|, wR_2 = \{\sum w(F_o^2 - F_c^2)^2/\sum w(F_o^2)^2\}^{\frac{1}{2}}$

[c] Obtained with synchrotron (λ = 0.8856 Å) radiation.

Table 4.S8. Crystallographic data for **4.10(μ-Cl)** and **4.10CF$_3$SO$_3$**. [a]

	4.10(μ-Cl)	**4.10CF$_3$SO$_3$**
formula	$C_{164}H_{96}B_3ClF_{67}N_{10}O_2V_2$	$C_{68}H_{41}BF_{29}N_5O_3SV$
crystal system	monoclinic	triclinic
fw, g mol^{-1}	3681.26	1620.87
T, K	273(2)	273(2)
space group	Cc	$P\bar{1}$
habit	block	block
color	red	red
Z (Z′)	4 (1)	8 (1)
a, Å	24.8964(9)	17.793(4)
b, Å	24.8904(9)	23.387(7)
c, Å	25.6058(9)	31.530(11)
α, °	90	90.04(2)
β, °	90.186(3)	90.742(14)
γ, °	90	90.848(14)
V, Å^3	15867.4(10)	13118(7)
ρ_{calc}, g cm^{-3}	1.541	1.641
μ_{calc}, mm^{-1}	0.318	0.403
2θ range, °	2.522 to 55.858	2.366 to 54.936
total reflections	59784	108036
data / restr / parameters	25753 / 5 / 2238	41255 / 0 / 3897
F(000)	7388	6504
$T_{\text{min}}/T_{\text{max}}$	0.975	0.820
crystal size, mm^3	0.15 × 0.15 × 0.15	0.15 × 0.08 × 0.08
Largest diff. peak/hole / e Å^{-3}	1.28 / −0.66	0.97 / −0.83
R_1 (wR_2),[b] % [$I > 2\sigma(I)$]	9.47 (23.33)	6.19 (15.83)
R_1 (wR_2), % (all data)	12.28 (25.63)	7.79 (17.12)

[a] Obtained with synchrotron (λ = 0.7749 Å) radiation.

[b] $R_1 = \sum\big||F_o| - |F_c|\big|/\sum|F_o|, wR_2 = \{\sum w(F_o^2 - F_c^2)^2/\sum w(F_o^2)^2\}^{\frac{1}{2}}$

4.7. References

(1) Zee, D. Z.; Chantarojsiri, T.; Long, J. R.; Chang, C. J. Metal–Polypyridyl Catalysts for Electro- and Photochemical Reduction of Water to Hydrogen. *Acc. Chem. Res.* **2015**, *48* (7), 2027–2036.

(2) Karunadasa, H. I.; Chang, C. J.; Long, J. R. A Molecular Molybdenum-Oxo Catalyst for Generating Hydrogen From Water. *Nature* **2010**, *464* (7293), 1329–1333.

(3) Karunadasa, H. I.; Montalvo, E.; Sun, Y.; Majda, M.; Long, J. R.; Chang, C. J. A Molecular MoS_2 Edge Site Mimic for Catalytic Hydrogen Generation. *Science* **2012**, *335* (6069), 698–702.

(4) Sun, Y.; Bigi, J. P.; Piro, N. A.; Tang, M. L.; Long, J. R.; Chang, C. J. Molecular Cobalt Pentapyridine Catalysts for Generating Hydrogen From Water. *J. Am. Chem. Soc.* **2011**, *133* (24), 9212–9215.

(5) Nippe, M.; Khnayzer, R. S.; Panetier, J. A.; Zee, D. Z.; Olaiya, B. S.; Head-Gordon, M.; Chang, C. J.; Castellano, F. N.; Long, J. R. Catalytic Proton Reduction with Transition Metal Complexes of the Redox-Active Ligand bpy2PYMe. *Chem. Sci.* **2013**, *4* (10), 3934–3945.

(6) King, A. E.; Surendranath, Y.; Piro, N. A.; Bigi, J. P.; Long, J. R.; Chang, C. J. A Mechanistic Study of Proton Reduction Catalyzed by a Pentapyridine Cobalt Complex: Evidence for Involvement of an Anation-Based Pathway. *Chem. Sci.* **2013**, *4*, 1578–1587.

(7) Sundstrom, E. J.; Yang, X.; Thoi, V. S.; Karunadasa, H. I.; Chang, C. J.; Long, J. R.; Head-Gordon, M. Computational and Experimental Study of the Mechanism of Hydrogen Generation From Water by a Molecular Molybdenum-Oxo Electrocatalyst. *J. Am. Chem. Soc.* **2012**, *134* (11), 5233–5242.

(8) Gutmann, V. Solvent Effects on the Reactivities of Organometallic Compounds. *Coord. Chem. Rev.* **1976**, *18* (2), 225–255.

(9) Strauss, S. The Search for Larger and More Weakly Coordinating Anions. *Chem. Rev.* **1993**, *93* (927), 942.

(10) Reed, C. A. Carboranes: a New Class of Weakly Coordinating Anions for Strong Electrophiles, Oxidants, and Superacids. *Acc. Chem. Res.* **1998**, *31* (3), 133–139.

(11) Krossing, I.; Raabe, I. Noncoordinating Anions—Fact or Fiction? A Survey of Likely Candidates. *Angew. Chem. Int. Ed.* **2004**, *43* (16), 2066–2090.

(12) Bernskoetter, W. H.; Schauer, C. K.; Goldberg, K. I.; Brookhart, M. Characterization of a Rhodium(I) σ-Methane Complex in Solution. *Science* **2009**, *326* (5952), 553–556.

(13) Adams, G. M.; Chadwick, F. M.; Pike, S. D.; Weller, A. S. A CH_2Cl_2 Complex of a $[Rh(Pincer)]^+$ Cation. *Dalton Trans.* **2015**, *44* (14), 6340–6342.

(14) Tsay, C.; Peters, J. C. Thermally Stable N_2 And H_2 Adducts of Cationic Nickel(II). *Chem. Sci.* **2012**, *3* (4), 1313–1318.

(15) Bechlars, B.; D'Alessandro, D. M.; Jenkins, D. M.; Iavarone, A. T.; Glover, S. D.; Kubiak, C. P.; Long, J. R. High-Spin Ground States via Electron Delocalization in Mixed-Valence Imidazolate-Bridged Divanadium Complexes. *Nature Chem.* **2010**, *2* (5), 362–368.

(16) Heintz, R. A.; Smith, J. A.; Szalay, P. S.; Weisgerber, A.; Dunbar, K. R. Useful Reagents and Ligands. *Inorg. Synth.* **2002**, *33*, 75–121.

(17) Boudier, A.; Breuil, P.-A. R.; Magna, L.; Olivier-Bourbigou, H.; Braunstein, P.

Nickel(II) Complexes with Imino-Imidazole Chelating Ligands Bearing Pendant Donor Groups (SR, or, NR_2, Pr_2) As Precatalysts in Ethylene Oligomerization. *J. Organomet. Chem.* **2012**, *718*, 31–37.

(18) Edema, J. J. H.; Duchateau, R.; Gambarotta, S.; Hynes, R.; Gabe, E. Novel Titanium(II) Amine Complexes L_4TiCl_2 [L = 1/2 *N*,*N*,*N*′,*N*′-Tetramethylethylenediamine (TMEDA), 1/2 *N*,*N*,*N*′-Trimethylethylenediamine, Pyridine, 1/2 2,2′-Bipyridine]: Synthesis and Crystal Structure of Monomeric Trans-$(TMEDA)_2TiCl_2$. *Inorg. Chem.* **1991**, *30* (2), 154–156.

(19) Bergbreiter, D. E.; Killough, J. M. Reactions of Potassium-Graphite. *J. Am. Chem. Soc.* **1978**, *100* (7), 2126–2134.

(20) Kern, R. J. Tetrahydrofuran Complexes of Transition Metal Chlorides. *J. Inorg. Nucl. Chem.* **1962**, *24* (9), 1105–1109.

(21) Jones, N. A.; Liddle, S. T.; Wilson, C.; Arnold, P. L. Titanium(III) Alkoxy-N-Heterocyclic Carbenes and a Safe, Low-Cost Route to $TiCl_3(THF)_3$. *Organometallics* **2007**, *26* (3), 755–757.

(22) Brookhart, M.; Grant, B.; Volpe, A. F., Jr. $[(3,5\text{-}(CF_3)_2C_6H_3)_4B]\text{-}[H(OEt_2)_2]^+$: A Convenient Reagent for Generation and Stabilization of Cationic, Highly Electrophilic Organometallic Complexes. *Organometallics* **1992**, *11* (11), 3920–3922.

(23) Tempel, D. J.; Johnson, L. K.; Huff, R. L.; White, P. S.; Brookhart, M. Mechanistic Studies of Pd(II)−A-Diimine-Catalyzed Olefin Polymerizations 1. *J. Am. Chem. Soc.* **2000**, *122* (28), 6686–6700.

(24) Hoye, T. R.; Eklov, B. M.; Voloshin, M. No-D NMR Spectroscopy as a Convenient Method for Titering Organolithium (RLi), RMgX, and LDA Solutions. *Org. Lett.* **2004**, *6* (15), 2567–2570.

(25) Love, B. E.; Jones, E. G. The Use of Salicylaldehyde Phenylhydrazone as an Indicator for the Titration of Organometallic Reagents. *J. Org. Chem.* **1999**, *64* (10), 3755–3756.

(26) Hughes, R. P.; Rose, P. R.; Rheingold, A. L. Transition-Metal Chemistry of Hexafluorobutadiene. Facile Hydrolysis of (Hexafluoro-1-Metalla-3-Cyclopentene)Rhodium Complexes to Give Tetrafluoro-1-Metalla-3-Cyclopenten-2-One and Tetrafluoro-1-Metalla-2-Cyclopenten-4-One Complexes. Crystal and Molecular Structures of Trans-[Cyclo][$(RhCF_2CF{=}CFCO)Cl(PPh_3)_2$], Mer-[Cyclo][$(RhCF_2CF{=}CFCF_2)Cl(PMe_3)_3$], And Mer-[Cyclo][$(RhCF{=}CFCOCF_2)Cl(PMe_3)_3$]. *Organometallics* **1993**, *12* (8), 3109–3117.

(27) Connelly, S. J.; Kaminsky, W.; Heinekey, D. M. Structure and Solution Reactivity of (Triethylsilylium)Triethylsilane Cations. *Organometallics* **2013**, *32* (24), 7478–7481.

(28) APEX2. v. 2009; Bruker Analytical X-ray Systems, Inc; Madison, WI, 2009.

(29) Sheldrick, G. M. Version 2.03; Bruker Analytical Systems, Inc.: Madison, WI, 2000.

(30) Sheldrick, G. SHELXT - Integrated Space-Group and Crystal-Structure Determination. *Acta Crystallogr A Found Adv* **2015**, *71* (1), 3–8.

(31) Sheldrick, G. A Short History of SHELX. *Acta Crystallogr A Found Crystallogr* **2008**, *64* (1), 112–122.

(32) Sheldrick, G. Crystal Structure Refinement with SHELXL. *Acta Crystallogr C Struct Chem* **2015**, *71* (1), 3–8.

(33) Müller, P. Practical Suggestions for Better Crystal Structures. *Crystallography Reviews* **2009**, *15* (1), 57–83.

(34) Edema, J. J. H.; Stauthamer, W.; Van Bolhuis, F.; Gambarotta, S.; Smeets, W. J. J.;

Spek, A. L. Novel Vanadium(II) Amine Complexes: a Facile Entry in the Chemistry of Divalent Vanadium. Synthesis and Characterization of Mononuclear L_4VCl_2 [L = Amine, Pyridine]: X-Ray Structures of Trans-$(TMEDA)_2VCl_2$ [TMEDA = *N*,*N*,*N′*,*N′*-Tetramethylethylenediamine] and Trans-$Mz_2V(Py)_2$ [Mz = *o*-$C_6H_4CH_2N(CH_3)_2$, Py = Pyridine]. *Inorg. Chem.* **1990**, *29* (7), 1302–1306.

(35) Araya, M. A.; Cotton, F. A.; Matonic, J. H.; Murillo, C. A. An Efficient Reduction Process Leading to Titanium(II) and Niobium(II): Preparation and Structural Characterization of Trans-$MCl_2(Py)_4$ Compounds, M = Ti, Nb, and Mn. *Inorg. Chem.* **1995**, *34* (22), 5424–5428.

(36) Wijeratne, G. B.; Zolnhofer, E. M.; Fortier, S.; Grant, L. N.; Carroll, P. J.; Chen, C.-H.; Meyer, K.; Krzystek, J.; Ozarowski, A.; Jackson, T. A.; Mindiola, D. J.; Telser, J. Electronic Structure and Reactivity of a Well-Defined Mononuclear Complex of Ti(II). *Inorg. Chem.* **2015**, *54* (21), 10380–10397.

(37) Howells, R. D.; Mc Cown, J. D. Trifluoromethanesulfonic Acid and Derivatives. *Chem. Rev.* **1977**, *77* (1), 69–92.

(38) Lawrance, G. A. Coordinated Trifluoromethanesulfonate and Fluorosulfate. *Chem. Rev.* **1986**, *86* (1), 17–33.

(39) Dixon, N. E.; Lawrance, G. A.; Lay, P. A.; Sargeson, A. M.; Taube, H. Trifluoromethanesulfonates and Trifluoromethanesulfonato-O Complexes. *Inorg. Synth.* **1990**, *28*, 70–76.

Appendix A. Improved Syntheses of Molybdenum Complexes of $PY5Me_2$

A.1. Overview

The molybdenum(IV)-oxo and disulfide complexes of the ligand 2,6-bis(1,1-di(pyridin-2-yl)ethyl)pyridine ($PY5Me_2$) are electrocatalysts for the reduction of water to H_2.[1,2] The investigations of these complexes centered on their trifluoromethanesulfonate salts, which are appreciably soluble in polar organic solvents such as acetonitrile as well as water for electrochemical study.

The literature preparation of $[(PY5Me_2)MoO](CF_3SO_3)_2$ and $[(PY5Me_2)MoS_2](CF_3SO_3)_2$ utilizes the divalent, seven-coordinate molybdenum precursor $MoI_2(CO)_3(CH_3CN)_2$.[3] Refluxing the ligand $PY5Me_2$ with 1.5 equivalents of $MoI_2(CO)_3(CH_3CN)_2$ for 3 days in toluene affords the *trivalent* $[(PY5Me_2)MoI]I_2$ complex (Scheme A.1). This slow metalation possibly involves disproportionation of the $MoI_2(CO)_3(CH_3CN)_2$ reagent into $Mo(CO)_6$ and a soluble MoI_3 source, which is then captured by the $PY5Me_2$ ligand (Scheme A.2). Metathesis of the iodide ions with silver trifluoromethanesulfonate afforded the molybdenum(III) trifluoromethanesulfonate complex $[(PY5Me_2)Mo(CF_3SO_3)](CF_3SO_3)_2$, which was reduced with potassium graphite to give the Mo(II) complex $[(PY5Me_2)Mo(CF_3SO_3)](CF_3SO_3)$. Perhaps owing to the low solubility of the $[(PY5Me_2)Mo(CF_3SO_3)](CF_3SO_3)_2$ complex in tetrahydrofuran, the reduction with potassium graphite occasionally led to a side reaction that formed a dark purple impurity. Finally, oxidation of the $[(PY5Me_2)Mo(CF_3SO_3)](CF_3SO_3)$ complex with water or elemental sulfur affords $[(PY5Me_2)MoO](CF_3SO_3)_2$ and $[(PY5Me_2)MoS_2](CF_3SO_3)_2$, respectively.

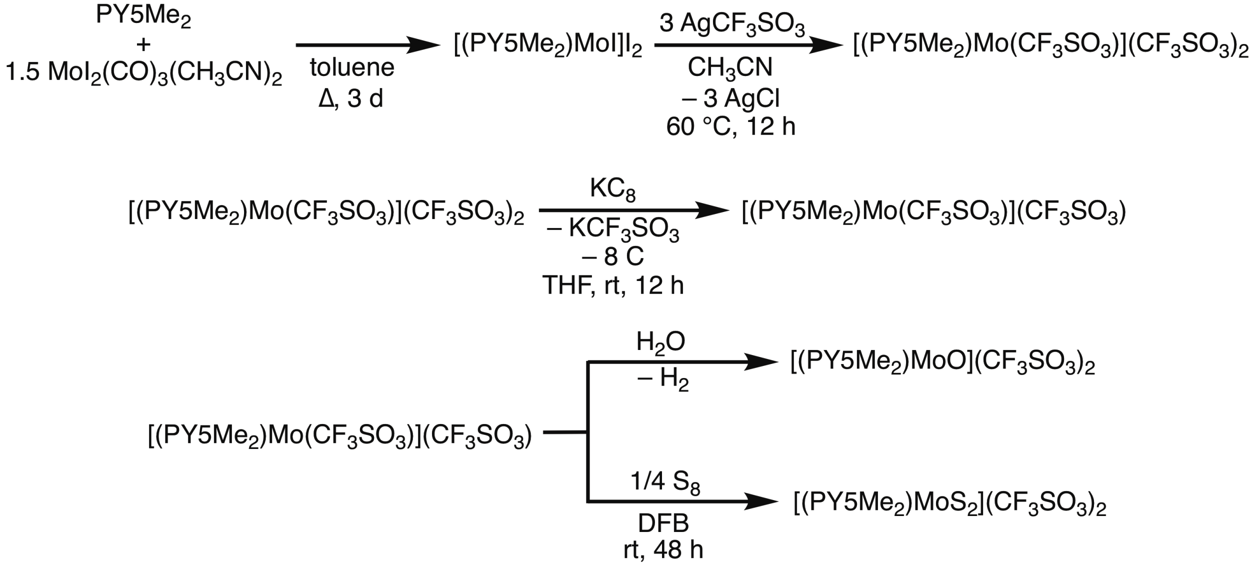

Scheme A.1. The reported preparation of $[(PY5Me_2)MoO](CF_3SO_3)_2$ and $[(PY5Me_2)MoS_2](CF_3SO_3)_2$.

$$3\ MoI_2(CO)_3(CH_3CN)_2 \longrightarrow 2\ MoI_3(CH_3CN)_3 + Mo(CO)_6 + 3\ CO$$

Scheme A.2. Possible disproportionation pathway of dichlorotricarbonylbis(acetonitrile)molybdenum.

In lieu of the long reaction times and complications involving the $MoI_2(CO)_3(CH_3CN)_2$ reagent, a new synthetic entry to the set of $PY5Me_2$ molybdenum complexes was developed and is presented here (Scheme A.3). The synthesis of the molybdenum(III) complex

$[(PY5Me_2)Mo(CF_3SO_3)](CF_3SO_3)_2$ now utilizes $Mo(CF_3SO_3)_3$, which shortened the preparation time by around three days. Additionally, the reduction of $[(PY5Me_2)Mo(CF_3SO_3)](CF_3SO_3)_2$ is now performed in acetonitrile, in which it is soluble, instead of in tetrahydrofuran. Due to the lower reductive stability of acetonitrile (versus tetrahydrofuran), potassium cyclopentadienyldicarbonyl ferrate (E = ~−1.8 V versus $Fe(C_5H_5)_2^{+/0}$)[4] is the chosen reductant, which is ~300 mV more negative than the Mo(III/II) redox couple.[1]

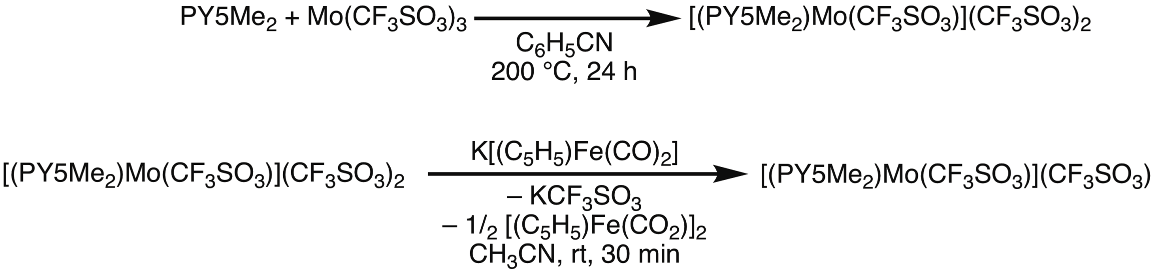

$$PY5Me_2 + Mo(CF_3SO_3)_3 \xrightarrow[\substack{C_6H_5CN \\ 200\ °C,\ 24\ h}]{} [(PY5Me_2)Mo(CF_3SO_3)](CF_3SO_3)_2$$

$$[(PY5Me_2)Mo(CF_3SO_3)](CF_3SO_3)_2 \xrightarrow[\substack{-\ KCF_3SO_3 \\ -\ 1/2\ [(C_5H_5)Fe(CO_2)]_2 \\ CH_3CN,\ rt,\ 30\ min}]{K[(C_5H_5)Fe(CO)_2]} [(PY5Me_2)Mo(CF_3SO_3)](CF_3SO_3)$$

Scheme A.3. Improved syntheses of the molybdenum complexes $[(PY5Me_2)Mo(CF_3SO_3)](CF_3SO_3)_2$ and $[(PY5Me_2)Mo(CF_3SO_3)](CF_3SO_3)$.

Also presented here is the preparation of a molybdenum(IV)-oxo complex of $PY5Me_2$ with $[B(C_6H_3(CF_3)_2)_4]$ anions (Scheme A.4). Relative to the trifluoromethanesulfonate complexes, the $[(PY5Me_2)MoO][B(C_6H_3(CF_3)_2)_4]_2$ complex is highly soluble in tetrahydrofuran. This property may prove useful for the study and isolation of low-valent molybdenum-oxo intermediates. The molecular structure of $[(PY5Me_2)MoO][B(C_6H_3(CF_3)_2)_4]_2$ is shown in Figure A.1. Important crystallographic data is presented in Table A.1.

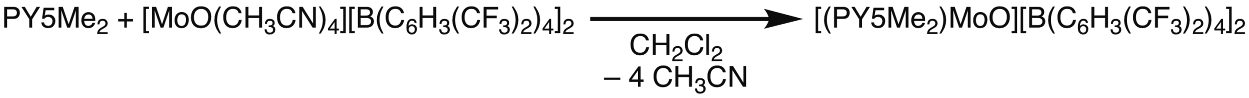

$$PY5Me_2 + [MoO(CH_3CN)_4][B(C_6H_3(CF_3)_2)_4]_2 \xrightarrow[\substack{CH_2Cl_2 \\ -\ 4\ CH_3CN}]{} [(PY5Me_2)MoO][B(C_6H_3(CF_3)_2)_4]_2$$

Scheme A.4. Synthesis of $[(PY5Me_2)MoO][B(C_6H_3(CF_3)_2)_4]_2$.

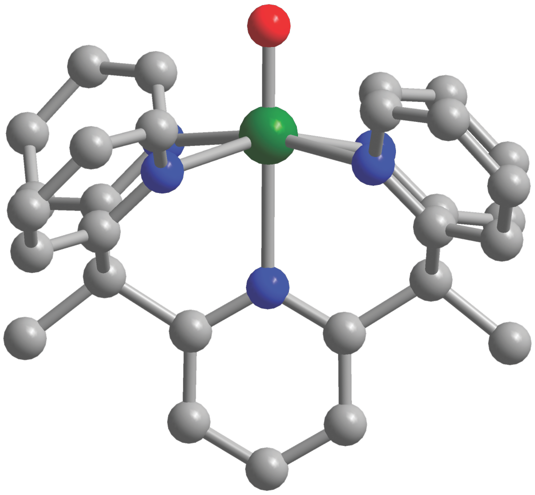

Figure A.1. Single crystal X-ray structure of the complex $[(PY5Me_2)MoO][B(C_6H_3(CF_3)_2)_4]_2$. Green, blue, red, and gray spheres represent Mo, N, O, and C atoms, respectively. H atoms, $[B(C_6H_3(CF_3)_2)_4]^-$ anions, and solvent molecules are omitted for clarity.

Table A.1. Crystallographic details for complex $[(PY5Me_2)MoO][B(C_6H_3(CF_3)_2)_4]_2$.[a]

	$[(PY5Me_2)MoO][B(C_6H_3(CF_3)_2)_4]_2$
formula	$C_{99}H_{63}B_2F_{48}MoN_5O$
crystal system	monoclinic
fw, g mol^{-1}	2368.10
T, K	100(2)
space group	$C2/c$
habit	block
color	green
Z (Z')	4 (1)
a, Å	19.9016(5)
b, Å	16.6100(4)
c, Å	28.8304(7)
α, °	90
β, °	90.7410(10)
γ, °	90
V, Å^3	9529.5(4)
ρ_{calc}, g cm^{-3}	1.651
μ_{calc}, mm^{-1}	0.285
2θ range, °	3.352 to 50.722
total reflections	95430
data / restr / parameters	8740 / 0 / 734
$F(000)$	4736
$T_{\min}/T_{\max}$	0.894
crystal size, mm^3	0.25 × 0.11 × 0.11
Largest diff. peak/hole / e Å^{-3}	0.78 / −0.50
R_1 (wR_2),[b] % [$I > 2\sigma(I)$]	3.90 (9.98)
R_1 (wR_2), % (all data)	4.21 (10.23)

[a] Obtained with graphite-monochromated Mo Kα (λ = 0.71073 Å) radiation.

[b] $R_1 = \sum\left||F_o| - |F_c|\right|/\sum|F_o|, wR_2 = \{\sum w(F_o^2 - F_c^2)^2/\sum w(F_o^2)^2\}^{\frac{1}{2}}$

A.2. Experimental

A.2.1. Materials and Methods

Air- and/or moisture-sensitive compounds were synthesized and manipulated under air-free conditions, using either a Vacuum Atmospheres glovebox or standard Schlenk techniques under a dry nitrogen or argon atmosphere. Anhydrous tetrahydrofuran (THF), diethyl ether (Et_2O), acetonitrile, hexanes, dichloromethane, and toluene were dried and deoxygenated with a commercial solvent purification system from JC Meyer Solvent Systems, then stored under an inert atmosphere over beads of 3 Å molecular sieves. Benzonitrile was dried over phosphorus pentoxide, distilled under reduced pressure (retaining the 16–80% fraction), de-oxygenated by three freeze-pump-thaw cycles, and stored over activated 3 Å molecular sieves.

The compounds $PY5Me_2$,[5] $Mo(CF_3SO_3)_3$,[6] and potassium cyclopentadienyldicarbonyl ferrate[7] were prepared according to literature procedures. The synthesis of the compound $[MoO(CH_3CN)_4][B(C_6H_3(CF_3)_2)_4]_2$ was adapted from a literature procedure,[8] substituting $[H(OEt_2)_2][B(C_6H_3(CF_3)_2)_4]$ for $[H(OEt_2)_2][B(C_6F_5)_4]$.

NMR spectra were obtained using a Bruker AVANCE III instrument and referenced relative to tetramethylsilane using residual solvent signals. Deuterated solvents were purchased from Cambridge Isotopes. CD_3CN (99.8% D) was dried over powdered 3 Å molecular sieves for 48 h, separated from the sieves by vacuum transfer, deoxygenated by freeze-pump-thaw cycles, and stored over beads of 3 Å molecular sieves under an inert atmosphere.

Electrospray ionization mass spectrometry (ESI-MS) measurements were performed using an Agilent 6230 time-of-flight mass spectrometer equipped with an Agilent Jet Stream source. Carbon, hydrogen, and nitrogen analyses were obtained from the Microanalytical Laboratory at the University of California, Berkeley. Infrared spectra were collected on a Perkin Elmer Spectrum 400 FTIR spectrometer at 4 cm^{-1} resolution with an attenuated total reflectance accessory (diamond crystal).

A.2.2. Syntheses

$[(PY5Me_2)Mo(CF_3SO_3)](CF_3SO_3)_2$. In a N_2-filled glovebox, $PY5Me_2$ (0.500 g, 1.13 mmol), $Mo(CF_3SO_3)_3$ (0.612 g, 1.13 mmol), and 10 mL of benzonitrile were transferred into a 50 mL Schlenk-style storage flask equipped with a Teflon-coated stir bar and a Teflon valve. The flask was sealed, removed from the glovebox, and opened to an atmosphere of inert gas on a Schlenk line after three vacuum-refill cycles. The flask was then heated to 200 °C, and subsequently the Teflon valve was closed off. This sequence of operations was carried out to prevent an excessive buildup of pressure inside the flask. The reaction was stirred at 200 °C for 24 h, then cooled to room temperature, giving a dark brown-red solution with a fine light green crystalline precipitate. Further product was precipitated by adding 40 mL of diethyl ether, and the supernatant was removed using a 22-gauge cannula. The product was then triturated under inert atmosphere with 7 × 40 mL of diethyl ether to remove colored, ether-soluble impurities and most of the benzonitrile. Each trituration was performed for approximately 5 min before decanting the ether wash via the 22-gauge cannula. The product was then suspended in diethyl ether and transferred using a 16-gauge cannula into a 100 mL round-bottomed Schlenk flask. The diethyl ether was removed under reduced pressure, and residual benzonitrile was then removed from the solid by heating at 180 °C under a flow of inert gas (~1 bubble per second, or 4 mL/min) for 6 h, with the exhaust fed into an oil bubbler to prevent backwards diffusion of oxygen and/or moisture. The resulting light green, free-flowing powder was stored under an inert atmosphere, such as in a N_2-filled glovebox. Yield: 0.957 g (86%). Anal. Calcd. for $C_{32}H_{25}F_9MoN_5O_9S_3$: C, 38.95; H, 2.55; N, 7.10. Found: C, 38.98; H, 2.31; N, 7.10. UV-vis (CH_3CN): λ_{max} (ε_M, M^{-1} cm^{-1}) 204 (5.5×10^4), 255 (2.5×10^4), 331 (sh, 2400), 420 (750), 484 (sh, 15), 728 (15) nm.

[(PY5Me$_2$)Mo(CF$_3$SO$_3$)](CF$_3$SO$_3$). In a N_2-filled glovebox, [(PY5Me$_2$)Mo(CF$_3$SO$_3$)](CF$_3$SO$_3$)$_2$ (0.500 g, 0.507 mmol) was weighed into a 20 mL vial and dissolved in 10 mL of acetonitrile to give a light green solution. Solid potassium cyclopentadienyldicarbonylferrate (0.110 g, 0.507 mmol) was added to the solution in one portion, immediately resulting in a solution color change to dark green. The reaction was stirred at room temperature for another 30 min, then filtered and concentrated to dryness. The dark green-brown residue was triturated twice with 20 mL of THF, each time for 1 h, to remove the soluble potassium trifluoromethanesulfonate and cyclopentadienyliron dicarbonyl dimer byproducts. The dark green solid was collected by vacuum filtration on a fine porosity frit, washed with 3 × 2 mL of THF. The initial washes were red-purple due to the cyclopentadienyliron dicarbonyl dimer, while the latter washes were faint green due to the product being slightly soluble in tetrahydrofuran. The solid was additionally washed with 3 × 2 mL of diethyl ether. The dark green solid was recollected and dried under reduced pressure at room temperature until its mass was constant. Yield: 0.359 g (85%). Anal. Calcd. for $C_{31}H_{25}F_6MoN_5O_6S_2$: C, 44.45; H, 3.01; N, 8.36. Found: C, 44.74; H, 2.96; N, 8.31. UV-vis (THF): λ_{max} (ε_M, M^{-1} cm^{-1}) 254 (2.5×10^4), 346 (5900), 426 (7400), 466 (sh, 7100), 494 (7800), 595 (sh, 3800), 724 (8600) nm.

[(PY5Me$_2$)MoO](CF$_3$SO$_3$)$_2$. In a N_2-filled glovebox, a 100 mL Schlenk flask was charged with [(PY5Me$_2$)Mo(CF$_3$SO$_3$)](CF$_3$SO$_3$) (0.100 g, 0.119 mmol), sealed, removed from the glovebox, and opened to an atmosphere of inert gas on a Schlenk line after three vacuum-refill cycles. A round-bottomed flask containing 50 mL of deionized water was sparged with N_2 for 1 h. Afterwards, the water was transferred into the Schlenk flask, giving a green, effervescent solution. The solution was stirred for 12 h, then filtered through a medium porosity Schlenk frit. The filtrate was reduced to dryness to afford a green solid. The solid was extracted into 5 mL of acetonitrile and layered with 15 mL of diethyl ether to afford the product as green crystals. Yield: 0.085 g (83%). ^{1}H NMR (500 MHz, CD_3CN) δ 8.37 (d, *J* = 4.7 Hz, 4H), 7.95 (t, *J* = 8.0, 1H), 7.90 (d, *J* = 7.5, 4H), 7.41 (m, 4H), 7.38 (d, *J* = 8.1 Hz, 2H), 7.32 (d, *J* = 8.1, 4H), 2.19 (s, 6H). IR (neat): 966 (s, $\nu_{Mo=O}$) cm^{-1}. Anal. Calcd. for $C_{31}H_{25}F_6MoN_5O_7S_2$: C, 43.62; H, 2.95; N, 8.20. Found: C, 43.99; H, 3.15; N, 8.45. UV-vis (CH_3CN): λ_{max} (ε_M, M^{-1} cm^{-1}) 204 (1100), 209 (sh, 3500), 261 (1.1×10^4), 291 (sh, 3400), 349 (sh, 2300), 420 (6800), 492 (2900), 704 (1100) nm.

[(PY5Me$_2$)MoO][B(C$_6$H$_3$(CF$_3$)$_2$)$_4$]$_2$. In a N_2-filled glovebox, the compounds [MoO(CH$_3$CN)$_4$][B(C$_6$H$_3$(CF$_3$)$_2$)$_4$]$_2$ (451 mg, 225 μmol) and PY5Me$_2$ (100 mg, 225 μmol) were weighed into a 20 mL scintillation vial and stirred in ~4 mL of CH_2Cl_2 at room temperature for 2 days. During this time, a small amount of brown precipitate formed in the green solution. The solution was filtered through Celite® to remove the insoluble material. Addition of ~16 mL of hexanes precipitated the product as a green, microcrystalline solid. The crystals were isolated from the supernatant, washed with portions of hexanes (3 × ~1 mL), and dried under vacuum at room temperature for 1 h to give a green crystalline solid. Yield = 331 mg (61%). ^{1}H NMR (600 MHz, CD_3CN) δ 9.37 (dd, *J* = 5.8, 1.6 Hz, 4H), 8.27 (d, *J* = 8.5 Hz, 4H), 8.18 – 8.10 (m, 5H), 7.98 (d, *J* = 8.3 Hz, 2H), 7.73 (ddd, *J* = 7.3, 5.7, 1.3 Hz, 4H), 7.71 – 7.68 (m, 16H), 7.66 (s, 8H), 2.84 (s, 6H). Anal. Calcd. for $C_{93}H_{49}B_2F_{48}MoN_5O$: C, 48.95; H, 2.16; N, 3.07. Found: C, 48.60; H, 2.10; N, 3.14.

A.2.3. Crystal Structure Determinations

Crystals suitable for single crystal X-ray diffraction analysis were grown by layering hexanes over solutions of $[(PY5Me_2)MoO][B(C_6H_3(CF_3)_2)_4]_2$ (~5 mg) in ~0.5 mL of CH_2Cl_2 allowing the solvents to diffuse over 3 days at room temperature. Data collection was performed on single crystals coated with Paratone-N oil and mounted on Kaptan loops. The crystals were cooled under a stream of N_2 (100 K; Oxford Cryostream 700) during measurements. Data were collected using a Bruker APEX II QUAZAR diffractometer equipped with a Microfocus Sealed Source (Incoatec IμS; Mo-K_α $\lambda = 0.71073$ Å), or using monochromated X-ray radiation generated by a synchrotron. Raw data were integrated and corrected for Lorentz and polarization effects using Bruker APEX2.[9] Absorption corrections were applied using SADABS.[10] Space group assignments were determined by examination of systematic absences, E-statistics, and successive refinement of the structures. Structures were solved using SHELXT[11] and all non-hydrogen atoms were refined anisotropically by full-matrix least-squares (SHELXL).[12,13] Carbon-bound hydrogen atoms were inserted at idealized positions and refined isotropically using a riding model with the appropriate HFIX command in SHELXL. Disorder in the trifluoromethyl groups of the $[B(C_6H_3(CF_3)_2)_4]^-$ anions was addressed using SADI, RIGU, and SIMU commands.[14]

A.3. Acknowledgments

This includes work from Axelson, J. C. A.; Zee, D. Z.; Chantarojsiri, T. C.; Jung, C. L.; Chang, C. J.; Long, J. R. Transition Metal Complexes of 2,6-Bis[1,1-bis(2-pyridyl)ethyl]]pyridine ($PY5Me_2$) and Its Derivatives. *Submitted.* This research was supported by the National Science Foundation (NSF) through Grant No. CHE-1464841 to J.R.L. and U.S. Department of Energy/Lawrence Berkeley National Laboratory Grant No. 101528-002 to C.J.C. J.C.A and D.Z.Z. thank the NSF for Graduate Research Fellowships. T.C is supported by a scholarship from the Development and Promotion of Science and Technology scholarship, Thailand. C.L.J thanks the Aachen-California Network of Academic Exchange for financial support. C.J.C is an Investigator with the Howard Hughes Medical Institute.

A.4. References

(1) Karunadasa, H. I.; Chang, C. J.; Long, J. R. A Molecular Molybdenum-Oxo Catalyst for Generating Hydrogen From Water. *Nature* **2010**, *464* (7293), 1329–1333.

(2) Karunadasa, H. I.; Montalvo, E.; Sun, Y.; Majda, M.; Long, J. R.; Chang, C. J. A Molecular MoS_2 Edge Site Mimic for Catalytic Hydrogen Generation. *Science* **2012**, *335* (6069), 698–702.

(3) Baker, P. K.; Fraser, S. G.; Keys, E. M. The Synthesis and Spectral Properties of Some Highly Reactive New Seven-Coordinate Molybdenum(II) and Tungsten(II) Bisacetonitrile Dihalogenotricarbonyl Complexes. *J. Organomet. Chem.* **1986**, *309* (3), 319–321.

(4) Connelly, N. G.; Geiger, W. E. Chemical Redox Agents for Organometallic Chemistry. *Chem. Rev.* **1996**, *96* (2), 877–910.

(5) Bechlars, B.; D'Alessandro, D. M.; Jenkins, D. M.; Iavarone, A. T.; Glover, S. D.; Kubiak, C. P.; Long, J. R. High-Spin Ground States via Electron Delocalization in Mixed-Valence Imidazolate-Bridged Divanadium Complexes. *Nature Chem.* **2010**, *2* (5), 362–368.

(6) Mayer, J. M.; Abbott, E. H. Preparation of Octakis(Acetonitrile)Dimolybdenum(II) Trifluoromethanesulfonate, Bis(Trifluoromethanesulfonato)Tetraaquadimolybdenum(II) Trifluoromethanesulfonate and Molybdenum(III) Trifluoromethanesulfonate. *Inorg. Chem.* **1983**, *22*, 2774–2776.
(7) Plotkin, J. S.; Shore, S. G. Convenient Preparation and Isolation of Pure Potassium Cyclopentadienyldicarbonylferrate, K[(η^5-C_5H_5)Fe(CO)$_2$]. *Inorg. Chem.* **1981**, *20* (1), 284–285.
(8) Diebl, B. E.; Yeong, H. Y.; Cokoja, M.; Herdtweck, E.; Voit, B.; Kühn, F. E. Synthesis and Catalytic Application of Monometallic Molybdenum(IV) Nitrile Complexes. *Tet. Lett.* **2011**, *52* (9), 955–959.
(9) APEX2. v. 2009; Bruker Analytical X-ray Systems, Inc; Madison, WI, 2009.
(10) Sheldrick, G. M. Version 2.03; Bruker Analytical Systems, Inc.: Madison, WI, 2000.
(11) Sheldrick, G. SHELXT - Integrated Space-Group and Crystal-Structure Determination. *Acta Crystallogr A Found Adv* **2015**, *71* (1), 3–8.
(12) Sheldrick, G. A Short History of SHELX. *Acta Crystallogr A Found Crystallogr* **2008**, *64* (1), 112–122.
(13) Sheldrick, G. Crystal Structure Refinement with SHELXL. *Acta Crystallogr C Struct Chem* **2015**, *71* (1), 3–8.
(14) Müller, P. Practical Suggestions for Better Crystal Structures. *Crystallography Reviews* **2009**, *15* (1), 57–83.

Appendix B. Proton-Responsive Pentapyridine Ligands and their Cobalt Complexes

B.1. Overview

During the investigations described in Chapter 2, we realized that to enable efficient hydrogen evolution catalysis by pentapyridine cobalt complexes, we needed to develop ligand platforms that could stabilize several distinct oxidation states of the metal ion. One strategy, detailed in *Chapter 2*, leveraged a redox non-innocent, π-acidic ligand to stabilize the low-valent Co(I) ion. Concurrently, we pursued a strategy that utilized proton-coupled electron transfer.[1-3] Pertinently, the difference in the Co(III/II) and Co(II/I) redox potentials for $[(PY5Me_2)Co(CH_3CN)](CF_3SO_3)_2$ is ~1.7 V.[4] In water, the corresponding redox spread narrows to ~1.2 V for $[(PY5Me_2)Co(OH_2)](CF_3SO_3)_2$.[4] This 0.5 V decrease in the redox spread likely stems from PCET involving the aquo ligand, forming a $[CoOH]^{2+}$ unit that stabilizes the Co(III) ion by π-donation. This conjecture is supported by detailed Pourbaix studies[5] of the structurally related $[(PY5)Co(OH_2)]^{2+}$ system (PY5 = 2,6-(bis(bis-2-pyridyl)-methoxymethane)-pyridine)[6], which showed that the Co(III/II) redox wave was indeed proton-coupled.

Since the aquo ligand utilized the coordination site that we needed for catalytic chemistry, we sought a ligand platform that was proton-responsive, and upon coordination to a metal ion could participate in PCET. As such, we developed the ligand $HOPY5Me_2$, which possessed an ancillary protic site at the 4-position of the axial pyridine. In particular, we envisioned that the pK_a of the ligand backbone would vary with the oxidation state of the coordinated cobalt ion (Figure B.1). Thus, we speculated that the axial pyridine of the $HOPY5Me_2$ ligand could switch between being a σ-only pyridine donor and a π-basic pyridonate donor.

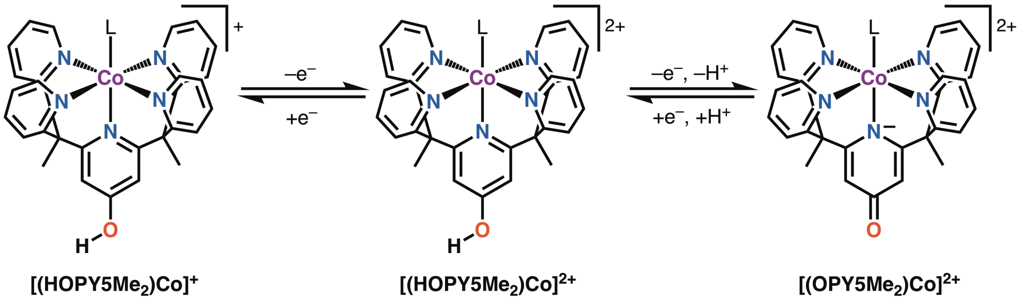

Figure B.1. Postulated ligand-assisted proton-coupled electron transfer in $[(HOPY5Me_2)Co]^{n+}$ complexes.

The synthesis of the $HOPY5Me_2$ ligand is summarized in Scheme B.1, and the full experimental procedures are detailed in Section B.2. Notably, the ligand $EtOPY5Me_2$, which lacks the acidic proton but possesses a similar electronic environment to $HOPY5Me_2$, conveniently serves as a control ligand. The infrared spectrum of the $HOPY5Me_2$ ligand shows a strong absorption at 1610 cm^{-1}, corresponding to a carbonyl stretching mode and indicating that the free ligand exists as the 4-pyridone tautomer rather than the 4-hydroxypridine tautomer.

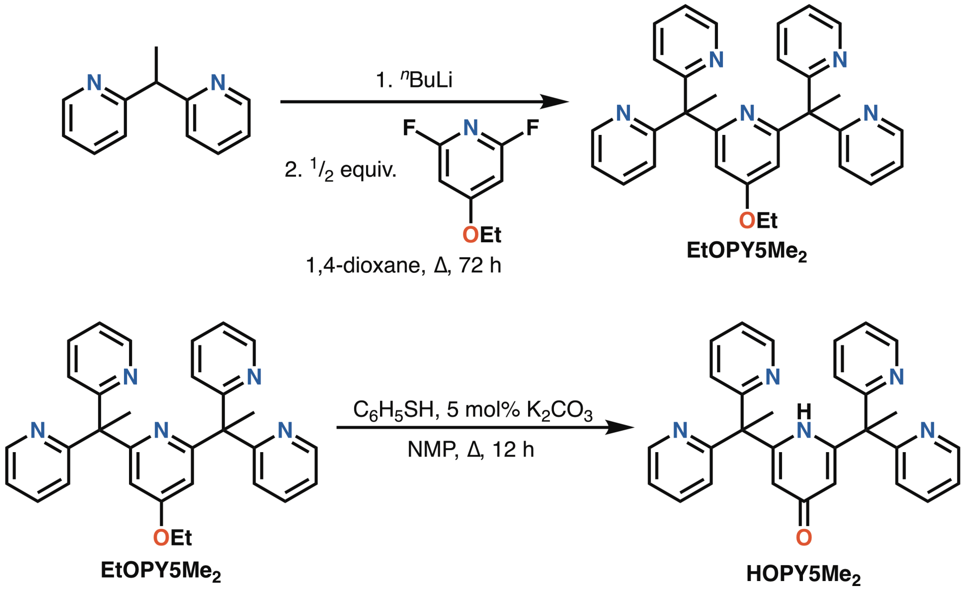

Scheme B.1. Synthesis of the EtOPY5Me$_2$ and HOPY5Me$_2$ ligands.

Both the EtOPY5Me$_2$ and HOPY5Me$_2$ ligands are metalated with cobalt trifluoromethanesulfonate to give the corresponding cobalt(II) complexes [(EtOPY5Me$_2$)Co(CH$_3$CN)(CF$_3$SO$_3$)$_2$ and [(HOPY5Me$_2$)Co(CH$_3$CN)](CF$_3$SO$_3$)$_2$ (Scheme B.2). Complex formation with the HOPY5Me$_2$ ligand requires a protic solvent, such as methanol, to help tautomerize the ligand.

$$\text{EtOPY5Me}_2 + \text{Co(CF}_3\text{SO}_3)_2 \xrightarrow[\text{CH}_3\text{CN}]{} [(\text{EtOPY5Me}_2)\text{Co(CH}_3\text{CN)}](\text{CF}_3\text{SO}_3)_2$$

$$\text{HOPY5Me}_2 + \text{Co(CF}_3\text{SO}_3)_2 \xrightarrow[\substack{\text{1. CH}_3\text{OH} \\ \text{2. CH}_3\text{CN}}]{} [(\text{HOPY5Me}_2)\text{Co(CH}_3\text{CN)}](\text{CF}_3\text{SO}_3)_2$$

Scheme B.2. Synthesis of cobalt complexes [(EtOPY5Me$_2$)Co(CH$_3$CN)(CF$_3$SO$_3$)$_2$ and [(HOPY5Me$_2$)Co(CH$_3$CN)](CF$_3$SO$_3$)$_2$.

Diffusion of diethyl ether into acetonitrile solutions of the metal complexes afforded crystals suitable for single crystal X-ray crystallography. Their molecular structures are shown in Figure B.2, and highlighted bond distances are shown in Table B.1. Their full crystallographic data are presented in Table B.2. As expected, the two complexes are isostructural. The C–O bond distances in [(EtOPY5Me$_2$)Co(CH$_3$CN)(CF$_3$SO$_3$)$_2$ and [(HOPY5Me$_2$)Co(CH$_3$CN)](CF$_3$SO$_3$)$_2$ are 1.344(2) Å and 1.347(2) Å, respectively, indicating a single bond between the carbon and oxygen atoms. This confirms that upon coordination to the Co(II) ion, the HOPY5Me$_2$ ligand exists as the hydroxypyridine tautomer. The H atom of the HOPY5Me$_2$ ligand in [(HOPY5Me$_2$)Co(CH$_3$CN)](CF$_3$SO$_3$)$_2$ participates in a hydrogen bonding interaction with a trifluoromethanesulfonate anion. A broad absorption at 3136 cm^{-1} in the IR spectrum of [(HOPY5Me$_2$)Co(CH$_3$CN)](CF$_3$SO$_3$)$_2$ is assigned to the O–H stretching mode of the ligand.

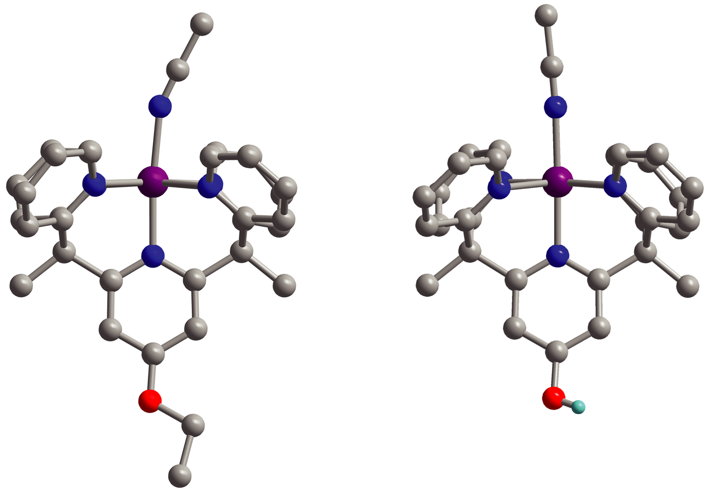

[(EtOPY5Me$_2$)Co(CH$_3$CN)]$^{2+}$ **[(HOPY5Me$_2$)Co(CH$_3$CN)]$^{2+}$**

Figure B.2. Molecular structures of the dications in compounds [(EtOPY5Me$_2$)Co(CH$_3$CN)(CF$_3$SO$_3$)$_2$ and [(HOPY5Me$_2$)Co(CH$_3$CN)](CF$_3$SO$_3$)$_2$. Purple, blue, gray, red, and light blue spheres represent Co, N, C, O, and H atoms, respectively. Carbon-bound H atoms, CF$_3$SO$_3^-$ anions, and solvent molecules are omitted for clarity.

Table B.1. Highlighted bond distances in complexes [(EtOPY5Me$_2$)Co(CH$_3$CN)(CF$_3$SO$_3$)$_2$ and [(HOPY5Me$_2$)Co(CH$_3$CN)](CF$_3$SO$_3$)$_2$.

Bond distance (Å)	[(EtOPY5Me$_2$)Co(CH$_3$CN)(CF$_3$SO$_3$)$_2$	[(HOPY5Me$_2$)Co(CH$_3$CN)](CF$_3$SO$_3$)$_2$
Co – N$_{ax}$	2.077(1)	2.090(1)
Co – N$_{eq}$ (average)	2.133(1)	2.131(1)
Co – N$_{acetonitrile}$	2.126(1)	2.113(1)
C – O	1.344(2)	1.347(2)

The redox properties of the complexes [(EtOPY5Me$_2$)Co(CH$_3$CN)(CF$_3$SO$_3$)$_2$ and [(HOPY5Me$_2$)Co(CH$_3$CN)](CF$_3$SO$_3$)$_2$ were interrogated using cyclic voltammetry in acetonitrile. The compound [(EtOPY5Me$_2$)Co(CH$_3$CN)(CF$_3$SO$_3$)$_2$ exhibits two redox features, corresponding to the Co(III/II) and Co(II/I) redox couples, at $E_{1/2}$ = +0.16 V and −1.50 V vs Fe(C$_5$H$_5$)$_2^{+/0}$, respectively (Figure B.3). The compound [(HOPY5Me$_2$)Co(CH$_3$CN)](CF$_3$SO$_3$)$_2$ has a quasi-reversible Co(III/II) at the same potential of $E_{1/2}$ = +0.16 V, consistent with the similar electronic influences by the OH and OEt groups. An irreversible redox wave appears with E_p = −1.48 V. We speculate that the irreversibility of this redox couple stems from the chemical lability of the OH proton.

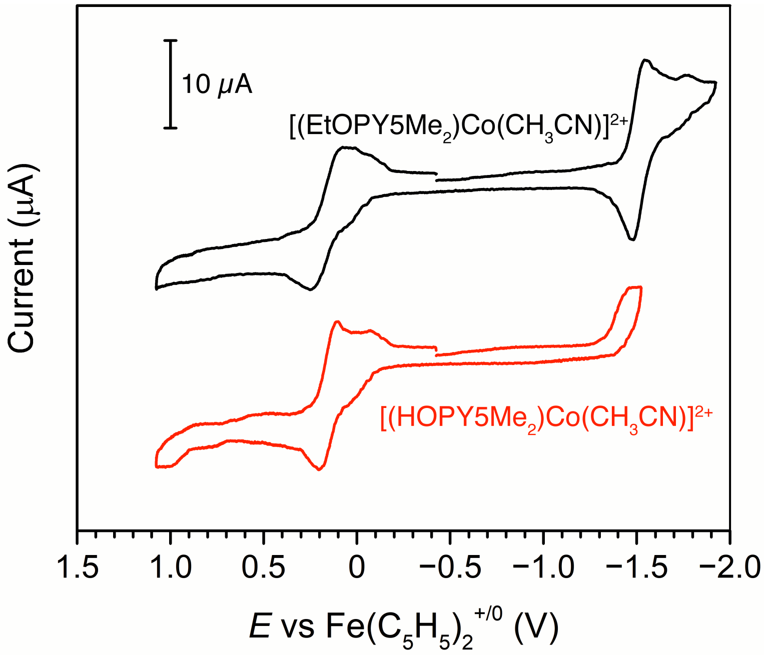

Figure B.3. Cyclic voltammograms of 1 mM solutions of $[(EtOPY5Me_2)Co(CH_3CN)(CF_3SO_3)_2$ and $[(HOPY5Me_2)Co(CH_3CN)](CF_3SO_3)_2$ in acetonitrile

The compound $[(HOPY5Me_2)Co(CH_3CN)](CF_3SO_3)_2$ was treated with Brønsted bases to evaluate how the protic state of the ligand backbone affects the electronic properties of the metal ion. Adding 1–5 equivalents of simple bases such as potassium *tert*-butoxide to acetonitrile solutions of $[(HOPY5Me_2)Co(CH_3CN)](CF_3SO_3)_2$ resulted in a color change from yellow-orange to red-orange, then formed an amorphous, red-orange precipitate. This precipitate was insoluble in acetonitrile, methanol, dichloromethane, and water. The IR spectrum of the solid does not show any adsorptions in the 3300 to 3000 cm^{-1} range, nor at ~1600 cm^{-1}, suggesting the both the O–H and C=O vibrations are absent. We postulate that, upon deprotonation of the OH group, the $^{-}OPY5Me_2$ ligand binds to another cobalt ion, forming a coordination polymer. Due to this complication, this ligand platform was not pursued further for hydrogen evolution catalysis studies. However, the ligand scaffold may yet prove useful other systems.

B.2. Experimental

B.2.1. Materials and Methods

Air- and/or moisture-sensitive compounds were synthesized and manipulated under air-free conditions, using either a Vacuum Atmospheres glovebox or standard Schlenk techniques under a dry nitrogen or argon atmosphere. Anhydrous diethyl ether (Et_2O), acetonitrile, and 1,4-dioxane were dried and deoxygenated with a commercial solvent purification system from JC Meyer Solvent Systems, then stored under an inert atmosphere over beads of activated 3 Å molecular sieves. Methanol (EMD Millipore, DriSolv grade) was sparged with N_2 for 1 h and further dried over activated 3 Å molecular sieves for 24 h prior to use. The compounds *n*-butyllithium (^{n}BuLi), benzenethiol, and *N*-methyl-2-pyrrolidone (NMP) were purchased from Sigma-Aldrich and used as received.

The compounds 1,1-bis(pyridyl)ethane[7] and 4-ethoxy-2,6-difluoropyridine[8] were prepared according to literature procedures. The compound $Co(CF_3SO_3)_2(CH_3CN)_2$ was prepared by the reaction of finely divided cobalt metal with trifluoromethanesulfonic acid in dry acetonitrile, akin to the preparation of iron trifluoromethanesulfonate by Hagen.[9]

NMR spectra were obtained using a Bruker AVANCE III instrument and referenced relative to tetramethylsilane using residual solvent signals. Deuterated solvents were purchased from Cambridge Isotopes. $CDCl_3$ (99.8% D) was treated with anhydrous K_2CO_3. CD_3CN (99.8% D) was dried over powdered 3 Å molecular sieves for 48 h, separated from the sieves by vacuum transfer, deoxygenated by freeze-pump-thaw cycles, and stored over beads of 3 Å molecular sieves under an inert atmosphere.

Electrospray ionization mass spectrometry (ESI-MS) measurements were performed with a Shimadzu 2020 liquid chromatography/mass spectrometer. C, H, and N analyses were performed at the Microanalytical Laboratory at the University of California, Berkeley. Infrared spectra were collected on a Perkin Elmer Spectrum 400 FTIR spectrometer at 4 cm^{-1} resolution with an attenuated total reflectance accessory (diamond crystal).

Electrochemical measurements were performed with acetonitrile (EMD Millipore, OmniSolv Gradient grade). NBu_4PF_6 (Oakwood Chemical) was recrystallized from ethanol/water and dried under vacuum at 100 °C for 24 h before use. Cyclic voltammetry measurements were obtained with 1 mM of complex in CH_3CN using a glassy carbon disk (3.0 mm dia.) working electrode, a nonaqueous $Ag/AgNO_3$ (0.1 mM) reference electrode, and a graphite counter electrode with 0.1 M NBu_4PF_6 as supporting electrolyte. Between experiments, the working electrode was polished with agglomerate-free 0.05 μm alumina. Ferrocene was added after each CV experiment as an internal reference.

B.2.2. Syntheses

2,2′,2″,2‴-((4-ethoxypyridine-2,6-diyl)bis(ethane-1,1,1-triyl))tetrapyridine (EtOPY5Me$_2$). 1.1-Bis(pyridyl)ethane (9.29 g, 50.4 mmol) was added to a 200 mL Schlenk flask equipped with a magnetic stir bar and dissolved into 1,4-dioxane (100 mL). The solution was cooled with an ice bath. While stirring, *ⁿ*BuLi (2.5 M in hexanes, 9.72 mL, 24.3 mmol) was slowly added, resulting in a color change from light yellow to dark red. Stirring was continued for 15 min, then a solution of 4-ethoxy-2,6-difluoropyridine (2.00 g, 12.6 mmol) in anhydrous 1,4-dioxane (~25 mL) was added with a cannula. The cooling bath was removed, then the reaction was heated to reflux for 72 h. The reaction mixture was cooled to room temperature, then quenched with ~125 mL of water and the aqueous and organic layers were separated. At this point the workup was conducted under air. The aqueous layer was extracted with 3 × ~150 mL of ethyl acetate, and the organic layers were combined, then extracted with ~100 mL of water, then with ~100 mL of brine, and then dried over $MgSO_4$. After filtration, the solvent was removed under reduced pressure to afford an orange oil. Purification by flash chromatography (silica, 1:2 hexanes:ethyl acetate, $R_f = 0.07$) followed by solvent removal afforded the product as a white, crystalline solid. Yield: 3.72 g (61%). ^1H NMR (400 MHz, $CDCl_3$) δ 8.50 (ddd, $J = 4.9, 1.9, 0.9$ Hz, 4H), 7.48 – 7.39 (m, 4H), 7.07 (dd, $J = 7.6, 4.7$ Hz, 4H), 6.88 (d, $J = 8.1$ Hz, 4H), 6.66 (s, 2H), 3.97 (q, $J = 7.0$ Hz, 2H), 2.21 (s, 6H), 1.33 (t, $J = 7.0$ Hz, 3H). IR (neat): 3049 (w), 2999 (w), 2989 (w), 2976 (w), 2934 (w), 1585 (s), 1570 (s), 1561 (s), 1466 (s), 1448 (m), 1424 (s), 1396 (m), 1363 (m), 1356 (w), 1321 (s), 1291 (m), 1255 (w), 1219 (w), 1173 (m), 1152 (m), 1132 (w), 1113 (m), 1100 (m), 1094 (m), 1070 (m), 1044 (s), 991 (s), 987 (s), 956 (w), 923 (w), 876 (w), 864 (w), 852 (w), 823 (w), 798 (m), 788 (m), 782 (m), 764 (s), 749 (s), 683 (m), 663 (m), 656 (m), 621 (m), 609 (m), 599 (w), 590 (w), 577 (m), 550 (m), 518 (w), 511 (w) cm^{-1}. ESI-MS for $[C_{31}H_{29}N_5O + H]^+$ requires 488.24, found 488.30. Anal. Calcd.

for $C_{31}H_{29}N_5O$: C, 76.36; H, 5.99; N, 14.36. Found: C, 76.45; H, 6.17; N, 14.19.

2,6-bis(1,1-di(pyridin-2-yl)ethyl)pyridin-4(1*H*)-one (HOPY5Me$_2$). Into a 100 mL Schenk flask equipped with a magnetic stir bar was added EtOPY5Me$_2$ (3.00 g, 6.15 mmol), benzenethiol (630 μL, 679 mg, 6.16 mmol), K_2CO_3 (42.8 mg, 0.310 mmol), and *N*-methyl-2-pyrrolidone (60 mL). The reaction was heated to reflux for 12 h, giving a yellow-orange solution. The reaction was allowed to cool to room temperature, then diluted with ~100 mL of 1 M aqueous NaOH solution. At this point, the workup was conducted in air, inside a well-ventilated fume hood due to the obnoxious odors of the sulfur-containing compounds. The basic aqueous phase was washed with 3 × ~100 mL of Et_2O to remove the ethyl phenyl sulfide byproduct. Solid NH_4Cl was added to the aqueous solution until its pH was approximately 8 or 9. The aqueous phase was extracted with 3 × ~100 mL of CH_2Cl_2, then the organic phases were combined and washed with 3 × ~50 mL of water to remove the bulk of the *N*-methyl-2-pyrrolidone. The organic solvent was removed under reduced pressure to give a yellow solution, from which white crystalline solids occasionally precipitated (if most of the *N*-methyl-2-pyrrolidone was removed). Addition of ~30 mL of Et_2O to this mixture precipitated a white crystalline solid, which was isolated and dried under high vacuum at 100 °C to afford the product as a white powder. Yield: 1.66 g (59%). ^{1}H NMR (400 MHz, CD_3CN) δ 8.20 – 8.15 (m, 4H), 7.64 (td, *J* = 7.8, 1.9 Hz, 4H), 7.16 (ddd, *J* = 7.6, 4.8, 1.0 Hz, 4H), 7.12 (d, *J* = 8.0 Hz, 4H), 2.02 (s, 6H). IR (neat): 3471 (w), 3355(w), 3248 (w), 3147 (w), 3056 (w), 2978 (w), 2825 (w), 2853 (w), 2657 (w), 1734 (w), 1672 (w), 1610 (s, $\nu_{C=O}$), 1582 (s), 1569 (s), 1550 (m), 1509 (m), 1483 (m), 1460 (s), 1428 (s), 1364 (m), 1330 (m), 1291 (m), 1241 (w), 1172 (w), 1157 (w), 1133 (w), 1091 (w), 1071 (w), 1046 (w), 1009 (m), 991 (m), 969 (w), 943 (w), 872 (m), 851 (w), 839 (w), 823 (w), 782 (m), 745 (s), 676 (m), 618 (w), 598 (m), 541 (s) cm^{-1}. ESI-MS *m/z* for $[C_{29}H_{25}N_5O + H]^+$ requires 460.21, found 460.25. Anal. Calcd. for $C_{29}H_{25}F_6N_5O$: C, 75.80; H, 5.48; N, 15.24. Found: C, 75.26; H, 5.48; N, 15.06.

[(EtOPY5Me$_2$)Co(CH$_3$CN)](CF$_3$SO$_3$)$_2$. In a N_2-filled glovebox, EtOPY5Me$_2$ (120 mg, 246 μmol) and $Co(CF_3CO_3)_2(CH_3CN)_2$ (108 mg, 246 μmol) were weighed into a 20 mL scintillation vial and stirred in acetonitrile (~5 mL) at room temperature for 12 h to afford a clear yellow-orange solution. The solution was filtered through a pipette of Celite® to remove any trace solids. Diffusion of Et_2O into this solution over 72 h afforded orange crystals. The crystals were isolated from the mother liquor, washed with Et_2O (3 × ~3 mL), and dried under vacuum to give the product as an orange crystalline solid. Yield: 131 mg (60%). ESI-MS *m/z* for $[(\mathrm{EtOPY5Me_2})Co(CF_3SO_3)]^+$ requires 695.12, found 695.00. IR (neat): 3126 (w), 3036 (w), 2993 (w), 2944 (w), 2916 (w), 2303 (w), 2273 (w), 1606 (m), 1579 (m), 1562 (m), 1484 (w), 1469 (m), 1442 (m), 1400 (w), 1326 (m), 1308 (w), 1225 (m), 1271 (m), 1255 (s), 1225 (m), 1167 (m), 1144 (s), 1109 (m), 1083 (w), 1063 (m), 997 (m), 972 (m), 937 (w), 921 (w), 892 (m), 873 (m), 845 (w), 833 (w), 824 (w), 801 (m), 759 (s), 672 (m), 664 (w), 597 (m), 573 (m), 493 (m), 483 (m), 468 (w), 457 (w) cm^{-1}. Anal. Calcd. for $C_{35}H_{32}CoF_6N_6O_7S_2$: C, 47.46; H, 3.64; N, 9.49. Found: C, 47.55; H, 3.44; N, 9.43.

[(HOPY5Me$_2$)Co(CH$_3$CN)](CF$_3$SO$_3$)$_2$. In a N_2-filled glovebox, HOPY5Me$_2$ (229 mg, 499 μmol) and $Co(CF_3CO_3)_2(CH_3CN)_2$ (219 mg, 499 μmol) were weighed into a 20 mL scintillation vial, dissolved into methanol (~4 mL), and stirred at room temperature for 12 h to afford a clear yellow solution. The solvent was removed under vacuum to afford a yellow solid. The solid was dissolved into ~30 mL of acetonitrile, filtered through a pipette of Celite® to remove any trace solids, yielding a light yellow-orange solution. The solution was portioned equally into two 20-mL scintillation vials. Diffusion of Et_2O into these solutions over 72 h afforded orange block-shaped crystals. The crystals were isolated from the mother liquor, combined into one batch, washed with Et_2O (3 × ~4 mL), and dried under vacuum to give the product as an orange crystalline solid. Yield: 305 mg (71%). IR (neat): 3136 (br, w), 2941 (w), 2305 (w), 2276 (w), 2252 (w), 1614 (m), 1589 (m), 1485 (w), 1469 (m), 1442 (m), 1396 (w), 1374 (w), 1331 (w), 1305 (m), 1264 (s), 1237 (s), 1223 (s), 1155 (s), 1108 (w), 1081 (w), 1062 (m), 1026 (s), 987 (m), 879 (m), 837 (w), 802 (m), 758 (s), 667 (m), 633 (s), 596 (m), 573 (m), 516 (s), 486 (m) cm^{-1}. ESI-MS *m*/*z* for $[(\text{HOPY5Me}_2)\text{Co}(\text{CF}_3\text{SO}_3)]^+$ requires 667.09, found 667.18. Anal. Calcd. for $\text{C}_{33}\text{H}_{28}\text{CoF}_6\text{N}_6\text{O}_7\text{S}_2$: C, 46.21; H, 3.29; N, 9.80. Found: C, 46.27; H, 3.35; N, 9.66.

B.2.3. Crystal Structure Determinations

Slow diffusion of diethyl ether into acetonitrile solutions of cobalt complexes afforded single crystals suitable for X-ray diffraction analysis. Data collection was performed on single crystals coated with Paratone-N oil and mounted on Kapton loops. The crystals were cooled under a stream of N_2 (100 K; Oxford Cryostream 700) during measurements. Data were collected using a Bruker APEX II QUAZAR diffractometer equipped with a Microfocus Sealed Source (Incoatec IμS; Mo-K_α $\lambda = 0.71073$ Å) and APEX-II detector. Raw data were integrated and corrected for Lorentz and polarization effects using Bruker APEX2.[10] Absorption corrections were applied using SADABS.[11] Space group assignments were determined by examination of systematic absences, E-statistics, and successive refinement of the structures. Structures were solved using SHELXT[12] and all non-hydrogen atoms were refined anisotropically by full-matrix least-squares (SHELXL).[13,14] Carbon-bound hydrogen atoms were inserted at idealized positions and refined isotropically using a riding model with the appropriate HFIX command in SHELXL. The phenolic proton in $[(\text{HOPY5Me}_2)\text{Co}(\text{CH}_3\text{CN})](\text{CF}_3\text{SO}_3)_2$ was located in the Fourier difference map and refined freely.

B.3. Acknowledgments

This work was funded by the Joint Center for Artificial Photosynthesis, a DOE Energy Innovation Hub, supported through the Office of Science of the U.S. Department of Energy award DE-SC0004993 to Jeffrey R. Long. The author thanks the National Science Foundation Graduate Research Fellowship program for financial support. Single-crystal X-ray structure determination was supported by the NIH Shared Instrumentation Grant S10-RR027172.

B.4. Supporting Information

Table B.S1. Crystallographic data for complexes [(EtOPY5Me$_2$)Co(CH$_3$CN)(CF$_3$SO$_3$)$_2$ and [(HOPY5Me$_2$)Co(CH$_3$CN)](CF$_3$SO$_3$)$_2$.[a]

	[(EtOPY5Me$_2$)Co(CH$_3$CN)(CF$_3$SO$_3$)$_2$	[(HOPY5Me$_2$)Co(CH$_3$CN)](CF$_3$SO$_3$)$_2$
formula	$C_{35}H_{32}CoF_6N_6O_7S_2$	$C_{33}H_{33}CoF_6N_5O_9S_2$
crystal system	monoclinic	triclinic
fw, g mol^{-1}	885.72	880.69
T, K	100(2)	100(2)
space group	$P2_1/n$	$P\bar{1}$
habit	block	block
color	orange	orange
Z	4	2
a, Å	13.6601(10)	10.6364(3)
b, Å	15.5388(11)	13.8266(4)
c, Å	17.5697(12)	13.8564(4)
α, °	90.00	65.5960(10)
β, °	100.471(3)	77.5440(10)
γ, °	90.00	76.0660(10)
V, Å^3	3667.3(4)	1785.49(9)
ρ_{calc}, g cm^{-3}	1.604	1.638
μ_{calc}, mm^{-1}	0.671	0.692
2θ range, °	3.48 to 50.76	3.28 to 50.8
total reflections	59784	22208
data / restr / parameters	6699 / 0 / 518	6471 / 0 / 521
F(000)	1812	902
$T_{\text{min}}/T_{\text{max}}$	0.961	0.824
crystal size, mm^3	0.05 × 0.05 × 0.03	0.17 × 0.08 × 0.04
Largest diff. peak/hole / e Å^{-3}	0.38 / −0.35	0.36 / −0.34
R_1 (wR_2),[b] % [$I > 2\sigma(I)$]	2.58 (6.27)	2.51 (6.62)
R_1 (wR_2), % (all data)	2.91 (6.47)	2.66 (6.72)

[a] Obtained with graphite-monochromated Mo Kα ($\lambda = 0.71073$ Å) radiation.

[b] $R_1 = \sum\left||F_o| - |F_c|\right|/\sum|F_o|, wR_2 = \{\sum w(F_o^2 - F_c^2)^2/\sum w(F_o^2)^2\}^{\frac{1}{2}}$

B.5. References

(1) Hammes-Schiffer, S. Theory of Proton-Coupled Electron Transfer in Energy Conversion Processes. *Acc. Chem. Res.* **2009**, *42* (12), 1881–1889.

(2) Weinberg, D. R.; Gagliardi, C. J.; Hull, J. F.; Murphy, C. F.; Kent, C. A.; Westlake, B. C.; Paul, A.; Ess, D. H.; McCafferty, D. G.; Meyer, T. J. Proton-Coupled Electron Transfer. *Chem. Rev.* **2012**, *112* (7), 4016–4093.

(3) Solis, B. H.; Hammes-Schiffer, S. Proton-Coupled Electron Transfer in Molecular Electrocatalysis: Theoretical Methods and Design Principles. *Inorg. Chem.* **2014**, *53* (13), 6427–6443.

(4) Sun, Y.; Bigi, J. P.; Piro, N. A.; Tang, M. L.; Long, J. R.; Chang, C. J. Molecular Cobalt Pentapyridine Catalysts for Generating Hydrogen From Water. *J. Am. Chem. Soc.* **2011**, *133* (24), 9212–9215.

(5) Wasylenko, D. J.; Tatlock, H. M.; Bhandari, L. S.; Gardinier, J. R.; Berlinguette, C. P. Proton-Coupled Electron Transfer at a [Co-OHx]Z Unit in Aqueous Media: Evidence for a Concerted Mechanism. *Chem. Sci.* **2013**, *4* (2), 734.

(6) Jonas, R. T.; Stack, T. C–H Bond Activation by a Ferric Methoxide Complex: a Model for the Rate-Determining Step in the Mechanism of Lipoxygenase. *J. Am. Chem. Soc.* **1997**, *119* (36), 8566–8567.

(7) Bechlars, B.; D'Alessandro, D. M.; Jenkins, D. M.; Iavarone, A. T.; Glover, S. D.; Kubiak, C. P.; Long, J. R. High-Spin Ground States via Electron Delocalization in Mixed-Valence Imidazolate-Bridged Divanadium Complexes. *Nature Chem.* **2010**, *2* (5), 362–368.

(8) Schlosser, M.; Bobbio, C.; Rausis, T. Regiochemically Flexible Substitutions of Di-, Tri-, and Tetrahalopyridines: the Trialkylsilyl Trick. *J. Org. Chem.* **2005**, *70* (7), 2494–2502.

(9) Hagen, K. S. Iron(II) Triflate Salts as Convenient Substitutes for Perchlorate Salts: Crystal Structures of $[Fe(H_2O)_6](CF_3SO_3)_2$ And $Fe(MeCN)_4(CF_3SO_3)_2$. *Inorg. Chem.* **2000**, *39* (25), 5867–5869.

(10) APEX2. v. 2009; Bruker Analytical X-ray Systems, Inc; Madison, WI, 2009.

(11) Sheldrick, G. M. Version 2.03; Bruker Analytical Systems, Inc.: Madison, WI, 2000.

(12) Sheldrick, G. SHELXT - Integrated Space-Group and Crystal-Structure Determination. *Acta Crystallogr A Found Adv* **2015**, *71* (1), 3–8.

(13) Sheldrick, G. A Short History of SHELX. *Acta Crystallogr A Found Crystallogr* **2008**, *64* (1), 112–122.

(14) Sheldrick, G. Crystal Structure Refinement with SHELXL. *Acta Crystallogr C Struct Chem* **2015**, *71* (1), 3–8.

Appendix C. Automated Extraction of Gas Chromatograph Data

C.1. Motivation

Previously, our laboratory quantified gas evolution by catalysts in a batch fashion.[1-4] Typically, the headspace of an electrolysis cell would be sampled once after a specified duration (e.g. 12 to 24 h). A known volume of a gas known not to result from nor interfere with catalysis (e.g. ethylene for a hydrogen-evolving catalyst), would be injected into the headspace (of a known volume) of the electrolysis cell. This gas served as an internal standard. After allowing the system to equilibrate, an aliquot of the headspace would be taken and injected into a gas chromatograph (GC) or micro gas chromatograph (MicroGC) for quantification against the internal standard.

In our study of CO_2 reduction by polypyridyl Fe systems (Chapter 3), we developed a new method for quantifying time-dependent gas evolution. With the effluent of the headspace plumbed directly into the sampling loop of the gas chromatograph, we were able to sample the headspace as frequently as every 10 min, limited only by the time it took for CO_2 to elute off the GC column. This resulted in a six-fold increase in data density for every hour of electrolysis, which also meant data workup became extremely cumbersome. In particular, the Agilent 490 MicroGC we used did not have the capabilities to export the data into a useful, tractable manner. Opening each dataset in Agilent's GC analysis software and manually recording the data took a lot of time and allowed for errors during data (re)entry.

As such, we developed the following Python script that can automatically parse the GC data and produce a .csv file, which can be readily opened using typical spreadsheet software such as Microsoft Excel. We hope that this Script will be useful to other researchers, so we have detailed the Script and its instructions are below.

C.2. Instructions

Note: These instructions are written for a Mac user.

1. Download the Python script **acaml.py**. Alternatively, use Python's Integrated DeveLopment Environment to compile the text in Section C.3 and name it **acaml.py**.

2. Copy the raw GC data from the GC computer onto your computer, in a folder called **GC data**. Typically, each time point will be in a folder titled ***run name_date_time_*.dat.rslt**. For example, **GC01 2015-03-03 19-23-03 (GMT -08-00).dat.rslt**. Note: the filename convention can be adjusted in the Agilent program. For these purposes, it is most convenient to have the run name listed first in the file.

3. Copy **acaml.py** into the parent directory that contains **GC data** as a subdirectory.

4. Open Terminal. Use Terminal to change directory to the one containing **acaml.py** and **GC data**.

5. Enter into Terminal:

```
python acaml.py results.csv GC\ data/GC01*/*.acaml
```

6. Hit return. The results will be tabulated into a file called **results.csv**.
7. How to interpret the data table: each timepoint is listed as one row. The first column of

each row is the filename from which the data was extracted. The next set columns corresponds to names of gases identified in the Agilent GC. The number of columns here depends on the number of gases that were identified/calibrated. The final set of columns display the concentration measured, in parts per million, for each gas (Figure C.1).

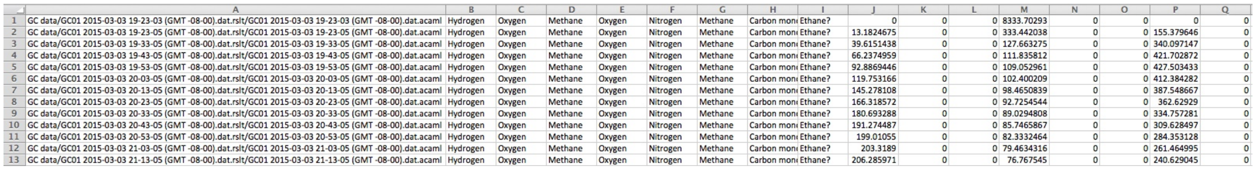

	A	B	C	D	E	F	G	H	I	J	K	L	M	N	O	P	Q
1	GC data/GC01 2015-03-03 19-23-03 (GMT -08-00).dat.rslt/GC01 2015-03-03 19-23-03 (GMT -08-00).dat.acaml	Hydrogen	Oxygen	Methane	Oxygen	Nitrogen	Methane	Carbon mon	Ethane?	0	0	0	8333.70293	0	0	0	0
2	GC data/GC01 2015-03-03 19-23-05 (GMT -08-00).dat.rslt/GC01 2015-03-03 19-23-05 (GMT -08-00).dat.acaml	Hydrogen	Oxygen	Methane	Oxygen	Nitrogen	Methane	Carbon mon	Ethane?	13.1824675	0	0	333.442038	0	0	155.379646	0
3	GC data/GC01 2015-03-03 19-33-05 (GMT -08-00).dat.rslt/GC01 2015-03-03 19-33-05 (GMT -08-00).dat.acaml	Hydrogen	Oxygen	Methane	Oxygen	Nitrogen	Methane	Carbon mon	Ethane?	39.6151438	0	0	127.663275	0	0	340.097147	0
4	GC data/GC01 2015-03-03 19-43-05 (GMT -08-00).dat.rslt/GC01 2015-03-03 19-43-05 (GMT -08-00).dat.acaml	Hydrogen	Oxygen	Methane	Oxygen	Nitrogen	Methane	Carbon mon	Ethane?	66.2374959	0	0	111.835812	0	0	421.702872	0
5	GC data/GC01 2015-03-03 19-53-05 (GMT -08-00).dat.rslt/GC01 2015-03-03 19-53-05 (GMT -08-00).dat.acaml	Hydrogen	Oxygen	Methane	Oxygen	Nitrogen	Methane	Carbon mon	Ethane?	92.8869446	0	0	109.052961	0	0	427.503433	0
6	GC data/GC01 2015-03-03 20-03-05 (GMT -08-00).dat.rslt/GC01 2015-03-03 20-03-05 (GMT -08-00).dat.acaml	Hydrogen	Oxygen	Methane	Oxygen	Nitrogen	Methane	Carbon mon	Ethane?	119.753166	0	0	102.400209	0	0	412.384282	0
7	GC data/GC01 2015-03-03 20-13-05 (GMT -08-00).dat.rslt/GC01 2015-03-03 20-13-05 (GMT -08-00).dat.acaml	Hydrogen	Oxygen	Methane	Oxygen	Nitrogen	Methane	Carbon mon	Ethane?	145.278108	0	0	98.4650839	0	0	387.548667	0
8	GC data/GC01 2015-03-03 20-23-05 (GMT -08-00).dat.rslt/GC01 2015-03-03 20-23-05 (GMT -08-00).dat.acaml	Hydrogen	Oxygen	Methane	Oxygen	Nitrogen	Methane	Carbon mon	Ethane?	166.318572	0	0	92.7254544	0	0	362.62929	0
9	GC data/GC01 2015-03-03 20-33-05 (GMT -08-00).dat.rslt/GC01 2015-03-03 20-33-05 (GMT -08-00).dat.acaml	Hydrogen	Oxygen	Methane	Oxygen	Nitrogen	Methane	Carbon mon	Ethane?	180.693288	0	0	89.0294808	0	0	334.757281	0
10	GC data/GC01 2015-03-03 20-43-05 (GMT -08-00).dat.rslt/GC01 2015-03-03 20-43-05 (GMT -08-00).dat.acaml	Hydrogen	Oxygen	Methane	Oxygen	Nitrogen	Methane	Carbon mon	Ethane?	191.274487	0	0	85.7465867	0	0	309.628497	0
11	GC data/GC01 2015-03-03 20-53-05 (GMT -08-00).dat.rslt/GC01 2015-03-03 20-53-05 (GMT -08-00).dat.acaml	Hydrogen	Oxygen	Methane	Oxygen	Nitrogen	Methane	Carbon mon	Ethane?	199.01055	0	0	82.3332464	0	0	284.353128	0
12	GC data/GC01 2015-03-03 21-03-05 (GMT -08-00).dat.rslt/GC01 2015-03-03 21-03-05 (GMT -08-00).dat.acaml	Hydrogen	Oxygen	Methane	Oxygen	Nitrogen	Methane	Carbon mon	Ethane?	203.3189	0	0	79.4634316	0	0	261.464995	0
13	GC data/GC01 2015-03-03 21-13-05 (GMT -08-00).dat.rslt/GC01 2015-03-03 21-13-05 (GMT -08-00).dat.acaml	Hydrogen	Oxygen	Methane	Oxygen	Nitrogen	Methane	Carbon mon	Ethane?	206.285971	0	0	76.767545	0	0	240.629045	0

Figure C.1. An example of the output file provided by the data extraction script.

```
  #!/usr/bin/env python

  import argparse
  import csv
  from xml.etree.ElementTree import ElementTree

  parser = argparse.ArgumentParser()
  parser.add_argument('output_file')
  parser.add_argument('input_file', nargs='+')
  args = parser.parse_args()

  with open(args.output_file, 'w') as ofp:
      writer = csv.writer(ofp)

      for filename in args.input_file:
          t = ElementTree()
          t.parse(filename)

          # create a look-up dictionary that maps compound ids to
compound names
          # NOTE: this mapping is unique per file, hence building
it fresh for each file
          compounds      =      t.findall('{urn:schemas-agilent-
com:acaml14}Doc/{urn:schemas-agilent-
com:acaml14}Content/{urn:schemas-agilent-com:acaml14}Compound')
          compound_names_by_id = {}
          for c in compounds:
              c_id = c.get('id')
              c_name      =      c.find('{urn:schemas-agilent-
com:acaml14}Name').text
              compound_names_by_id[c_id] = c_name

          # pull the data out of each injection compound section,
and look up the compound name
          injection_compounds = t.findall('{urn:schemas-agilent-
com:acaml14}Doc/{urn:schemas-agilent-
```

```
com:acaml14}Content/{urn:schemas-agilent-
com:acaml14}Injections/{urn:schemas-agilent-
com:acaml14}Result/{urn:schemas-agilent-
com:acaml14}InjectionCompound')
          c_names = []
          c_vals = []
          for ic in injection_compounds:
              reaction_type   =   ic.find('{urn:schemas-agilent-
com:acaml14}Type').text
              if reaction_type == 'Expected':
                  c_val     =     ic.find('{urn:schemas-agilent-
com:acaml14}Amount').get('val')
                  id_compound  =  ic.find('{urn:schemas-agilent-
com:acaml14}IdentifiedCompound')
                  compound_id  =  id_compound.find('{urn:schemas-
agilent-com:acaml14}Compound_ID').get('id')
                  compound_name                                 =
compound_names_by_id[compound_id]
                  c_names.append(compound_name)
                  c_vals.append(c_val)
              elif reaction_type == 'NotIdentifiedExpected':
                  c_val     =     ic.find('{urn:schemas-agilent-
com:acaml14}Amount').get('val')
                  id_compound  =  ic.find('{urn:schemas-agilent-
com:acaml14}IdentifiedCompound')
                  compound_id  =  id_compound.find('{urn:schemas-
agilent-com:acaml14}Compound_ID').get('id')
                  compound_name                                 =
compound_names_by_id[compound_id]
                  c_names.append(compound_name)
                  c_vals.append(c_val)


          # finally, write the filename, then the compound names,
then the compound values to a single row
          writer.writerow([filename] + c_names + c_vals)
```

C.3. Acknowledgements

This Script was written with the generous assistance of Matthew J. Singleton.

C.4. References

(1) Karunadasa, H. I.; Chang, C. J.; Long, J. R. A Molecular Molybdenum-Oxo Catalyst for Generating Hydrogen From Water. *Nature* **2010**, *464* (7293), 1329–1333.

(2) Karunadasa, H. I.; Montalvo, E.; Sun, Y.; Majda, M.; Long, J. R.; Chang, C. J. A Molecular MoS_2 Edge Site Mimic for Catalytic Hydrogen Generation. *Science* **2012**,

335 (6069), 698–702.

(3) Sun, Y.; Bigi, J. P.; Piro, N. A.; Tang, M. L.; Long, J. R.; Chang, C. J. Molecular Cobalt Pentapyridine Catalysts for Generating Hydrogen From Water. *J. Am. Chem. Soc.* **2011**, *133* (24), 9212–9215.

(4) Nippe, M.; Khnayzer, R. S.; Panetier, J. A.; Zee, D. Z.; Olaiya, B. S.; Head-Gordon, M.; Chang, C. J.; Castellano, F. N.; Long, J. R. Catalytic Proton Reduction with Transition Metal Complexes of the Redox-Active Ligand bpy2PYMe. *Chem. Sci.* **2013**, *4* (10), 3934–3945.